Cold polar molecules for novel collision experiments at low energies
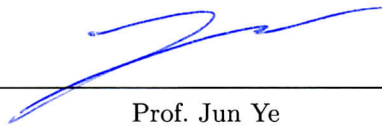
by

Brian Sawyer
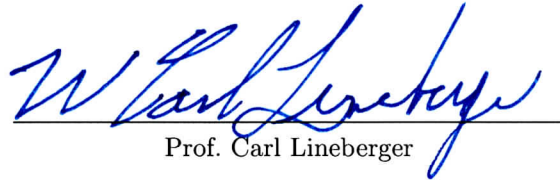
B.S., University of Arkansas, 2003

A thesis submitted to the

Faculty of the Graduate School of the

University of Colorado in partial fulfillment

of the requirements for the degree of

Doctor of Philosophy

Department of Physics

2010

This thesis entitled:
Cold polar molecules for novel collision experiments at low energies
written by Brian Sawyer
has been approved for the Department of Physics

_____

Prof. Jun Ye

_____

Prof. Carl Lineberger

Date _____

The final copy of this thesis has been examined by the signatories, and we find that both the content and the form meet acceptable presentation standards of scholarly work in the above mentioned discipline.

Sawyer, Brian (Ph.D., Physics)

Cold polar molecules for novel collision experiments at low energies

Thesis directed by Prof. Jun Ye

Research in the field of cold polar molecules is progressing rapidly. An array of interesting topics is being developed including precision measurement and fundamental tests, quantum phase transitions, and ultracold chemistry. In particular, dipolar molecules in well-defined quantum states enable exquisite control of their interactions via applied electric fields. The long-range, anisotropic interaction between dipolar molecules leads to new collision dynamics that could be used for novel collective effects, quantum state engineering, and information processing. The focus of this Thesis is the production of cold samples of neutral OH molecules via Stark deceleration and magnetic trapping for novel collision experiments. This novelty results from our combination of cold external beams and trapped target molecules which facilitates observation of dipolar effects as well as low-temperature collision resonances. The large permanent electric dipole moment of OH allows us to precisely tune the lab-frame velocity of the molecular packets from ~ 500 m/s to rest. We have magnetically trapped OH packets at the terminus of our Stark decelerator at a temperature of 70 mK and density of 10^6 cm^{-3}. With improved understanding of Stark deceleration, we optimize the decelerator efficiency and its coupling to the magnetic trap. Our latest trap design uses permanent ring magnets to create a three-dimensional magnetic quadrupole field. Use of magnetically trapped OH molecules for collision experiments with external beams allow us the unique opportunity of observing both elastic and inelastic collisions. In addition, the trap confinement yields sensitivity to differential elastic cross sections at low collision energies. This open magnetic trap has allowed measurement of collision cross sections between trapped OH and external supersonic beams of He and D_2, the latter of which is of astrophysical interest due to the role of H_2-OH collisions in pumping interstellar OH megamasers. The combination of trapped OH molecules and temperature-tuned beams of He and D_2 has facilitated measurement of the lowest-energy D_2-OH collision cross

sections yet reported. More recently, we report the first observation of electric-field dependent cross sections between two different species of cold polar molecules - OH and ND_3 - thereby demonstrating control over molecular scattering in the cold regime. By combining for the first time the production techniques of Stark deceleration and buffer gas cooling, we increase the molecular interaction time by $\sim 10^5$ over traditional crossed-beam experiments to gain enhanced sensitivity at the characteristic densities of cold molecule production.

Dedication

To Liz.

Acknowledgements

I have a number of people to thank for helping either directly or indirectly with the completion of my Ph.D. First off, I would like to thank Jun for giving me a spot in his cold molecule group seven years ago. At the time, I was not completely sure which AMO group would be the best fit, but I could not have picked a better experiment or group of people with whom to work. I went from measuring OH spectra in flames as an undergraduate to producing and trapping the coldest OH samples in the world in the Ye group. I am also grateful to my undergraduate research advisor, Dr. Raj Gupta at the University of Arkansas, for taking a chance on a freshman physics major with little to offer besides enthusiasm. Going even farther back, my high school physics teacher Jerrel Boast was instrumental in cultivating my interest in experimental physics. If the class had been taught by someone else or if I had taken it before getting my act together, I can't imagine what I would be doing today.

I have worked with a number of great people during my time at JILA. I have to thank Eric Hudson for welcoming me into the cold molecules group, showing me the ropes, and repeatedly demonstrating that sometimes you just have to turn the knob and see what happens. I will never forget the long days of bluegrass and jam music that I was forced to endure, and I'm sure I will never be as good a ping-pong player as I was in 2005. Jason Bochinski first introduced me to the black art of supersonic beam production, and Heather Lewandowski still gives me advice on ammonia detection and photolysis sources since becoming a faculty member. Ben Lev worked in the group for two years as an NRC postdoc and was a major part of our first magnetic trapping experiment. Ben Stuhl joined the lab a few years after me, and we worked together on the trapping

and collision experiments. He and I rarely run out of experimental issues to discuss, and I believe our often different points of view helped keep the experiments moving forward. He is also an amazing programmer who has improved a number of our data-taking and control codes. Mark Yeo has done a great job bringing more advanced optics techniques into the cold molecule experiments, and he and I share a love of bacon and extreme metal. Matt Hummon recently joined our group as an NRC postdoc, and he has brought with him a wealth of knowledge about cryogenics and buffer gas sources. I know that I am leaving the OH experiment in good hands, and look forward to reading some exciting papers in the near future.

Doing research at JILA is an amazing experience. I have to thank the staff machinists Kim, Hans, Tracy, Ariel, Blaine, Alan, Tom, Dave, and Todd for building pieces that, in many cases, are as artistically appealing as they are useful. The electronics shop staff of Paul, Carl, James, Mike, and Terry also helped immensely with the construction and operation of many of our cold molecule experiments. Our buffer gas source collaboration with the group of John Doyle at Harvard was very fruitful and culminated in our most recent OH-ND$_3$ collision measurement. Dave Patterson from John's group is a very talented experimentalist and also a fun guy to hang with.

My parents always encouraged me to follow my own interests and never placed any specific career expectations on me, and for that I am grateful. I can imagine that philosophy requires an immense amount of restraint, especially when your son says he wants to forego college or graduate school for a career in the music industry. Nevertheless, my mom always expected the best out of me and has remained supportive through everything. My dad has always been a free spirit, and the combination of him and my mom helped to make me simultaneously cautious and rebellious. I have enjoyed being the oldest of five kids. Layne, Max, Mike, and Will have always shown me an amazing amount of love and support, and I have missed them all since starting college and only rarely finding time to get back to Arkansas.

When I first moved to Colorado for graduate school in 2003 I only knew two or three people in the Boulder/Denver area, but I was determined to start a band with talented, like-minded musicians. The only person who ever answered my online ad was Ryan Conner of Denver, and

we've been best friends ever since forming Cryogen in 2004. Since then, we've developed a solid lineup with Aaron Lande, Mike Papajohn, and Chris Giggliotti. I want to thank all of these guys for the countless hours of writing/rehearsing and the four albums we've released as a band. As the only two guys who can stay awake in a moving vehicle, Mike and I had some interesting political discussions at 4 am on tour between Salt Lake City, Milwaukee, Chicago, Indianapolis, Des Moines, and Cincinnati. I want to thank Ryan, Mike, Aaron, and Chris for contributing to some great extreme music and for allowing me to play shows with bands whose posters I used to hang on my wall in high school. They gave me something to do between the hours of 10 pm and 4 am that had nothing to do with cold molecule physics.

Finally, I would like to thank Liz for coming into my life as a rock star photographer slumming it shooting local bands on weeknights. I can't imagine my life without her, as she has helped me through some tough experiences. Her unwavering support and realism keep me grounded and help me maintain a sense of perspective when I'm taking work or music too seriously. She has endured my long hours away at the lab and on the road, but she understands and loves me in spite of my obsessive tendencies.

Contents

Chapter

Tables

Table

Figures

Chapter 1

Introduction

1.1   Why Polar Molecules?

Tremendous progress in the field of laser cooling and trapping of neutral alkali atoms has allowed observation of exotic ultracold phases of matter [6, 7, 8], realization of fundamental condensed-matter systems [9], and precision measurements [10]. Interestingly, these novel physical systems rely on purely isotropic interatomic potentials. Nevertheless, the ability to exert control over atomic interactions via Feshbach resonances has proven invaluable [11]. Inspired by these successes, researchers began to imagine the possibilities for cold or ultracold systems in the presence of *anisotropic* inter-particle interactions [12]. Such anisotropy has been realized in atomic species with large magnetic dipoles [13], but polar molecules can also provide this anisotropy due to their dipole-dipole interaction potential in the presence of an external electric field that takes the form

$$U(r) = \frac{1}{4\pi\epsilon_0} \frac{\mu^2[1 - 3(\hat{\mu} \cdot \hat{r})^2]}{r^3} \tag{1.1}$$

where μ is the molecular permanent electric dipole moment, r is the intermolecular distance, and $\hat{r}$ is a unit vector along this intermolecular spacing. Immediately, we see that an ensemble of molecules mutually aligned in a homogeneous electric field will experience attractive head-to-tail interactions but repulsive side-to-side interactions. Furthermore, compared to the contact interactions with delta-function potentials between colliding ultracold atoms, polar molecules display a long-range r^{-3} potential that significantly alters their collision dynamics. In an ultracold dipolar molecular system, this long-range interaction may even be exploited to perform quantum computation [14, 15]

or, in the not-too-distant future, direct simulation of quantum Hamiltonians [16]. In the following sections, two applications of cold and ultracold neutral polar molecules are briefly discussed – namely, dipolar collisions and precision measurements.

1.1.1   Cold and Ultracold Collisions

The expectation value of the molecular electric dipole moment is entirely dependent on the magnitude of an applied external field (see Chapter 2). As such, polar molecules not only offer anisotropic interactions in an electric (E) field; they present an opportunity for direct control of the intermolecular potential through the application of E-fields as small as 1 kV/cm. However, the relative influence of the long-range portion of the intermolecular potential depends on the collision energy of the interacting molecules. In Ref. [4], Bohn et al define convenient energy (U_D) and length (D) scales for two colliding polar molecules with dipole moments, μ_1/μ_2, and reduced mass, M, as (in atomic units)

$$D \quad = \quad M\mu_1\mu_2 \tag{1.2}$$

$$U_D \quad = \quad \frac{1}{M^3\mu_1^2\mu_2^2}. \tag{1.3}$$

Inserting appropriate values for the OH molecule ($\langle\mu\rangle = 1.0$ D, $M = 8.5$ amu), one obtains $U_D^{OH} = 3.6$ μK and $D^{OH} = 2400$ a_0 (a_0 is the Bohr radius). At energies below U_D, the collision cross section is dominated by a single partial wave that is either an s ($l = 0$) or p ($l = 1$) wave depending on the quantum statistics of the colliding molecules. In this ultracold regime, the elastic cross section due to the dipolar interaction is energy-independent and scales as μ^4. As the collision energy is increased above U_D, the molecular collision becomes semiclassical in nature as more partial waves contribute to the cross section. We denote this as scattering in the cold regime. At these higher temperatures, the elastic cross section decreases as $U^{-1/2}$ and elastic collision rates defined as σv are energy-independent. Figure 1.1 provides a schematic depiction of the behavior of cross sections in these two energy regimes.

The cold molecule labs at JILA are leading the field with respect to cold and ultracold dipolar

collisions. Recent experiments with ultracold samples of KRb molecules have demonstrated E-field dependent chemical reactions in the quantum collision regime [17], and future KRb experiments in traps of reduced dimensionality promise to directly probe the universal elastic scattering behavior described in Ref. [4]. Also, as detailed in Chapter 7 of this Thesis and Ref. [18], we have demonstrated electric-field enhancement of elastic collision cross sections between samples of polar OH and ND_3 molecules at a temperature of 5 K. The history of low-temperature dipolar molecular collisions is just beginning to be written, and the future promises a host of new discoveries in the field of cold collisions and chemistry [12].
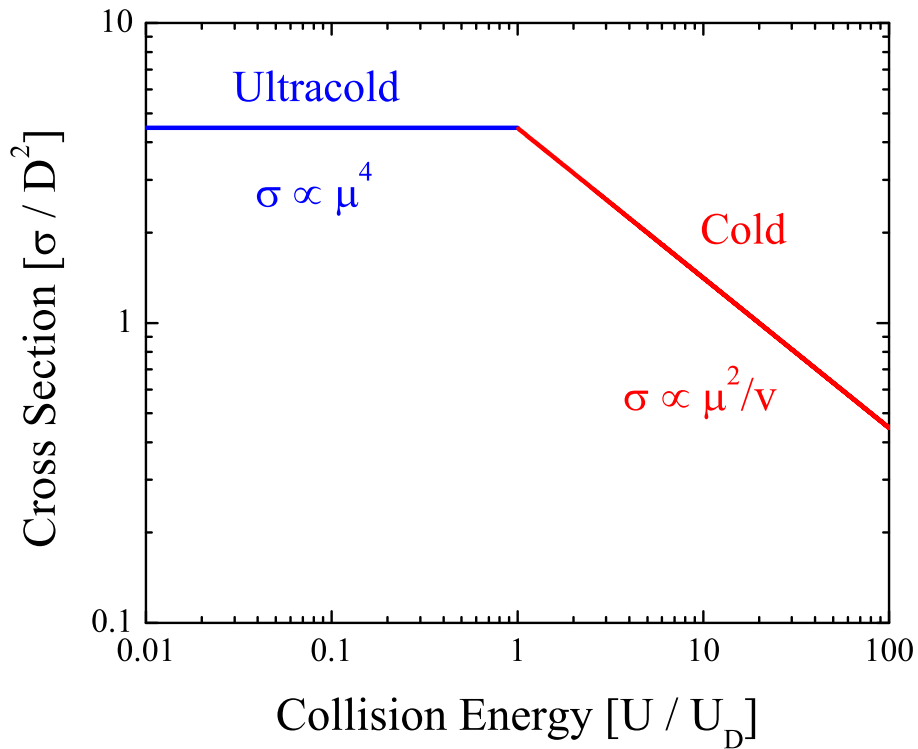
Figure 1.1: Schematic view of dipolar scattering as a function of collision energy in units of the dipole energy, U_D. At ultracold temperatures ($U < U_D$), the Born approximation is valid and cross sections are independent of temperature. At energies above U_D, the cross section decreases as the inverse of the relative collision velocity. This plot is adapted from a more accurate numerical calculation presented in Ref. [4].

1.1.2   Precision Spectroscopy

Precision measurements represent another enticing application for cold polar molecules. With the development of molecular Stark deceleration [19] and buffer gas cooling [20] techniques more than a decade ago, it became possible to significantly increase one's interaction time with the species of interest and, at the same time, reduce the sample temperature while simultaneously increasing its rotational/vibrational state purity. Additionally, the rich internal structure of molecules provides a host of transitions from microwave to ultraviolet wavelengths with differing sensitivity to a number of fundamental constants. This range of spectra within a given species can be used to compare molecular transition frequencies over galactic timescales with the goal of constraining the time evolution of fundamental constants [21]. By using different molecular transitions as opposed to different atomic species, one can minimize systematic errors common to space-based measurements [22]. As described in the following sections, different groups have made use of cold polar species for precision molecular spectroscopy in both beams and trapped samples.

1.1.2.1   Cold Beams

Using Stark decelerated OH molecules coupled to a microwave cavity, our group has improved upon previous measurements of the main ($\Delta F = 0$)) and satellite ($\Delta F = \pm 1$) ground-state Λ-doublet transitions by an order-of-magnitude [21, 23, 24]. By combining these measurements with those of large-redshift OH megamasers of similar precision, we will be able to restrict the fractional variation of the fine structure constant, α, to 10^{-6} over $\sim 10^{10}$ years. Furthermore, we have quantified the differential magnetic g-factor between the upper and lower Λ-doublet states [24]. The 100 mK temperature, low velocity, and high state purity of the Stark decelerated OH molecules all contributed to these improved measurements of the Λ-doublet transitions. Through comparison with our laboratory measurements, recent astrophysical OH spectra have hinted at possible temporal variation of the fine structure constant over $\sim 2.9 \times 10^9$ yrs [25]. Additional astrophysical atomic spectra have suggested possible spatial variation of α [26].

With their internal electric fields as large as 100 GV/cm, heavy polar molecules can provide enhanced sensitivity for fundamental symmetry tests like the search for an electron electric dipole moment(eEDM) [27]. Two eEDM searches using beams of neutral polar molecules produced via buffer gas cooling are currently underway. These experiments are separately probing metastable PbO ($a(1)^3\Sigma^+$) [28] and ThO ($H^3\Delta_1$) molecules [29]. Stark decelerators readily produce colder molecular samples with larger state purity than buffer gas beams — generally at the expense of molecular density. However, given the large masses and small rotational constants of candidate eEDM molecules, thus far only one such Stark deceleration experiment has been proposed [30].

1.1.2.2   Trapped Molecules

By confining molecules in magnetic or electrostatic traps, one gains unprecedented interrogation times of ~ 1 s with cold, state-selected molecular samples. The group of G. Meijer has directly measured the 59 ms lifetime of vibrationally-excited ($v = 1$) OH molecules trapped within an electrostatic quadrupole, thereby reducing the uncertainty of the Einstein A-coefficient to $\sim 3\%$ [31]. In a similar experiment, the same group directly measured the decay fluorescence from trapped metastable CO molecules [32]. The group of J. Doyle has also performed direct vibrational lifetime measurements on buffer gas cooled NH ($^3\Sigma^-, v = 1$) molecules confined within a magnetic trap [33]. These unique spectroscopy experiments with trapped cold molecules are likely just the beginning for this relatively new research field.

Chapter 2

Molecular Spectroscopy

Molecules possess rich internal structure that spans the electromagnetic spectrum from microwave to ultraviolet. In contrast to atoms, the $\sim 1\text{Å}$ separation of constituent nuclei allows for rotations and vibrations at energies far below those of electronic excitations. While this complicated structure has precluded development of a general molecular laser cooling technique [34], it makes molecules ideal candidates for certain precision measurement [29, 35, 36, 37], quantum information [38], and controlled collision experiments [17, 39, 40], as well as future experiments in quantum many-body physics [16]. The goal of this chapter is to acquaint the reader with the basic molecular theory necessary to perform experiments with polar symmetric top molecules.

2.1   Hund's Coupling Cases

Before delving into full molecular Hamiltonians, it is useful to review the Hund's cases (a)-(e) that describe coupling of electronic and orbital angular momenta within diatomic molecules. Although the five cases summarized here are idealizations, they provide a convenient starting point for spectroscopy calculations. Generally, one will begin with a basis of angular momenta that is nearly diagonal considering appropriate coupling constants for the molecule of interest. Of course, upon diagonalization of their Hamiltonian, many molecules will be best described by intermediate coupling cases. For the following overview, I define angular momentum vectors as shown below:

L,   Orbital electronic angular momentum

Λ,   Vector component of **L** along the internuclear axis

S,   Total spin electronic angular momentum

Σ,   Vector component of **S** along the internuclear axis

N,   Nuclear rotational angular momentum

$\mathbf{J}_a$,   Vector sum of **L**, **S** in the absence of coupling to the internuclear axis

Ω,   Vector component of (**L**+**S**) along the internuclear axis

K,   Vector sum of **Λ**, **N**

R,   Total angular momentum excluding nuclear, electron spin (**J** - **S** = **L** + **N**)

J,   Total angular momentum excluding nuclear spin (**L** + **N** + **S**).

2.1.1   Case (a)

The first Hund's case deals with molecular states possessing a large spin-orbit coupling as well as strong electrostatic coupling of **L** to the internuclear axis as illustrated in Fig. 2.1a. The large spin-orbit coefficient A ensures that **S** is also coupled to the internuclear axis. We may then define the quantum numbers Λ and Σ as the projections of **L** and **S** along this axis, respectively. These projections sum to form Ω, which assumes all values $|\Lambda - \Sigma|$, $|\Lambda - \Sigma| + 1,...|\Lambda + \Sigma|$. The total angular momentum **J** is defined as $\mathbf{J} = \mathbf{\Omega} + \mathbf{N}$ and satisfies the condition $J \geq \Omega$, which is a direct result of $\mathbf{\Omega} \perp \mathbf{N}$. The good quantum numbers are Λ, Σ, Ω, and J. As will be discussed later, since Ω, Λ, and Σ may all take positive or negative values, these molecules possess so-called Λ-doublets arising from a breaking of this projection degeneracy. Assuming a rigid rotor with rotational constant $B = \hbar^2/2\mu r^2$, where μ is reduced mass and r is internuclear separation, the rotational energy of a given quantum state in this basis is

$$E_{rot} = B\frac{\langle \mathbf{N}^2 \rangle}{\hbar^2} = B[J(J+1) - \Omega^2]. \tag{2.1}$$

Some good examples of Hund's case (a) states are NO, ClO and BrO, all of which are $^2\Pi$ molecules in their ground states satisfying $A \gg B$. Our cold molecule of choice, OH, deviates from

pure case (a) due to its small moment of inertia which yields $A/B \approx -7.5$. In this intermediate regime, Ω strictly ceases to be a good quantum number due to a non-negligible mixing of different Ω states possessing the same J. Generally speaking, case (a) molecules move closer to case (b) as J increases.

2.1.2   Case (b)

When $\mathbf{S}$ is weakly coupled to the internuclear axis due to either weak or absent ($\Lambda = 0$) spin-orbit mixing and $\Lambda \neq 0$ is strongly coupled to the axis, a state is classified as Hund's case (b). The simplest example of a case (b) molecule is one in a $^2\Sigma$ state. Molecular states with $^2\Pi$ symmetry may also be included if J is sufficiently large. Returning to hydroxyl, the electronically excited $A^2\Sigma^+$ state used for laser-induced fluorescence detection is case (b). The good quantum numbers for this case are Λ, N, K, and J, where $\mathbf{K} = \mathbf{\Lambda} + \mathbf{N}$ as shown in Fig. 2.1b. Case (b) molecules with $\Lambda \neq 0$ exhibit what can be considered a 'true' Λ-doubling arising exclusively from a breaking of degeneracy between $\pm\Lambda$ projections.

2.1.3   Case (c)

If the $\mathbf{L} \cdot \mathbf{S}$ term in the molecular Hamiltonian is sufficiently strong so as to overcome any electrostatic coupling of $\mathbf{L}$ to the internuclear axis, then a state exhibits case (c) coupling. Heavy diatomics such as AsF and SO (both $^3\Sigma^-$) are best described as case (c), where Λ and Σ are no longer good quantum numbers but the projection $\Omega = \mathbf{J}_a \cdot \hat{R} = (\mathbf{L} + \mathbf{S}) \cdot \hat{R}$ is still well-defined. As with cases (a) and (b), these molecules can possess parity-doublets known as Ω-doublets since they originate from the different Ω projections along $\hat{R}$. The good quantum numbers are J_a, Ω, and J. In fact, one may consider case (c) a more general form of (a) and (b) where Λ and Σ are not well-defined.
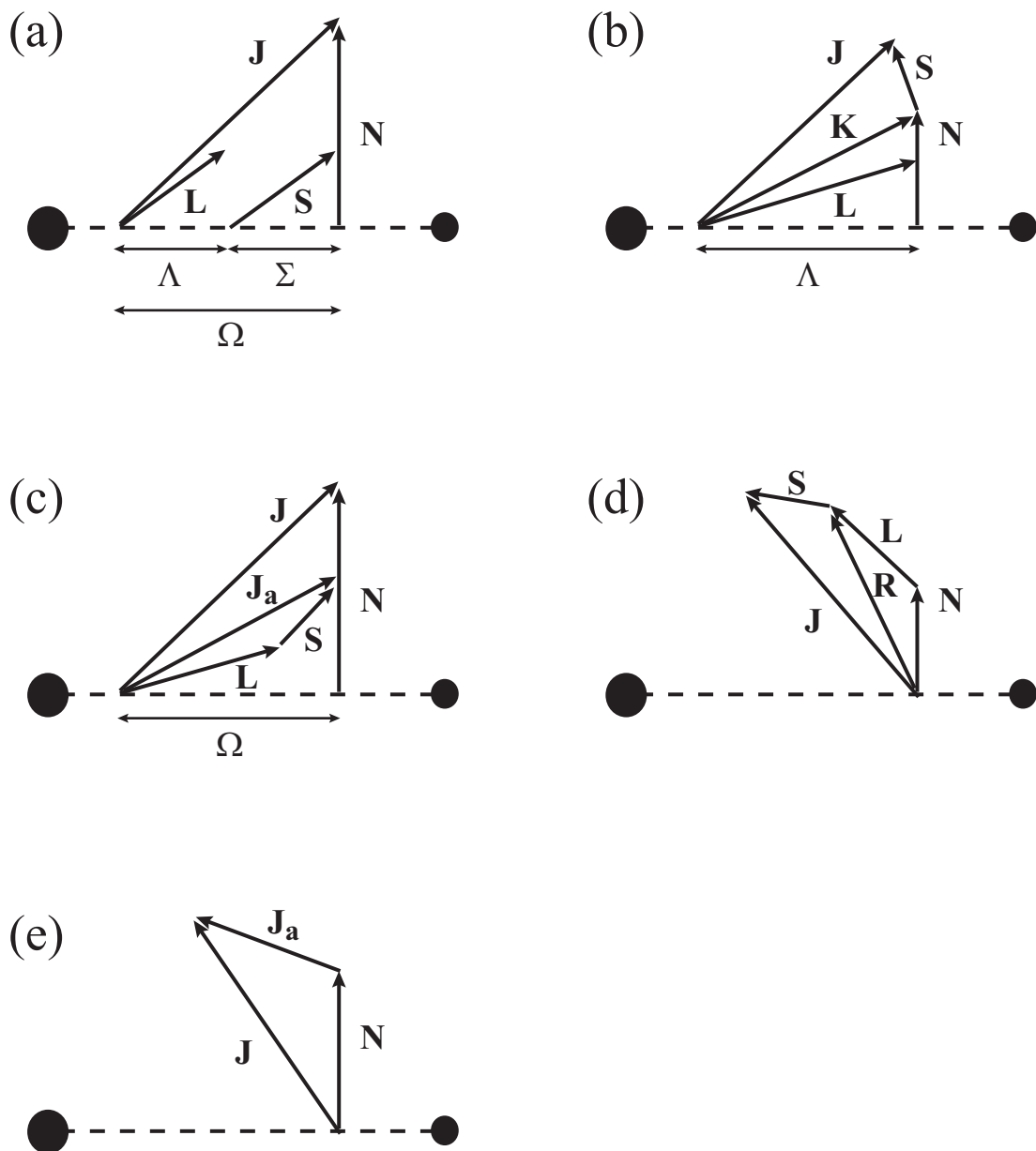
Figure 2.1: Illustration of the five Hund's Cases for angular momentum coupling in diatomic molecules. (a) Both $\mathbf{L}$ and $\mathbf{S}$ are strongly coupled to the internuclear axis ($\mathbf{L}$ due to electrostatic forces and $\mathbf{S}$ through the spin-orbit coupling), forming the quantum number $\Omega = \Lambda + \Sigma$ along the axis. (b) Spin $\mathbf{S}$ is weakly coupled to the axis due to small or absent ($\Lambda = 0$) spin-orbit mixing but instead couples to the resultant $\mathbf{K} = \mathbf{\Lambda} + \mathbf{N}$. (c) Neither $\mathbf{L}$ nor $\mathbf{S}$ are strongly coupled to the internuclear axis, but these vectors add to form $\mathbf{J}_a$ whose projection on the axis is given by Ω. (d) Orbital angular momentum $\mathbf{L}$ couples more strongly to nuclear rotation $\mathbf{N}$ than to the axis. (e) The vector $\mathbf{J}_a = \mathbf{L} + \mathbf{S}$ results from strong spin-orbit mixing and couples to $\mathbf{N}$.

2.1.4 Cases (d) and (e)

In this section, I combine the discussion of Hund's cases (d) and (e) molecules due to both their similarity and rarity. Both cases are characterized by a loss of Λ, Σ, and Ω as good quantum numbers. Shown in Fig. 2.1d, case (d) molecules exhibit a strong $\mathbf{L} \cdot \mathbf{N}$ coupling term forming the resultant $\mathbf{R}$. Total angular momentum is then defined as $\mathbf{J} = \mathbf{R} + \mathbf{S}$, and the good quantum numbers are L, N, R, S, and J. Rydberg molecules, defined by their large principal quantum number, possess very small valence-core interactions and may be considered case (d). If the spin-orbit term in the Hamiltonian is large enough to render L and S undefined, we move to a final case (e) coupling in which only J_a, N, and J are well-defined. Molecules possessing case (e) states are rare, with the only known example being the exotic vibrationally-excited $HeKr^+$.

2.2 Spectra of Polar Symmetric Tops

Molecular rotations may be described by three moments of inertia (I_x, I_y, I_z) about three orthogonal principal axes $(\hat{x}, \hat{y}, \hat{z})$. If two or more of these moments are identical (e.g. all diatomics and molecules of the form XY_3), the molecule is a symmetric top. If all three moments are identical as in C_{60}, a molecule is a spherical top. In this section, I will describe the structure of two symmetric top molecules that we have used in cold collision experiments - namely OH and ND_3. These two species provide a nice overview of molecular Hamiltonians since both require non-trivial calculations to get an accurate view of their spectroscopy. For ND_3, this is especially true in the case of three-photon ionization which is commonly used for detection.

When a molecule's electron distribution is asymmetric along a particular dimension, it possesses a permanent electric dipole moment and is dubbed 'polar.' The simplest examples of polar molecules are the heteronuclear diatomics (e.g. OH, HCl, SrO, etc.), wherein electrons are more likely to be found near the most electronegative atom. The most common unit for molecular dipoles is the Debye (D), where $1D = 0.39 e a_0 = 3.33 \times 10^{-30} Cm$ (e is the electron charge and $a_0 = 0.5 Å$ is the Bohr radius). Perhaps a more familiar unit to physicists is the atomic unit $e a_0$, but the Debye

was originally defined in cgs units as 10^{-18}statC cm, or the dipole moment of two opposite charges of 10^{-10}statC $= 3.3 \times 10^{-20}$C at a separation of 1Å. The actual expectation value of the dipole moment is state-dependent and will be discussed later in the context of the molecular Stark effect.

2.2.1 Hydroxyl Radical (OH)

The hydroxyl radical is a unique molecule due to its combination of low mass and $^2\Pi$ ground electronic structure. As described in the previous section, the molecule's relatively large rotational constant resulting from the small moment of inertia yields an intermediate coupling in the ground state. While most closely resembling a Hund's case (a) molecule, the $^2\Pi_{3/2}$ ground state displays non-negligible mixing with the spin-orbit split $^2\Pi_{1/2}$ state which makes the description more complicated than for heavier $^2\Pi$ molecules like CH. Furthermore, OH possesses a small ($\sim$1.7 GHz) Λ-doublet splitting resulting from coupling of the angular momentum projection Λ with nuclear rotation of excited electronic states.

We begin with the following effective Hamiltonian to describe the rotational, fine structure, and Λ-doublet energies [41]:

$$\hat{H}_{eff} = \hat{H}_{rot} + \hat{H}_{fs} + \hat{H}_\Lambda \tag{2.2}$$

where

$$\hat{H}_{rot} \quad = \quad = \quad B\mathbf{R}^2 \quad = \quad B(\mathbf{J} - \mathbf{S})^2 \quad = \quad B(J^2 + S^2 - 2\mathbf{J} \cdot \mathbf{S}) \tag{2.3}$$

$$\hat{H}_{fs} \quad = \quad A\mathbf{L} \cdot \mathbf{S} + \gamma \mathbf{R} \cdot \mathbf{S} \quad = \quad A\mathbf{L} \cdot \mathbf{S} + \gamma \left[\mathbf{J} \cdot \mathbf{S} - S^2 \right] \tag{2.4}$$

$$\hat{H}_\Lambda \quad = \quad -\frac{1}{2}q(J_+^2 \exp^{-2i\phi} + J_-^2 \exp^{2i\phi}) + \frac{1}{2}(p + 2q)(J_+ S_+ \exp^{-2i\phi} + J_- S_- \exp^{2i\phi}). \tag{2.5}$$

In the above Hamiltonian, A is the spin-orbit coupling, B is the rotational constant, and γ is the electron spin-rotation parameter. The values p and q are the Λ-doubling parameters resulting from interactions between ($\mathbf{S}$, $\mathbf{R}$) and ($\mathbf{R}$, $\mathbf{R}$), respectively. As a result, for singlet states only the q parameter is non-zero while, for triplet states, there is an additional o parameter describing the ($\mathbf{S}$, $\mathbf{S}$) interaction. Note that the Λ-doubling parameters p, q, o are set by these interactions

across electronic states (e.g. $\Pi \leftrightarrow \Sigma$) and therefore depend on the shapes of the different electronic potentials.

We will now define a parity basis in order to obtain eigenvalues of Eq. 2.2. For a $^2\Pi$ molecule, this basis consists of the usual case (a) quantum numbers $(\Lambda, \Sigma, \bar{\Omega} = |\Omega|, J, M_J)$ with the added parameter $\epsilon = \pm 1$ which will give the symmetry of each state. The overall parity of a state $|\Lambda \Sigma \bar{\Omega} J M_J \epsilon\rangle$ is given by $\epsilon(-1)^{J-1/2}$ and we define

$$|J M_J \bar{\Omega} \pm\rangle = \left(\frac{|J M_J \bar{\Omega}, \Lambda\Sigma\rangle + \epsilon|J M_J \bar{\Omega}, -\Lambda - \Sigma\rangle}{\sqrt{2}} \right). \tag{2.6}$$

Using the angular momentum operator identity $\mathbf{A} \cdot \mathbf{B} = A_z B_z - \frac{1}{2}(A_+ B_- + A_- B_+)$, where $A_+ = (A_x + iA_y)$ and $A_- = (A_x - iA_y)$, we obtain the following 4×4 matrix using Eqs. 2.2 and 2.6:

$$\begin{pmatrix} a_{11} & a_{12} & 0 & 0 \\ a_{21} & a_{22} & 0 & 0 \\ 0 & 0 & a_{33} & a_{34} \\ 0 & 0 & a_{43} & a_{44} \end{pmatrix} \tag{2.7}$$

where

$$a_{11} = \frac{1}{2}A + B\left[J(J+1) - \frac{7}{4}\right]$$

$$a_{12} = a_{21} = -\sqrt{(J+\tfrac{3}{2})(J-\tfrac{1}{2})}\left[\left(B - \frac{\gamma}{2}\right) - (-1)^{J-1/2}\left(\frac{q}{2}\right)\left(J + \frac{1}{2}\right)\right]$$

$$a_{22} = -\frac{1}{2}A + B\left[J(J+1) + \frac{1}{4}\right] - \gamma - \frac{1}{2}(-1)^{J-1/2}(p+2q)\left(J + \frac{1}{2}\right)$$

$$a_{33} = \frac{1}{2}A + B\left[J(J+1) - \frac{7}{4}\right]$$

$$a_{34} = a_{43} = -\sqrt{(J+\tfrac{3}{2})(J-\tfrac{1}{2})}\left[\left(B - \frac{\gamma}{2}\right) + (-1)^{J-1/2}\left(\frac{q}{2}\right)\left(J + \frac{1}{2}\right)\right]$$

$$a_{44} = -\frac{1}{2}A + B\left[J(J+1) + \frac{1}{4}\right] - \gamma + \frac{1}{2}(-1)^{J-1/2}(p+2q)\left(J + \frac{1}{2}\right). \tag{2.8}$$

The above matrix represents a general result for $^2\Pi$ molecules. We can immediately see that the off-diagonal elements $a_{12} = a_{21}$ and $a_{34} = a_{43}$ couple the $\bar{\Omega} = 1/2$ and $\bar{\Omega} = 3/2$ states, and that this coupling increases with J in a given molecule. This leads to a transition from case (a) to case (b) at large J. Also, the dependence of these terms on B tells us that light molecules
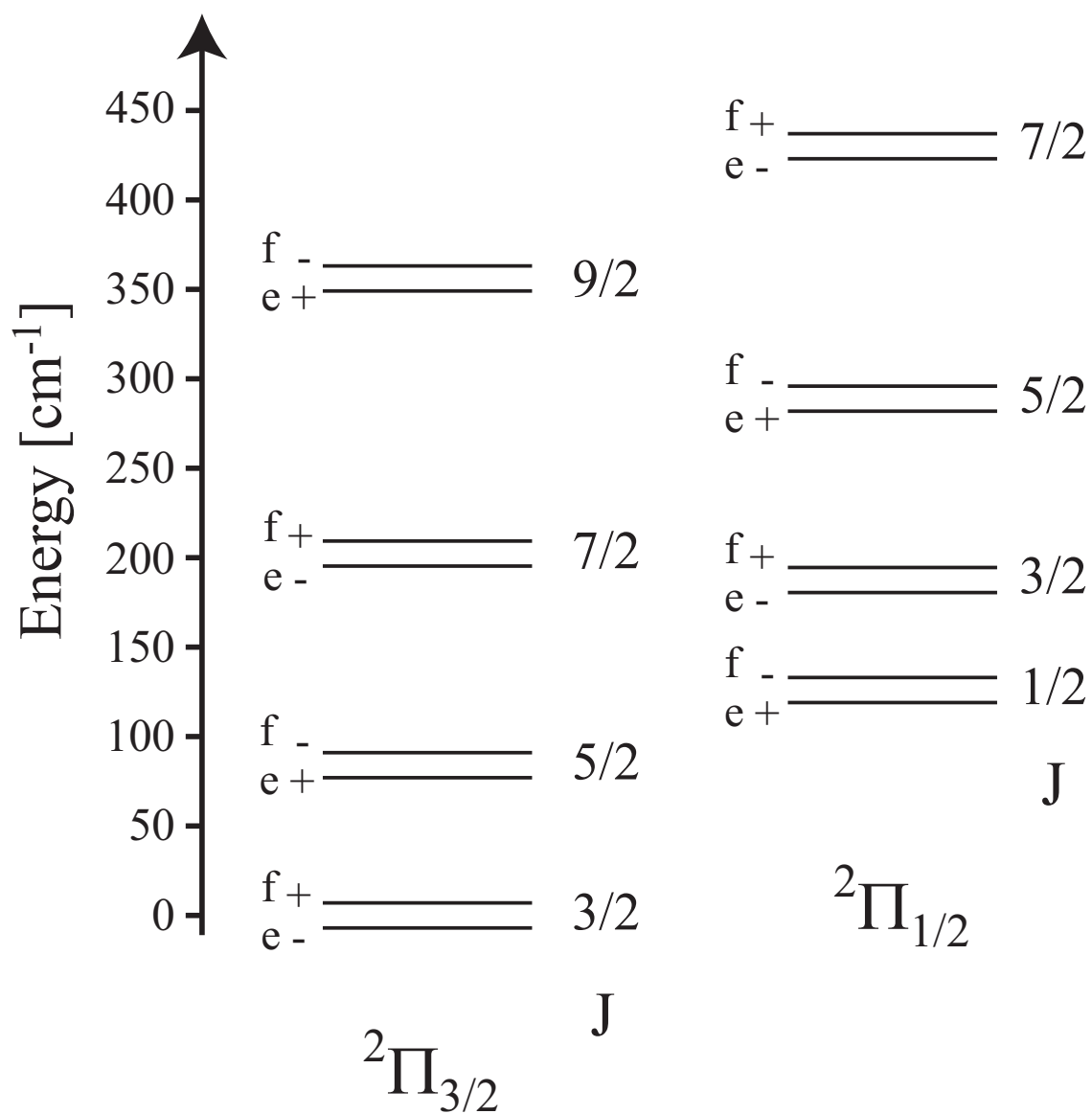
Figure 2.2: Illustration of the rotational structure of the OH electronic and vibrational ground state. The Λ-doublet splitting of each rotational level has been exaggerated for clarity. The (e,f) quantum numbers represent the symmetry of the given Λ-doublet component, while the ± denotes the overall J-dependent parity of the state.

Table 2.1: OH Rotation and Fine-Structure Constants (obtained from Ref. [1])

	Parameter	Frequency [cm^{-1}]			
		$v = 0$	$v = 1$	$v = 2$	$v = 3$
$X^2\Pi$	B	18.5348734	17.8239122	17.1224586	16.4278912
	A	-139.050895	-139.320532	-139.5881	-139.8431
	γ	-0.119190	-0.113753	-0.10831	-0.10249
	p	0.235266041	0.22467831	0.21392702	0.202883
	q	-0.03869315652	-0.036939875	-0.035175264	-0.03338660
$A^2\Sigma^+$	B	16.965060	16.129332	15.286447	14.42222
	D	0.002063218	0.002045047	0.00204786	0.00206501
	γ	0.22555	0.2161	0.2066	0.1975

will deviate from case (a) at lower J than their heavier counterparts. Specializing to OH, we use the $(v = 0)$ molecular constants of Table 2.1 to compute the ground rotational structure shown in Fig. 2.2. All of the matrix elements and molecular constants of this section are based on our initial choice of $\hat{H}_{rot} = B\mathbf{R}^2 = B(\mathbf{J} - \mathbf{S})^2$. Note that if a different choice is made (i.e. $\hat{H}_{rot} = B\mathbf{N}^2 = B(\mathbf{J} - \mathbf{L} - \mathbf{S})^2$), then the values of fitted molecular constants will change if $\Lambda \neq 0$. Reference [42] gives the appropriate expressions for transforming spectroscopic constants between these two regimes.

2.2.1.1 OH LIF Spectroscopy

Hydroxyl is readily detected using laser-induced fluorescence (LIF) at ultraviolet wavelengths along the $A^2\Sigma^+_{1/2} \leftarrow X^2\Pi_{3/2}$ electronic transition. To calculate the positions of the dipole-allowed $\Delta R = \{-2, -1, 0, 1, 2\} = \{O, P, Q, R, S\}$ lines satisfying $\Delta J = 0, \pm 1$, we must consider the molecular constants for the $^2\Sigma^+$ excited state, which is best described by Hund's case (b). The vibration-changing $A^2\Sigma^+_{1/2}(v = 1) \leftarrow X^2\Pi_{3/2}(v = 0)$ transitions are the most useful for fluorescence detection since the excitation and decay wavelengths are well-separated, allowing for effective filtering of the pump light. This separation arises from the large Franck-Condon overlap of $\Delta v = 0$ transitions relative to $\Delta v \neq 0$, which forces spontaneous decay primarily along $A^2\Sigma^+_{1/2}(v = 1) \rightarrow X^2\Pi(v = 1)$.

Table 2.2: OH Vibration Constants (obtained from Ref. [2]). The constant T_e is defined at the energy minimum of the given electronic potential.

	Frequency [cm^{-1}]		
	T_e	ω_e	$\omega_e x_e$
$X^2\Pi$	0	3178.8	92.91
$A^2\Sigma^+$	32684.1	3737.76	84.881

The relevant spectroscopic constants for the $^2\Sigma^+$ state of OH are given in Table 2.1, while the case (b) Hamiltonian for this excited state is

$$
\begin{aligned}
\hat{H}_{eff} &= \hat{H}_{rot} + \hat{H}_{fs} \\
&= B\mathbf{N}^2 - D(\mathbf{N}^2)^2 + \gamma\mathbf{N}\cdot\mathbf{S}
\end{aligned}
\tag{2.9}
$$

whose eigenvalues are simply

$$
[B - DN(N+1)]\,N(N+1) + \frac{\gamma}{2}\left[J(J+1) - N(N+1) - S(S+1)\right].
\tag{2.10}
$$

The diagonal nature of Eq. 2.9 makes inclusion of the additional centrifugal stretching term (D) trivial. Since we are interested in transitions between different vibrational levels in the $^2\Pi$ and $^2\Sigma$ electronic states, we must also consider the vibrational structure of each electronic state whose energy is given by

$$
U_{vib} = \omega_e(v + \frac{1}{2}) - \omega_e x_e(v + \frac{1}{2})^2
\tag{2.11}
$$

where v is the vibrational quantum number ($v = 0, 1, 2, ...$) and ω_e, $\omega_e x_e$ are the vibrational spectroscopic constants given in Table 2.2.

To fully describe OH dipole transitions, we must also define the spectroscopic number F, which is (confusingly) distinct from the hyperfine quantum number F. Levels are designated F = 1 by default, but the value F = 2 is used wherever there exists an angular momentum doublet, and in such cases the lower-energy partner is given the value F = 1 while the higher-energy component is labelled F = 2. This label is affixed to the spectroscopic terms {O, P, Q, R, S} as either F$'$F$''$
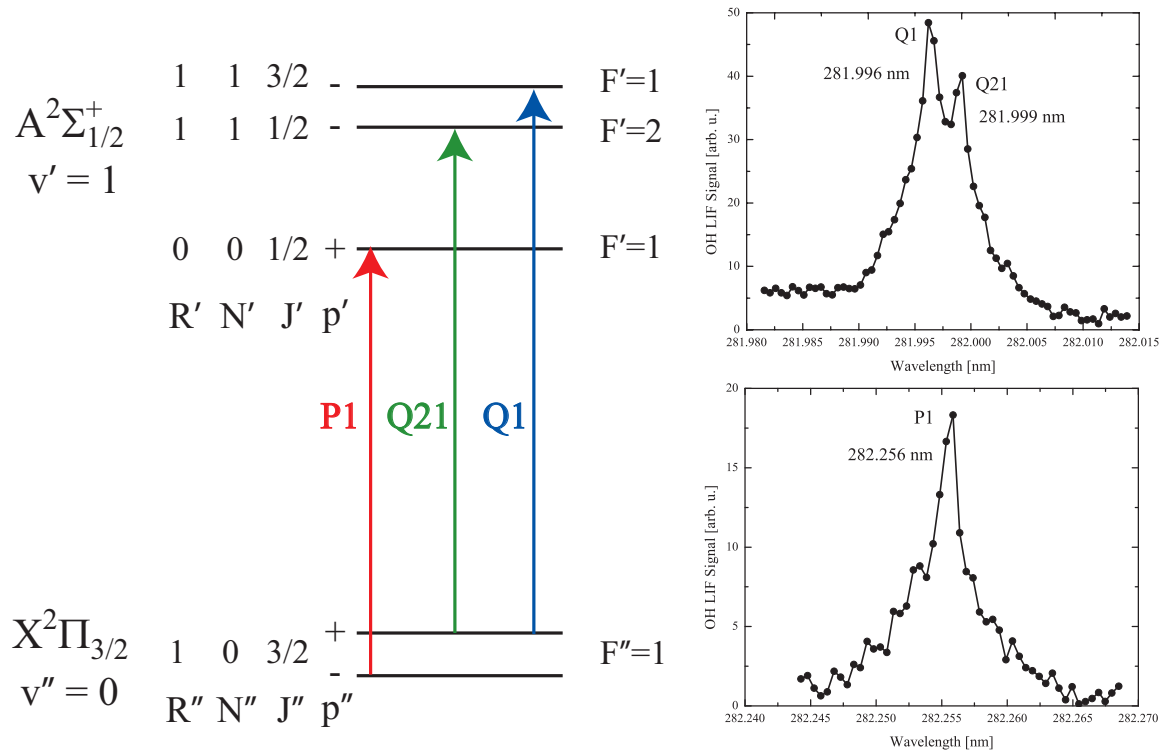
Figure 2.3: Illustration of the dipole-allowed P1, Q21, and Q1 transitions for $^2\Pi_{3/2}$ OH molecules with corresponding measured LIF spectra of a supersonic beam. Generally, the $\Delta v = 1$ transition is used to allow filtering of the 282 nm excitation light from the 313 nm fluorescence photons.

(F$'$ $\neq$ F$''$) or just F$'$ (F$'$ = F$''$), where prime and double-prime indicate upper and lower states, respectively.

Combining Eqs. 2.10 and 2.11 with the constants of Tables 2.1 and 2.2, one can calculate line positions for all $A^2\Sigma^+ \leftarrow X^2\Pi$ electric dipole transitions[*] . Figure 2.3 illustrates the P1, Q21, and Q1 transitions along $A^2\Sigma^+(v = 1) \leftarrow X^2\Pi_{3/2}(v = 0)$ and shows corresponding experimental spectra obtained from a supersonic beam of hydroxyl seeded in Kr. Even though the linewidth of our pulsed LIF laser ($\sim 2 - 3$ GHz) is larger than the 1.7 GHz ground Λ-doublet splitting, the dipole parity selection rule causes the P and Q transitions to be split by $2B$ ($\sim$32 cm^{-1}), leaving the Λ-doublet completely resolved. This is a nice feature of $\Sigma \leftarrow \Pi$ transitions in molecules with large rotational constants. As we will see, ND$_3$ also exhibits this feature of resolved parity-doublets in its REMPI spectrum, albeit from a completely different coupling mechanism. To calculate the relative strengths of these transitions, refer to Eq. 2.24 and replace the symmetric top quantum number K with Ω.

2.2.2 Ammonia (ND$_3$)

Ammonia is arguably the prototypical polyatomic molecule. A symmetric top in its normal (NH$_3$) and fully-deuterated (ND$_3$) forms, ammonia serves as a nice introduction to polyatomics and concepts such as hindered motions, *para*/*ortho* symmetry, l-type doubling, and resonance-enhanced multiphoton ionization (REMPI). Deuterated ammonia is ubiquitous in cold molecule experiments due to its large static polarizability (see Section 2.3.1), low mass, and chemical stability in the gas phase at standard temperature and pressure.

A full description of the group theory of polyatomic molecules is beyond the scope of this section, but a detailed discussion can be found in Chapter 3 of Ref. [43]. The pyramidal structure of ground-state ($\tilde{X}^1A_1'$) ammonia gives it a $\mathbf{C}_{3v}$ point group symmetry, which means that it has an axis with three-fold rotational symmetry. The v subscript indicates that it also possesses three

---

[*] Note that, for large J, one must add the centrifugal distortion term $D\mathbf{R}^4 = D(\mathbf{J} - \mathbf{S})^4$ to the ground state rotational Hamiltonian of Eq. 2.3 and recalculate the matrix elements.

vertical planes of symmetry passing through the vertical symmetry axis. The Mulliken symbol A communicates that the ground state is singly degenerate and possesses $\mathbf{C}_3$ rotation symmetry, its subscript tells us that the sign of the electronic wavefunction does not change upon reflection of the molecule about its center, and the prime indicates an additional horizontal symmetry plane σ_h. As with diatomics, the leading superscript gives the overall electron spin multiplicity $2S + 1$.

For diatomic molecules, the moment of inertia about the symmetry (z) axis is vanishingly small. As a result, rotational excitations in this dimension are not observed. This leads to only one rotational constant, B, which corresponds to the total rotational energy about the two remaining, identical x- and y-axes. However, polyatomic molecules can possess bonds in directions other than the z-axis, which necessitates consideration of the moment of inertia about this axis. Since we are only considering symmetric tops here, the moments I_x and I_y are still identical and are denoted I_B. The third moment, I_z, is denoted I_C in ND_3 since it is larger than $I_x = I_y$ (otherwise it would be labeled I_A). This leads to the following rotational Hamiltonian:

$$
\begin{aligned}
\hat{H}_{rot} &= \frac{\hbar^2}{2I_B}\hat{J}_x^2 + \frac{\hbar^2}{2I_B}\hat{J}_y^2 + \frac{\hbar^2}{2I_C}\hat{J}_z^2 \\
&= \frac{\hbar^2}{2I_B}\mathbf{J}^2 + \left(\frac{\hbar^2}{2I_C} - \frac{\hbar^2}{2I_B}\right)\hat{J}_z^2 \\
&= B\mathbf{J}^2 + (C - B)\hat{J}_z^2
\end{aligned}
\tag{2.12}
$$

whose eigenvalues are

$$
U_{rot} = BJ(J + 1) + (C - B)K^2.
\tag{2.13}
$$

The projection quantum number K can take the usual values $K = -J, ..., J$ and, in the absence of interactions such as l-type doubling, $\pm K$ values are degenerate. Adding the requisite centrifugal stretching terms with associated constants D_J, D_{JK}, and D_K to Eq. 2.12, we obtain the eigenvalues

$$
U_{rot} = BJ(J + 1) + (C - B)K^2 - D_J J^2(J + 1)^2 - D_{JK}J(J + 1)K^2 - D_K K^4.
\tag{2.14}
$$

The three identical deuterium nuclei in ND_3 yield an additional symmetry which divides rotational states into *ortho* and *para* categories according to their K projection. Since the D nuclei are bosonic, the overall molecular wavefunction (including both spin and rotation) must be
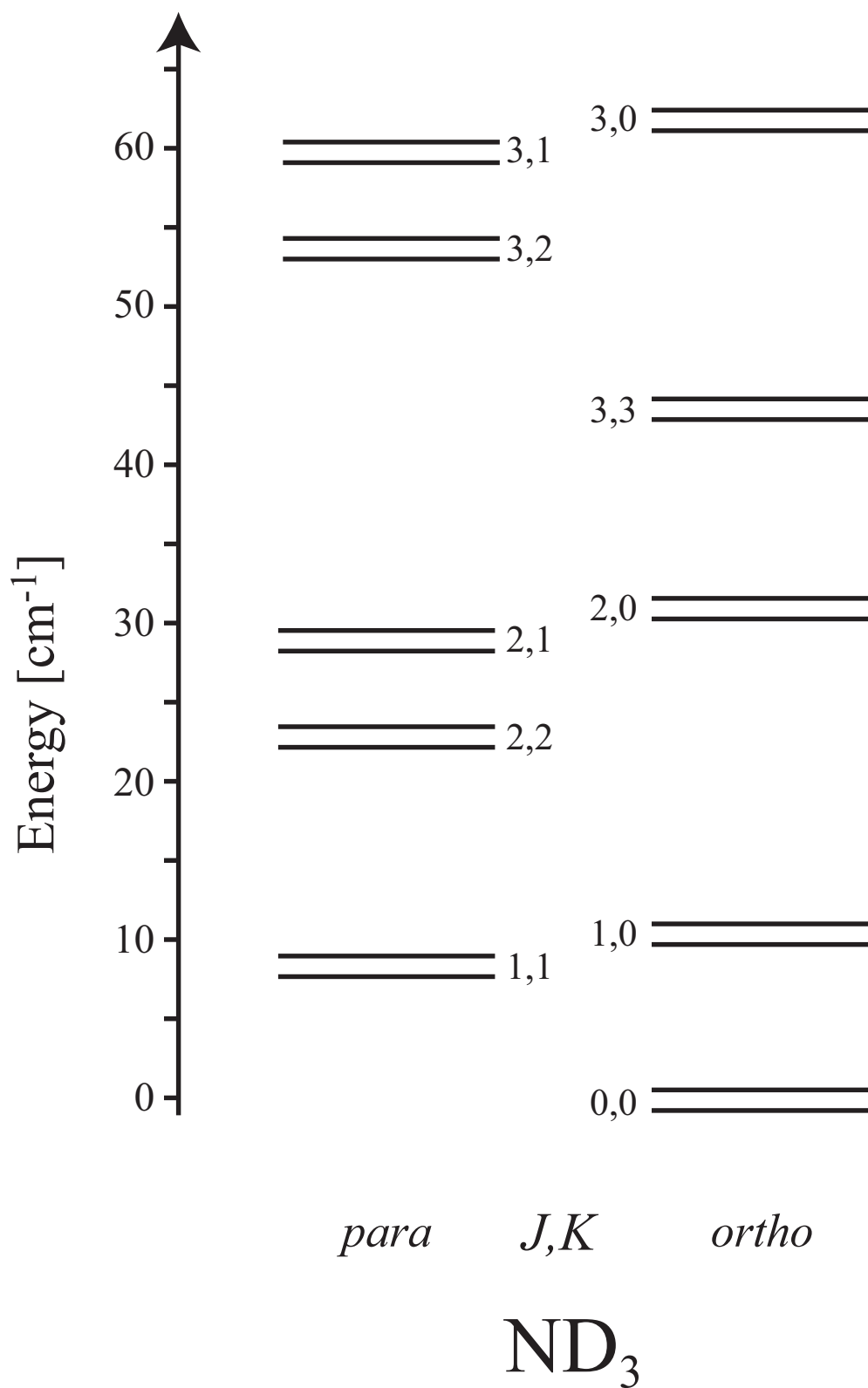
Figure 2.4: Ground state $(\tilde{X}^1 A'_1)$ structure of deuterated ammonia showing the inversion doublet (expanded for clarity) of each rotational level.

symmetric under exchange of deuterons. Therefore, we obtain two distinct "ladders" of rotational states corresponding to *ortho* ($K \bmod 3 = 0$) and *para* ($K \bmod 3 \neq 0$) symmetry as shown in Fig. 2.4. Interconversion between *ortho/para* states is heavily suppressed due to the extremely weak interaction between nuclear spin and molecular rotation. Experimentally, it can be useful to think of p-ND$_3$ and o-ND$_3$ as distinct molecules each with their own rotational structure. This viewpoint is especially useful when fitting the rotational temperature of a supersonic beam of ammonia, which will often possess two distinct *ortho* and *para* rotational temperatures.

The pyramidal structure of the electronic ground state of ammonia allows for tunnelling of the nitrogen atom through the plane of hydrogen/deuterium nuclei. This inversion occurs because the Coulomb energy barrier corresponding to N lying in the H/D plane is finite. Despite the large vibrational constant of the NH$_3$ (ND$_3$) ground state measuring 950 cm^{-1} (748 cm^{-1}) [2], the central potential barrier of 2072 cm^{-1} significantly "hinders" the motion of the $v_2 = 0, 1$ ($v_2 = 0, 1, 2$) states and produces closely-spaced levels of opposite parity. The quantum nature of this tunnelling process is apparent in the isotope shift of the resulting inversion doublets, which displays an exponential dependence of the inversion splitting on the molecular reduced mass. The dependence of the inversion splitting on the rotational level is parametrized as [44]

$$\Delta U_{inv} = v_0 - v_a \left[J(J+1) - K^2 \right] - v_b K^2 \tag{2.15}$$

where $v_0 = 0.7934$ (0.05337) cm^{-1}, $v_a = 5.05 \times 10^{-3}$ (2.39×10^{-4}) cm^{-1}, and $v_b = 1.998 \times 10^{-3}$ (9.61×10^{-5}) cm^{-1} are the NH$_3$ (ND$_3$) inversion constants. Examining v_0, we see that merely increasing the reduced mass by a factor of 1.7 reduces the tunnelling rate by a factor of ~ 15.

2.2.2.1   ND$_3$ 2+1 REMPI Spectroscopy

We have thus far discussed one form of spectroscopic molecular detection in Section 2.2.1.1, namely laser-induced fluorescence. Fluorescence detection can be quite sensitive (limited to ≥ 100 molecules) with the correct choice of excitation and fluorescence wavelengths in addition to good stray light baffling. However, one can never detect 100% of the photons scattered into 4π sr. On

the other hand, since ions can be very efficiently guided and detected, state-sensitive molecular ionization serves as a useful alternative to fluorescence when the molecular structure allows for accessible ionizing wavelengths, and the former is usually more sensitive.

Resonance-enhanced multiphoton ionization (REMPI) is commonly used for spectroscopy and detection of neutral atomic and molecular species. By making use of a real (as opposed to virtual) intermediate state, one can ionize the species of interest in multiple excitation steps. This technique carries the advantage that by energetically separating ionization steps one can use longer, more accessible wavelengths to ionize. Furthermore, the use of resonant excitation light yields large enhancements in atomic/molecular absorption cross sections. When a multiphoton transition is used for the intermediate step, different dipole selection rules apply and allow one to probe transitions inaccessible by single photons. Generally, REMPI is characterized as $p+1$, where p is the number of photons used to reach the intermediate state and a single photon ionizes. In the case of ammonia, 2+1 REMPI is most commonly used [45, 46], but 3+1 spectra have been observed [47]. It is worth noting that OH can be ionized by REMPI [48, 49], but the wavelengths for even the 2+1 step lay below 250 nm.

One electronic intermediate employed in 2+1 REMPI of ND_3 is the $\tilde{B}^1E''$ Rydberg state. In this case, the Mulliken symbol E denotes a doubly-degenerate symmetry class and the double-prime indicates that the wavefunction is anti-symmetric with respect to a horizontal symmetry plane. In short, the structure of $\tilde{B}$ is planar, which has the immediate consequence of removing the inversion doublets common to the pyramidal $\tilde{X}$ state. Transitions between vibrational states in the ground and intermediate levels are parametrized as $2_{v''}^{v'}$, where the number 2 indicates that the vibrations are of the v_2 'umbrella' mode. Figure 2.5 illustrates three of the allowed ionization pathways (2_0^4, 2_0^5, 2_0^6) from an inversion doublet in the ground electronic and vibrational state. Vibrational selection rules require that the upper and lower states have the same symmetry, which means that closely-spaced inversion doublets in the ground state connect to alternating vibrational levels in the intermediate $\tilde{B}$ state. As with the aforementioned $\Sigma \leftarrow \Pi$ transitions in hydroxyl, this feature allows one to easily distinguish between electrically high- and low-field seeking states.
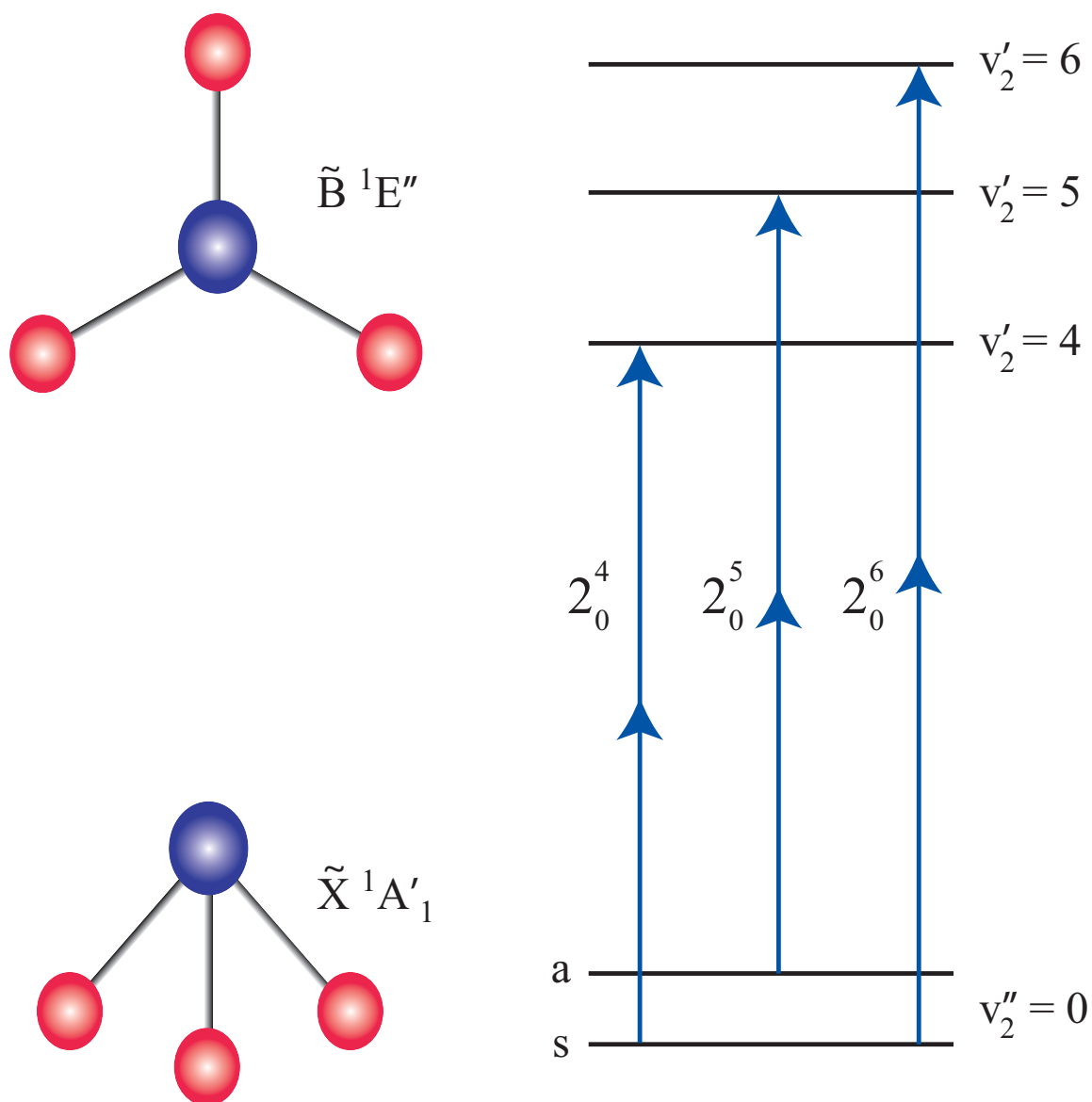
Figure 2.5: Illustration of three intermediate two-photon transitions used in 2+1 REMPI spectroscopy of ND_3. Vibrational selection rules result from the different (alternating) symmetries of the excited vibrational levels. The structure of ND_3 transitions from pyramidal to planar after the two-photon excitation. The rotational structure is excluded for clarity.

The Hamiltonian for the $\tilde{B}^1 E''$ state of ND_3 is more complicated than that of the ground state due to l-type doubling. The complete Hamiltonian is [46]

$$\hat{H} = T_v + \hat{H}_{rot} + \hat{H}_{VR} \tag{2.16}$$

where

$$\hat{H}_{rot} = BJ(J+1) + (C-B)K^2 - D_J J^2(J+1)^2 - D_{JK}J(J+1)K^2 - D_K K^4 \tag{2.17}$$

$$\hat{H}_{VR} = -2C\zeta lK + \eta_J J(J+1)lK + \eta_K K^3 l + \frac{1}{2}q(\hat{L}_+^2 \hat{J}_-^2 + \hat{L}_-^2 \hat{J}_+^2). \tag{2.18}$$

The spectroscopic term T_v gives the location of each v_2 vibrational state, while the vibration-rotation term $\hat{H}_{VR}$ breaks the degeneracy between $\pm K$ projections with the vibrational angular momentum projection l. In the $\tilde{X}$ state, $l = 0$ since there is no vibrational angular momentum along the molecular axis. However, the doubly-degenerate $\tilde{B}$ state possesses $l = \pm 1$. Note that the first three terms of Eq. 2.18 do not completely lift the degeneracy of K states — only the product $\pm Kl$ are split. However, the last term of $\hat{H}_{VR}$ mixes $l = \pm 1$ states and yields so-called "l-type doubling" [44]. In spectroscopic fits of $2_0^{v'}$ transitions where $v' > 4$, the parameters η_J and η_K of Eq. 2.18 are constrained to zero due to their negligibly-small fitted values [50].

To find the eigenvalues of the above Hamiltonian, one can either build and numerically diagonalize the full $2(2J+1) \times 2(2J+1)$ matrix for each J' level in the excited state or only diagonalize the necessary 2×2 matrices that include the two-state coupling terms $\hat{L}_\pm^2 \hat{J}_\mp^2$. The latter method allows for more simplified, scalable code and will be described here as in Ref. [46]. Keeping in mind that the quantum number l represents vibrational angular momentum about the symmetry axis, we obtain

	$|J,K\rangle|l=-1\rangle$	$|J,K+2\rangle|l=+1\rangle$
$\langle J,K|\langle l=-1|$	U_0	$\frac{1}{2}qf$
$\langle J,K+2|\langle l=+1|$	$\frac{1}{2}qf$	U_0'

$$\tag{2.19}$$

where

$$
\begin{aligned}
U_0 &= T_v + BJ(J+1) + (C-B)K^2 - D_J J^2(J+1)^2 - D_{JK}J(J+1)K^2 \\
&\quad - D_K K^4 + 2C\zeta K
\end{aligned} \tag{2.20}
$$

$$
\begin{aligned}
U_0' &= T_v + BJ(J+1) + (C-B)(K+2)^2 - D_J J^2(J+1)^2 \\
&\quad - D_{JK}J(J+1)(K+2)^2 - D_K(K+2)^4 - 2C\zeta(K+2)
\end{aligned} \tag{2.21}
$$

$$
f = \sqrt{[J(J+1) - K(K+1)][J(J+1) - (K+1)(K+2)]}. \tag{2.22}
$$

For completeness, the eigenvalues and normalized eigenvectors of the above 2×2 Hamiltonian are

$$
\begin{aligned}
U^\pm &= \frac{(U_0 + U_0') \pm \sqrt{(U_0' - U_0)^2 + q^2 f^2}}{2} \\
|\psi^\pm\rangle &= \frac{\frac{1}{2}qf|J,K\rangle|l=-1\rangle + (U^\pm - U_0)|J,K+2\rangle|l=+1\rangle}{\sqrt{(U^\pm - U_0)^2 + \frac{1}{4}q^2 f^2}}.
\end{aligned} \tag{2.23}
$$

In order to properly simulate a REMPI spectrum, one also needs the relevant transition strengths for a given set of rotational $2_{v''}^{v'}$ transitions. In the special case of single-photon transitions, these are known as the Hönl-London factors S_J [51]. However, Dixon et al derive a compact form for all k-photon transition strengths based on generalized spherical tensor transition matrix elements $\langle J', K'(\Omega'), M'|T_q^k|J'', K''(\Omega''), M''\rangle$ that is better suited for numerical evaluation [52]. Quoting only the result of their derivation, the transition strength (S) for a k-photon ro-vibrational transition is given by

$$
S(J', J'', K', K'', k, q) \propto \sum_q |\langle \eta_2|T_q^k|\eta_1\rangle|^2 \, (2J'+1)(2J''+1) \begin{pmatrix} J' & k & J'' \\ K' & -q & -K'' \end{pmatrix}^2. \tag{2.24}
$$

The first term involving η_1 and η_2 reflects the vibrational transition strength and includes the necessary Franck-Condon factor. This term can be ignored for transitions in a given $2_{v''}^{v'}$ manifold. The J, K-dependent terms give the generalized Hönl-London factors for a k-photon transition with spherical tensor components q, where $q = -k, .., k$. The M', M'' components of J', J'' have been summed in the above expression since we are assuming there are no external fields. The symmetry of the Wigner 3j-symbol of Eq. 2.24 immediately gives the k-photon selection rules. Specializing to

2+1 REMPI of ND_3, previous experiments have found that the transition is completely carried by the $T_{\pm1}^2$ tensor. This yields the following two-photon selection rules:

$$\Delta J = 0, \pm1, \pm2 \qquad \Delta K = \Delta l = q = \pm1. \qquad (2.25)$$

Equation 2.24 is sufficient to determine transition strengths at low J, but as l-uncoupling increases it becomes necessary to transform to the basis given by Eq. 2.23. This new basis allows for "intensity mixing" between coupled $|J', K'\rangle|l = -1\rangle$ and $|J', K' + 2\rangle|l = +1\rangle$ states. Using the phase convention for reduced matrix elements of Ref. [52] wherein $\langle \tilde{B}||T_1^2||\tilde{X}\rangle = -\langle \tilde{B}||T_{-1}^2||\tilde{X}\rangle$, we obtain the transition matrix

$$
\begin{array}{c|c}
 & |\tilde{X}, l = 0\rangle \\
\hline
\langle \tilde{B}, l = -1| & s(J', J'', K', K'', k, q) \\
\langle \tilde{B}, l = +1| & -s(J', J'', K', K'', k, -q)
\end{array}
\qquad (2.26)
$$

where

$$s(J', J'', K', K'', k, q) \propto \sum_q \langle \eta_2|T_q^k|\eta_1\rangle \ \sqrt{(2J'+1)(2J''+1)} \begin{pmatrix} J' & k & J'' \\ K' & -q & -K'' \end{pmatrix}. \qquad (2.27)$$

Combining the phase convention of Eq. 2.26 with the eigenstates and eigenvalues of Eq. 2.23, we can now accurately assign transition strengths to all $2_{v''}^{v'}$ lines in NH_3 and ND_3. Effective rotational temperatures can be calculated by multiplying transition strengths by the Boltzmann factor

$$S_{IK}(2J''+1)\exp\left[-U_{J''K''}/k_B T_{rot}\right] \qquad (2.28)$$

where $U_{J''K''}$ are the energies of the $|J'', K''\rangle$ ground states, $(2J''+1)$ is the degeneracy weighting factor for each J'' level, k_B is Boltzmann's constant, T_{rot} is the effective temperature of the rotational distribution, and S_{IK} accounts for the degeneracy due to the three identical H ($I = \frac{1}{2}$) or D ($I = 1$) nuclei in ammonia. The factor S_{IK} for three identical bosonic nuclei is defined in

Eq. 2.29 [44]. Note that, in the case of fermionic nuclei, one must flip the two $K = 0$ cases.

$$
S_{IK}^{\text{Bose}} =
\begin{cases}
4I^2 + 4I + 3 & K \bmod 3 = 0, \quad K \neq 0 \\[2mm]
(2I + 3)(I + 1) & K = 0, \ J \text{ even, lower inversion or } J \text{ odd, upper inversion} \\[2mm]
2I^2 - I & K = 0, \ J \text{ even, upper inversion or } J \text{ odd, lower inversion} \\[2mm]
4I^2 + 4I & K \bmod 3 \neq 0.
\end{cases}
\tag{2.29}
$$

The effect of different rotational temperatures on the measured 2_0^5 ND_3 spectrum is illustrated in Fig. 2.6, where each rotational transition has been given a Lorentzian FWHM linewidth of 0.3 cm^{-1}. See Appendix A for a list of line positions and strengths of the 2_0^5 2+1 REMPI lines of ND_3.
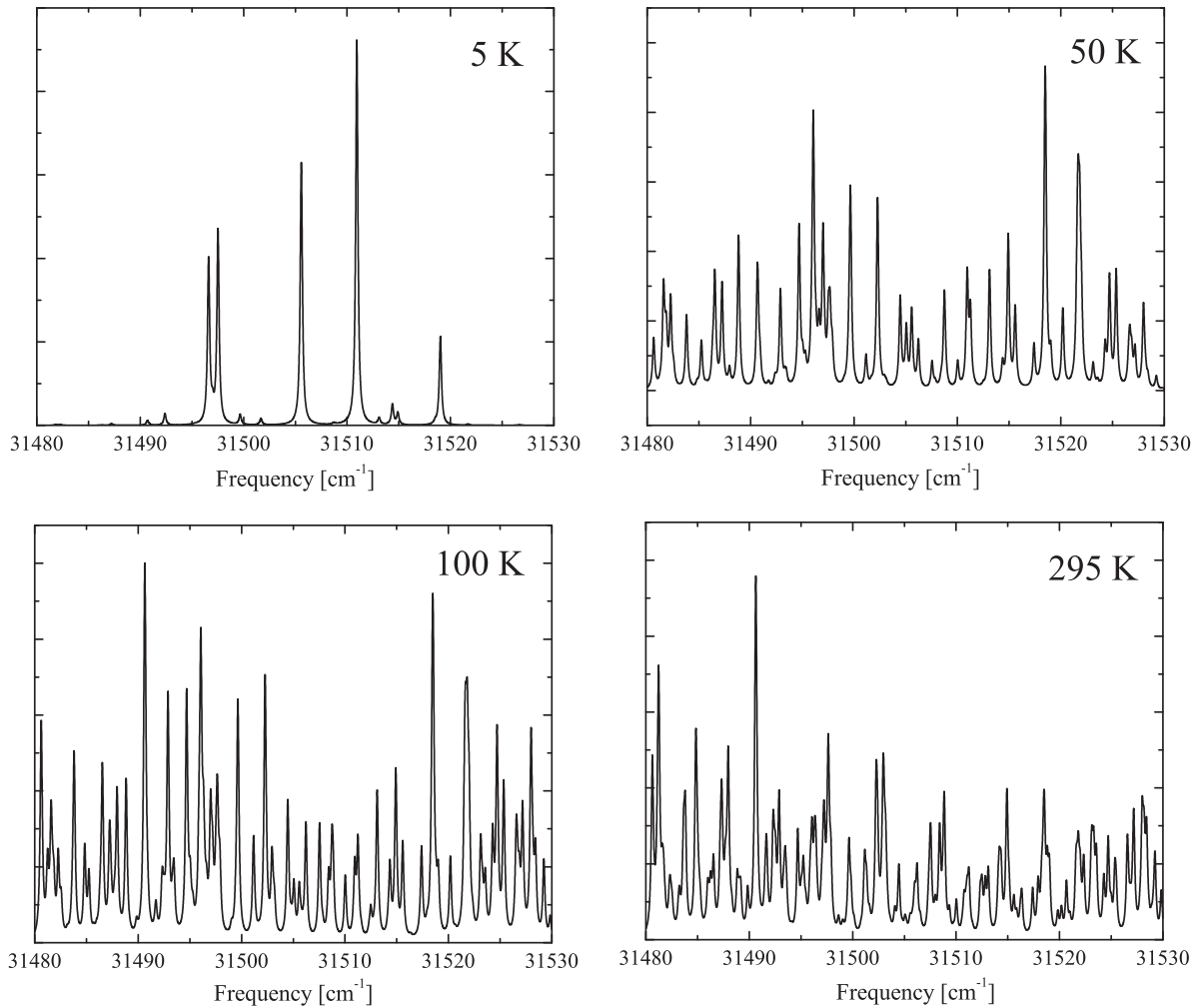
Figure 2.6: Simulated 2+1 REMPI spectrum of 2_0^5 rotational transitions in ND_3. The simulated rotational temperature is given for each plot. For consistency of presentation, a Lorentzian width of $0.3 \ cm^{-1}$ has been assumed for all spectral lines. Note that at high temperatures ($\gtrsim 100$ K), Doppler broadening necessitates application of a Voigt lineshape to correctly fit experimental spectra.

2.3   External Fields

2.3.1   Stark Effect

2.3.1.1   Strong Electric Fields - Fine Structure

When considering external electric fields of $\gtrsim 1$ kV/cm, one can ignore the hyperfine structure of polar molecules such as OH and ND_3 since $\mathbf{J}$ is decoupled from the nuclear spin $\mathbf{I}$ at these field magnitudes. To calculate the molecular Stark effect in this regime, we first consider the Hamiltonian

$$\hat{H}_{Stark} = -\boldsymbol{\mu} \cdot \mathbf{E} \tag{2.30}$$

where $\boldsymbol{\mu}$ is the permanent dipole moment vector and $\mathbf{E}$ is the external electric field. Using the parity basis for a Hund's case (a) or (c) molecule defined in the previous section and assuming that $\mathbf{E}$ lies along the z-axis, we compute

$$
\begin{aligned}
\langle JM_J\bar{\Omega}\epsilon| - \boldsymbol{\mu} \cdot \mathbf{E} |JM_J\bar{\Omega}\epsilon'\rangle &= -\frac{1}{2}(\langle JM_J\Omega| + \epsilon\langle JM_J - \Omega|)\mu E \cos\theta (|JM_J\Omega\rangle + \epsilon'|JM_J - \Omega\rangle) \\
&= -\frac{1}{2}\left[\langle JM_J\Omega|\mu E \cos\theta|JM_J\Omega\rangle + \epsilon\epsilon'\langle JM_J - \Omega|\mu E \cos\theta|JM_J - \Omega\rangle\right] \\
&= -\frac{\mu E M_J \Omega}{J(J+1)}\left(\frac{1 - \epsilon\epsilon'}{2}\right) \\
&= -\mu_{eff}E\left(\frac{1 - \epsilon\epsilon'}{2}\right). \tag{2.31}
\end{aligned}
$$

To arrive at the final result of Eq. 2.31, one needs the so-called 'direction-cosine matrix elements' given in Ref. [44]. It is immediately clear that the external electric field couples states of opposite parity ($\epsilon \neq \epsilon'$) to generate a non-zero Stark shift. Furthermore, in the absence of an electric field to couple these states, the expectation value of the dipole operator vanishes.

The above equation for a first-order Stark effect works well for symmetric top molecules with extremely small parity-doublet splittings (Δ) such that $\Delta \ll \mu_{eff}E$. However, we can better approximate the Stark shift at intermediate field strengths if we fully diagonalize the above Hamiltonian in the parity basis. Including diagonal terms that represent the parity-doublet splitting, we
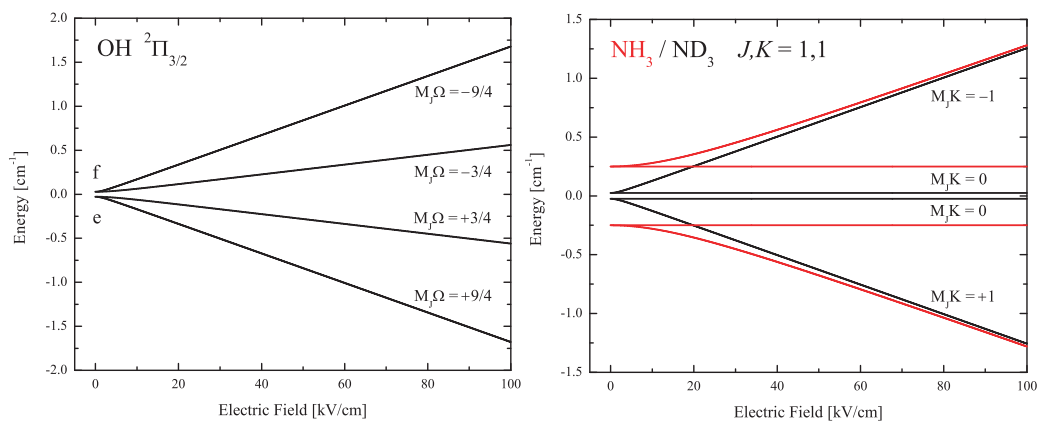
Figure 2.7: Stark shifts in both the OH and ammonia (NH_3/ND_3) molecules. Coincidentally, OH and ND_3 have nearly identical parity doublets and permanent dipole moments which gives them similarly large static polarizabilities. Partly for this reason, many cold molecule experiments have made use of these two species.

have

$$\hat{H}_{Stark} = \begin{pmatrix} -\frac{\Delta}{2} & -\mu_{eff}E \\ -\mu_{eff}E & \frac{\Delta}{2} \end{pmatrix} \tag{2.32}$$

whose eigenvalues are

$$U_{Stark}^{\pm} = \pm\sqrt{\left(\frac{\Delta}{2}\right)^2 + (\mu_{eff}E)^2}. \tag{2.33}$$

The normalized eigenstates of the above Hamiltonian are therefore

$$|\psi^+\rangle = \frac{\left(\frac{\Delta}{2} + U_{Stark}^+\right)|JM_J\bar{\Omega}+\rangle - \mu_{eff}E|JM_J\bar{\Omega}-\rangle}{\sqrt{U_{Stark}^+(2U_{Stark}^+ + \Delta)}} \tag{2.34}$$

$$|\psi^-\rangle = \frac{\left(\frac{\Delta}{2} - U_{Stark}^-\right)|JM_J\bar{\Omega}-\rangle + \mu_{eff}E|JM_J\bar{\Omega}+\rangle}{\sqrt{U_{Stark}^-(2U_{Stark}^- + \Delta)}}. \tag{2.35}$$

Note that as the electric field strength is increased, $|\psi^{\pm}\rangle$ transitions from a state of well-defined parity $\epsilon(-1)^{J-\frac{1}{2}}$ to a mixed parity state. When the Stark effect overcomes the parity-doublet splitting $(E > \Delta/2\mu_{eff})$, the molecule enters the linear Stark shift regime and is often said to be 'polarized.' When considering nonlinear symmetric top molecules such as ND_3, the above Stark shift still applies, but you must replace the quantum number Ω with K, which represents the projection of J along the molecular symmetry axis. The Stark shifts for ground state hydroxyl and ammonia (NH_3, ND_3) are shown in Fig. 2.7.

Equation 2.34 presents an opportunity to not only quantify state mixing due to an external electric field, but to measure the value of such a field. In cases where the molecular sample resides in a single parity state (e.g. Stark decelerated beams), one can directly measure the state-mixing ratio between the upper ($|\uparrow\rangle$) and lower ($|\downarrow\rangle$) doublets as a function of electric field. Stark decelerated and electrostatically-filtered beams are selected for weak-field seeking states. Therefore, we can monitor the ratio of lower- to upper-doublet "population" as a measure of the local electric field. From Eq. 2.34, we predict

$$\frac{|\langle\downarrow|\psi^+\rangle|^2}{|\langle\uparrow|\psi^+\rangle|^2} = \left[\frac{\mu_{eff}E}{\frac{\Delta}{2} + \sqrt{\left(\frac{\Delta}{2}\right)^2 + (\mu_{eff}E)^2}}\right]^2. \tag{2.36}$$

The graph of Fig. 2.8 compares the prediction of Eq. 2.36 (black line) with a measured population ratio of guided, state-selected ND_3 molecules (red point). We ionize ND_3 in the presence of a calculable electric field and measure both lower- and upper-doublet populations of ground state ND_3. The excellent agreement between measurement and theory suggests that this technique can be employed to measure large electric fields ($\gtrsim 1$ kV/cm) in the molecule detection region.
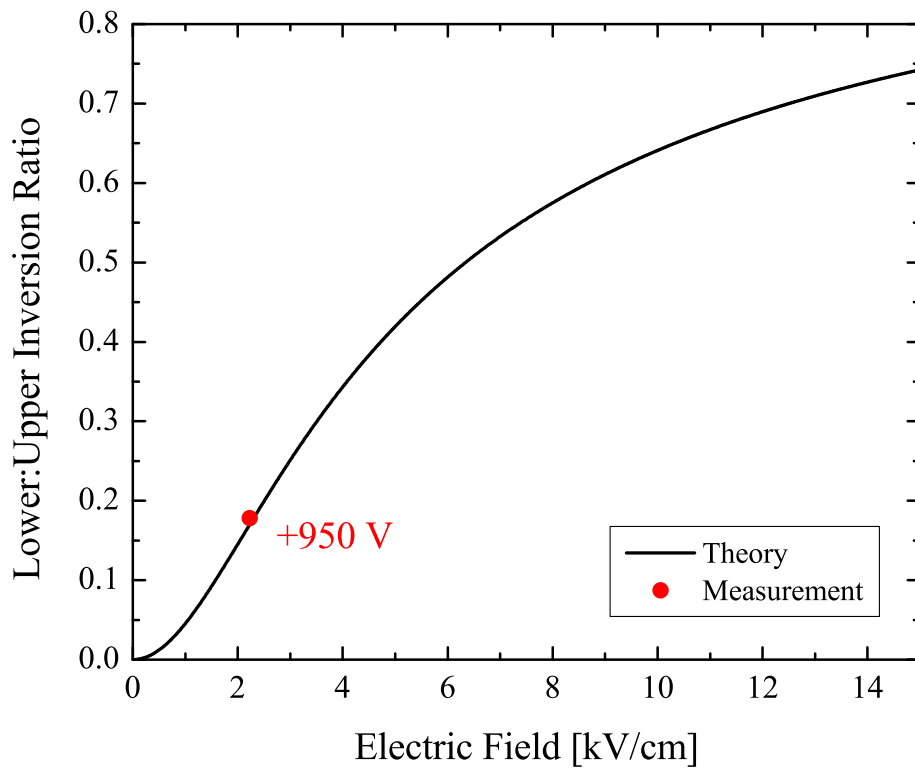
Figure 2.8: Theoretical (black line) and measured (red point) doublet population ratios as a function of external electric field. For this measurement, we perform 2+1 REMPI of a state-selected beam of ND_3 molecules while applying +950 V to one of the trap magnets in the ionization region. Following Eq. 2.36, the ratio of lower- to upper-inversion doublet populations allows accurate characterization of this applied electric field.

2.3.1.2 Weak Electric Fields - Hyperfine Structure

For very weak electric fields ($\lesssim$0.5 kV/cm for OH) acting on molecules with a net non-zero nuclear spin, we must include the hyperfine structure to accurately calculate Stark shifts. When forming the resultant $\mathbf{F}=\mathbf{J}+\mathbf{I}$, we use Clebsch-Gordon coefficients to transform from the basis of $|JM_J\bar{\Omega}\epsilon\rangle$ states to states with quantum numbers F and M_F, where M_F is the projection of F on the electric field axis. The transformation takes the form

$$|FM_F\epsilon\rangle = \sum_{M_J,M_I} |JM_J\bar{\Omega}\epsilon\rangle|IM_I\rangle\langle JM_JIM_I|FM_F\rangle \qquad (2.37)$$

and, for a $^2\Pi$ molecule such as OH, yields the off-diagonal matrix elements [53]

$$
\langle FM_F\epsilon|\hat{H}_{Stark}|F'M_F'\epsilon'\rangle = -\mu E \left(\frac{1 + \epsilon\epsilon'(-1)^{J+J'+2\bar{\Omega}+1}}{2} \right) (-1)^{J+J'+F+F'+I-M_F-\bar{\Omega}+1}
$$
$$
\times \sqrt{(2F+1)(2F'+1)(2J+1)(2J'+1)}
$$
$$
\times \begin{pmatrix} J & 1 & J' \\ -\bar{\Omega} & 0 & \bar{\Omega}' \end{pmatrix} \begin{pmatrix} F' & 1 & F \\ -M_F' & 0 & M_F \end{pmatrix} \begin{Bmatrix} F & F' & 1 \\ J' & J & 1 \end{Bmatrix}. \qquad (2.38)
$$

The expressions in parentheses and brackets are the Wigner 3j and 6j symbols, respectively. Given the symmetry properties of the 3j symbols and the first term in Eq. 2.44, we see that states must have the same M_F and $\bar{\Omega}$ projections and different parity to be coupled by the electric field. We then combine the above expression with diagonal matrix elements that include the OH Λ-doublet ($\Delta_\Lambda = 0.056$ cm^{-1}) and hyperfine ($\Delta_{hf} = 0.0026$ cm^{-1}) splittings. Numerically diagonalizing the resulting 16×16 matrix over a range of electric field magnitudes, we obtain the Stark shift curves for the $X^2\Pi_{3/2}$ ground state of OH shown in Fig. 2.9. As in the strong-field limit, only the parity of the given state determines whether it is strong-field seeking or weak-field seeking, and $\pm M_F$ projections within a given F state are degenerate. For reference, the 8×8 upper-right and lower-left off-diagonal blocks in the basis $\{|FM_F\epsilon\rangle = |1-1+\rangle, |10+\rangle, |11+\rangle, |2-2+\rangle, |2-1+\rangle, |20+\rangle,$

$|21+\rangle$, $|22+\rangle$, $|1-1-\rangle$, $|10-\rangle$, $|11-\rangle$, $|2-2-\rangle$, $|2-1-\rangle$, $|20-\rangle$, $|21-\rangle$, $|22-\rangle\}$ are both

$$\begin{pmatrix} -\frac{1}{2} & 0 & 0 & 0 & -\frac{\sqrt{3}}{10} & 0 & 0 & 0 \\ 0 & 0 & 0 & 0 & 0 & -\frac{1}{5} & 0 & 0 \\ 0 & 0 & \frac{1}{2} & 0 & 0 & 0 & -\frac{\sqrt{3}}{10} & 0 \\ 0 & 0 & 0 & -\frac{3}{5} & 0 & 0 & 0 & 0 \\ -\frac{\sqrt{3}}{10} & 0 & 0 & 0 & -\frac{3}{10} & 0 & 0 & 0 \\ 0 & -\frac{1}{5} & 0 & 0 & 0 & 0 & 0 & 0 \\ 0 & 0 & -\frac{\sqrt{3}}{10} & 0 & 0 & 0 & \frac{3}{10} & 0 \\ 0 & 0 & 0 & 0 & 0 & 0 & 0 & \frac{3}{5} \end{pmatrix}. \tag{2.39}$$

2.3.2 Zeeman Effect

2.3.2.1 Strong Magnetic Fields - Fine Structure

As with the discussion of external electric fields, we may treat the molecular Zeeman shift in two distinct cases — strong and weak fields. The primary difference between electric and magnetic field effects is that the Zeeman shift respects parity. Otherwise, both fields couple states with the same M_J, M_F projection quantum numbers. Defining the magnetic field ($\mathbf{B}$) to be along the z-axis, the molecular Zeeman Hamiltonian is

$$\begin{aligned} \hat{H}_{Zeeman} &= -\boldsymbol{\mu} \cdot \mathbf{B} \\ &= \mu_B \left(\mathbf{L} + g_e \mathbf{S} \right) \cdot \mathbf{B} \\ &= \mu_B B \left(\hat{L}_z + g_e \hat{S}_z \right) \end{aligned} \tag{2.40}$$

where μ_B is the Bohr magneton, g_e is the electron gyromagnetic ratio ($g_e = 2 + \alpha/\pi + ... \sim 2.002$), and $\hat{L}_z$, $\hat{S}_z$ are the usual electronic angular momentum operators. Using the same parity basis as before, we arrive at the following for the case $\Omega = |\Lambda| + |\Sigma|$:

$$\langle J M_J \bar{\Omega} \epsilon | \hat{H}_{Zeeman} | J M_J \bar{\Omega} \epsilon' \rangle = \frac{\mu_B B (\bar{\Lambda} + g_e \bar{\Sigma}) \bar{\Omega} M_J}{J(J+1)} \delta_{\epsilon \epsilon'} \tag{2.41}$$
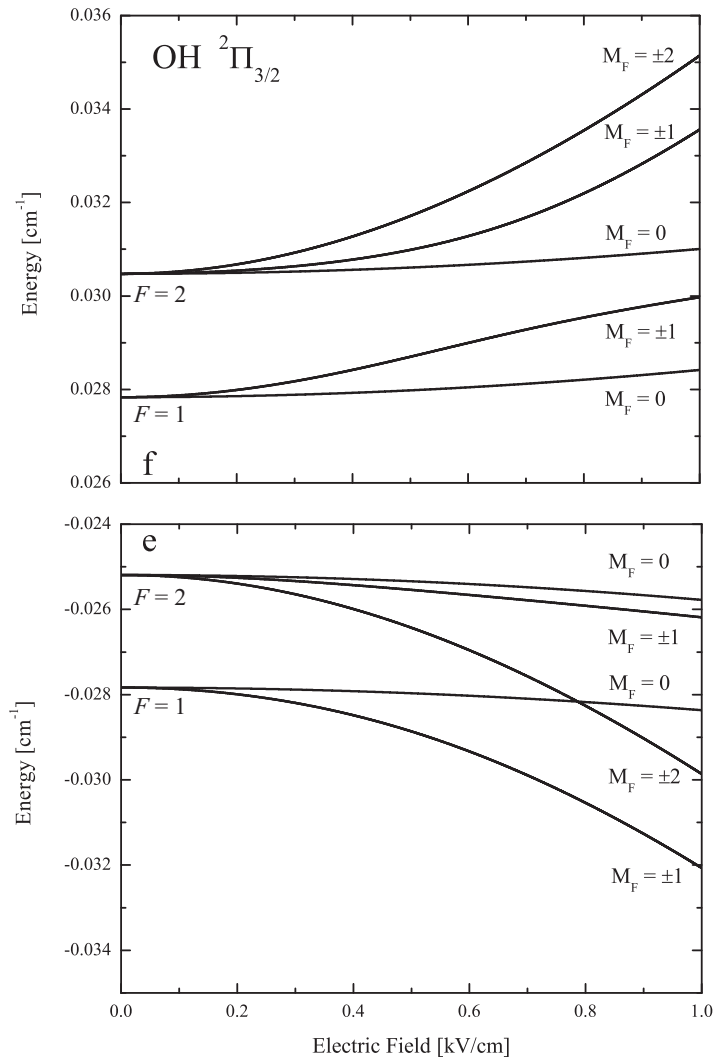
Figure 2.9: Stark shift of the $^2\Pi_{3/2}$ ground state of OH in the hyperfine basis. The two Λ-doublet states repel as the field is increased, creating strong- and weak-field seeking molecules. For electric fields above ~1 kV/cm, the structure approaches the strong-field limit of Fig. 2.7.

and for $\Omega = |\Lambda| - |\Sigma|$, we get

$$\langle JM_J\bar{\Omega}\epsilon|\hat{H}_{Zeeman}|JM_J\bar{\Omega}\epsilon'\rangle = \frac{\mu_B B(\bar{\Lambda} - g_e\bar{\Sigma})\bar{\Omega}M_J}{J(J+1)}\delta_{\epsilon\epsilon'}. \tag{2.42}$$

The Kronecker deltas of Eqs. 2.41 and 2.42 result from the fact that eigenstates of $\hat{H}_{Zeeman}$ must have well-defined parity. Excluding excited rotational levels, $\hat{H}_{Zeeman}$ is clearly diagonal in the $|JM_J\bar{\Omega}\epsilon\rangle$ basis. The strong-field Zeeman shift for the ground ($^2\Pi_{3/2}$) state of OH is shown in Fig. 2.10. Note that for states where $\Lambda = 2\Sigma$ and $\Omega = |\Lambda - \Sigma|$ (e.g. $^2\Pi_{1/2}$, $^3\Delta_1$), the magnetic dipole does not completely cancel but reduces to $\sim \alpha\mu_B/\pi \sim 0.002\mu_B$.

A special discussion is in order for the magnetic field shifts of vibrational (v_2) states within the excited $\tilde{B}^1E''$ state of ND$_3$. Rotational levels within this manifold exhibit a linear Zeeman effect even in the absence of a net electron spin. This Zeeman shift results from the vibrational angular momentum $l = \pm 1$ which effectively takes the place of Λ in Eq. 2.42. The resulting expression for large magnetic-field shifts in these levels is [54]

$$\langle JM_JKl|\hat{H}_{Zeeman}|JM_JKl\rangle = g_L\mu_B B\frac{lKM_J}{J(J+1)} \tag{2.43}$$

where the g-factor for vibrational angular momentum, g_L, is vibrational-state dependent and generally deviates from unity. For our intermediate REMPI state of interest ($v_2 = 5$), $g_L = 0.738$.

2.3.2.2   Weak Magnetic Fields - Hyperfine Structure

For magnetic fields inducing a Zeeman shift smaller than a molecule's hyperfine splitting ($B \lesssim \Delta_{hf}/\mu \sim 50$ G for OH), it is important to include the hyperfine structure to get accurate line shifts. Using the Clebsch-Gordon transformation of Eq. 2.37, we obtain the following matrix elements including the coupling between different F-sublevels:

$$\begin{aligned}
\langle FM_F\epsilon|\hat{H}_{Zeeman}|F'M_F'\epsilon'\rangle &= \mu_B B(\bar{\Lambda} + g_e\bar{\Sigma})\left(\frac{1 + \epsilon\epsilon'(-1)^{J+J'+2\bar{\Omega}}}{2}\right)(-1)^{J+J'+F+F'+I-M_F-\bar{\Omega}+1} \\
&\times \sqrt{(2F+1)(2F'+1)(2J+1)(2J'+1)} \\
&\times \begin{pmatrix} J & 1 & J' \\ -\bar{\Omega} & 0 & \bar{\Omega}' \end{pmatrix} \begin{pmatrix} F' & 1 & F \\ -M_F' & 0 & M_F \end{pmatrix} \begin{Bmatrix} F & F' & 1 \\ J' & J & 1 \end{Bmatrix}.
\end{aligned} \tag{2.44}$$
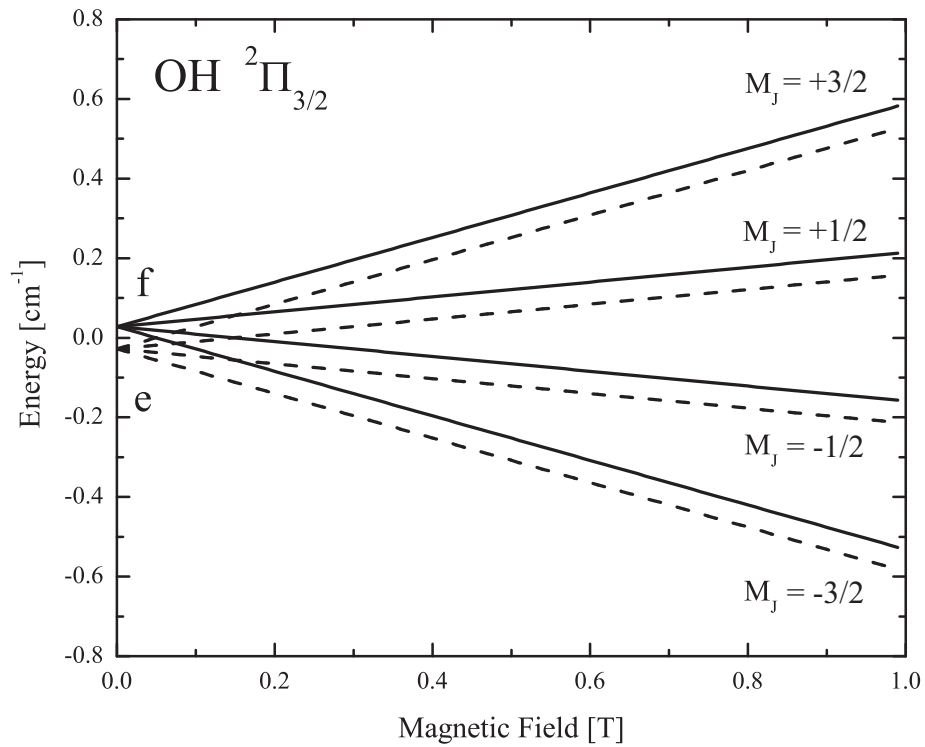
Figure 2.10: Zeeman shift of the $^2\Pi_{3/2}$ ground state of OH. Since the Zeeman Hamiltonian only couples states of like parity, the two Λ-doublet levels of OH show exactly the same field dependence. Also, the lack of coupling between e and f states causes only diabatic level crossings.

Note that the Wigner 3j- and 6j-symbols show exactly the same couplings as in the Stark shift expression, with the only substantive difference between the two cases being the parity-coupling term of the first line. Specializing once again to the case of OH ($^2\Pi_{3/2}$), we need only diagonalize two distinct 8×8 Hamiltonians given by Eq. 2.44 multiplied by an extra prefactor of $-\mu_B B(\bar{\Lambda}+g_e\bar{\Sigma})$ and added to the diagonal zero-field Λ-doublet and hyperfine energies given by:

$$
\begin{pmatrix}
\pm\frac{\Delta_\Lambda}{2} & 0 & 0 & 0 & 0 & 0 & 0 & 0 \\
0 & \pm\frac{\Delta_\Lambda}{2} & 0 & 0 & 0 & 0 & 0 & 0 \\
0 & 0 & \pm\frac{\Delta_\Lambda}{2} & 0 & 0 & 0 & 0 & 0 \\
0 & 0 & 0 & \pm\frac{\Delta_\Lambda}{2}+\Delta_{hf} & 0 & 0 & 0 & 0 \\
0 & 0 & 0 & 0 & \pm\frac{\Delta_\Lambda}{2}+\Delta_{hf} & 0 & 0 & 0 \\
0 & 0 & 0 & 0 & 0 & \pm\frac{\Delta_\Lambda}{2}+\Delta_{hf} & 0 & 0 \\
0 & 0 & 0 & 0 & 0 & 0 & \pm\frac{\Delta_\Lambda}{2}+\Delta_{hf} & 0 \\
0 & 0 & 0 & 0 & 0 & 0 & 0 & \pm\frac{\Delta_\Lambda}{2}+\Delta_{hf}
\end{pmatrix}.
$$

$$(2.45)$$

The result of this calculation is shown in Fig. 2.11. In the absence of differential g-factors between the two Λ-doublet levels, the e and f state Zeeman shifts are identical.

2.3.3 Combined Electric, Magnetic Fields

All of our magnetic trapping experiments have allowed for manipulation of OH within combined electric and magnetic fields. As such, we have observed interesting trap dynamics arising from these crossed E- and B-fields [55]. Experimental trapping results will be discussed in a later section, but we summarize here the mathematical formalism for treating a Hund's case (a) molecule in combined fields [56]. This example is interesting because of the strong coupling of $\mathbf{L}$ and $\mathbf{S}$ to the internuclear axis, which causes the axis to follow magnetic as well as electric field lines. In the same sense, the electron spin projection is influenced by external electric fields. It should be noted that one still needs an electric field to polarize a case (a) molecule since a lone magnetic field will not couple opposite-parity states, and will therefore still leave a vanishing expectation value for the
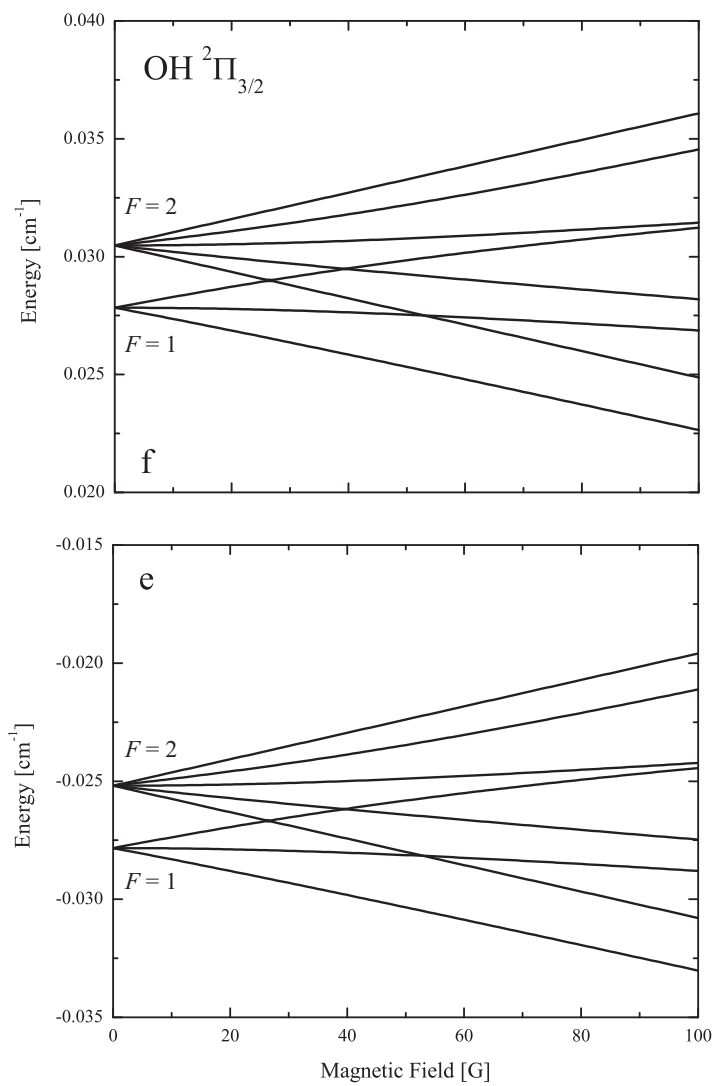
Figure 2.11: Zeeman shift of $^2\Pi_{3/2}$ OH molecules in the hyperfine basis. Both Λ-doublet states show the same effect since the magnetic field does not induce an interaction between e and f.

dipole moment.

Beginning with the combined-field Hamiltonian, we get the expected

$$\hat{H}_{E,B} = -\boldsymbol{\mu}_e \cdot \mathbf{E} - \boldsymbol{\mu}_b \cdot \mathbf{B} \qquad (2.46)$$

where $\boldsymbol{\mu}_e$ and $\boldsymbol{\mu}_b$ are the electric and magnetic dipoles, respectively. Without loss of generality, we let $\mathbf{B}$ lie along the z-axis and define β as the angle between $\mathbf{E}$ and $\mathbf{B}$. Ignoring hyperfine structure for simplicity, we obtain the following matrix elements for the $^2\Pi_{3/2}$ ground state of OH:

$$\begin{pmatrix}
-\frac{\Delta}{2}-\frac{6}{5}\mu_B B & 0 & 0 & 0 & \frac{3}{5}\mu E\cos\beta & -\frac{\sqrt{3}}{5}\mu E\sin\beta & 0 & 0 \\
0 & -\frac{\Delta}{2}-\frac{2}{5}\mu_B B & 0 & 0 & -\frac{\sqrt{3}}{5}\mu E\sin\beta & \frac{1}{5}\mu E\cos\beta & -\frac{2}{5}\mu E\sin\beta & 0 \\
0 & 0 & -\frac{\Delta}{2}+\frac{2}{5}\mu_B B & 0 & 0 & -\frac{2}{5}\mu E\sin\beta & -\frac{1}{5}\mu E\cos\beta & -\frac{\sqrt{3}}{5}\mu E\sin\beta \\
0 & 0 & 0 & -\frac{\Delta}{2}+\frac{6}{5}\mu_B B & 0 & 0 & -\frac{\sqrt{3}}{5}\mu E\sin\beta & -\frac{3}{5}\mu E\cos\beta \\
\frac{3}{5}\mu E\cos\beta & -\frac{\sqrt{3}}{5}\mu E\sin\beta & 0 & 0 & \frac{\Delta}{2}-\frac{6}{5}\mu_B B & 0 & 0 & 0 \\
-\frac{\sqrt{3}}{5}\mu E\sin\beta & \frac{1}{5}\mu E\cos\beta & -\frac{2}{5}\mu E\sin\beta & 0 & 0 & \frac{\Delta}{2}-\frac{2}{5}\mu_B B & 0 & 0 \\
0 & -\frac{2}{5}\mu E\sin\beta & -\frac{1}{5}\mu E\cos\beta & -\frac{\sqrt{3}}{5}\mu E\sin\beta & 0 & 0 & \frac{\Delta}{2}+\frac{2}{5}\mu_B B & 0 \\
0 & 0 & -\frac{\sqrt{3}}{5}\mu E\sin\beta & -\frac{3}{5}\mu E\cos\beta & 0 & 0 & 0 & \frac{\Delta}{2}+\frac{6}{5}\mu_B B
\end{pmatrix}.$$

$$(2.47)$$

The above matrix elements were calculated using the general spherical tensor expressions for Stark and Zeeman shifts in the fine-structure parity basis of Eq. 2.6. The relevant expressions can be found in Appendix A of Ref. [56]. The spherical tensor components of a vector $\mathbf{V} = (V_x, V_y, V_z)$ are

$$V_{\pm 1} = -\frac{1}{\sqrt{2}}(V_x \pm iV_y) = \mp\frac{1}{\sqrt{2}}|\mathbf{V}|\sin\theta e^{\pm i\phi} \qquad (2.48)$$

$$V_0 = V_z = |\mathbf{V}|\cos\theta. \qquad (2.49)$$

Figure 2.12 displays the OH level shifts in the presence of both E- and B-fields. The "fully-stretched" states corresponding to $|J\Omega M_J\epsilon\rangle = |\frac{3}{2},\frac{3}{2},+\frac{3}{2},f\rangle, |\frac{3}{2},\frac{3}{2},-\frac{3}{2},e\rangle$ remain the highest- and lowest-energy states, respectively, in combined fields. However, all other projections exhibit level crossings at intermediate field values.
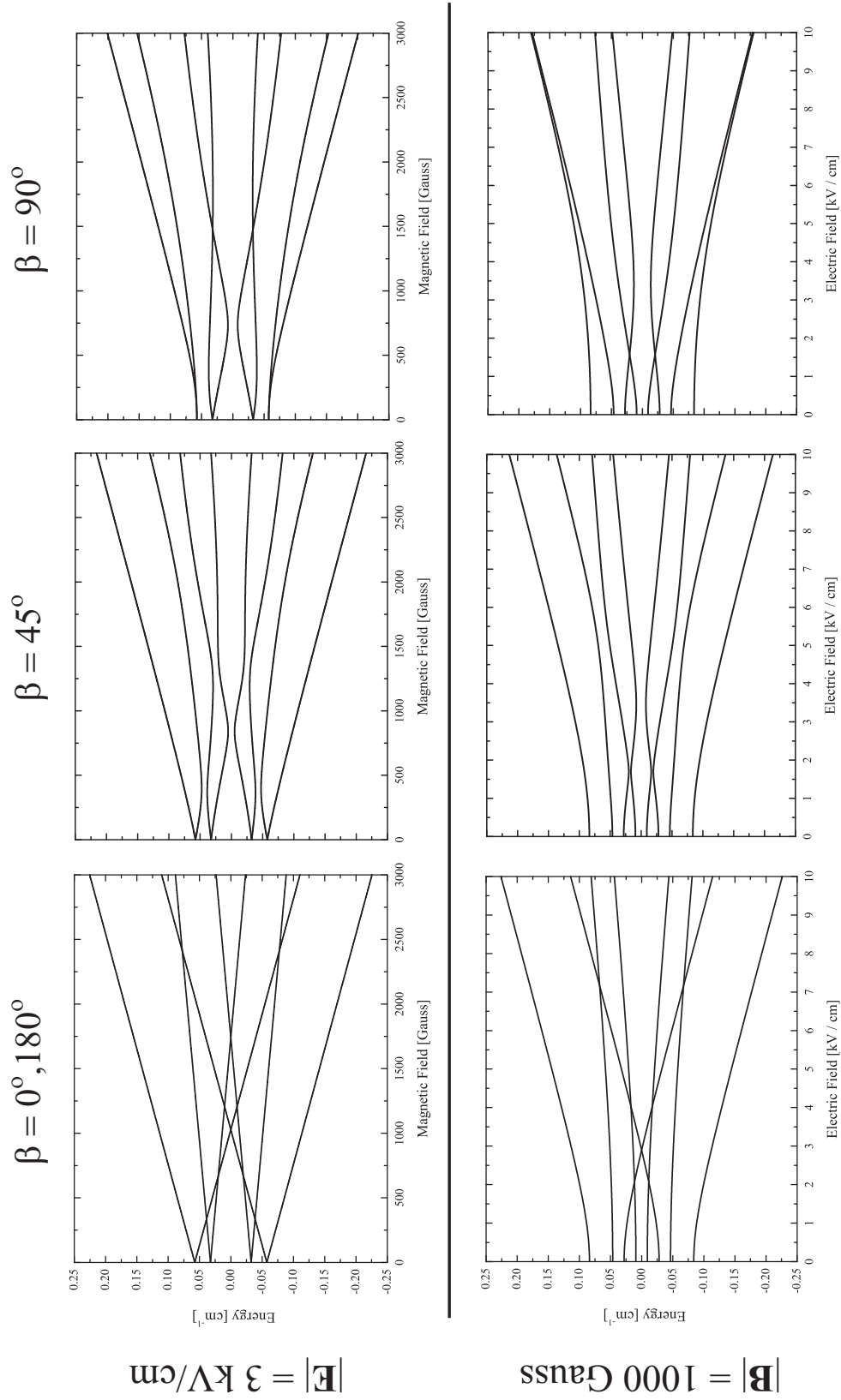
Figure 2.12: Level shifts for OH ($^2\Pi_{3/2}$) in combined electric and magnetic fields as a function of relative field angle β. The $\beta = 0°, 180°$ shifts are identical and plotted together. To keep track of the diabatic curves, it is useful to start from the far left of each graph where only the electric (upper plots) or magnetic (lower plots) field dominates. Of course, the adiabatic curves maintain energy ordering.

2.3.4 Diabatic vs. Adiabatic Level Crossings in Combined Fields

Interestingly, the curves of Fig. 2.12 show avoided crossings whose energy gaps depend on relative field angle, β, and electric field magnitude. In principle, if OH molecules are trapped within a magnetic quadrupole in the presence of an electric field, M_J projections different from the stretched $|\frac{3}{2}, \frac{3}{2}, +\frac{3}{2}, f\rangle$ and $|\frac{3}{2}, \frac{3}{2}, -\frac{3}{2}, e\rangle$ states will traverse these avoided crossings many times over a typical trap lifetime (~ 1 s). In the case of the experimentally-interesting $|\frac{3}{2}, \frac{3}{2}, +\frac{3}{2}, e\rangle$ state, one would prefer purely diabatic level crossings as shown in Fig. 2.13a to ensure an identical magnetic trapping potential to the stretched $|\frac{3}{2}, \frac{3}{2}, +\frac{3}{2}, f\rangle$ state. If the crossings are traversed adiabatically (Fig. 2.13b), the overall trap depth is reduced and, at low magnetic fields, removed altogether. To estimate the adiabatic (P_{ad}) and diabatic (P_{dia}) transition probabilities for a given molecule velocity (v) and magnetic field gradient (dB/dx), we use the Landau-Zener probability [57]:

$$
\begin{aligned}
P_{ad} &= 1 - P_{dia} \\
&= 1 - \exp\left(-2\pi \frac{V_{12}^2}{\hbar(dU/dt)}\right) \\
&= 1 - \exp\left(-2\pi \frac{(-\frac{\sqrt{3}}{5}\mu E \sin\beta)^2}{\hbar(dU/dB)(dB/dx)(dx/dt)}\right) \\
&= 1 - \exp\left(-2\pi \frac{(-\frac{\sqrt{3}}{5}\mu E \sin\beta)^2}{\hbar(\frac{6}{5}\mu_B)(dB/dx)\text{v}}\right) \\
&= 1 - \exp\left(-\frac{\pi}{5} \frac{\mu^2 E^2 \sin^2\beta}{\hbar\mu_B(dB/dx)\text{v}}\right).
\end{aligned}
\tag{2.50}
$$

For a magnetic trap gradient of ~ 1 T/cm and OH velocity of 5 m/s, we obtain the adiabatic transition probability curves of Fig. 2.13c. As either the angle between E and B or the electric field magnitude is increased, P_{ad} increases dramatically. This result suggests that trap loss due to adiabatic level crossings will be a serious problem for OH in magnetic quadrupole traps within a homogeneous E-field. The rather stringent requirement that $|\mathbf{E}| < 10$ V/cm places severe restrictions on tolerable stray E-fields in the trap region. Working in our group, Benjamin Stuhl and Mark Yeo have recently observed preliminary evidence of this trap loss mechanism.
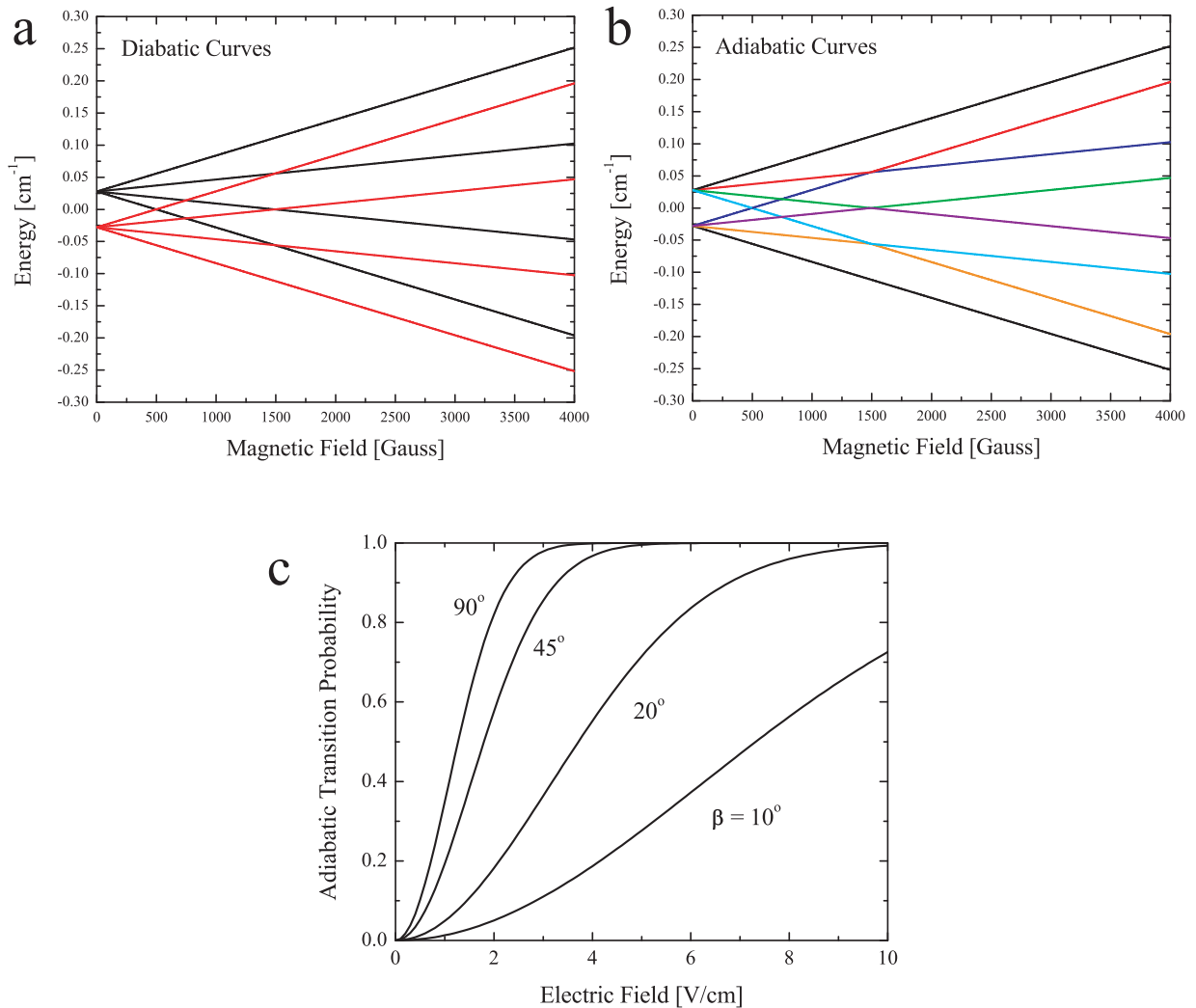
Figure 2.13: (a) Diabatic levels for ground state OH molecules. Upper-doublet (black) and lower-doublet (red) levels are completely uncoupled in this picture. (b) Color-coded adiabatic levels resulting from coupling between e and f parity states due to an external electric field. (c) Adiabatic transition probability (P_{ad}) for OH molecules within combined magnetic and electric fields. The probabilities shown are for coupling between the $|\frac{3}{2}, \frac{3}{2}, +\frac{3}{2}, e\rangle$ and $|\frac{3}{2}, \frac{3}{2}, +\frac{1}{2}, f\rangle$ states as a function of electric field and field angle β. Note that extremely small electric field magnitudes (< 10 V/cm) are sufficient to induce adiabatic transitions in this system.

Chapter 3

Production of Cold Molecular Samples

Accurate assignment of quantum numbers and fitting of spectroscopic constants to a room-temperature molecular gas are very difficult tasks. Most molecules possess rotational constants that are below 100 K, which leads to a wide distribution of population across different angular momentum and vibrational states at room temperature. Furthermore, Doppler broadening at 300 K gives inhomogeneous linewidths of ~ 10 GHz that can blend nearby rotational transitions in heavy molecules. In the context of molecular collision physics, cold samples of molecules promise a host of exciting novel collision dynamics including but not limited to external-field control of elastic/inelastic collisions and chemistry. Cooling molecular samples from 300 K to $\sim$10 K will alleviate the above spectroscopy issues and allow for further cooling to these collisionally-interesting temperature regimes, but begs the question "How can one produce gaseous molecular samples at temperatures far below their freezing point?"

Two primary molecular cooling methods – supersonic expansion and buffer gas cooling – have been developed to answer the fundamental question posed above. Both methods are rather simple in principle compared with atomic cooling techniques such as Doppler laser cooling, but the practical implementation of these cold molecule sources is anything but trivial. In this chapter, the theory behind these two production techniques will be presented along with experimental results and common pitfalls.

3.1   Supersonic Molecular Beams

3.1.1   Theory of Supersonic Expansions

A supersonic beam apparatus generally consists of a gas reservoir at temperature T_0 and pressure P_0 as well as an exit nozzle admitting this gas into a vacuum chamber at background pressure P_b. For molecular beams, the reservoir contains some dilute mixture of the molecule of interest within a noble gas carrier (commonly He, Ne, Ar, Kr, Xe, or some mixture of these). The use of a noble carrier gas insures minimum cluster formation and chemistry during the supersonic expansion, although the increased polarizability of the heavier species can lead to clustering (see Section 3.1.2). Pulsed beams include some valve actuation mechanism for both control of the temporal beam extent and limitation of overall gas load in the vacuum chamber. Furthermore, a molecular skimmer placed downstream from the valve orifice is commonly employed to separate the cold core of the molecular beam from the warmer gas envelope. The small diameter of the skimmer (usually ∼1 mm) also allows for large differential pressures between the supersonic expansion chamber and subsequent vacuum sections, which is critical for crossed-beam collisions and trapping experiments. A representative sketch of a supersonic beam assembly is shown in Fig. 3.1.

The thermodynamics of a supersonic expansion can be quite complicated. Especially in the case of a pulsed molecular beam, large swings in vacuum pressure throughout the valve pulse and subsequent gas expansion render simple analytical estimates of beam parameters such as terminal velocity (v_∞), ratio of beam speed to longitudinal velocity width ($S_\parallel$), and rotational temperature (T_{rot}) imprecise. However, the expressions for an ideal, continuous isentropic expansion give a nice starting point for predicting the behavior of pulsed beams and will be discussed here.

As a gas mixture expands into vacuum, the pressure difference $P_0 - P_b$ across the exit nozzle accelerates the particles and converts the enthalpy of the reservoir gas into forward velocity. Enthalpy per unit mass (h) is the most valid quantity for an isentropic expansion since the pressure differential does work on the molecules, thereby modifying the internal energy of the expanding particles. If the ratio of stagnation pressure to background pressure (P_0/P_b) exceeds the value

$[(\gamma + 1)/2]^{\gamma/(\gamma-1)}$, the velocity of the exiting beam will exceed the speed of sound and undergo further expansion within the vacuum region. The constant γ is the ratio of specific heats for the gas in question ($\gamma = 5/3$ for an ideal monatomic gas) [58]. Denoting the initial and final enthalpy of the gas as h_0 and h_f, respectively, and defining the final beam velocity as v, we obtain

$$h_0 = h_f + \frac{1}{2}\text{v}^2. \tag{3.1}$$

Assuming that the specific heat at constant pressure, C_p, does not change throughout the expansion (this assumption is species-dependent), we may express the final velocity as

$$\text{v}^2 = 2(h_f - h_0) = 2\int_T^{T_0} C_p dT = \frac{2k_B}{m}\left(\frac{\gamma}{\gamma - 1}\right)(T_0 - T). \tag{3.2}$$

In most instances, we make the approximation that $(T_0/T) = \infty$ and arrive at

$$\text{v}_\infty = \sqrt{\frac{2k_B T_0}{m}\left(\frac{\gamma}{\gamma - 1}\right)}. \tag{3.3}$$

One can see immediately from Eq. 3.3 that the experimentalist has two major adjustable parameters with which to tune the final velocity of a supersonic molecular beam — the mass (m) and temperature (T_0) of the noble carrier gas. The predicted velocities for different carrier gas species are given in the plot of Fig. 3.1. It is often desirable to produce beams at velocities between those shown in Fig. 3.1. In these instances, one can either change the temperature of the gas reservoir or mix different carrier gas species to obtain an effective mass ($\bar{m}$) given by $\bar{m} = \sum_i w_i m_i$ where w_i is the fraction of carrier-gas atoms of mass m_i.

Another important parameter of the supersonic beam is the speed ratio $S_\parallel$. This gives the longitudinal velocity width relative to the mean speed of the beam ($S_\parallel = \text{v}_\infty/\Delta\text{v}_\parallel$). When coupling a supersonic beam to a Stark decelerator with finite longitudinal velocity acceptance, one would like $S_\parallel$ to be as large as possible. Perhaps the most useful prediction for the parallel speed ratio is the empirical expression [59]

$$S_\parallel \sim 5.4(P_0 d[\text{torr} \cdot \text{cm}])^{0.32}, \tag{3.4}$$

where d is the diameter of the valve exit nozzle. At typical values of $P_0 \sim 1000$ torr and $d \sim 0.1$ cm, this expression predicts a 4% beam spread, which corresponds to a velocity width as small as
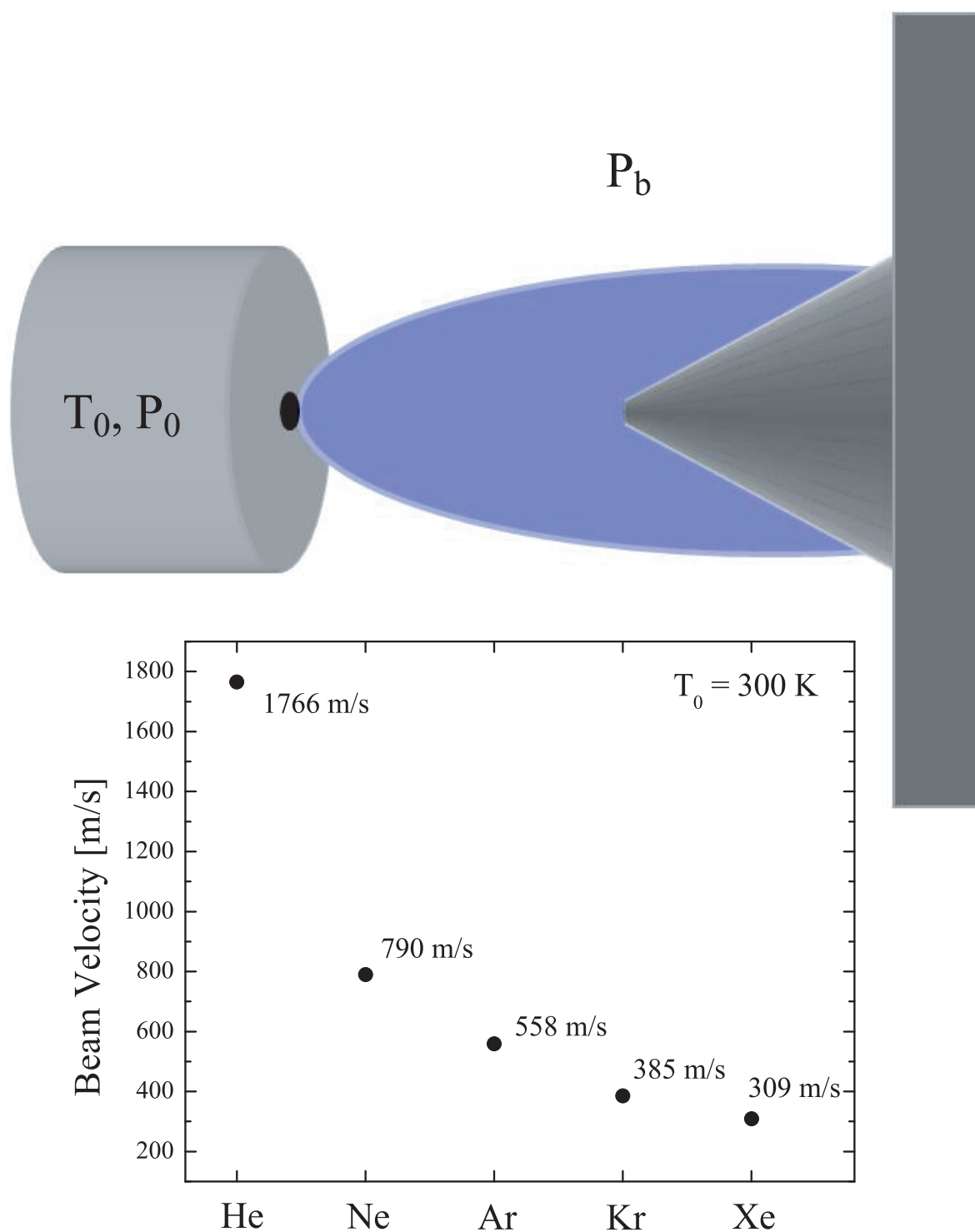
Figure 3.1: (Top) Illustration of a typical supersonic beam assembly featuring a gas reservoir at pressure and temperature P_0 and T_0, respectively and supersonic nozzle admitting the gas into a vacuum chamber at background pressure P_b. The skimmer is shown at right. (Bottom) Plot of predicted beam velocities for different noble carrier gases initially at room temperature.

13 m/s for an ideal Xe beam at $T_0 = 300$ K. Accurate prediction of the perpendicular temperature of a supersonic beam is much more difficult than for $S_\parallel$ [58]. However, we have found that for a beam of OH molecules seeded in either Kr or Xe, $T_\perp \sim T_\parallel/2$ where $T_\parallel \propto \Delta v_\parallel^2$.

Proper placement of the skimmer is critical to maximizing beam flux to subsequent experimental apparatus. Since a supersonic beam by definition possesses a mach number M larger than 1, shock waves form in the envelope of the expansion and re-collide with the beam itself at a distance L of

$$L = \frac{2}{3} d \sqrt{\frac{P_0}{P_b}}. \tag{3.5}$$

The distance L defines the downstream location of the so-called "Mach disk," and the ideal valve-to-skimmer distance (VSD) is generally well below this upper limit. However, for pulsed sources, the pressure ratio of Eq. 3.5 can easily exceed 10^7, yielding a mach disk location > 4 m downstream of a 1 mm nozzle! As one can imagine, other effects can become important at distances far below a meter. One such consideration is the transverse diameter of the expansion vacuum chamber. In small chambers, the carrier gas can reflect from the outer wall and collide with the supersonic beam before it has been extracted by the skimmer. In a small 11 cm-diameter source chamber, we have observed that skimmer throughput drops significantly for VSD > 6 cm. By moving the source to a much larger chamber with a diameter of 61 cm, we find optimal VSDs of $10 - 12$ cm. In both cases, skimmer throughput decreases monotonically as the VSD is decreased below 5 cm. This is likely due to gas scattering from the skimmer assembly itself, as we have seen improvements of $\sim 30\%$ in throughput by cooling the skimmer below the freezing point of the carrier gas (Xe in this case). Nevertheless, the absolute beam density remains largest at the aforementioned higher values of VSD.

Finally, it is important to characterize the rotational temperature (T_{rot}) of a supersonic molecular beam. It generally takes only 10-100 collisions to fully thermalize T_{rot} to $T_\parallel$, but the degree of rotational thermalization can vary depending on factors such as the carrier gas used (clustering), the rotational structure of the molecule, or whether additional heating mechanisms

(e.g. OH discharge sources) are necessary for beam production. For molecules with small rotational constants ($hB/k_B \lesssim T_{\parallel}$), the spectroscopically-detected rotational populations may be fit to a Boltzmann distribution given by

$$A_i \propto S_i(2J_i + 1)\exp\left(\frac{-U_i}{k_B T_{rot}}\right) \tag{3.6}$$

where A_i is the measured signal from state i, S_i is the strength of the transition probed to detect the given state, J_i is the total angular momentum of state i, k_B is Boltzmann's constant, and the last term is the usual Boltzmann factor for level i of energy U_i. When the rotational constant is large compared to $T_{\parallel}$, little or no population can be detected in higher-lying rotational states and a two-state temperature considering just the ground and first excited level is often quoted. This same technique is generally used for vibrational temperatures, T_{vib}. Denoting the ground and excited levels as $i = 0$ and $i = 1$, respectively, we obtain

$$T_{rot} = \frac{\Delta U}{k_B}\ln\left(\frac{A_0}{A_1}\frac{S_1}{S_0}\frac{(2J_1 + 1)}{(2J_0 + 1)}\right)^{-1} \tag{3.7}$$

where $\Delta U = (U_1 - U_0)$.

When molecules possess identical nuclei that divide rotational states into *ortho* and *para* levels due to a restriction on the overall exchange symmetry, as is the case with homonuclear diatomics and ammonia, it is often necessary to fit different temperatures to the distinct rotational ladders. This phenomenon results from the small coupling between nuclear spin and molecular rotation that impedes collisional transfer between *ortho/para* levels [60].

3.1.2   Clustering of Carrier Gases

In the quest for slow supersonic beams with ever-narrower velocity distributions, it is tempting to take Eq. 3.4 at face value and use the highest stagnation pressure and largest nozzle diameter possible with a high-mass (e.g. Kr or Xe) carrier. Unfortunately, the heavier noble gases also possess larger polarizabilities. The result is a species-dependent rate of cluster formation that scales roughly as $(P_0 d)/T_0^2$. Gas clustering has two primary negative effects: higher molecular

Table 3.1: Values of the clustering constant k for a range of atoms and molecules (obtained from Ref. [3]).

Gas	k	Gas	k
He	3.85	H_2	184
Ne	185	D_2	181
Ar	1650	N_2	528
Kr	2890	O_2	1400
Xe	5500	CO_2	3660
		CH_4	2360

rotational temperatures due to inefficient cooling in cluster-molecule collisions and larger beam velocities/widths from gas heating. Smith *et al.* fit an empirical functional form to quantify the onset of clustering, which is determined by the Hagena parameter (Γ^*) given by [3]

$$\Gamma^* = k\frac{(d[\mu\text{m}]/\tan\alpha)^{0.85}}{T_0[\text{K}]^{2.29}}P_0[\text{mbar}] \tag{3.8}$$

where k is a species-dependent constant and α is the opening half-angle of the valve nozzle. To insure that clustering does not occur, it is best to operate the expansion with $\Gamma^* < 100$. The average cluster size for larger values of Γ^* is then $\propto (\Gamma^*)^{2.0-2.5}$. Values of k for both atomic and molecular species are given in Table 3.1. To give a sense of scale, our pulsed valve assembly for OH molecules features a 1000 μm-diameter nozzle with a $20°$ half-angle and a carrier gas of Kr at 295 K and 2100 mbar. Applying Eq. 3.8 gives $\Gamma^* \sim 2000$, which suggests that some amount of clustering is unavoidable for noble gases heavier than Ne at standard stagnation temperatures and pressures.

Interestingly, Christen *et al.* have recently demonstrated that pure beams of CO and CO_2 formed from stagnation temperatures and pressures above their respective critical points show less cluster formation than seeded beams [61]. In fact, they find that the pure supercritical molecular beams have speed ratios exceeding 100. They attribute this affect to an enhanced value of γ near the critical point. Given the thermodynamic nature of clustering, it is not altogether surprising that moving beyond the critical point in the phase diagram (and hence avoiding phase transitions) would make cluster formation less energetically favorable. However, given the extremely large

critical points of many chemically-interesting molecules, this trick is not universally applicable. Nonetheless, certain crossed beam experiments might benefit greatly from the enhanced density that a pure supercritical molecular beam can provide.

3.1.3 Pulsed Supersonic Valves

Throughout the experimental history of pulsed supersonic beams, many different valve actuators have been developed and tested [58]. Given the countless number of articles on new valves and modifications to existing valves (see *Review of Scientific Instruments*), we restrict the discussion of this section to three specific valve designs that have been used in our OH supersonic beam experiments. Some pros and cons of each design are presented along with experimental data specific to OH production.

3.1.3.1 Current Loop Valve

The current loop valve (CLV) described here is a commercial unit (Jordan TOF Products, Inc. Model C-211) that uses very large currents (~ 4000 A $- 5000$ A) passed between two parallel conducting strips to open the valve nozzle. The CLV is capable of rather short gas pulses ($<100\mu$s) at repetition rates of up to 10 Hz. We have found the current loop valve to be extremely stable over long durations, and this stability is reflected both in the shot-to-shot and week-to-week measured molecular pulse densities. As such, we often use this system to debug new molecular beam experiments (e.g. new Stark decelerators or magnetic traps). However, there are two major drawbacks to this design as a pulsed beam source for cold, high-density molecular beam experiments: low overall output flux compared with other valve designs and time-dependent beam heating. Despite the manufacturer's claims that choke flow is obtained within the 60 μs gas pulse, we see as much as a 50% reduction in OH production with this valve compared with the solenoid and piezo valves. Furthermore, as described in Ref. [62], we see that the high currents within the actuator mechanism heat the leading edge of the gas pulse and produce faster/hotter molecular beams.

We employed this valve for both precision measurements of the OH Λ-doublet splitting [21, 24]

as well as the first Stark deceleration of formaldehyde (CH_2O) [63]. However, the lower densities produced by the CLV were not suitable for subsequent magnetic trapping or collision experiments [64, 40, 18].

3.1.3.2 Solenoid Valve

The solenoid valve (General Valve Series 9 or 99) is arguably the workhorse of pulsed beam experiments. Consisting of a stainless steel body surrounded by a solenoid wire wrap, this valve may be used with a large variety of corrosive substances with little or no adverse affects. The actuator mechanism consists of a PTFE-coated ferromagnetic armature within the stainless housing onto which is attached a (usually plastic) poppet that seals against the valve orifice. Since the drive current is well-isolated from the inner valve chamber, we observe no time-dependent heating effects with the solenoid valve (SV). Another feature unique to the SV Series 99 is its ability to operate at both cryogenic [65] and elevated [66] temperatures. In stock form, this valve produces gas pulses no shorter than ~ 200 μs due largely to its reliance on spring tension to close the armature. Furthermore, we often observe an initial "bounce" in the gas pulse within 100 μs of the initial voltage trigger wherein the gas density is momentarily reduced. At the end of the pulse, a closing "bounce" signified by a two-pulse structure can also be observed. Benjamin Stuhl, a graduate student in our group, has found that this trailing "bounce" can be removed by applying a second 260 V (200 μs) pulse to the solenoid 120 μs after the initial 400 μs opening pulse.

One fundamental problem with the long-term stability of the general valve is the plastic poppet tip that seals the nozzle. Since this tip seals against a stainless steel orifice, it necessarily deforms with each closing strike. Over time, the behavior of the valve (pulse width, output gas flux) will change unpredictably and necessitate removal and replacement of the poppet. For Stark deceleration and trapping experiments, these vacuum breaks can cost the experiment days or weeks. As a result of this long-term instability, we do not use the SV for our primary OH source. It is worth noting that other Stark deceleration groups, specifically the group of G. Meijer at the Max Planck Institute, use a modified general valve for many of their beam experiments [67].
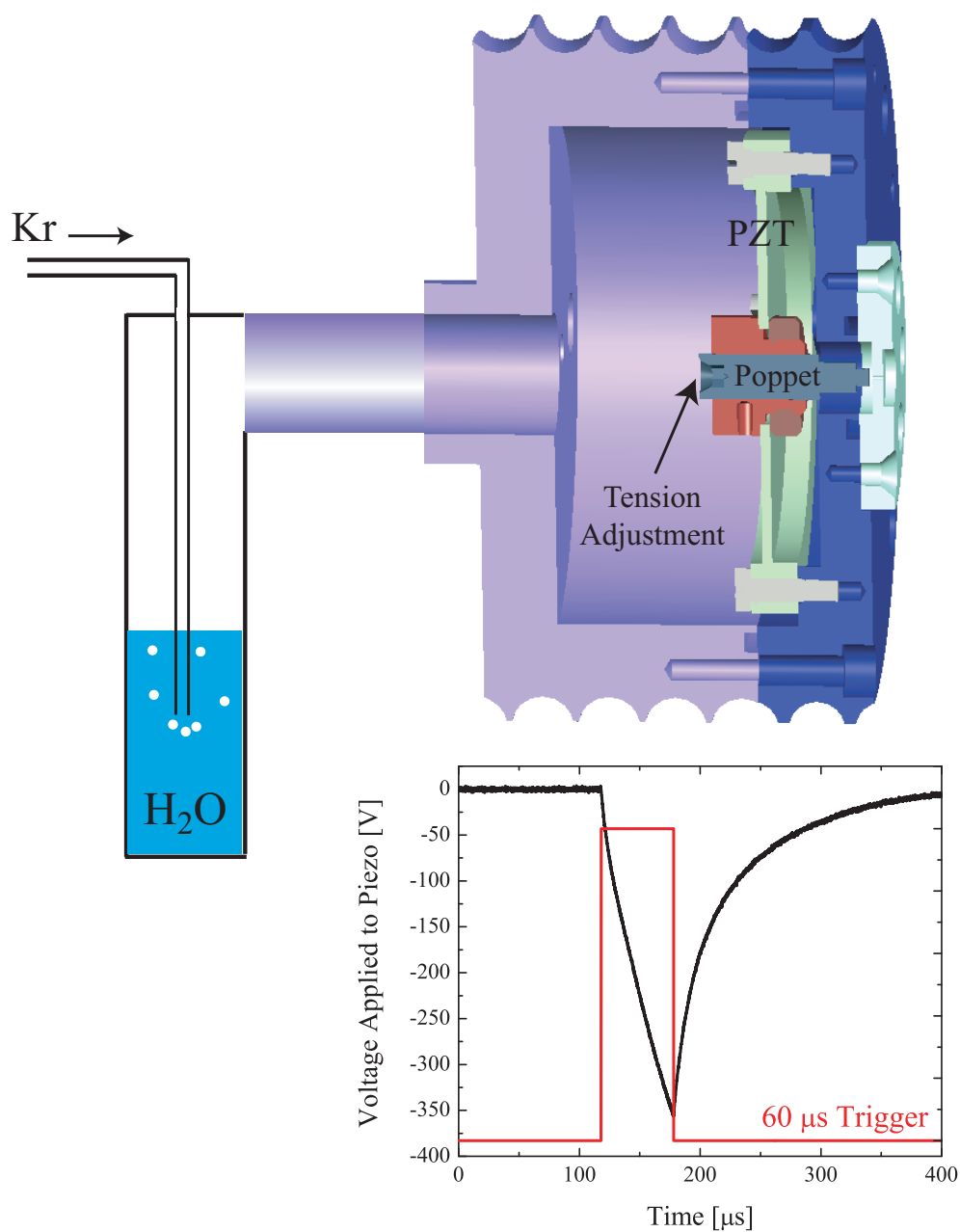
Figure 3.2: Drawing of the PZT valve assembly showing the adjustable poppet, disk piezo translator, and valve housing. The Kr/H_2O bubbler system for production of OH via pulsed electric discharge is also shown. (Inset) Measurement of the high voltage pulse applied to the PZT. It is critical that the RC time constant of the voltage pulse be $\gtrsim 40$ μs to avoid cracking the piezoelectric crystal.

3.1.3.3 Piezoelectric Transducer (PZT) Valve

As a compromise between the long-term operational stability of the CLV and the high output flux of the SV, we make use of a modified version of a piezoelectric transducer (PZT) valve originally developed by Proch and Trickl [68]. A drawing of our valve design is given in Fig. 3.2 showing our piezo disk actuator (Polytec PI 286.23) and stainless steel poppet sealing against an o-ring at the nozzle orifice. Proch and Trickl's primary improvement over the existing PZT valves was to implement a disk piezo actuator with a tenfold increase in excursion of ~ 100 μm. This allows for choke flow conditions and pulse widths as short as 150 μs. The use of a viton o-ring to seal the exit nozzle removes the issue of poppet wear associated with the solenoid valves, while the capacitive load of the PZT minimizes heating of the supersonic beam. To allow fine-tuning of the valve opening dynamics *in situ*, we have added a rod that inserts into the back of the steel poppet and adjusts its tension against the exit orifice (see Fig. 3.2).

When operating the PZT valve, it is critical that the piezo crystal is not exposed to corrosive substances or temperatures outside of the range 230 K - 350 K, otherwise it will crack and fail to open consistently. Furthermore, the output impedance of the voltage drive circuit must be large enough that the 65 nF piezo does not crack due to stress. We find that an RC time constant of ~ 40 μs and drive voltages below -600 V are sufficient to keep the valve running stably for months at a time. The actual shape of the applied drive pulse is plotted in the inset of Fig. 3.2 along with the corresponding 60 μs square-wave trigger.

3.1.4 Production of OH Supersonic Beams

It can be said that supersonic beam sources have a "personality" due to their sensitive dependence on many different experimental conditions. Optimizing a pulsed valve assembly involves tuning a large number of parameters that often interact with one another (e.g. valve pulse voltage/width and poppet backing tension). In the case of radical sources, the addition of a production method just before the supersonic expansion further complicates beam optimization and can dras-

tically modify beam parameters from the predicted values of Section 3.1.1. In this section, two OH beam production methods will be discussed and beam data from both will be compared.

3.1.4.1   Pulsed Electric Discharge of H_2O

The pulsed electric discharge of H_2O is currently our OH production method of choice due to its stability, longevity, and ease of operation. An illustration of the discharge "stack" mounted to our PZT valve nozzle is provided in the upper left of Fig. 3.4. The stack consists of alternating plates of ceramic insulator (Macor) and highly-polished stainless steel. After the valve is opened, we apply a voltage of ~ -1 kV to the outer steel plate to strike a ~ 10 μs discharge within the exiting mixture of Kr and H_2O vapor. Triggering the discharge voltage ensures that we create OH at the densest point within the gas pulse and avoid unnecessary heating from continuous operation. Furthermore, we are able to run at rather low discharge voltages by seeding the process with positive ions from a nearby ionizing pressure gauge [62]. This results in a colder, slower OH beam. We deduce that positive ions are responsible for this enhanced discharge efficiency since changing the polarity of the outer discharge plate and/or turning off the ionization gauge leave a very unstable discharge. Overall, we are able to reduce the necessary discharge voltage by a factor of 4-5 by seeding in this manner, thereby obtaining a colder, brighter OH pulse than is attained with unseeded continuous discharges. We measure beam densities of $\sim 10^9 - 10^{10}$ cm^{-3} in the source chamber with this production technique. The 40° opening angle of the nozzle beyond the discharge region has been shown to give an order-of-magnitude increase in beam flux due to beam collimation [69]. It is possible that our required VSD of 10 cm results from this enhanced density of the carrier gas, which can lead to "skimmer clogging" and reduced throughput.

Since our OH beam must travel a total of 15 cm to the Stark decelerator, we are also able to implement a multi-pulse discharge to increase beam flux within the longitudinal velocity acceptance of our deceleration sequence. To accomplish this, we break up the discharge over three short 6 μs pulses each separated by 3 μs. The three distinct OH pulses spatially combine over the long flight path to the Stark decelerator and yield a $> 50\%$ enhancement in beam density with a mere 8%
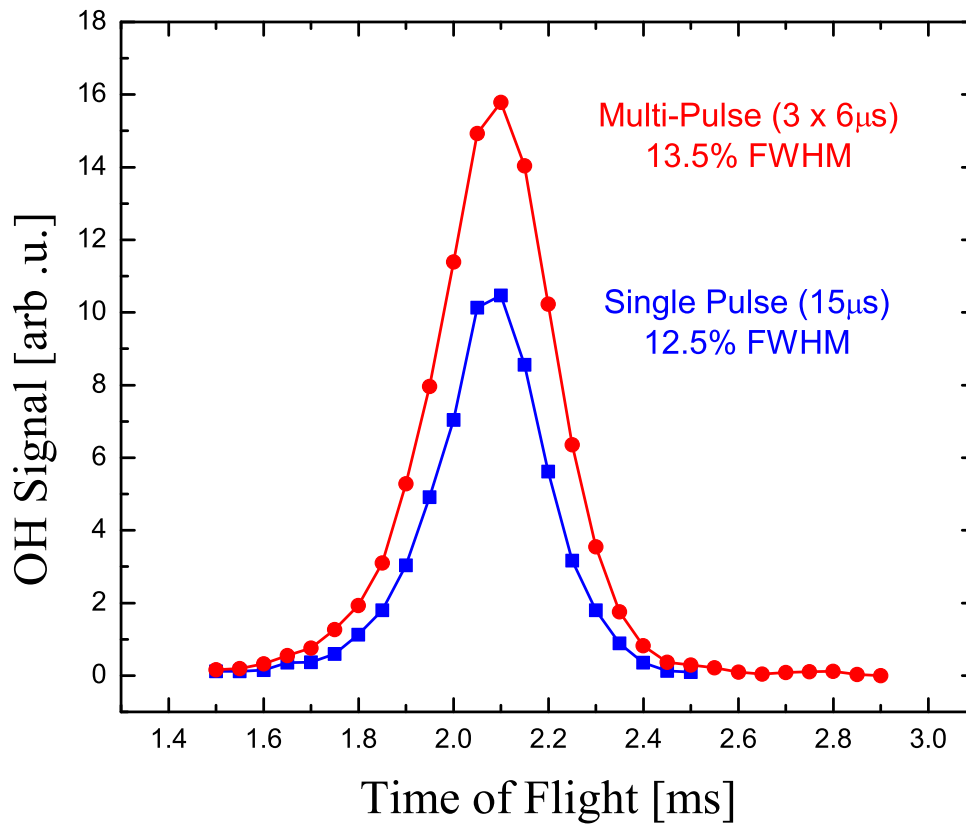
Figure 3.3: Comparison of a single-pulse electric discharge to a multi-pulse discharge of roughly the same duration. The three separate OH pulses spatially combine in free-flight to the detection region and yield > 50% improvement in beam density. The above data was taken 1 m downstream from the supersonic valve.

increase in $T_{\parallel}$. This result is displayed in the plot of Fig. 3.3.

3.1.4.2 Photolysis of HNO$_3$

One alternative to the comparatively violent electric discharge is a photolysis source that uses a pulse of UV photons to fragment a precursor molecule following the pathway $X + h\nu \rightarrow OH + Y$. For OH production, the most commonly used photolysis precursors are nitric acid (HNO$_3$) and peroxide (H$_2$O$_2$). Since photolysis produces the molecule of interest over the spatial and temporal extent of the excitation laser, the product molecular packet possesses a well-defined origin. The resulting beams are also translationally/rotationally colder than their counterparts produced from discharges. In fact, propensities for specific Λ-doublet and J states within the OH vibrational and electronic ground state have been identified for both nitric acid [70] and peroxide [71] precursors.

We have produced OH beams from HNO$_3$ photolysis at 193 nm using a pulsed ArF excimer laser (Lambda Physik OptexPro). An illustration of the photolysis setup is given in Fig. 3.4. We modified our existing PZT valve for use with the extremely corrosive nitric acid vapor by adding an additional chemically-resistive polyimide chamber to isolate the gas from the piezo crystal. The poppet was also machined from polyimide and passed through a double-sided o-ring through the Kr/HNO$_3$ chamber to seal against the valve orifice. In place of the electric discharge stack, we installed a UV-transmissive capillary with an inner diameter of 1 mm. The excimer laser was focused onto the capillary with a combination of two orthogonal 50 cm cylindrical lenses to allow for adjustment of the OH production volume as well as pulse intensity. As with the discharge source, we cut a 40° full-angle cone into the end of the capillary cell for improved molecular beam collimation [69]. The plot of Fig. 3.4 directly compares the density of this optimized OH source with that of the optimized discharge source. The data for both curves were taken on the same day with identical OH excitation laser beams and fluorescence collection optics. The discharge source produces a beam with a 6% larger velocity width than the photolysis source, but wins in density by a factor of ~ 2. Given the dangers of working with HNO$_3$ and the smaller yield produced by photolysis from our PZT valve, we now use the pulsed electric discharge exclusively for OH

Seeded Electric
Discharge

Photolysis of
HNO$_3$

193 nm ArF Pulse
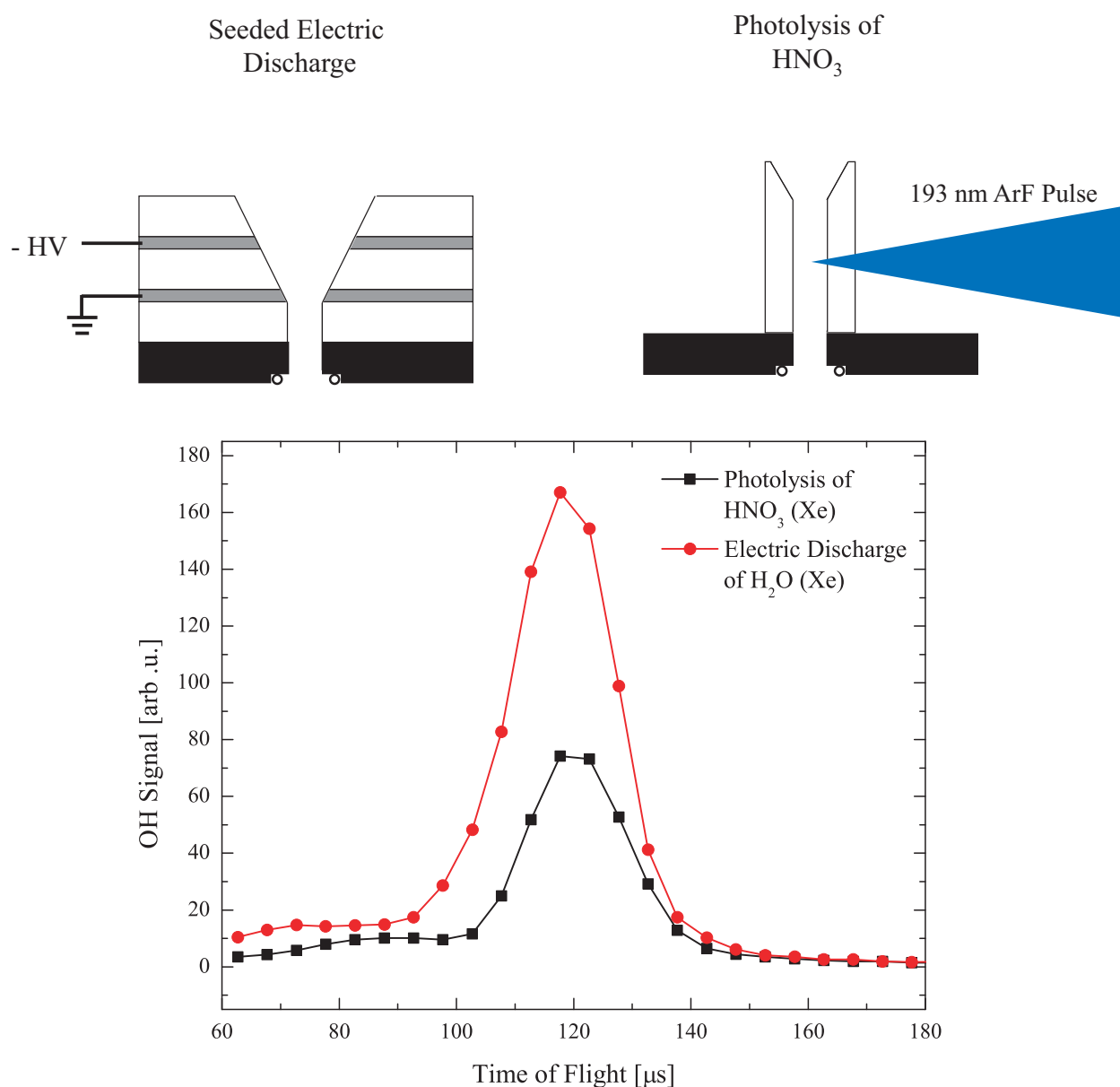
Figure 3.4: (Top) Illustrations of the pulsed electric discharge and photolysis sources for OH supersonic beam production. Note the 40° exit nozzle cut into both sources for enhanced OH beam density. (Bottom) Plot of relative OH yield for the discharge and photolysis sources measured within the source chamber. The photolysis precursor for this data was 99% pure HNO$_3$.

production.

3.2   Buffer Gas Beams

Buffer gas cooling is based on the rather simple concept of thermalizing a hot atomic or molecular sample with a cold inert gas (usually He). This thermalization occurs within a buffer gas cell anchored to a low-temperature cryostat assembly and, when combined with magnetic traps or coupled out as a beam, allows for a wide variety of atom-molecule [72, 73, 74] and molecule-molecule [18] cold collision experiments. In contrast with other cold molecule production techniques that rely on electric/magnetic dipole moments [19, 75, 76, 77] or ultracold alkali-atom precursors [78, 79], buffer gas techniques are in principle applicable to any atomic or molecular species. However, as we will see in the case of cold ND_3 beams, these sources have their own technical limitations. Our specific goals in developing a continuous buffer gas source for molecular collision experiments were (1) to obtain stable cold ND_3 beam flux for ~ 1 hr, (2) to produce a rotationally-cold ND_3 sample, and (3) to obtain guided, state-selected ND_3 densities of $> 10^8$ cm^{-3}. As will be discussed, the first goal was the most difficult to achieve, and the path to realizing goal 2 was not completely clear.

3.2.1   The JILA Buffer Gas Beam Machine

There are many useful texts covering construction of cryogenic systems. Two of our most commonly-used references are works by Pobell [80] and Ekin [81]. Far from being exhaustive, this section will only highlight certain techniques necessary for operation of our buffer gas beam. We will discuss some useful materials (both thermally conductive and insulating) as well as basic buffer gas cell design. We are grateful to D. Patterson, J. Rasmussen, and J. Doyle for their contribution to our development of an ND_3 buffer gas beam source at JILA.

Construction of a buffer gas system begins with a cryostat. The cryostat is an evacuated tube into which (in our case) two cold stages are mounted. These stages may be cooled by either cryogenic liquids (N_2,He,Ne) or with a cryogen-free refrigerator (e.g. pulse tube). The first stage

**4 K Helium Bath or
Pulse Tube Refrigerator 2nd Stage**

360 mW
Heater

285 K

Epoxy
Fiberglass
Composite

ND$_3$

Charcoal
Sorb

Radiation Shield (< 100 K)
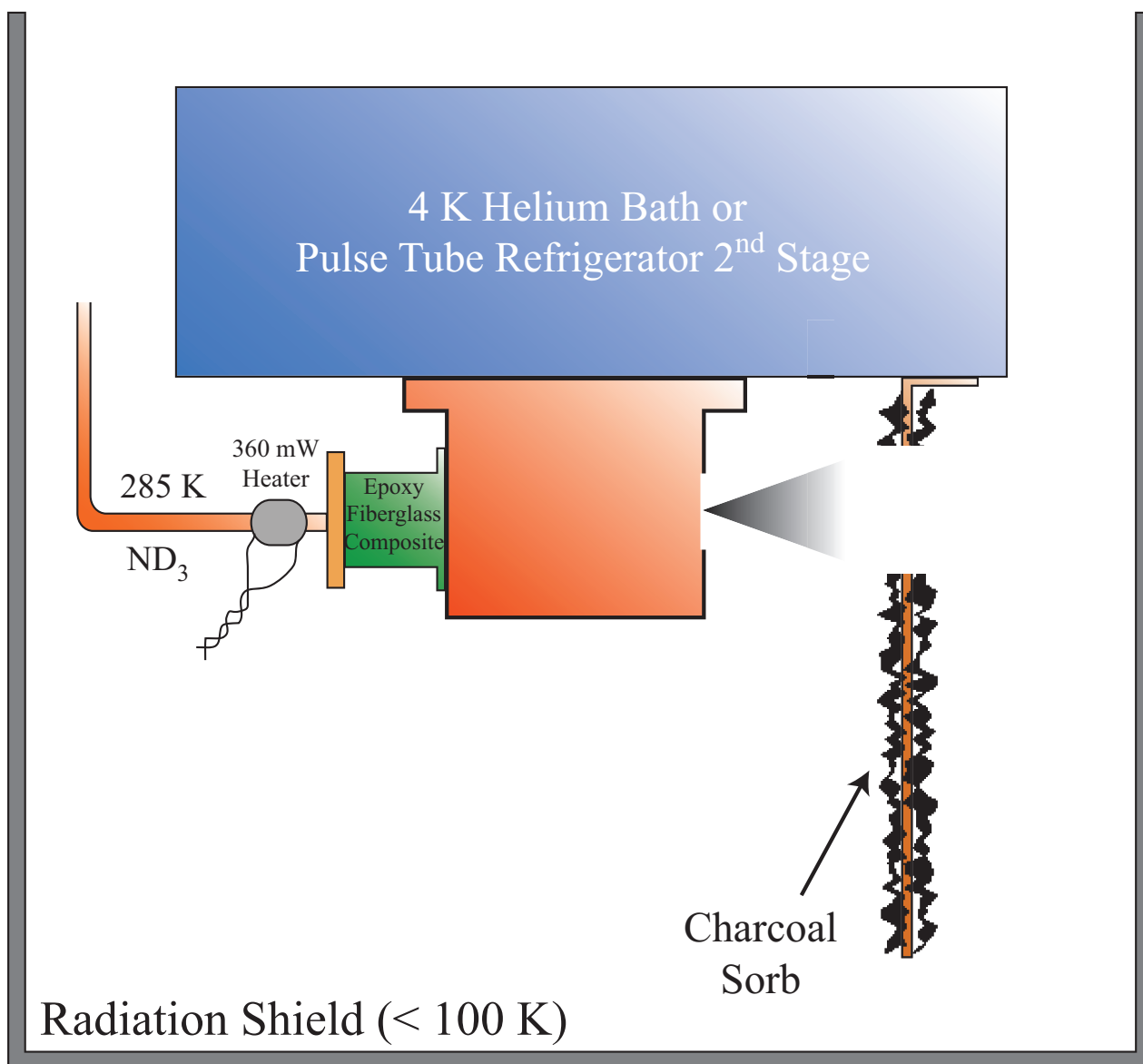
Figure 3.5: Illustration of our buffer gas beam assembly. The ND$_3$ gas is fed down a heated copper tube at 285 K. This hot supply tube is thermally isolated from the cold buffer gas cell via a polyetherimide (Ultem) insert and thin-walled epoxy-fiberglass composite (G10) tube. The pre-cooled He gas (not shown) is fed into the side of the cell. Charcoal sorb glued to copper plates ($\sim$ 2000 cm^2 total) acts as a vacuum pump for He and ND$_3$ gas.

of the cryostat is used to cool a few-mm-thick copper or aluminum radiation shield whose purpose is to absorb 300 K blackbody radiation from the outer vacuum can (OVC). In "wet" systems, this first stage is usually cooled with liquid nitrogen at 77 K. In cryogen-free systems, the first stage can be as cold as 30-40 K. From the Stefann-Boltzmann law, the intensity, I_B, radiated by a blackbody at temperature T is

$$I_B = \sigma T^4 \tag{3.9}$$

where $\sigma = 5.67^{-12}$ W/(cm^{2}K^4). From this, we expect a heat load of ~ 45 mW/cm^2 from the 300 K OVC* . For a cylindrical OVC with a radius of 10 cm and height of 50 cm, the radiation shield must absorb ~ 140 W of blackbody power. With its large heat of vaporization of 199 J/g, liquid nitrogen under a 140 W heat load will only boil at a rate of ~ 3 L/hr. Moving past the radiation shield to the second stage of the cryostat, the blackbody heat load drops by a factor of 230 due to the T^4 scaling of Eq 3.9. However, the second stage is generally cooled with liquid helium whose heat of vaporization is a much smaller 20.7 J/g. This means that a 1 W heat load burns 1.2 L/hr of liquid helium and that the experimenter must be diligent in minimizing second-stage heat sources. One relatively easy method for reducing blackbody effects is to lower the emissivity (absorbtivity) of cold surfaces. This basically means make them "shinier" to the infrared radiation at 300 K and below, and can be accomplished by either polishing cold metal surfaces or wrapping the system in highly-reflective aluminized mylar sheeting (also known as "space-blanket"). The emissivity of highly-polished stainless steel can reach as low as 0.1, which would correspond to an order-of-magnitude reduction in blackbody heat load.

Our buffer gas source is illustrated in Fig. 3.5. Originally, we developed this source within a liquid helium cryostat that holds 1.5 L of liquid helium and ~ 3 L of liquid nitrogen for the radiation shield. More recently, for the OH-ND$_3$ collision experiment [18], we have mounted our buffer gas cell to the second stage of a cryogen-free pulse tube refrigerator (Cryomech PT-410) to simplify daily operation. In both cryostats the second stage and buffer gas cell temperatures are

---

* The cryostat is generally constructed with sufficient thermal breaks between the OVC and cooled stages such that heat transfer is radiation-dominated.

$4.5 - 5$ K under typical operating conditions.

To produce the buffer gas cooled beam of ND_3 in He, we flow warm ND_3 down a heated 3/32" copper tube into the back of the buffer gas cell. The warm ammonia tube must be well-isolated from the cold cell to avoid unnecessary heating and, in the case of the "wet" cryostat, maximize runtime before refilling liquid helium. With a combination of polyetherimide (Ultem) and thin-walled (0.010") epoxy-fiberglass-composite (G10) thermal breaks, we have reduced our cell heat load to < 1 W when we are not flowing He. These thermal breaks are shown in Fig. 3.5. When we flow the pre-cooled He gas into the side of the cell, gas conduction from the warm ammonia inlet to the inner cell walls raises the heat load to 1 W. We control both the He and ND_3 gas flow rates with thermal flow controllers (MKS M100B). The primary vacuum pump in the cryostat is a cryopump consisting of 4.5 K copper sheets onto which are glued pieces of activated charcoal. When cooled to near the boiling point of He, the charcoal sorbs trap the gas and hold it until the temperature is increased. We find that ~ 2000 cm^2 of sorb is sufficient to keep the He pressure stable in the cryostat over our beam runtime of ~ 1 hr.

Our 4 cm-long buffer gas cell is machined from a solid 3.8 cm x 3.8 cm bar of oxygen-free high conductivity (OFHC) copper. A 2 cm-diameter bore is drilled down the center of the block from back to front. Tapped, helicoiled screw holes are also added to these ends for mounting of the ND_3 inlet and 6 mm exit aperture. A small hole is drilled into the side of the cell for mounting of the pre-cooled He gas inlet. We see no clear difference between mounting the ND_3 inlet from the side or the back, but other groups have reported more efficient molecular cooling with a side-mounted molecule inlet [82]. Furthermore, we have measured ND_3 beams produced in both 12-15 K Ne and 4.5 K He, with He being the clear winner by an order of magnitude with respect to ultimate guided molecular density in the $|J, K\rangle = |1, 1\rangle$ *para* ground state.

3.2.2   Translational and Rotational Cooling

Much of the language of buffer gas beam dynamics is similar to that of supersonic expansions with the exception that, in the case of buffer gas beams, one generally prefers as few collisions as

possible to cool the molecule of interest. The last thing we want is to work hard to cool ND_3 to 5 K only to significantly boost the beam to supersonic velocities as it exits the cell aperture. Patterson and co-workers identify three flow regimes each possessing different characteristic beam velocities (characterized here with the molecular mean free path ℓ and cell aperture diameter d) [83]:

Effusive $(\ell > d)$ Relatively few cold molecules are extracted from the cell before they stick to the cold walls, and the mean speed of the molecular beam is just the most probable speed of the molecule of interest given by $\sqrt{2k_B T/m_{molecule}}$.

Hydrodynamic $(\ell \sim d)$ As the mean free path approaches the aperture diameter, collisions within the expanding beam can cool the rotational degree of freedom below the thermal temperature. Also, the forward beam velocity is "boosted" to the most probable speed of the buffer gas given by $\sim \sqrt{2k_B T/m_{buffer}}$. Additionally, considerable increases in cell extraction are reported in this regime [84].

Supersonic $(\ell \ll d)$ This is the usual case covered in previous sections where significant rotational and translational cooling occurs and the beam is considerably boosted to the supersonic velocity of $\sim \sqrt{5k_B T/m_{buffer}}$. This expression for the supersonic velocity assumes an ideal monatomic buffer gas ($\gamma = 5/3$).

Also in Ref. [83], it is argued that a hydrodynamic Ne buffer gas source operating at 15 K should perform better than a 4.5 K He source with respect to both beam temperature and flux at low velocities. Interestingly, we have directly compared a 15 K Ne/ND_3 beam with a 5 K He/ND_3 in our system and determined that the guided flux of the 5 K He/ND_3 beam was larger by a factor of > 10. This signal corresponded to a guided density of $\sim 10^8$ cm^{-3}, fulfilling the first goal of the introduction. The corresponding data is shown in Fig. 3.6 for a fixed cell-to-guide distance of 1 cm. One possible reason for the different results could be scattering of the hydrodynamically-boosted Ne beam from the nearby hexapole electrodes. This is plausible since our optimal He:ND_3 flow rates were 1:6 sccm while no combination of Ne:ND_3 flows in the range (1-20):(1-15) sccm produced comparable guided beam densities. If the particle density is such that hydrodynamic boosting
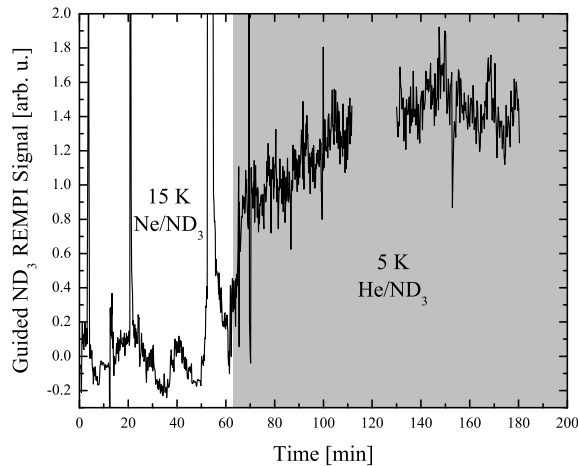
Figure 3.6: Data comparing electrostatically guided flux of a 15 K Ne/ND$_3$ beam with that of a 5 K He/ND$_3$ under otherwise identical conditions. Flow rates for both conditions were varied over the full range of the flow controllers in the time shown, and the cell-to-guide distance was fixed at 1 cm.

occurs, one would expect an enhanced sensitivity of beam parameters to nearby boundaries. For reference, 1 sccm = 4.4×10^{17} s^{-1}.

The data of Fig. 3.6 convinced us to focus primarily on He/ND$_3$ beams for production of a cold, dense beam suitable for molecular collision experiments. Moving the buffer gas cell closer to our hexapole guide (now 2.5 mm cell-to-guide), we gained an additional factor of 2 in guided beam density.

The science and technology of buffer gas beams is sufficiently new that only a handful of experimental groups are actively running such sources. As such, the subject of rotational cooling in buffer gas molecular beams has not been studied extensively. Prior to our work, no direct spectroscopic determinations of rotational temperatures had been published, although Sommer and co-workers had investigated ND$_3$ rotational temperatures using a state-dependent electrostatic guiding model [85]. In our system, we have demonstrated control over the rotational temperature of a He/ND$_3$ beam – varying the effective *para* temperature from 5 K to > 6 K. This is accomplished by adjusting the thermalization rate of ND$_3$ within the buffer gas cell with the relative flow rates of He and ND$_3$. At He:ND$_3$ flows of 2.0:2.5 sccm, we measure a rotationally hotter beam that is
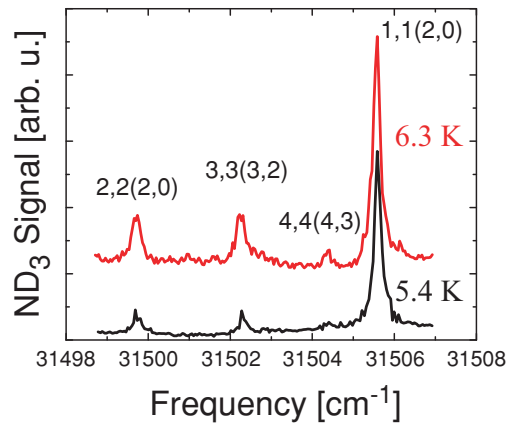
Figure 3.7: Measured spectra of a guided buffer gas source of ND_3 under two different buffer gas flow conditions. The red curve gives a *para* rotational temperature of 6.3 K for buffer as flows of 2.0 sccm He and 2.5 sccm ND_3. The black spectrum reflects the better rotational thermalization observed with flows of 3.5 sccm He and 1.0 sccm ND_3.

consistent with $T_{rot} = 6.3$ K. However, by increasing the flow ratio to 3.5:1.0, we observe $T_{rot} = 5.4$ K, which is only slightly above the temperature of the buffer gas cell itself. This supporting data is shown in Fig. 3.7. While the difference in T_{rot} seems rather small, the similarly small rotational constant of ND_3 results in a relative factor of 1.7 in the $|1,1\rangle : |2,2\rangle$ population ratio over this temperature range.

3.2.3   The "Pulsing" Phenomenon and Beam Runtime

Ammonia freezes at a temperature of 195 K. Therefore, if you expect ice formation within the 4.5 K buffer gas cell to play a major role in beam dynamics over long time periods, you would be correct. In fact, our first buffer gas cells were quite a bit smaller than our final design of 3.8 cm x 3.8 cm x 4 cm and possessed exit apertures of ~ 1 mm not unlike those used by the Rempe group. However, with cells smaller than 2 cm we see frequent disruptions in the cold beam flux accompanied by large pressure bursts and cell temperature increases. These flux dropouts can be seen in Fig. 3.8a. Having tried a host of different ND_3 tube mounting schemes, we always see this "pulsing" effect with small cells. Furthermore, we observe that small apertures clog with ammonia ice over time scales similar to those reported in Ref. [85]. While those authors use a heater to de-ice

their aperture, they still observe constant reduction in output flux over the intervening 1-2 hrs. To avoid this effect, we use the aforementioned 6 mm-diameter exit aperture. While this likely leads to more effusive beam behavior due to an inability to build up He pressure in the cell, we see no evidence of long-term icing with such a large exit nozzle.

We have found that the only solution to the "pulsing" effect is to scale up the dimensions of the cell so as to maximize the distance between the warm ND_3 inlet and any cold surface. This result suggests that ammonia ice accumulates on the cell wall over time and eventually bridges the gap to the warm inlet (see Fig. 3.8c). The "pulse" most likely results from rapid vaporization of ice at the warm ammonia tube and subsequent heating of the He gas within the cell. With a distance of ~ 1 cm between the ND_3 tube and cell wall, we obtain 1 hr of continuous, stable runtime of the cold beam as shown in Fig. 3.8b.

3.2.4   Electrostatic Velocity Filtering

The beam emitted from a buffer gas cell consists mostly of coolant atoms. The cooled molecular sample can also exhibit population in excited rotational levels. In order to gain control over both the translational and rotational temperature of the cooled molecular beam and filter the species of interest from the buffer gas, it is necessary to introduce a state- and velocity-selective guide. Both magnetic octopole [86] and electrostatic quadrupole [87] guides have been employed in previous buffer gas beam experiments. For our system, we chose to implement a curved electrostatic hexapole to ensure maximum transverse guide depth and field homogeneity. An illustration of our buffer gas cell and electrostatic guide are given in Fig. 3.9. Note that we use separate straight and curved guide sections to allow isolation of the buffer gas source from the ultra-high vacuum of the OH trap chamber via a thin (3 mm) gate valve. This feature is absolutely necessary since ND_3 ice must be removed from the buffer gas cell after ~ 1 hr of continuous beam operation. To accomplish this, we warm the cryostat to room temperature over $\sim 4 - 6$ hrs and pump out the He and ND_3 released from the charcoal sorbs and buffer gas cell.

The transverse dynamics of confined ND_3 molecules is rather straightforward and, neglecting
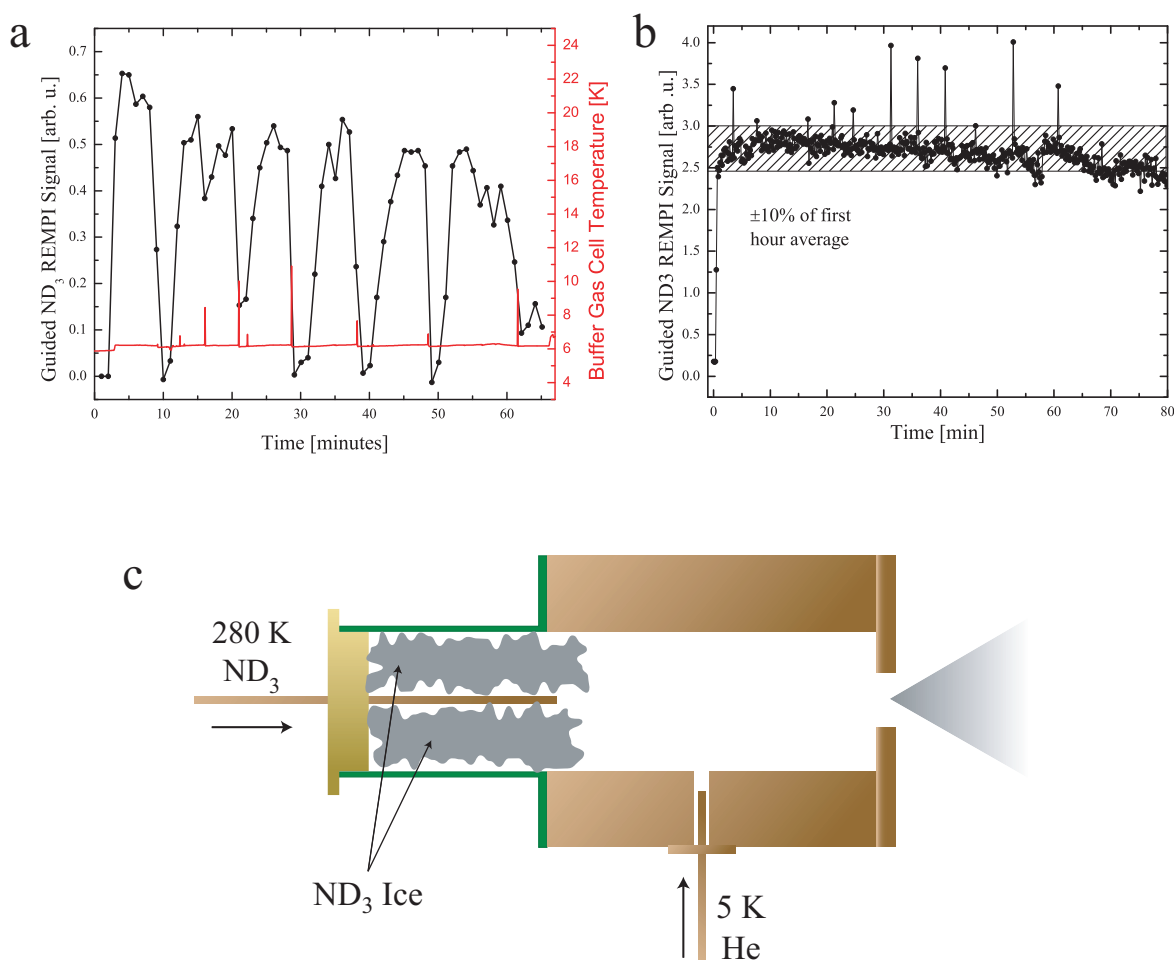
Figure 3.8: Comparison of pulsing behavior with (a) < 5 mm spacing between the ammonia inlet and cell wall and (b) the larger 3.8 cm x 3.8 cm x 4 cm cell with an inlet-to-wall spacing of 1 cm. The greater distance between the warm ND_3 inlet and the cold cell wall in (b) leads to significant improvement in beam stability over ∼ 1 hr. (c) Illustration of the buffer gas cell cross section showing regions of ND_3 ice buildup that eventually lead to pulsing as ice accumulates near the warm ND_3 inlet tube.
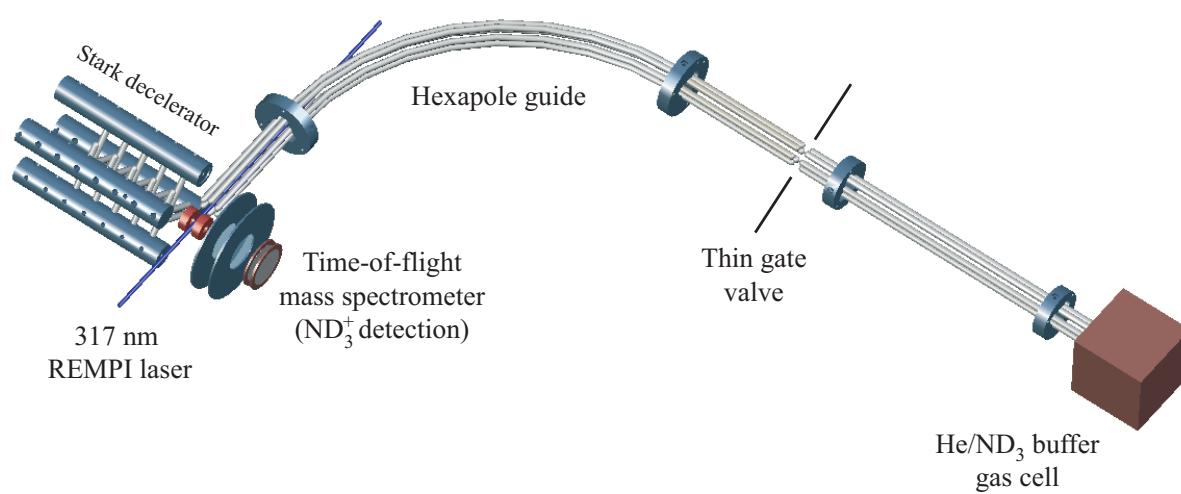
Figure 3.9: Drawing of the buffer gas beam assembly and electrostatic velocity filter for cold ND_3 molecules. The ionization region and time-of-flight mass spectrometer assembly for ND_3^+ detection are displayed at the terminus of the hexapole guide. Cold ND_3 is ionized 1 cm from the guide exit with the 317 nm pulsed REMPI laser.

the ammonia inversion splitting, conforms to a harmonic oscillator model. Ignoring the finite extent of the hexapole rods (generally a safe approximation), one can write the following expression for the electric field within a hexapole of inner radius r_0 as a function of radial position r as

$$|\vec{E}(r)| = \frac{3Vr^2}{r_0^3}. \tag{3.10}$$

The absolute value of the two symmetric voltages applied to the hexapole rods is denoted by V ($V = 5$ kV for applied rod voltages of ± 5 kV). Of course, the potential energy of a molecule with an effective electric dipole moment μ_{eff} within the hexapole is (ignoring inversion splitting)

$$|U(r)| = |\mu \cdot \vec{E}| = \frac{3\mu_{eff}Vr^2}{r_0^3}. \tag{3.11}$$

Now, we obtain the force on the molecule $\vec{F}(r) = -\vec{\nabla}U(r)$ which comes out to

$$\vec{F}(r) = -\frac{6\mu_{eff}Vr}{r_0^3}\hat{r} = -kr\hat{r} \tag{3.12}$$

$$\text{for} \quad k = \frac{6\mu_{eff}V}{r_0^3}. \tag{3.13}$$

Using Hooke's Law, we can now define a transverse oscillation frequency, ν, for the guided molecules of mass m as

$$\nu = \frac{1}{2\pi}\sqrt{\frac{k}{m}} = \frac{1}{2\pi}\sqrt{\left(\frac{6\mu_{eff}V}{mr_0^3}\right)}. \tag{3.14}$$

Specializing to ND$_3$, we set $V = 5$ kV and $r_0 = 3$ mm to obtain $\nu = 1.47$ kHz.

By bending the guide, we can filter fast species — both buffer gas atoms and molecules — from the cold ND$_3$ beam. Using Newton's Second Law, we can estimate the maximum guidable velocity (v_{max}) for a hexapole bend of radius R as

$$v_{max} = \sqrt{\frac{6\mu_{eff}VR}{mr_0^2}} \tag{3.15}$$

where, assuming the experimental condition of $R = 13.5$ cm, we get $v_{max} = 186$ m/s. More accurate Monte Carlo simulations yield a maximum velocity of 150 m/s, but Eq. 5.2 gives the correct scaling behavior in bend radius R. Given the following expression for the μ_{eff} of a symmetric top molecule:

$$\mu_{eff} = \mu\frac{KM_J}{J(J+1)} \tag{3.16}$$

we see that all $K = 0$ (*ortho*) states of ND_3 are unguided. Furthermore, the guide depth and transverse oscillation frequencies increase as $J = K$ increases, leading to more efficient guiding of excited, fully-aligned rotational states. These factors result in a non-thermal distribution of rotational state populations at the exit of the bent guide.

3.2.4.1 Measurement of Beam Velocity

Measuring the velocity of a continuous beam is tricky. Since there is no well-defined temporal pulse origin, one cannot simply take time-of-flight measurements at different distances from the source, as is commonly done with supersonic beams. The flow controllers used for introduction of He and ND_3 into our buffer gas source cannot be gated on time scales fast enough for creating pulses. However, our electrostatic velocity filter gives us a method for measuring the translational energy distribution. Not unlike recent work done in the group of G. Rempe [88], where pulses were created by switching an electrostatic guide, we switch our guide on for different durations (Δt) and record the guided flux of ND_3 as a function of this switch time. Since our guide is 50 cm in path length and includes a 90° bend, we can only detect molecules that have been guided throughout the full flight time. The guide length (L) and duration (Δt) allow us to set a minimum guidable velocity defined as $v_{min}(\Delta t) = L/\Delta t$. One can then deduce that the measured density as a function of v_{min}, here defined as $f(v_{min})$, can be written as

$$f(v_{min}) = \int_{v_{min}}^{\infty} g(v')dv' \tag{3.17}$$

where $g(v)$ is the actual velocity distribution of the continuous guided beam. Since determination of $g(v)$ requires differentiation of $f(v_{min})$, we first fit f with a high-order polynomial. This smoothes and interpolates the curve so that small variations do not cause un-physical features in g. One can imagine fitting f with an error function (Gaussian integral), but we find that the guided velocity distributions are not perfectly Gaussian.

The measured function $f(v_{min})$ is displayed in Fig. 3.10a along with its associated velocity distribution in Fig. 3.10b. The data is taken with hexapole voltages of ±5 kV. Combining this with

the guide bend radius of 13.5 cm, we see that most of the ND$_3$ molecules lie below the predicted 150 m/s velocity cutoff.
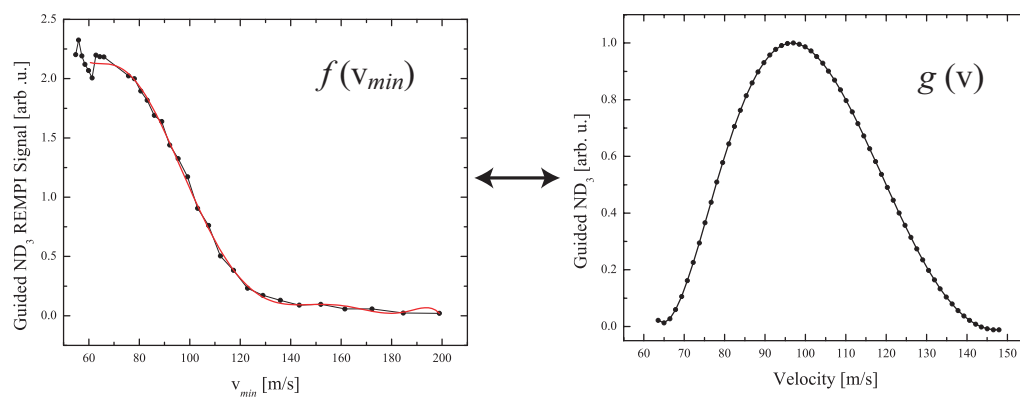
Figure 3.10: Measured velocity distribution of electrostatically guided ND$_3$ molecules. The process of obtaining $g(v)$ from the measured $f(v_{min})$ is described by Eq. 3.17.

Chapter 4

Molecular Detection Techniques

4.1   Time of Flight Mass Spectrometry

Ionization with time-of-flight mass spectrometry is a rather sensitive detection technique for neutral molecules or atoms. Using resonance-enhanced multiphoton ionization (REMPI) in concert with a time of flight mass spectrometer (ToFMS) allows for both internal state and charge-to-mass ratio resolution. The most commonly used ToFMS design is based on that of Wiley and McClarin [89] in which a sample is ionized and the product ions are subsequently accelerated towards a sensitive ion detector (usually an electron multiplier device). Provided that stray electric fields are well-shielded, ions may be guided to the detector with near-unit efficiency. This device can therefore be used with even the smallest molecular densities when coupled with an efficient ionization technique. As described in Chapter 2, we use 2+1 REMPI to characterize our cold guided beam of ND_3 molecules. In order to detect ND_3 within the experimental collision region (i.e. between the OH trap magnets), we use the magnets themselves to apply an electric field for ND_3^+ extraction.

The design of our ToFMS is illustrated in Fig. 4.1. To ionize ND_3, we focus a 317 nm pulsed laser between the two permanent ring magnets of our OH trap. The magnets are grounded for the ionization step to avoid inducing Stark shifts on the REMPI transition and concomitant state mixing of inversion-doublet levels. After the ND_3^+ is produced, we pulse a voltage of +950 V onto the front magnet to accelerate the ions out of the magnetic trap region. The large magnetic fields within the trap do not have a significant effect on the ion flight path since they are axial near the
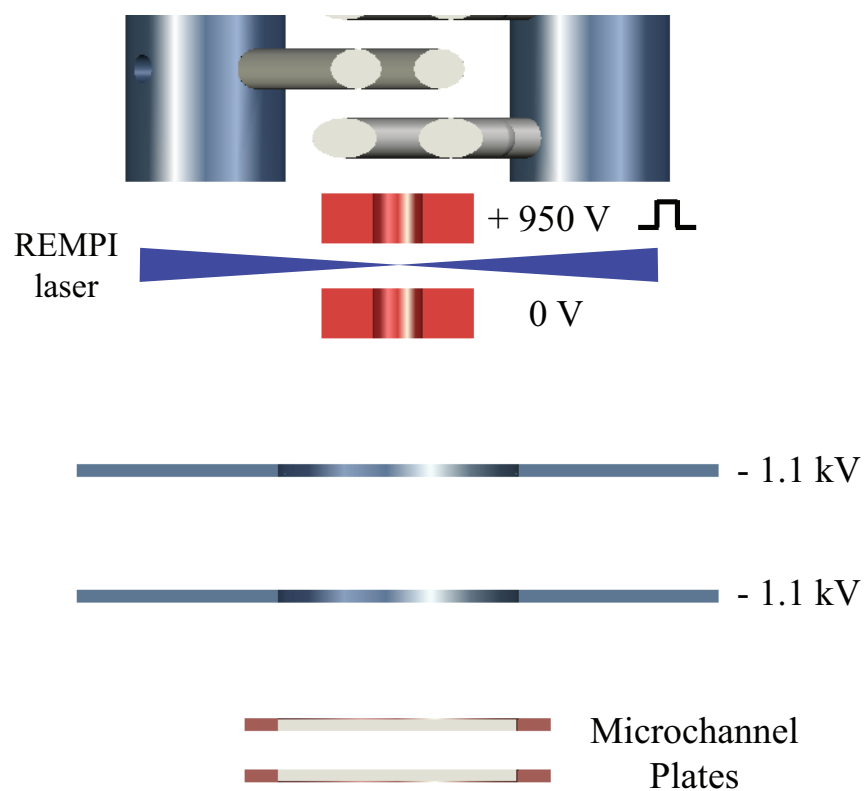
Figure 4.1: Top-view illustration of our ToFMS for detection of guided ND_3 molecules within the OH-ND_3 collision region. For initial ND_3^+ extraction, a pulse of +950 V is applied to the front magnet after the ionization laser. Ions are then accelerated to the microchannel plate detector.

magnet surface and because the period of cyclotron oscillations near the magnets is ~ 1 μs, which is 100x longer than the ion extraction time at the applied electric field. After exiting the trap, ND_3^+ is further accelerated by an additional charged plate 1 cm behind the back magnet. The region between the two plates at -1.1 kV is field-free and is generally installed to allow ions with different charge-to-mass ratios to spatially separate on their way to the microchannel plate detector. With a sufficiently long drift region, one can achieve mass resolutions below one atomic mass unit, thereby separating different atomic or molecular species produced in the ionization region. Due to space constraints, our ToFMS features a 2 cm drift region which is not sufficiently long to reach this level of mass discrimination (many drift regions are 50 cm to 1 m). Nevertheless, the purity of our ND_3 source and ultra-high vacuum conditions give a negligible amount of background ions.

4.1.1   Calibration of Amplified Ion Signals

Determining absolute densities of neutral atomic or molecular samples from amplified ion currents produced via REMPI is often difficult. When multiple photons are used to excite an atom or molecule to an intermediate electronic state, the saturation behavior of the given transition makes ionization efficiency rather sensitive to excitation laser parameters such as waist size and transverse beam profile. The use of pulsed dye lasers for REMPI renders accurate determination of these parameters unlikely. Microchannel plate (MCP) detectors, which boast current gains of $\sim 10^6 - 10^9$, are commonly used to amplify ion signals as part of a time-of-flight mass spectrometer. Unfortunately, the gain of a given MCP assembly can change over the lifetime of the unit and vacuum breaks or complete replacement of the MCP stack would all require careful re-characterization of the system gain for reliable calibrations.

In order to accurately calibrate the density of our cold, guided ND_3 buffer gas beam, we choose to compare the amplified 2+1 REMPI ion yield from the cold beam to that of a calculable thermal source of ND_3 molecules introduced into the ionization region. This procedure makes the density measurement insensitive to long-term fluctuations in MCP gain and laser size/profile since both the cold beam ion yield and the density scaling factor obtained from the thermal signal include

these effects. Since REMPI laser parameters and buffer gas source flux can change on a daily basis, this density calibration is performed for each realization of the collision experiment to allow for consistent averaging of many cross section measurements. We determine the density, n, of ND_3 using

$$n = \frac{S_\text{b}(\nu)}{S_\text{th}(\nu')C_\text{overlap}(\nu')} \times \frac{P}{k_B T} \times f_{JK}(T) \times C_\text{pressure} \tag{4.1}$$

where $S_\text{b}(\nu)$ is the amplified ion signal for a given REMPI line of cold ND_3 at a laser single-photon energy of ν, $S_\text{th}(\nu')$ is the amplified ion signal from the thermal ND_3 at pressure P and temperature T, k_B is Boltzmann's constant, and $f_{JK}(T)$ is the thermal fraction of ND_3 molecules in the state J, K at temperature T. The constants $C_\text{overlap}(\nu')$ and C_pressure allow one to correct for the requisite overlap of transition lines in the hot spectrum and pressure differences at different positions in the vacuum chamber, respectively. In principle, the frequencies ν and ν' need not be identical so long as the laser beam profile and position are stable over the range $(\nu - \nu')$.

It is necessary to simulate the 2+1 REMPI spectrum of ND_3 in order to accurately assign a value for C_overlap. Therefore, we calculate all positions and line strengths for $\tilde{B}(v_2 = 5) \leftarrow \tilde{X}(v_2 = 0)$ rotational transitions using $J'', J' < 20$ and assuming that the two-photon transition strengths are determined exclusively by the transition hyperpolarizability tensor $\mathbf{T}_{\pm 1}^2$ [52]. When describing 2+1 REMPI transitions, we use $|J'', K''\rangle$ and $|J', K'\rangle$ to represent the ground $\tilde{X}^1 A_1'(v_2 = 0)$ and intermediate $\tilde{B}^1 E''(v_2 = 5)$ molecular states, respectively. Molecular constants for the ground state are obtained from Ref. [90] while constants for the intermediate level are taken from Ref. [50]. Accounting for mixing of transition strengths due to l-uncoupling (mixed $K, K + 2$ states) at high-J [46], we obtain the simulated spectrum of Fig. 4.2a shown in red. Accompanying the spectrum simulation is the measured thermal spectrum (black points) taken at a pressure $P = 2.5 \times 10^{-7}$ Torr and laser pulse energy of 3 mJ. A 30 cm lens is placed one focal distance from the magnetic trap center. When calibrating the cold ND_3 beam, we restrict P to below 10^{-6} Torr to avoid nonlinearities in the response of our calibrated quadrupole mass spectrometer (Stanford Research Systems RGA200) and MCP detector.

The constant $C_{\text{overlap}}(\nu') \leq 1$ is the fraction of ions produced from the state J, K within the background of other lines overlapping ν' in the thermal room-temperature spectrum. At $T = 295$ K, the most populous angular momentum states are $J = 5 - 6$. As such, ions resulting from REMPI of the $|1, 1\rangle$ state make up a fraction of the total ion yield at a given line position ν'. For the OH-ND$_3$ collision experiment described in Chapter 7, we used the $\tilde{B}|2, 0\rangle \leftarrow \tilde{X}|1, 1\rangle$ line at a single-photon frequency of 31505.6 cm^{-1} for calibration of the cold ND$_3$ density. The position and relative ion yield of this transition is shown in blue in Fig. 4.2a. Integrating ion yield over the range of the REMPI laser FWHM of 0.3 cm^{-1} obtained from spectroscopy of the 5 K ND$_3$ beam, we obtain $C_{\text{overlap}}(31505.6 \text{ cm}^{-1}) = 0.16$. The discrepancy between the simulated and measured 295 K spectra at this line position is addressed in the following section concerning error estimation of C_{overlap}. For comparison, we include a measured (black) cold ND$_3$ spectrum and corresponding simulation (red) in Fig. 4.2b. The cold beam spectrum reflects a rotational temperature of 8 K.

To compute the Boltzmann fraction $f_{JK}(T)$ in Eq. 4.1, we use the following expression for symmetric top molecules [44]

$$f_{JK}(T) = \frac{1}{2Z} \sum_{J,K} S(I = 1, K)(2J + 1) \exp\left(-U_{JK}/k_B T\right) \tag{4.2}$$

where Z is the partition function and $S(I, K)$ is the degeneracy due to the three identical D atoms each possessing nuclear spin $I = 1$. The remaining terms comprise the standard Boltzmann fraction for a $|J, K\rangle$ state of energy U_{JK}. The extra factor of two multiplying the partition function is necessary since the 2_0^5 transitions in ND$_3$ connect only antisymmetric $v_2 = 0$ levels with $v_2 = 5$ intermediate rotational states, while our pressure measurement is sensitive to all states. Using this formula, we obtain $f_{11}(295 \text{ K}) = 4.7 \times 10^{-3}$.

The constant C_{pressure} is the ratio of actual pressure in the magnetic trap to measured pressure at the quadrupole mass spectrometer (QMS) when gas is leaked into the trap chamber. To quantify this term, we physically move our QMS from its customary position between the OH magnetic trap and turbomolecular pump to a port parallel to the trap itself. Using a calibrated mass flow controller, we inject Ne through the usual ND$_3$ leak valve port and measure the pressure at
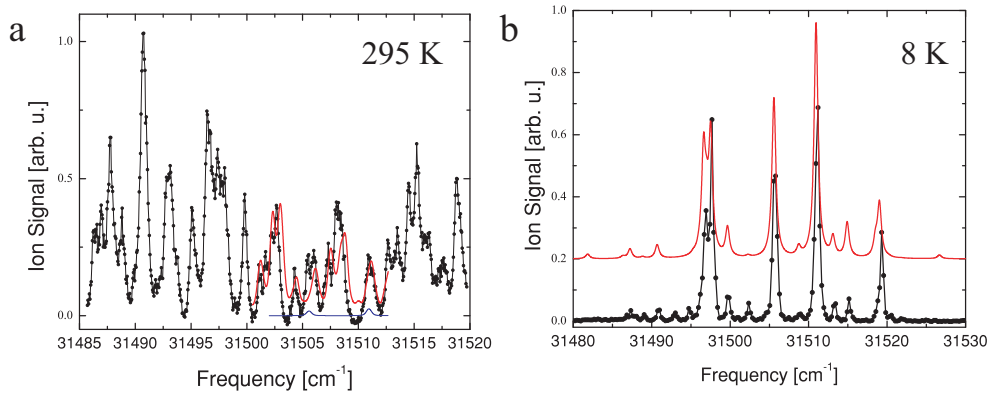
Figure 4.2: (a) Measured (black points) and simulated (red line) ND_3 spectra at 295 K. The experimental 2+1 REMPI spectrum was taken within the OH-ND_3 collision region. The relative strengths and line positions for two of the $|J'', K''\rangle = |1, 1\rangle$ transitions at the single-photon frequencies of 31505.6 cm^{-1} and 31510.9 cm^{-1} are shown in blue. (b) Measured (black points) and simulated (red line) spectrum of a guided ND_3 beam with a rotational temperature of 8 K.

each QMS position. Repeating this procedure multiple times, we obtain $C_{\mathrm{pressure}} = 1.4(1)$. Neon gas is substituted for ND_3 in this measurement due to their identical mass and neon's chemical compatibility with the mass flow controller. Under molecular flow conditions, the identical mass of Ne will yield the same pressure differentials as ND_3.

4.1.1.1   Estimating the Error of C_{overlap}

To estimate the systematic error of our line overlap correction factor $C_{\mathrm{overlap}}(\nu')$, we compare the spectrum simulation results of Fig. 4.2a with an experimental measurement of the ratio $\rho_{\mathrm{exp}} = (C_{\mathrm{overlap}}(\nu_1')/C_{\mathrm{overlap}}(\nu_2'))$. To obtain ρ_{exp}, we calibrate the density of the cold ND_3 at two different ν' corresponding to distinct REMPI transitions from the $|1, 1\rangle$ antisymmetric ground state. The positions and relative ion yields of these two transitions with $\nu_1' = 31510.9$ cm^{-1} and $\nu_2' = 31505.6$ cm^{-1} are plotted as the blue line in Fig. 4.2a. We compare this measured ratio with that predicted by the spectroscopy simulation (ρ_{sim}=0.73). Our measured ρ_{exp} of 1.38(7) yields a 47% fractional uncertainty estimate in our determination of C_{overlap}. The imperfection in our spectrum simulation at 31505.6 cm^{-1} is causing this large fractional uncertainty in the determination of absolute ND_3 densities and, consequently, loss cross sections.

4.2   Laser Induced Fluorescence

The concept of laser induced fluorescence (LIF) detection is much simpler than that of REMPI and time of flight mass spectrometry. In the case of OH, we excite the molecule along the $^2\Sigma^+(v = 1) \leftarrow {}^2\Pi_{3/2}(v = 0)$ electronic transition at 282 nm and detect the shifted fluorescence photons generated by decay along the $^2\Sigma^+(v = 1) \rightarrow {}^2\Pi_{3/2}(v = 1)$ transition at 313 nm. Making use of different vibrational pathways for excitation and decay allows for filtering of stray 282 nm photons from the pulsed UV laser and, due to the favorable Franck-Condon factor for $(v = 1) \rightarrow (v = 1)$ electronic transitions, 70% of the excited OH molecules emit photons at 313 nm over the 750 ns lifetime of the excited state.

In contrast with REMPI, we collimate the 282 nm LIF laser to a diameter of ~ 3 mm to maximize the interrogation volume within the OH magnetic trap. With this laser size, we observe saturation of the fluorescence signal over the full laser diameter at a pulse energy of ~ 300 μJ. For maximum signal-to-noise, it is critical to place light-collection optics within the vacuum chamber as shown in Fig. 4.3. We mount a short focal length lens ($f = 2.5$ cm) one focal distance from the trap center. This light is then refocused onto a photomultiplier tube (PMT) outside of vacuum using an identical lens placed 5 cm after the first lens. To reduce the photon signal due to scattered excitation light, we employ a combination of color-glass and interference filters to block wavelengths below 300 nm and heavily red-shifted fluorescence above 400 nm. These red-shifted photons are generated by UV surface scattering from different materials near the magnetic trap. We obtain the largest signal-to-noise ratios using a bialkali PMT mounted in a UV-transmissive glass housing (Hamamatsu R3788). While one can use a wavelength-sensitive PMT quantum efficiency to further filter light below 300 nm (as with the Hamamatsu 1P21), we measure signal-to-noise gains of ~ 2 using the former model.

Photomultiplier tubes exhibit rather large current gains of $10^6 - 10^7$, which can lead to nonlinear effects such as "after-pulsing" events due to large numbers of stray photons from the excitation laser. As described in Eric Hudson's Ph.D. thesis [23], we reverse-bias the individual

dynodes of the PMT to restrict electron multiplication to time periods after the laser fire. Gating the PMT in this manner drastically reduces the number of electrons produced during the 10 ns laser pulse and thereby decreases the "after-pulse" counts during the OH fluorescence lifetime.
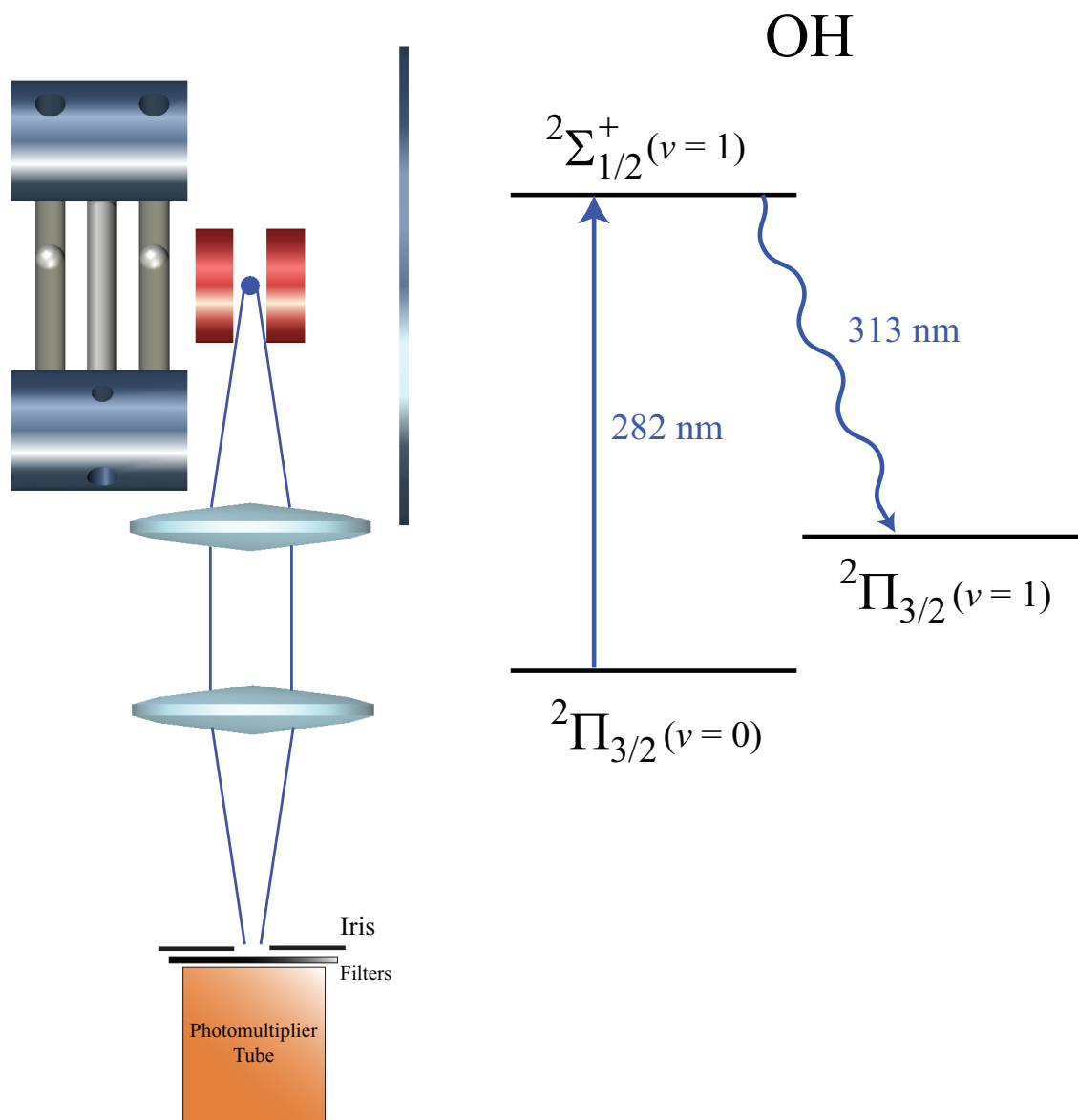
Figure 4.3: (Left) Side-view illustration of the Stark decelerator, magnetic trap, and OH laser-induced fluorescence detection assembly. Fluorescence photons are collected at 313 nm with a 2.5 cm-diameter lens placed 2.5 cm from the center of the magnetic trap. (Right) Level structure showing the excitation and decay pathways used for LIF detection of OH molecules.

4.2.1   Calibration of LIF Signals

Since OH is detected by counting fluorescence photons over the 750 ns lifetime of the excited $^2\Sigma^+(v=1)$ state, underestimation of the OH density is all but guaranteed. The trick to accurately calibrating LIF signals is to correctly account for all photon loss mechanisms between the excitation laser and photomultiplier tube output — all of which increase the final calibrated density of the molecular sample. The first consideration is to confirm that the photon counter is not saturating due to overlapping photon pulses. With our multichannel scaler/averager (Stanford Research Systems SR430), we can reduce the counting bin size to a minimum of 5 ns and check that every bin is counting less than 1 photon per laser shot. Next, one must calculate the percentage of 4π steradians subtended by the fluorescence-collection lens (hereafter denoted as $d\Omega/4\pi$). Finally, one needs the quantum efficiency (QE) of the PMT used for light collection. Assuming that all molecules within a laser volume, V, are excited, we may estimate the number density, n, of the molecular sample as

$$n \sim \frac{S \,[\text{photons / laser shot}]}{(V)(\text{Losses})(\text{QE})(\text{FC})(d\Omega/4\pi)} \qquad (4.3)$$

where FC is the Franck-Condon factor for decay at the detected wavelength, S is the measured fluorescence signal, and (Losses) represents combined losses due to imperfect UV transmission through various optics and filters. Since the spatial profile of pulsed UV lasers is generally not well-defined, estimating the exact laser excitation volume is fraught with error. Therefore, density estimates for LIF detection are usually only trusted to within an order-of-magnitude. For reference, Table 4.1 gives our typical and best observed S values for OH under different experimental conditions.

Table 4.1: Typical and best detected OH ($^2\Pi_{3/2}$) signals under various experimental conditions. All numbers shown are for detection within the permanent magnet trap. Quoted errors are standard deviations from a number of different measurements.

Condition	Typical [photons/shot]	Best [photons/shot]
Background Scatter	0.18 ± 0.07	0.06
Bunching (490 m/s)	7.6 ± 1.85	9.7
Slowing (36 m/s)	0.5 ± 0.1	0.6
Trapped	0.23 ± 0.07	0.37

Chapter 5

Stark Deceleration

Recent development of cold polar-molecule sources promises to reveal many interesting, and hitherto unexplored, molecular interaction dynamics. The permanent electric dipole moment possessed by polar molecules provides a new type of interaction in the ultracold environment. This electric dipole-dipole interaction (and control over it) should give rise to unique physics and chemistry including novel cold-collision dynamics [91, 92, 18] and quantum information processing [93].

To date, cold polar-molecule samples have been produced most successfully via three different mechanisms: buffer gas cooling [94, 73]; photo- and magneto-association [95, 96, 79]; and Stark deceleration [97]. Buffer gas cooling achieves temperatures below 1 K through thermalization of molecules with a He buffer. This technique produces relatively large densities (10^8 cm^{-3}) of polar ground-state molecules. Ultracold atom association achieves the lowest molecular temperatures of these techniques ($\sim$100 nK), but is limited to molecules whose atomic constituents are amenable to laser-cooling. Stark deceleration exists as an alternative to these methods as the technique employs well-characterized supersonic beam methods [58] to produce large densities of ground state polar molecules ($\sim 10^9$ cm^{-3}), albeit at high packet velocities. One limitation of this technique for trapping of decelerated molecules is an observed drastic loss of slowed molecules at very low mean velocities in both our own group's work and the Berlin group of G. Meijer [67].

The first successful implementation of Stark deceleration was reported in 1999 [19]. The group of G. Meijer slowed a supersonic beam of metastable CO molecules from 225 m/s to 98 m/s. In collaboration with their group, we subsequently demonstrated the first Stark deceleration of a

free-radical species (OH) [75]. A number of chemically-relevant neutral polar molecules have been Stark decelerated in the intervening years including: ND_3 [98], H_2CO [63], NH [99], LiH [100], and SO_2 [101].

5.1   Decelerator Operation

The key concepts of Stark deceleration are similar to those of charged-particle accelerators. However, since we are interested in decelerating neutral polar molecules, our slowing forces must be provided by electric field *gradients* ($\vec{F} = \nabla(\vec{\mu} \cdot \vec{E})$) rather than the electric fields necessary to apply forces to charged particles ($\vec{F} = q\vec{E}$). The largest electric fields that can be applied to polished stainless steel surfaces in vacuum are ~ 100 kV/cm (~ 10 MV/m) [102]. Assuming the molecule of interest has a permanent dipole moment of 1 D fully aligned with the local field, one can induce a linear Stark shift of ~ 1 cm^{-1} at this electric field magnitude. Supersonic molecular beams are produced at mean velocities of ~ 500 m/s (assuming a Kr carrier gas) which, for the OH molecule, corresponds to an initial kinetic energy of 177 cm^{-1}. By combining an array of ~ 100 of these high-field stages and successively removing 1 cm^{-1} of molecular kinetic energy per stage, one can expect to be able to decelerate or even stop molecular pulses using the Stark effect. However, one must have the ability to switch the electric fields on time scales much shorter than a molecular transit time, otherwise the polar molecule will fully traverse the potential maximum and exit with its initial kinetic energy unchanged. Assuming that each stage has a length of 1 cm, this suggests that we must switch the electric fields much faster than 20 μs. While this concept of Stark deceleration of molecular beams has existed for decades, the technology needed to switch high voltage pulses (± 15 kV) on time scales of 1 μs did not exist until the 1990s.

Figure 5.1 illustrates the design of our Stark decelerator assembly. First, we create a supersonic beam of polar molecules at the pulsed valve by seeding the molecule of interest within a carrier gas of either Kr or Xe. These heavier noble gases are employed since they produce slower beams better matched to the slowing capabilities of our decelerator. After passing through a skimmer, the molecular pulse enters an electrostatic hexapole with an inner diameter of 6 mm and length of

Pulsed Supersonic Valve

Hexapole

Skimmer

Stark Decelerator (142 Stages)
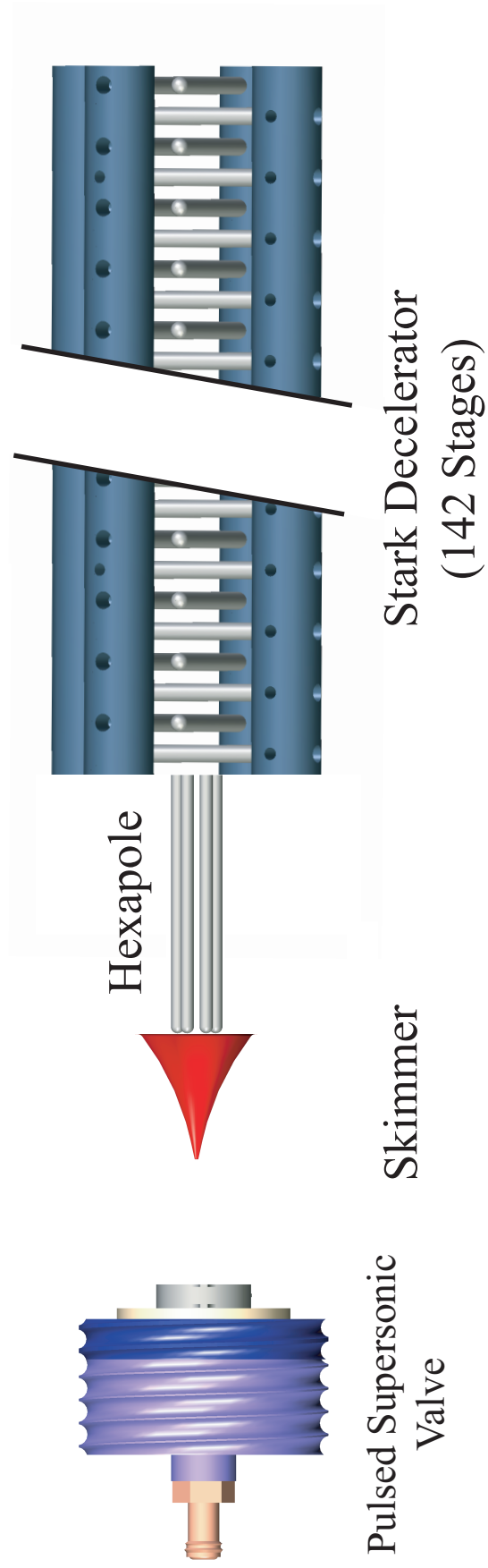
Figure 5.1: Illustration of the Stark decelerator and pulsed supersonic molecular beam source. A packet of OH is created at the valve using a pulsed electric discharge positioned at the valve nozzle. After passing through the skimmer 10 cm downstream from the discharge plates, the packet is focused into the decelerator via a a 5 cm hexapole with an inner diameter of 6 mm. The decelerator rod pairs are spaced by 5.5 mm center-to-center along the beam flight (longitudinal) direction and are mounted 2 mm apart in the transverse dimension.

5 cm. To minimize discharge events between the hexapole and decelerator rods, we only charge the hexapole when the molecular packet is present. This hexapole is effectively a mode-matching optic that optimizes the transverse velocity and spatial widths of the packet to match the transverse phase-space acceptance of the Stark decelerator. The Stark decelerator is mounted such that there is a 3 mm gap between the hexapole and first rod pair. The longitudinal center-to-center distance between successive rod pairs is 5.5 mm, while the transverse distance between parallel rods comprising a single stage is 2 mm. These two parameters define the spatial acceptance of the decelerator and, under identical electric field distributions, the number of molecules within a decelerated packet scales simply as the volume defined by these two lengths. Although decelerators possessing a 4 mm transverse width and 1 cm longitudinal stage spacing have been constructed [103], the two-fold increase in required voltage (±20 kV) over the smaller design introduces many technical challenges. The longitudinal velocity acceptance of a decelerator is determined by the electric field gradients therein. In our system, we apply ±12.5 kV to our rod pairs to obtain a maximum electric field of 125 kV/cm between the rods.

To describe the deceleration sequence, it is necessary to first define the phase angle $\phi = 180°(z/L)$, where z is the longitudinal position and $L = 5.5$ mm is the stage periodicity of our slower. The concept of a phase is natural for the deceleration process since the electric field distribution within our decelerator repeats over 142 stages. To remove kinetic energy from the molecular packet, we switch between two distinct electric field configurations provided by alternating rod pairs in the decelerator. As shown in Fig. 5.2a, by allowing a molecule to traverse the left side of the potential defined by the central (red) curve, we convert some of its kinetic energy to potential energy. By quickly grounding the rod pair that is providing this Stark potential and charging the two neighboring rod pairs, the molecule will have lost that kinetic energy and will again traverse a potential hill given by the black curve. Repeating this process, we can sensitively control the longitudinal speed of a molecular packet. We define the deceleration phase angle, ϕ_0, to be the point at which the electric fields are switched between these two configurations. The $\phi_0 = 0°$ point is defined as the position where the two potentials of Fig. 5.2a cross. No net deceleration occurs
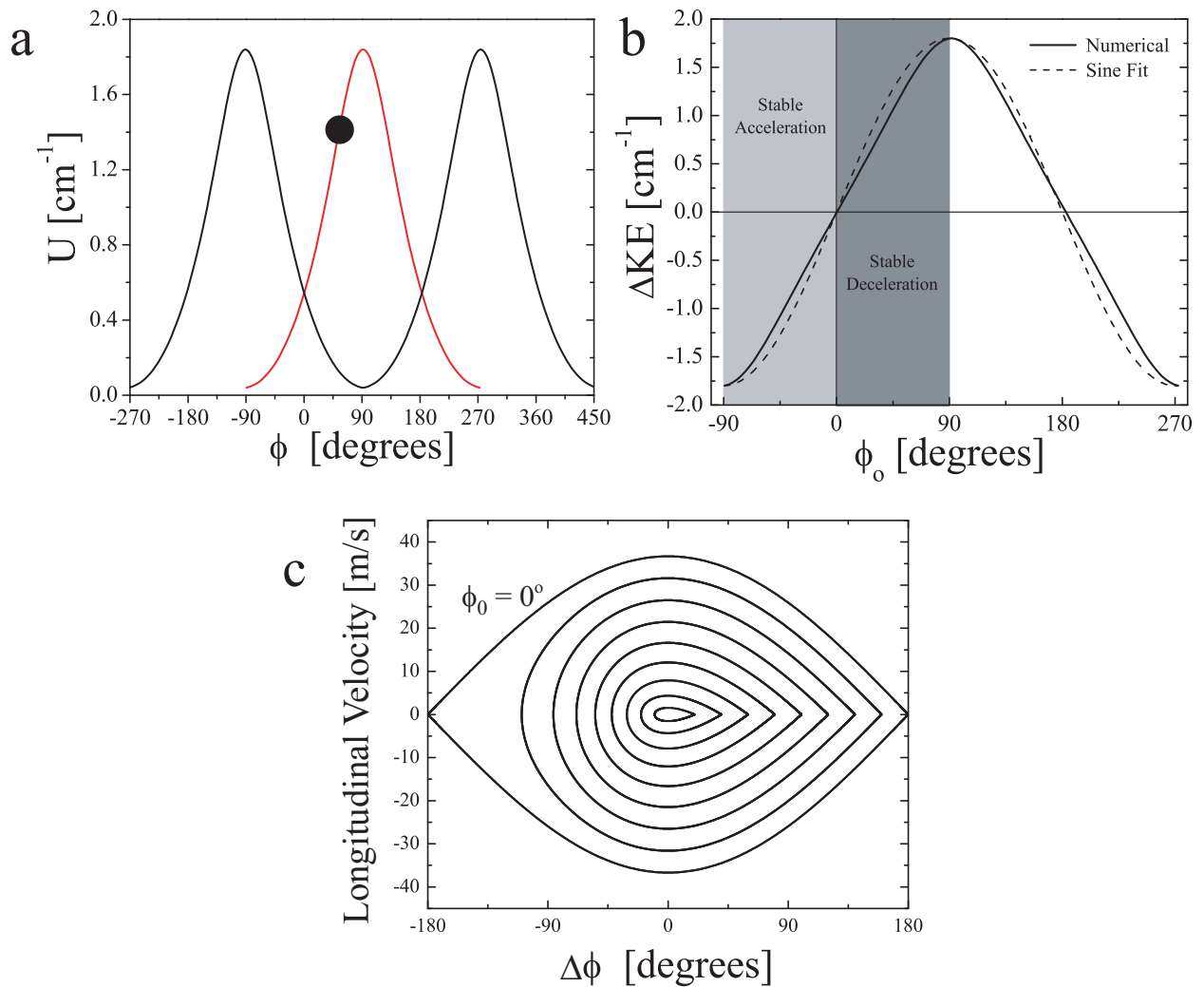
Figure 5.2: (a) Simulation of the longitudinal Stark potentials for OH created by the two distinct rod pairs within the decelerator. To slow a packet of molecules, we switch between the red and black potentials to continually remove kinetic energy at a well-defined position relative to the rod pair (ϕ_0). (b) The difference between the two Stark potentials shown in panel (a), which represents the amount of kinetic energy removed from OH molecules in one stage as a function of the fixed slowing phase angle ϕ_0. Stable acceleration occurs for $-90° < \phi_0 < 0$ while phase-stable deceleration is observed for $0 < \phi_0 < 90°$. We denote operation at $\phi_0 = 0°$ as "bunching" since no net kinetic energy is removed from the molecular packet, but the molecules are nevertheless confined within a moving longitudinal potential well. The form of the kinetic energy difference closely follows that of a sine function as demonstrated by the fit curve (dashed line). (c) Longitudinal phase-space acceptance of a deceleration sequence as a function of ϕ_0 assuming a one-dimensional sine-function form for the slowing potential of panel (b). Note that the separatrices shown are incremented by $10°$ starting from $0°$ at the outer edge. Molecules with longitudinal velocities and positions within the separatrix for a given ϕ_0 will be phase-stably decelerated.

for this "bunching" sequence. Furthermore, we set $\phi_0 = 90°$ to be the point of maximum kinetic energy loss. In a given deceleration sequence, ϕ_0 is a constant, which means that we remove a fixed amount of energy per stage. Because of this, the frequency of high-voltage pulses to our deceleration stages must be chirped as the packet velocity changes. For the specific case of OH, the change in kinetic energy (ΔKE) versus deceleration phase angle is plotted in Fig. 5.2b. This energy removal per stage closely resembles a sine function as shown by the fit (dashed curve).

The dynamics of Stark deceleration may be mathematically modelled using the following second-order differential equation, which is that of a pendulum driven at constant torque [104]:

$$\frac{d^2\Delta\phi}{dt^2} + \frac{W_{max}\pi}{mL^2}[\sin(\Delta\phi + \phi_0) - \sin\phi_0] = 0 \tag{5.1}$$

where $\Delta\phi = (\phi - \phi_0)$ at time t, W_{max} is the maximum amount of kinetic energy removed per stage, and m is the mass of the particle. This model represents an idealized one-dimensional slowing potential and does not include transverse guiding effects or the deviation of the longitudinal potential from a sine wave. Nevertheless, we may solve Eq. 5.1 at ϕ_0 for different initial conditions to obtain the phase space acceptance for different deceleration sequences. The phase-space boundary between stable and unstable molecule orbits is defined by a separatrix. The separatrices for different ϕ_0 are given in Fig. 5.2c in increments of 10° beginning from $\phi_0 = 0°$. The phase space acceptance decreases monotonically as the molecular packet is slowed more aggressively, and the maximum velocity acceptance, Δv_{max}, may be computed as

$$\Delta v_{max} = 2\sqrt{\frac{2W_{max}}{m\pi}\left[\cos\phi_0 - \frac{\pi}{2}\left(1 - \frac{\phi_0}{90°}\right)\sin\phi_0\right]}. \tag{5.2}$$

The above maximum velocity acceptance exists for $\phi = \phi_0$ at the so-called "synchronous molecule" position. Similarly, we may define the largest allowed forward excursion ($\Delta\phi_{max}$) from the position of the synchronous molecule at the synchronous molecule velocity ($\Delta v = 0$):

$$\Delta\phi_{max} = 180° - 2\phi_0. \tag{5.3}$$

To accurately model the dynamics of a deceleration sequence and simulate experimental time of flight profiles, we forego the approximations of Eq. 5.1 and use potential curves simulated from

a three-dimensional finite element analysis of our electric field distributions. There are a number of commercial programs available for this application. We primarily use SIMION or COMSOL and find that a grid spacing of 0.1 mm along with linear interpolation between points is sufficient to accurately model the electric field gradients within our slower. To generate a high-voltage switching sequence for deceleration at ϕ_0, we simulate the longitudinal position versus time of a single synchronous molecule flying along the axis of the decelerator. We subsequently simulate the flight of a packet of $\sim 10^6$ molecules through this slowing sequence and, given some detection volume at the end of the decelerator, generate a time of flight profile. The results of these Monte Carlo simulations are compared with actual deceleration data as shown in Fig. 5.3. Note that we only scale the overall height of the curve to match the data for the first bunching trace, and all subsequent simulations at different ϕ_0 have no free parameters. The experimental curves were obtained from a decelerated OH beam initially seeded in a Xe expansion. The excellent agreement between data and simulation ensures that we understand both the dimensions (and hence electric fields) of our decelerator as well as the molecular dynamics of a slowing sequence.

The experimental signature of Stark deceleration is the removal of a phase-stable slice of molecules from the the broader molecular distribution. We can see from Fig. 5.3 that, as the phase angle is increased, the stable packet lags further and further behind the unstable background of non-decelerated molecules. One can also see that multiple phase-stable packets are decelerated. This occurs when the longitudinal spatial spread of the incoming molecular beam occupies more than one stage length. Molecules one stage ahead of the synchronous molecule see one less deceleration stage and exit at a higher velocity while molecules loaded one stage behind the synchronous molecule see one more stage and exit slower. This is most obvious for the slow peaks shown in the bottom two panels of Fig. 5.3. In these instances, the molecules one stage behind the synchronous molecule are stopped within the decelerator (not detected) and the packet one stage ahead is faster and denser than the central packet of interest.

Since the magnitude and sign of a molecule's Stark shift is state-dependent, a given deceleration sequence is unique to F, M_F total angular momentum quantum numbers as well as the zero-field
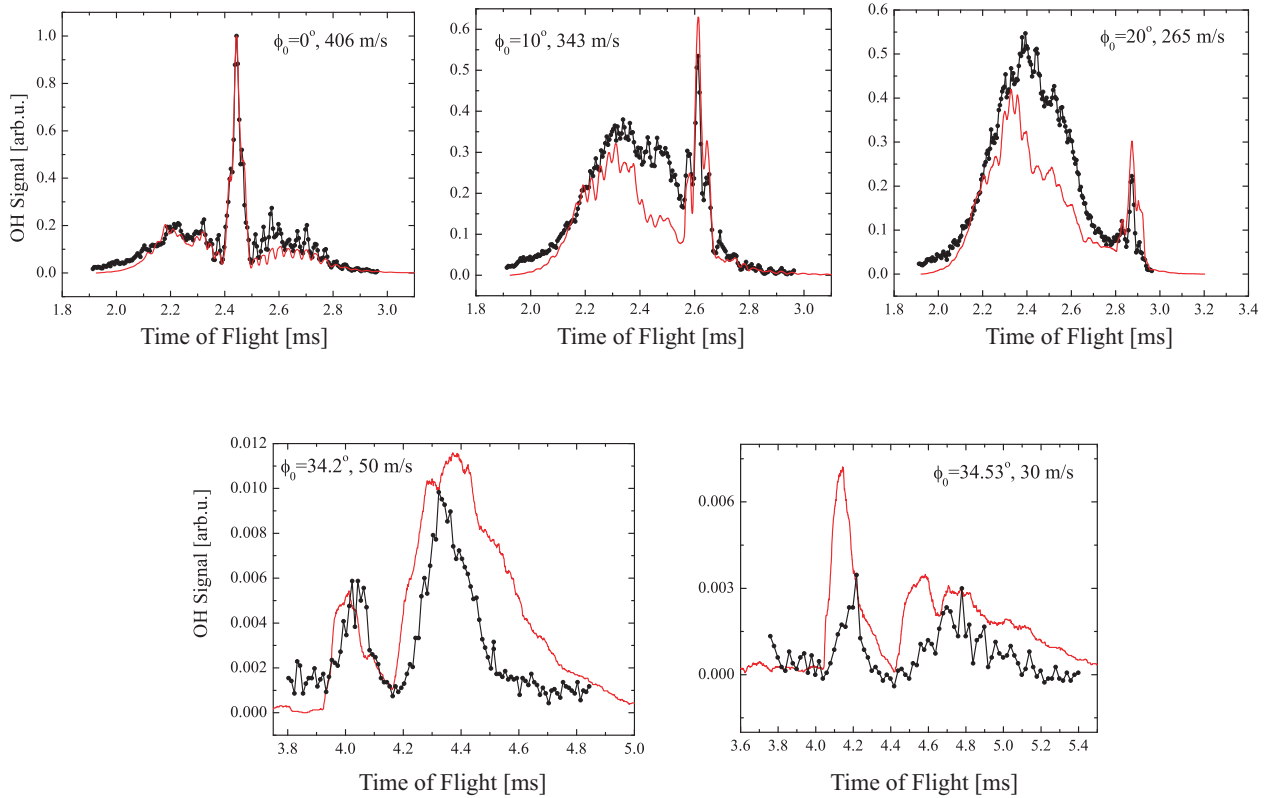
Figure 5.3: Time of flight data (black) and Monte Carlo simulation results (red) for Stark deceler-ated OH molecules showing the excellent agreement between finite-element calculations of slowing electric fields and real decelerating fields. Note that as the phase angle is increased, the decelerated packet is continually removed from the central background of unstable molecules in time of flight. for clarity, the two bottom panels show only the decelerated packet.

parity of the state. In the case of OH, we decelerate only the ground $|F, M_F, p\rangle = |2, \pm 2, +\rangle$ state. However, simply changing the timing of the deceleration sequence allows for selection of excited rotational states as well as different M_F projections. Given that the Stark shift for a fixed angular momentum state depends weakly on the vibrational quantum number for low-lying vibrational levels, populations residing in these different vibrational levels may be decelerated simultaneously as demonstrated in Ref. [31].

Stark deceleration relies on conservative potentials and is therefore not technically a molecular cooling mechanism. The phase space density of the slowed packet does not increase as a result of slowing — we only remove some fraction of the mean kinetic energy. In general, colder packets can only be obtained at the expense of molecule number. We obtain OH densities of $\sim 10^7$ cm^{-3} from our decelerator at a velocity width corresponding to 130 mK in the moving frame of the slowed packet. The detected molecule number at some distance from the decelerator exit is reduced as ϕ_0 increases due to both decreased stable phase-space area and spreading of the packet in free-flight to the detection region. Furthermore, we have identified additional loss mechanisms at the lowest velocities (< 50 m/s for OH) that reduce this detected molecule number [105]. These loss mechanisms are discussed in the following sections.

5.2   Loss at Low Velocities

In Refs. [5, 106], the assumption is made that all motion parallel and transverse to the decelerator axis is stable up to some maximum excursion velocity and position from the beam center, enabling the derivation of an analytical solution to predict stable-molecule phase-space area. However, there are several important instances where the assumptions of this model become invalid. In the case of very slow molecules (<50 m/s) * , we identify two distinct phenomena leading to reduced decelerator efficiency at the final deceleration stages: transverse overfocusing and longitudinal reflection. Transverse overfocusing occurs when the decelerated molecules' speed

---

* This lower velocity limit depends on the molecule of interest as well as decelerator electrode geometry. In general, we expect this velocity limit to scale as $\sqrt{\mu/m}$, where μ is the effective electric dipole moment and m is the mass of the given molecule.
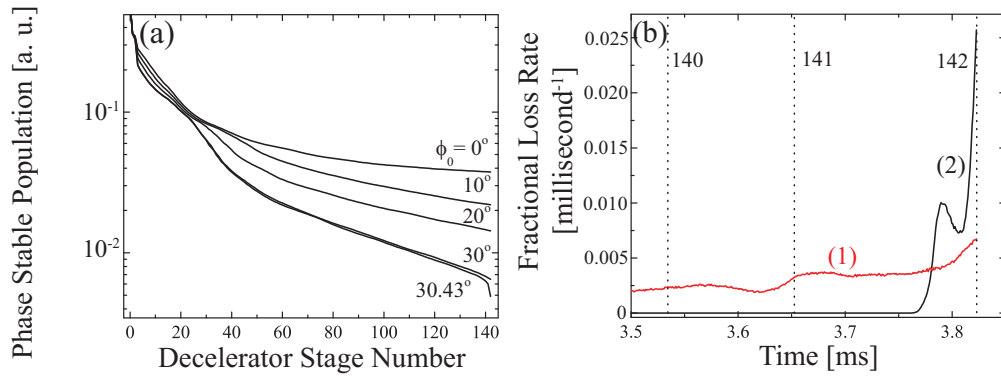
Figure 5.4: (a) Simulations of the phase-stable molecule number as a function of stage number in our 142-stage decelerator. Note the dramatic decrease in number in the last several stages for $\phi_o = 30.43°$. This decrease is due to transverse overfocusing and longitudinal reflection of these slow (14 m/s) molecules. (b) Simulated transverse (trace 1) and longitudinal (trace 2) fractional loss rates as a function of time within the final three stages at $\phi_o = 30.43°$. The vertical dashed lines denote the times of the given stage switches.

becomes so low that the decelerating electrodes focus the molecules too tightly (transversely) and they either make contact with the electrodes or are strongly dispersed upon exiting the decelerator. Longer decelerators tend to exacerbate this effect due to the fact that molecules can travel at low speeds for many stages. Nonetheless, there are several motivating factors for constructing a longer decelerator. First, longer decelerators allow less energy per stage to be removed and consequently lead to larger longitudinal phase-space acceptance. Second, a longer decelerator may allow deceleration of molecules possessing an unfavorable Stark shift to mass ratio. We will discuss critical issues for use of such long decelerators for slow molecule production.

A second low-velocity effect, which we have denoted "longitudinal reflection," is a direct result of the spatial inhomogeneity of the electric field at the final deceleration stage. As highlighted in the context of transverse guidance in Ref. [99], the longitudinal potential is largest for those molecules passing–in the transverse dimension–nearest to the decelerator rods. However, the decelerator switching sequence is generally only synchronous to a molecule on-axis traveling at the mean speed of the packet. As a result, when the mean longitudinal kinetic energy of the slowed packet becomes comparable to the Stark potential barrier at the last stage, molecules off-axis can be stopped or

reflected, resulting in a spatial filtering effect. Furthermore, the longitudinal velocity spread of the molecular packet at the final stage, if larger than the final mean velocity, can lead to reflection of the slowest portion of the packet. It is important that the phenomena of overfocusing and longitudinal reflection be addressed since molecule traps fed by Stark decelerators require slow packets for efficient loading.

To illustrate these low-velocity effects, the number of phase-stable molecules predicted by three-dimensional (3D) Monte Carlo simulation is shown in Fig. 5.4(a) as a function of stage number for increasing phase angle. All Monte Carlo simulation results presented in this Thesis are based on three-dimensional models. The quoted phase-stable molecule number is determined at each time step by counting the number of molecules within the instantaneous three-dimensional spatial acceptance defined relative to the synchronous molecule. Quasi-stable molecules—those that do not remain in the acceptance volume for the full slowing sequence—can initially lead to an over-estimate of the stable molecule number. However, we observe that such molecules exit the decelerator within the first 40 stages, therefore we reserve comparisons between deceleration schemes to the region beyond stage 40. We define the deceleration phase angle, ϕ_0, exactly as in previous publications, where $\phi_0 = (z/L)180°$ [5]. The length of one slowing stage is given by L (5.5 mm for our machine), while the molecule position between successive stages is denoted as z. We define $z = 0$ to be exactly between two slowing stages, therefore, $\phi_0 = 0°$ (bunching) yields no net deceleration. Phase angles satisfying $0° < \phi_0 < 90°$ lead to deceleration of the molecular packet, while the maximum energy is removed for $\phi_0 = 90°$. The 3D simulation results displayed in Fig. 5.4(a) include both longitudinal and transverse effects. The molecules have an initial velocity ($v_{initial}$) of 380 m/s, corresponding to the mean velocity of a molecular pulse created via supersonic expansion in Xe. All simulations and experimental data hereafter possess this $v_{initial}$ unless otherwise noted.

As expected, a higher phase angle leads to a smaller number of decelerated molecules. However, there is a sharp loss of molecules in the last several deceleration stages for the highest phase of $\phi_0 = 30.43°$. This value of ϕ_0 produces a packet possessing a final velocity (v_{final}) of 14 m/s. This loss is attributed to transverse overfocusing and longitudinal reflection. These distinct effects

are illustrated in Fig. 5.4(b), which displays the transverse (trace 1) and longitudinal (trace 2) fractional loss rate of molecules traversing the final three slowing stages at $\phi_0 = 30.43°$, $v_{final} = 14$ m/s. The switching time for each stage is denoted by a vertical dashed line, which is labeled by the corresponding stage number. Longitudinal reflection of molecules is clearly the dominant loss mechanism for the lowest final velocity shown in Fig. 5.4(a). Nonetheless, there also exists a non-negligible rise in transverse losses at the final stage. That is, because the molecular beam is moving very slowly in the last few deceleration stages, the transverse guiding fields of the decelerator electrodes have a greater focusing effect on the molecules (see Eq. 3 of Ref. [75]) and focus the molecules so tightly that they collide with a deceleration stage and are lost. In the case of our decelerator, this leads to loss of 20% of the decelerated molecule number between $\phi_o = 30°$ (50 m/s) and $\phi_o = 30.43°$ (14 m/s). Such a dramatic loss is not predicted by analytical theory, as the stable phase-space area decreases by <1% over this range of ϕ_0. This number is calculated directly after the decelerator is switched-off and is thus an upper bound, since experiments employing these cold molecules require them to travel out of the decelerator where transverse spread can lead to dramatic loss of molecule number.

Experimental evidence of this sudden decrease in molecule number at very low velocities is given in Fig. 5.5, which displays data from time-of-flight (ToF) measurements along with corresponding Monte Carlo simulation results at various phase angles. The decelerated OH molecules are in the weak-field seeking $|F = 2, m_F = \pm 2, +\rangle$ state. The first two quantum numbers of the state denote its hyperfine components, while the third number indicates the parity of the state in the absence of electric fields. The total detected and simulated molecule numbers are plotted in Fig. 5.5 as a function of final velocity, along with the theoretically expected decelerator efficiency (dashed line) [5]. Note that the sudden population decrease in both simulation and experimental results is not reflected in the one-dimensional theoretical model, which does not account for the transverse dynamics or field inhomogeneities that cause such behavior. This effect is detrimental to the production of dense samples of cold molecules. The difference between experiment and 3D simulation in Fig. 5.5 is indicative of an inability to account for imperfections in decelerator

construction. At low velocities, we observe smaller longitudinal velocity widths than predicted by simulation. Small errors in simulated detection aperture also have larger effects as final speed is reduced. Nonetheless, the experimentally observed dramatic molecule loss is reproduced by 3D simulation.

To remove the overfocusing effect at low velocities, the transverse focusing of the last several decelerator stages needs to be reduced. Different types of transverse focusing elements may be inserted into the deceleration beam line to compensate for this phenomenon. This idea is discussed in detail in Sections 4 and 5. We note that the proposed solutions, while successful in addressing the detrimental longitudinal/transverse coupling effects, do not mitigate the problem of longitudinal reflection at low velocities.

5.3   Distributed Loss

As noted in previous work [99, 101, 55], coupling between transverse and longitudinal motion throughout the deceleration sequence invalidates the assumptions made for 1D simulations in Refs. [5, 106], thereby necessitating 3D Monte Carlo simulations. The fact that the transverse guidance of the molecular beam comes from the same electrodes that provide the deceleration means that the longitudinal and transverse motions are necessarily coupled. While this phenomenon is well understood in the field of accelerator physics [107], it was first pointed out in the context of Stark deceleration in Ref. [99]. The result can be seen in the left column of Fig. 5.6, where the longitudinal phase space of OH packets is shown versus increasing phase angle. In Fig. 5.6, the dark lines represent the separatrix, partitioning stable deceleration phase space from that of unstable motion as calculated from Eq. 2 in Ref. [5]. Each dot represents the position in phase space of a simulated molecule. In the absence of coupling between the longitudinal and transverse motions, one would expect the entire area inside the separatrix to be occupied. Therefore, the structure in these graphs is evidence of the importance of the transverse motion. The S parameter labeling each column of Fig. 5.6 was previously defined in Ref. [99, 108]. $S = 1$ refers to a standard deceleration scheme in which stages are switched sequentially, while $S = 3, 5, 7...$ denote "overtone" sequences

in which the molecules traverse $S - 2$ charged stages before fields are switched.

In the left column of Fig. 5.6, the coupling of longitudinal and transverse motions is responsible for two effects[†] : First, in the center of the stable area at $\phi_0 = 0°$–near the synchronous molecule– the density of stable molecules is less than in the surrounding area. This is because molecules that oscillate very near the synchronous molecule experience little transverse guiding [99]. This effect is not dramatic and is only discernable for an exceedingly large number of stages. Furthermore, this effect is even less important for the increased phase angles typically used for deceleration, since for these switching sequences the synchronous molecule experiences more of the transverse guiding forces than it does during bunching. The second effect, which is much more evident, is the absence of molecules at intermediate distances from the synchronous molecule as shown in the left column of Fig 5.6. This so-called 'halo' is due to parametric amplification of the transverse motion and is similar to the effects seen in cold molecule storage rings [106] as well as charged particle accelerators [109]. Essentially, the longitudinal oscillation frequency of a molecule in this region is matched to the transverse oscillation frequency, leading to amplification of the transverse and longitudinal motion and consequent loss [110].

There is a compromise between decreasing longitudinal phase-space area and increasing transverse guidance for increasing ϕ_0. To demonstrate this effect, we decelerate molecules to a fixed v_{final} and vary the phase angle used to reach this velocity. This is done either by changing the voltage applied to the decelerator rods or by modifying the effective length of the decelerator itself for each ϕ_0 of interest. The experimental data shown in Fig. 5.7 is the result of varying the voltage applied to our decelerator rods (squares) and the effective decelerator length (circles). Both lowering the decelerator voltage and using shorter lengths of the decelerator for slowing requires increasing ϕ_0 to observe the same v_{final} of 50 m/s. We are able to effectively shorten the decelerator by initially bunching the packet for a given number of stages before beginning a slowing sequence. Note that we use $S = 3$ bunching to remove any transverse/longitudinal couplings during these first stages,

---

[†] For these phase space simulations, the input molecular beam has longitudinal spatial and velocity distributions that overfill the acceptance area.
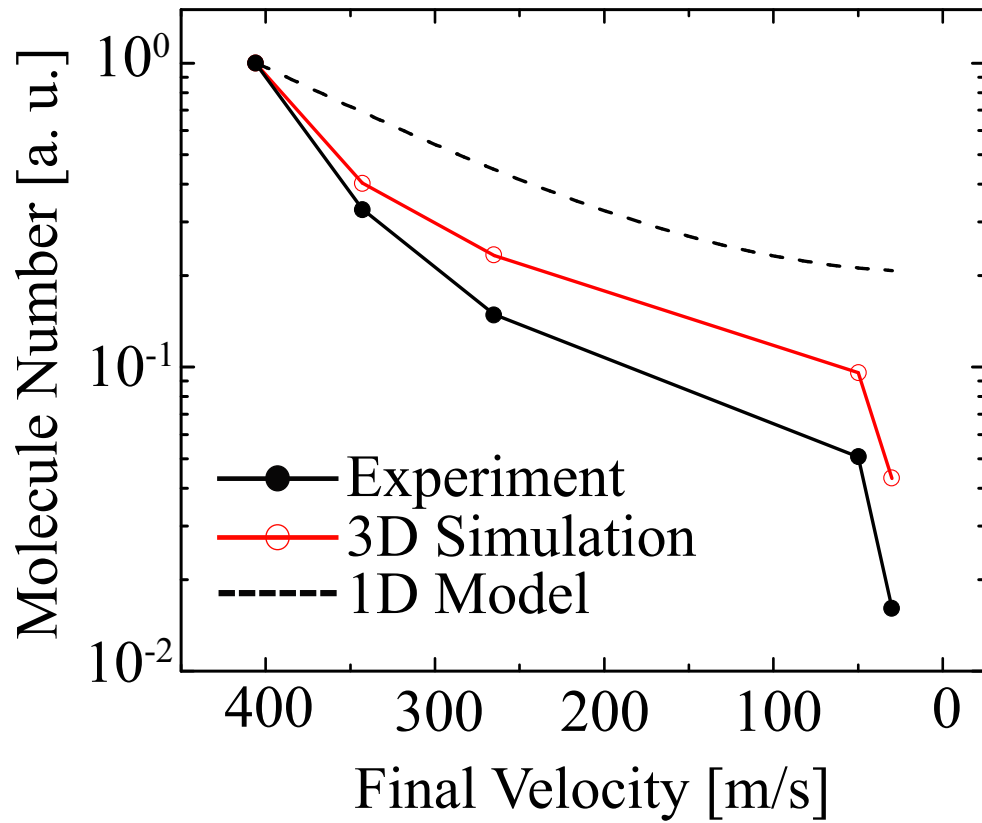
Figure 5.5: Experimental (dots) and Monte Carlo simulation (open circles) results for total molecule number as a function of final velocity. The dashed curve is the expected decelerator efficiency calculated from the one-dimensional (1D) theoretical model of Ref. [5].
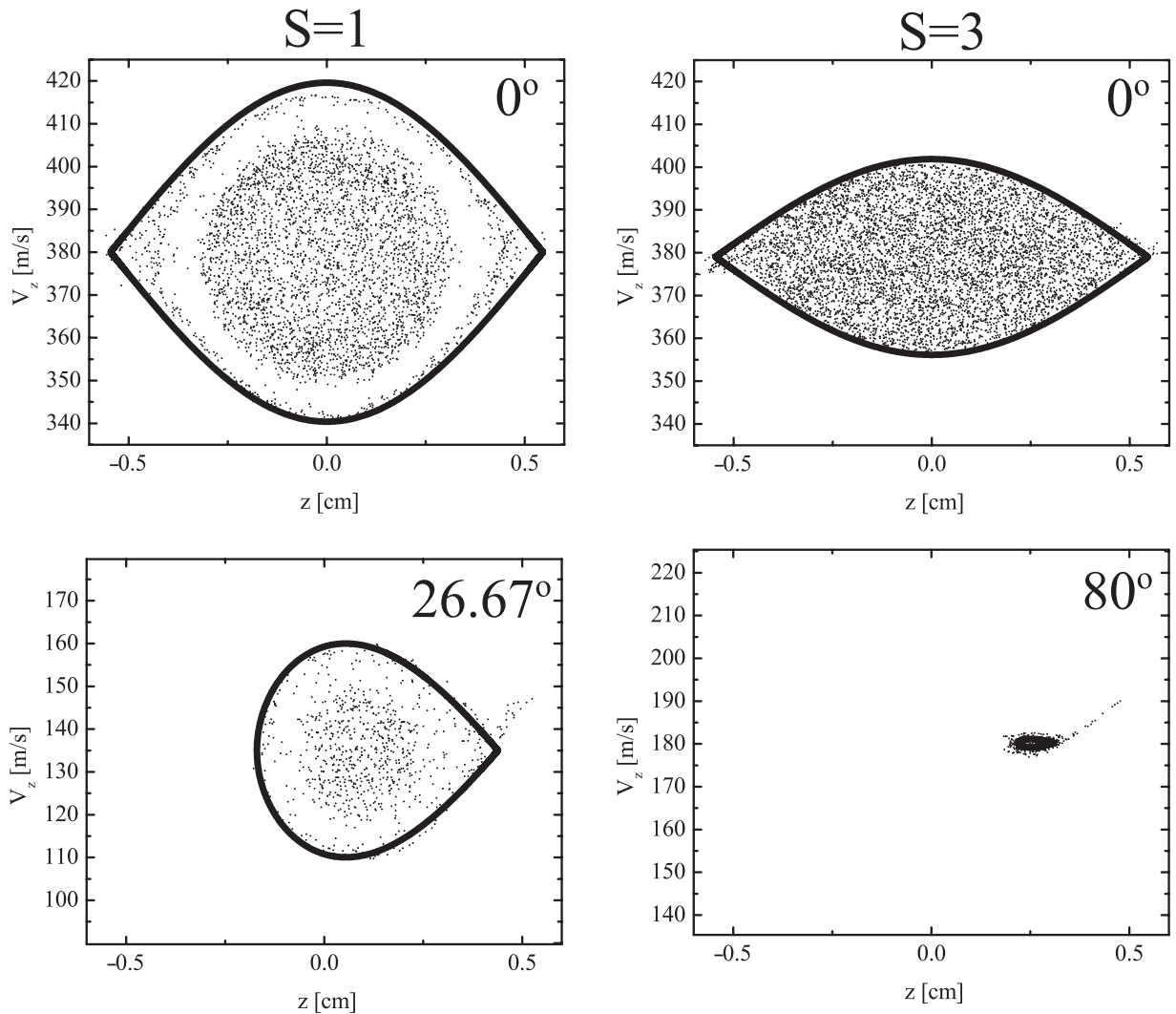
Figure 5.6: Monte Carlo simulation results for the longitudinal phase space of decelerated molecules. The left column shows $\phi_o = 0°$ and $26.67°$ for S = 1 slowing, while the right column shows $\phi_o = 0°$ and $80°$ for S = 3 deceleration. The factor of three between $S = 1$ and $S = 3$ phase angles ensures that molecules have roughly the same final velocities. The observed velocity difference at the higher phase angle occurs because the 142 stages of our slower is not a multiple of three. Note that, although the $S = 3$ phase plot is more densely populated than that of $S = 1$ at $\phi_o = 0°$, its phase-space acceptance decreases dramatically relative to $S = 1$ at the lowest velocities. All plots are generated using an identical initial number of molecules, and therefore the density of points is meaningful for comparison.

then switch back to $S = 1$ slowing for the remainder of the decelerator. The phase stable region of $S = 1$ for $\phi_0 \geq 40°$ is entirely contained within that of $S = 3$ at $\phi_0 = 0°$, therefore no artifacts from initial velocity filtering are present in this data. We observe that, contrary to the predictions of the one-dimensional theory [5], a higher phase angle can lead to greater decelerator efficiency up to some maximum ϕ_0. This is a direct consequence of distributed transverse/longitudinal couplings illustrated in Fig. 5.6. At even larger phase angles, the longitudinal phase-space acceptance becomes a limiting factor. The labels next to each data point correspond to either the voltage applied to the decelerator rods (squares) or the number of utilized $S = 1$ slowing stages (circles). Figure 5.7 further illustrates that the transverse/longitudinal couplings outlined by Ref. [110] reduce decelerator efficiency, and are highly dependent on phase angle.

The coupling between longitudinal and transverse motion is detrimental to efficient operation of a Stark decelerator, reducing the total number of decelerated molecules. This effect will be even worse for decelerating molecules with an unfavorable Stark shift-to-mass ratio. Fortunately, the transverse and longitudinal motions can be decoupled by introducing a transverse focusing element to the deceleration beam line that overwhelms the transverse focusing provided by the deceleration electrodes in analogy to the focusing magnets of charged-beam machines. This technique also has the advantage of providing a larger stable region in the transverse phase space which further enhances the decelerated molecule number. The remainder of this manuscript discusses methods of implementing a transverse focusing element to decouple the longitudinal and transverse motion. We note that while $S = 3$ bunching has been previously discussed [99, 108], the dynamics of decelerated packets under such operation have not been investigated. In Section 4 we discuss the effectiveness of $S = 3$ deceleration as well as other modified "overtone" schemes. Section 5 presents an improved design for a Stark decelerator that solves this problem of distributed longitudinal and transverse loss and also reduces the previously described overfocusing losses at the final stage.
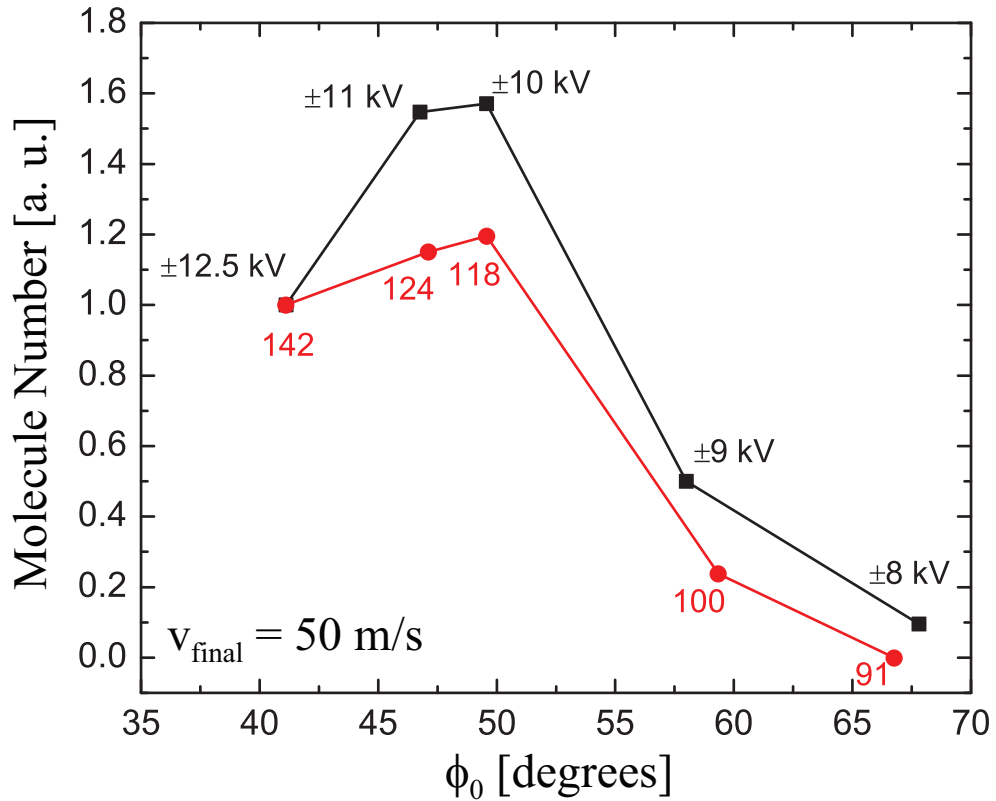
Figure 5.7: Experimental results from changing the voltage on decelerator rods (squares) and decreasing the effective decelerator length (circles). Effective slower length is modified by initially operating the decelerator at $\phi_0 = 0°$, $S = 3$, then slowing with $S = 1$ to $v_{final} = 50$ m/s for the number of stages labeled. Both curves illustrate that transverse/longitudinal couplings are strongly dependent on phase angle, and have a marked effect on decelerator efficiency.

5.4   Decelerator Overtones

The simplest method for introducing a transverse focusing element to the decelerator beam line is to let the molecules fly through an energized deceleration stage without removing the field. In this manner, molecules experience the transverse focusing of the entire stage without their longitudinal motion affected. Traditional longitudinal phase stability requires the switching of the fields to occur on an upward slope of the molecular potential energy, i.e., faster molecules are slowed more while slower molecules are slowed less than the synchronous molecule. Hence, it is necessary to de-sample the bunching switching rate by an odd factor (3,5,7...): the so-called decelerator overtones [108]. For convenience, we define the quantity $S = v_o/v_{Switch}$, where v_o is the synchronous molecule velocity and the switching speed v_{Switch} is given as the stage spacing L divided by the switching time-interval. Reference [108] considered only the bunching case. In this work, we generalize to the case of actual deceleration. However, the above definition of S is still valid. That is, S is constant despite the fact that both v_o and v_{Switch} vary when $\phi_o > 0°$. With this definition we see that traditional deceleration can be described by $S = 1$, while the method of de-sampling the switch rate by a factor 3 is described by $S = 3$. These two methods of deceleration can be seen in Figs. 5.8 (b) and (c), where their respective switching schemes are shown for $\phi_o = 0°$. By switching at one-third the rate, the molecule packet flies through a deceleration stage that is energized and experiences enhanced transverse guiding.

Longitudinal phase space simulations of $S = 3$ slowing at various phase angles are shown in the right column of Fig. 5.6. No structure is present in these plots. Also, the region of longitudinal phase stability for $S = 3$–even at $\phi_0 = 0°$–is reduced compared to $S = 1$. This is because the maximum stable velocity, as calculated from Eqs. 2 and 6 of Ref. [5], depends on the spacing between deceleration stages as $L^{-1/2}$, and thus, the separatrix velocity bound is reduced by a factor of $\sqrt{3}$ [‡] . Nonetheless, the absence of coupling to the transverse motion leads to a larger number of molecules for the $\phi_o = 0°$ case shown in the uppermost panel of Fig. 5.6. In a given

---

[‡] Physically, this is because the molecules fly longer between deceleration stages, and thus, the velocity mismatch can lead to a larger accumulation of spatial mismatch.
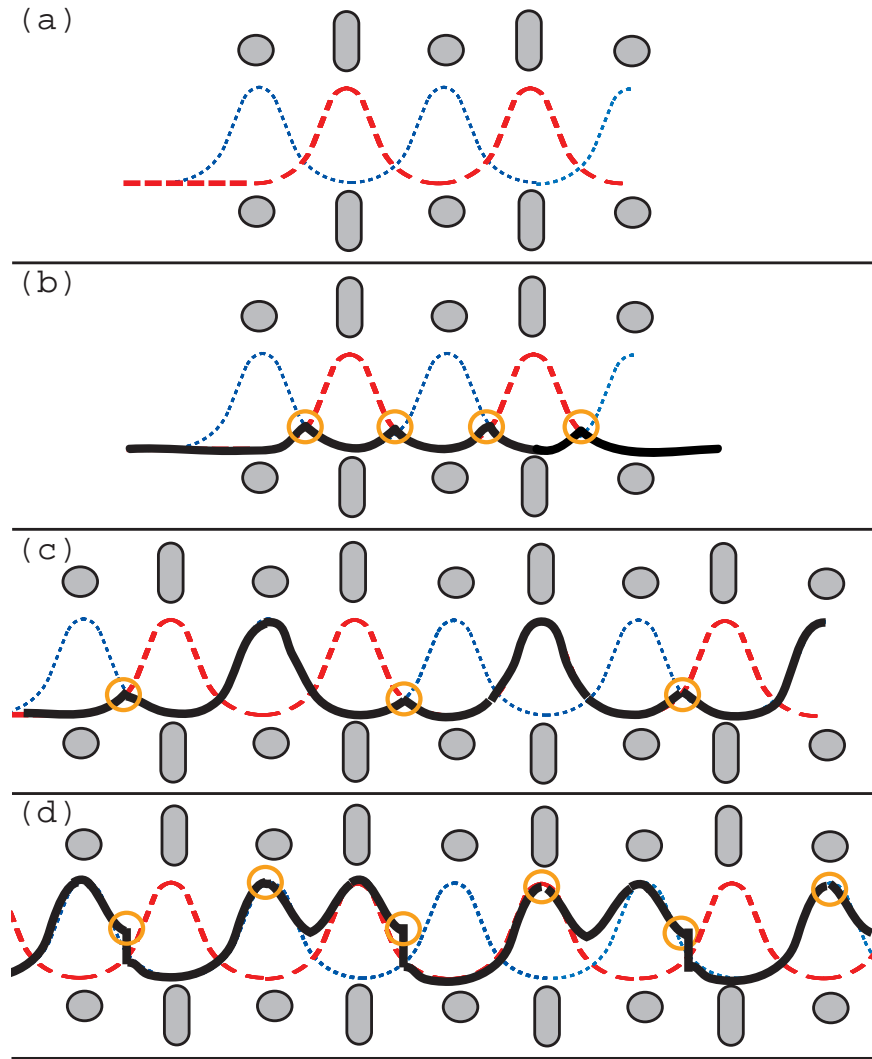
Figure 5.8: Deceleration schemes. (a) Potential energy shift of polar molecules in the Stark decelerator. The dotted (blue) curves show the potential energy shift when the horizontal (circular cross section) electrodes are energized, while the dashed (red) curves show the potential energy shift when the vertical (elongated cross section) electrodes are energized. Deceleration proceeds by switching between the two sets of energized electrodes. In panels (b)-(d), the thick black line indicates the potential experienced by the molecules. The empty circles indicate a switching event. (b) Traditional (S = 1) operation at $\phi_o = 0°$. For phase stability, the switching always occurs when the molecules are on an upward slope, and as such the molecules are never between a pair of energized electrodes. Thus, the maximum transverse guiding is never realized. (c) First overtone operation (S = 3) at $\phi_o = 0°$. By switching at one-third of the S = 1 rate, the molecules are allowed to fly directly between an energized electrode pair, and thus, experience enhanced transverse guiding. (d) Optimized first overtone operation (S = 3+) at $\phi_o = 0°$: Initially, the packet rises the Stark potential created by one set of electrodes. When the molecules reach the apex of this potential, the alternate set of electrodes is energized in addition. In this way, the molecules experience one more stage of maximum transverse guiding for each slowing stage. Note that, to minimize the un-bunching effect, the grounded-set of electrodes is switched on when the molecules are directly between the energized electrodes.

decelerator, $S = 3$ slowing requires a factor of three higher phase angle than $S = 1$ to reach the same final velocity. As illustrated in Fig. 5.6, this fact severely limits the practicality of $S = 3$ as a deceleration scheme, as it implies a dramatic reduction in velocity acceptance at the highest phase angles.

Shown in Fig. 5.9(a) are experimental decelerated molecular packets for $S = 3$ (upper) and $S = 1$ (lower) versus increasing phase angle. For each successive packet, the $S = 3$ phase angle increases by $10°$ in the range $\phi_o = 0°$–$60°$, while the $S = 1$ phase angle increases by $10°/3$. In this manner, the packets are decelerated to roughly the same velocity. There is a slight difference at the highest phase angles shown because the total number of stages in our decelerator (142) is not an exact multiple of 3. In Fig. 5.9(b) the de-convolved total molecule number for each of these packets is plotted versus final speed. While the $S = 3$ method dominates over $S = 1$ for small phase angles, its effectiveness decreases as the deceleration becomes more aggressive–by 224 m/s, the $S = 1$ molecule number is already larger than that of $S = 3$. This behavior is expected since the phase angle used to decelerate to 224 m/s is $60°$, while the required $S = 1$ phase angle is only $20°$. Although the $S = 3$ longitudinal phase bucket does not exhibit structure, it is so much smaller in enclosed area than the $S = 1$ that its total molecule number is smaller. The simulation results of Fig. 5.9(c) and the theory results of Fig. 5.9(d) support this description. Figure 5.9(c) shows that, even at $\phi_o = 80°$, the transverse loss rate per stage is at all times greater for $S = 1$ than $S = 3$. However, the calculated longitudinal phase-space acceptance of Fig. 5.9(d) mirrors the behavior observed experimentally in Fig. 5.9(b) when the initial points are scaled to the experimental ratio of 2.75. This scaling accounts for the aforementioned 'halo' in the slowed $S = 1$ packet, which persists relatively unchanged over the range of $S = 1$ phase angles used ($\phi_o = 0° - 20°$). The fact that the theory curves of Fig. 5.9(d) cross at a higher velocity than the data of Fig. 5.9(b) suggests there is increased transverse guiding of $S = 3$ slowing at high phase angles. Nevertheless, even with 142 stages of deceleration, $S = 3$ is unfavorable for velocities below 224 m/s due to reduced stable phase-space area. The peak in the loss rate observed in Fig. 5.9(c) at ~ 20 stages is due to loss of quasi-stable molecules near the beginning of the deceleration sequence and is not observed beyond

40 stages.

At this point, one would expect that operation at lower phase angles would permit realization of the gain produced by the $S = 3$ method. This can be accomplished by naively using a longer decelerator. A simulation of this kind is presented in Fig. 5.10, which plots the number of molecules present after deceleration at $\phi_o = 20°$ versus final velocity [§] . The number next to a data point represents the number of deceleration stages used. Initially the decelerated molecule number is relatively flat versus final velocity. However, after about 500 stages (180 m/s), the number of decelerated molecules begins to decrease and dramatically falls off after 550 stages (150 m/s). Very few molecules survive below 100 m/s. This is because for $S = 3$ the decelerated molecules must fly through an entire stage while experiencing a guiding force in only one dimension [see Fig. 5.8(c)]. Once the molecules are at slower speeds they can spread out in one transverse dimension or be over-focused in the other and collide with the rods. As the mean kinetic energy of the slowed packet becomes comparable to the full potential height, the packet can be nearly stopped as it traverses the intermediate charged stage. This has two consequences: (1) longer transit time leading to more intense transverse focusing; and (2) velocity filtering of the low-speed packet as slower molecules are longitudinally reflected from this potential.

The transverse loss responsible for the extreme drop in molecule number for $S = 3$ deceleration also occurs in traditional deceleration, but to a lesser degree. Because of this decrease in molecule number at low speeds, the usefulness of slowing with $S = 3$ is generally limited to experiments that do not require the lowest velocities, such as microwave spectroscopy and collision experiments [21, 24, 111]. We note also that our simulations predict no low-velocity gain when using slowing sequences containing combinations of deceleration at $S = 1$ and bunching at $S = 3$.

A natural extension of the above overtone deceleration is the use of what we have termed a "modified decelerator overtone," denoted by an additional plus sign, i.e., $S = 3+$. Deceleration in this manner is shown in Fig. 5.8(d) for $\phi_o = 0°$. In this method, deceleration proceeds similarly to

[§] In this simulation, $\phi_o = 20°$ is chosen because it produces the most gain over $S = 1$ in our deceleration experiments.
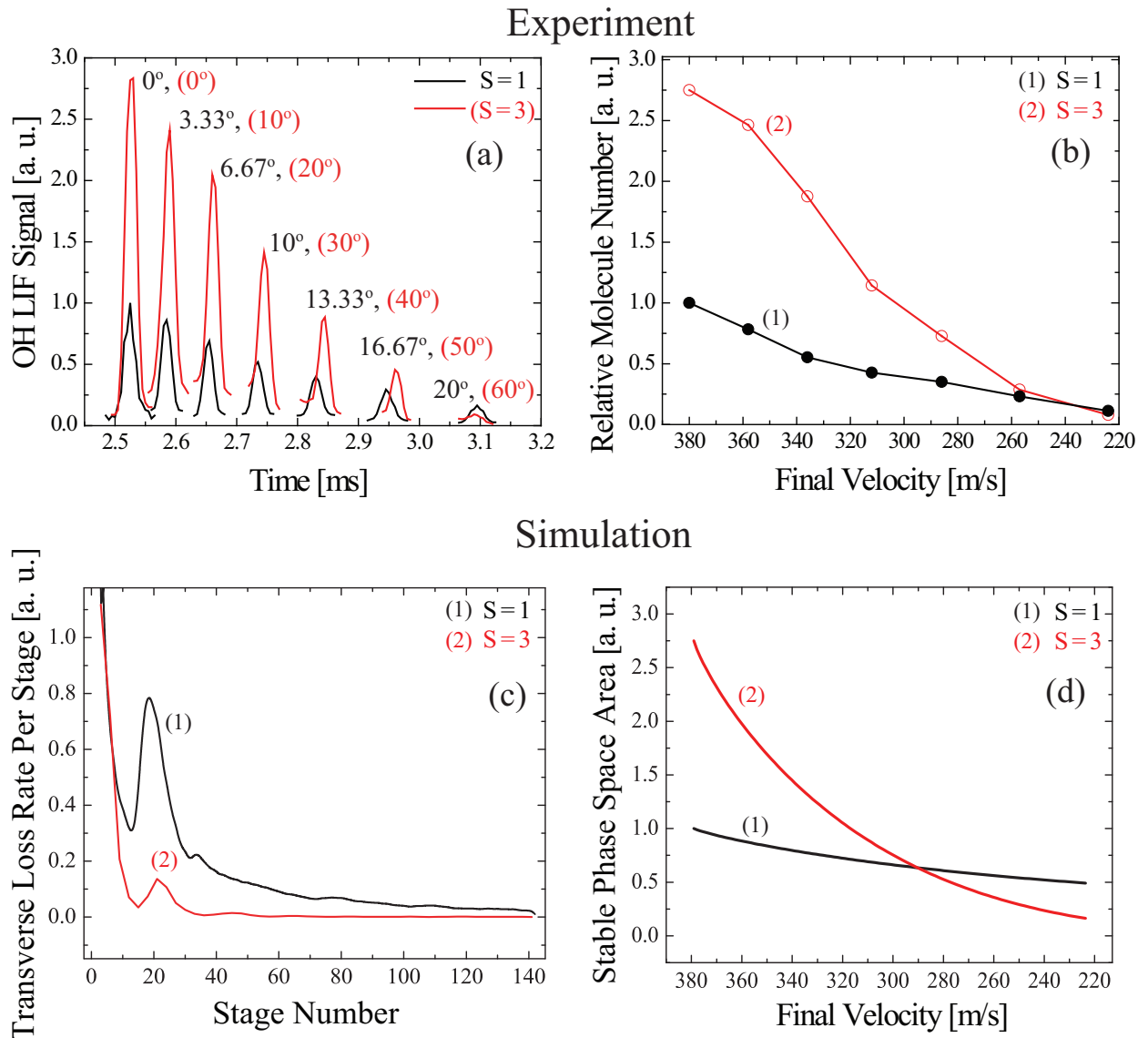
Figure 5.9: Comparison of deceleration using $S = 3$ versus $S = 1$. (a) Experimental ToF data of decelerated OH packets with $S = 3$ (top) and $S = 1$ (bottom). Note the factor of three between $S = 1$ and $S = 3$ phase angles. (b) De-convolved, integrated molecule number for $S = 3$ (trace 2) and $S = 1$ (trace 1) for the packets shown in panel (a). (c) Simulated transverse loss rate per stage for $S = 1$ (trace 1) and $S = 3$ (trace 2) deceleration. As expected, $S = 1$ results in larger transverse loss rates throughout. (d) Calculated stable longitudinal phase-space area for $S = 1$ (trace 1) and $S = 3$ (trace 2), with initial points scaled to the experimental ratio of 2.75. The above panels highlight that the observed shortcoming of $S = 3$ deceleration is entirely due to loss of longitudinal velocity acceptance at high phase angles.
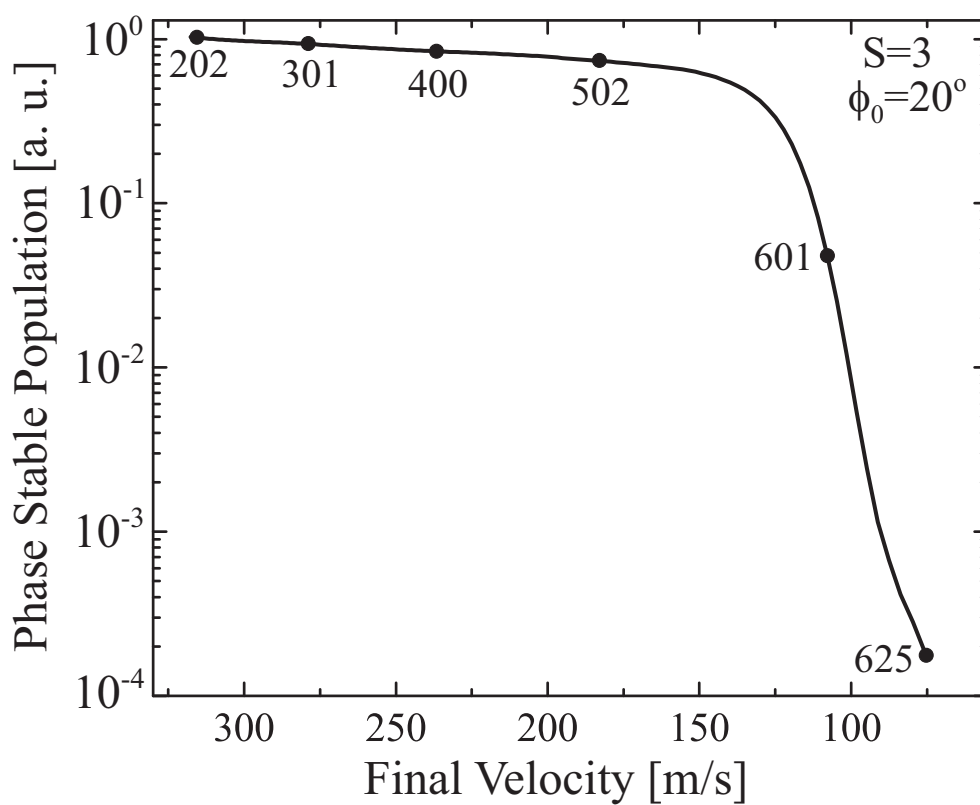
Figure 5.10: Monte Carlo results for decelerated molecule number using $S = 3$ and $\phi_o = 20°$ versus final velocity. The number next to each data point is the number of stages used. Because of transverse overfocusing and longitudinal velocity filtering, essentially no molecules survive below 100 m/s.
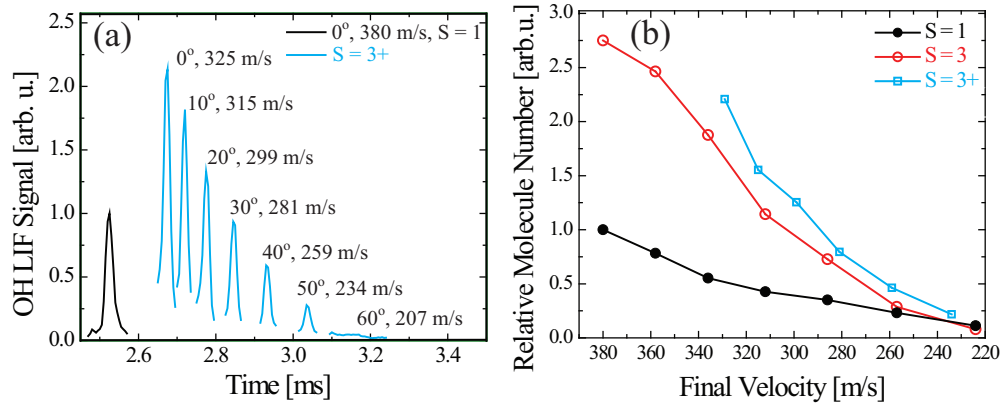
Figure 5.11: (a) Experimental ToF data of decelerated OH packets produced using the $S = 3+$ modified overtone. Also shown for comparison is the experimental bunching packet for operation at $S = 1$. (b) The de-convolved, integrated molecule number calculated from $S = 3+$ (open squares), $S = 3$ (open circles), and $S = 1$ (dots) data.

conventional $S = 3$. However, $S = 3+$ sequences yield confinement of the packet in both transverse dimensions. This is achieved by charging all slower rods for the period in which the synchronous molecule is between switching stages. In order to minimally disrupt the longitudinal dynamics of the synchronous molecule, the second set of slower rods is charged only when the molecule is at the peak of the longitudinal potential from the first rod set. The packet then traverses two charged rod pairs before reaching the next switching stage, at which point the rod pair that was originally charged is grounded. While this does create a slight anti-bunching effect, i.e., molecules in front of the synchronous molecule gain a small amount of energy, it provides an extra stage of transverse guidance in comparison to $S = 3$. Experimental results of this method of slowing are shown in Fig. 5.11 for comparison to deceleration using both $S = 1$ and $S = 3$. Fig. 5.11(a) displays a unique consequence of the $S = 3+$ switching sequence, where operation at $\phi_o = 0°$ leads to deceleration. Figure 5.11(b) shows that operation with $S = 3+$ provides slightly more molecules than $S = 3$, but the loss of molecules due to decreased longitudinal velocity acceptance remains a problem. The increase in molecule number for $S = 3+$ over $S = 3$ is due to the extra stage of transverse guidance, which for the higher-velocity packets we measured leads to a larger transverse acceptance.

To determine whether the extra stage of transverse guidance would counter the overfocusing

effects [¶] , we perform simulations of $S = 3+$ deceleration at $\phi_o = 20°$ for a varying number of deceleration stages. The results of these simulations, shown in Fig. 5.12, are similar to the results for $S = 3$. Namely, as the decelerator length is increased and the molecules' speed is reduced, there is a marked molecule number loss for velocities below 200 m/s. In our simulations, we could not observe any molecules below 100 m/s. Again, transverse overfocusing and longitudinal filtering of the molecular packet by the deceleration electrodes are responsible for large losses in the decelerator, and this suggests that measures beyond modified switching schemes are required to overcome these loss mechanisms.

5.5 Quadrupole-Guiding Decelerator

In addition to modifying the timing sequences of existing decelerators, it is possible, and perhaps preferable, to uncouple the longitudinal motion inside the Stark decelerator from the transverse motion by redesigning the decelerator electrode geometry. One simple redesign, which we call the quadrupole-guiding decelerator (QGD), is shown in Fig. 5.13(a). In this decelerator, a quadrupole-guiding stage (Fig. 5.13(b)) is interleaved between each deceleration stage. While it may not be necessary to have a quadrupole-guiding stage between each deceleration stage (especially in the beginning of the decelerator), it simplifies the analysis and will be used here. The switching of the electric fields inside a QGD is similar to a traditional decelerator operated with $S = 1$. Figure 5.13(c) shows the potential energy experienced by a molecule decelerated at $\phi_o \approx 45°$ and is represented by a thick black curve. In this panel, the quadrupole-guiding electrodes are omitted for clarity. Note that the quadrupoles are always energized and their center coincides with the $\phi_o = 0°$ position, while $\phi_o = 90°$ occurs between the deceleration electrodes.

Deceleration with a QGD enjoys the same longitudinal phase-stability as a traditional decelerator. In a QGD, the maximum stable excursion position $\Delta\phi_{max}$ and velocity Δv_{max} will differ from that of the traditional decelerator because the decelerating electrodes are most likely further

---

[¶] While this may seem counterintuitive, in some cases when the transverse overfocusing is not too strong, the addition of another focusing element can change the sign of the molecules transverse velocity, keeping the beam confined within the decelerator.
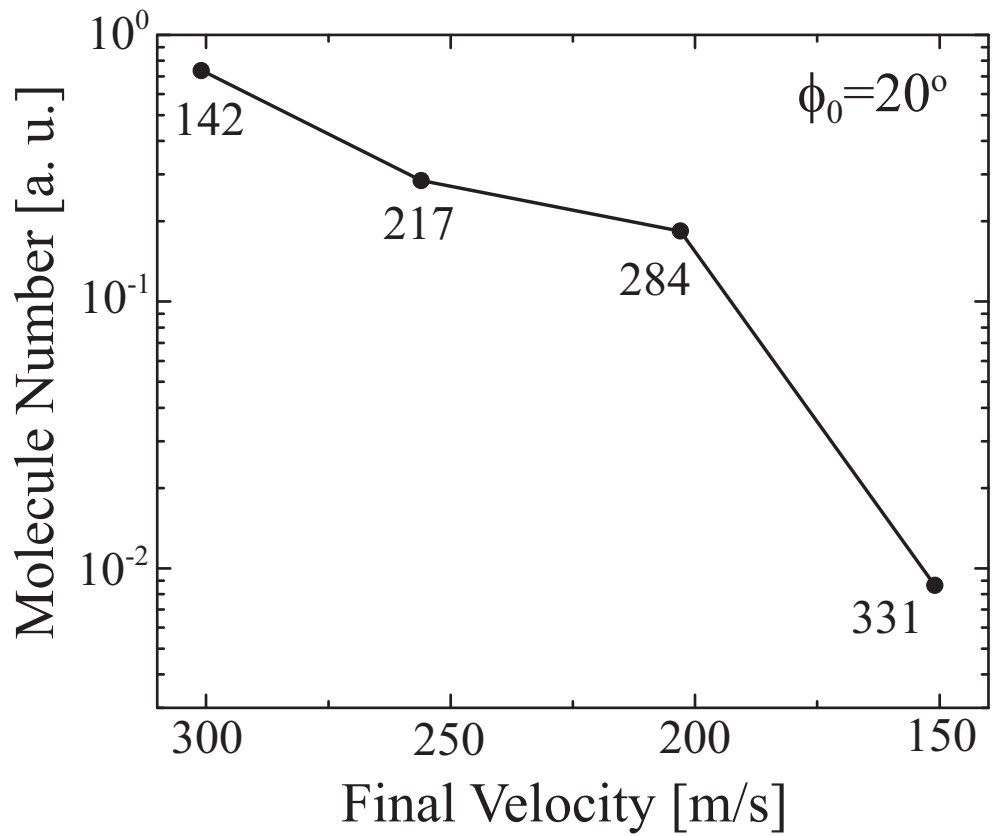
Figure 5.12: Monte Carlo results of decelerated molecule number using $S = 3+$ and $\phi_o = 20°$ versus final velocity. The number next to each data point is the number of stages used. Because of transverse overfocusing, essentially no molecules survive below 100 m/s.

(a)

Decelerator
Array

Skimmer

Pulsed
Valve

Hexapole

(b) Quadrupole Guide Stage

-V

+V

+V

-V

3(10^7) V/m

2(10^7) V/m

1(10^7) V/m

0 V/m

(c)

QG stage

QG stage

$\phi_o = 0^o$
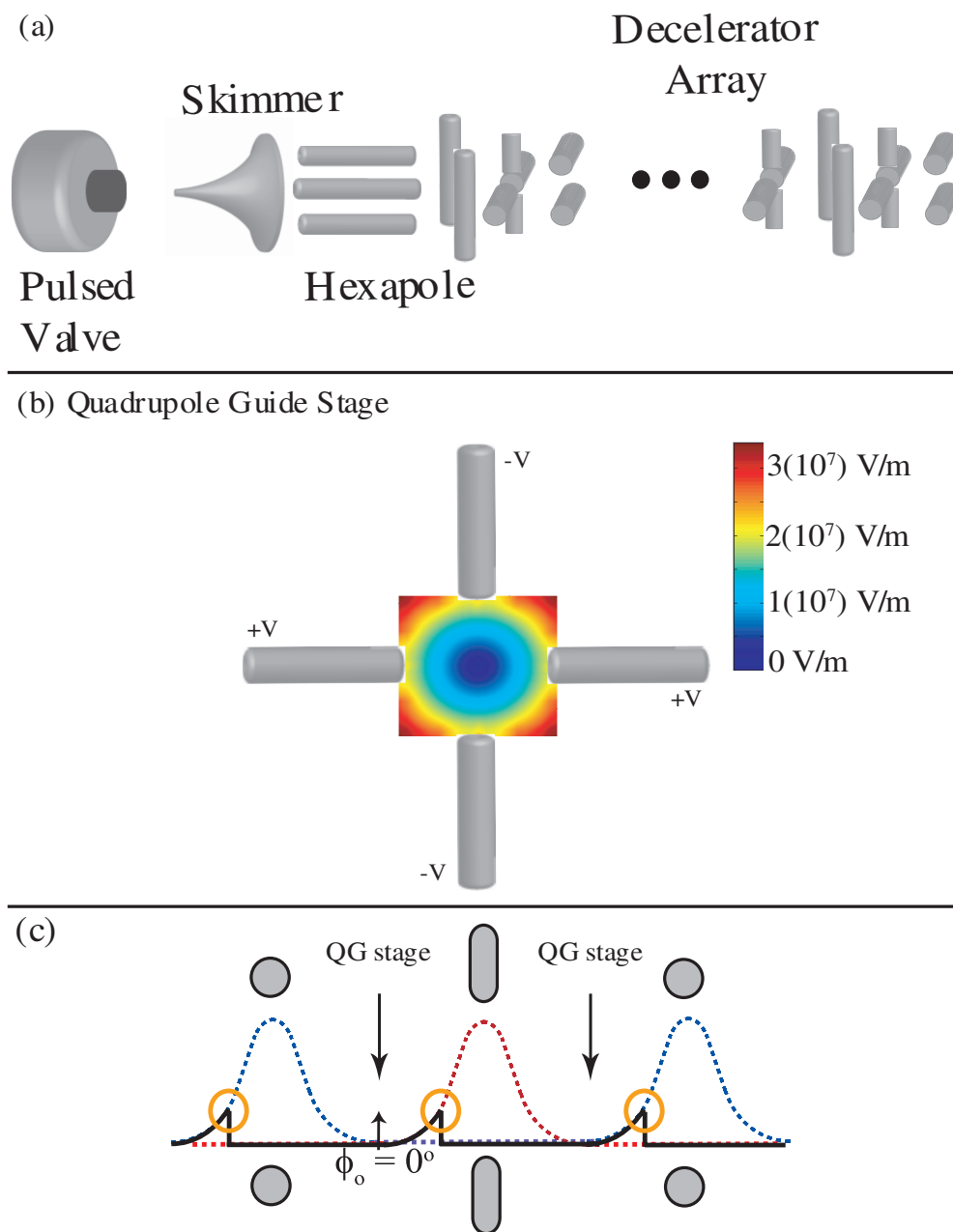
Figure 5.13: Quadrupole-guiding decelerator. (a) Schematic of QGD. (b) Electric field of quadrupole guiding stage energized to ± 12.5 kV. (c) Switching scheme for deceleration with the QGD.

apart. In other words, to prevent high-voltage breakdown, the quadrupole stages require the same inter-stage spacing as deceleration stages in a traditional decelerator. Thus, the decelerating electrodes for a QGD will be twice as far apart as in our traditional decelerator, which possesses an inter-stage spacing of 5.5 mm. Since the dependence of the decelerating force on ϕ_o is less steep, the shape of the stable longitudinal phase space will change. Understanding the shape of the stable longitudinal phase area is crucial for predicting the performance of the QGD, and can be derived by examining the longitudinal forces inside the QGD. Shown in Fig. 5.14(a) is the on-axis Stark shift of an OH molecule in the $|2, \pm 2, +\rangle$ state inside the unit cell, defined as 3 deceleration stages of the QGD. The quadrupole rods are held at a constant ± 12kV for this calculation, though their contribution to the longitudinal potential is negligible. The solid line is the Stark shift due to the slowing stage centered at 11 mm, while the dashed line is the Stark shift of the stages which will be energized when the fields are switched. The subtraction of these two curves, shown in Fig. 5.14(b) as a solid line, is the amount of energy removed each time the fields are switched, ΔKE. We represent ΔKE as sum of sine-functions [108]

$$\Delta KE(\phi) = \sum_{n=odd} a_n \sin(n\phi), \tag{5.4}$$

where we have used the definition of the phase angle $\phi = (z/L)180°$. A fit of the first three terms of this equation to the actual ΔKE for deceleration stages spaced by 11 mm is shown as a dashed line in Fig. 5.14, resulting in the fit values $a_1 = 1.221$ cm^{-1}, $a_3 = 0.450$ cm^{-1}, and $a_5 = 0.089$ cm^{-1}. Using this fit, we derive the equation of motion of the molecules about the synchronous molecule position as

$$\frac{d^2\Delta\phi}{dt^2} + \frac{\pi}{mL^2}(\Delta KE(\Delta\phi + \phi_0) - \Delta KE(\phi_0)) = 0, \tag{5.5}$$

where we have used the excursion of the molecule from the synchronous molecule $\Delta\phi = \phi - \phi_o$. The maximum stable forward excursion of a non-synchronous molecule is exactly the same as a traditional decelerator and is given as [5]

$$\Delta\phi_{max}^+(\phi_o) = 180° - 2\phi_o. \tag{5.6}$$

We calculate the work done in bringing a molecule starting at this position with zero velocity to the synchronous molecule position as

$$W(\phi_o) = \int_{Start}^{End} F dx = -\frac{1}{\pi} \int_{\Delta\phi_{max}^+(\phi_o)}^0 \sum_{n=odds} (a_n[\sin(n(\Delta\phi + \phi_o)) - \sin(n\phi_o)])d(\Delta\phi). \quad (5.7)$$

Integrating this equation and setting it equal to the kinetic energy yields the maximum stable excursion velocity:

$$\Delta v_{max}(\phi_o) = 2\sqrt{\sum_{n=odds} \frac{a_n}{m\pi} \left(\frac{\cos(n\phi_o)}{n} - (\frac{\pi}{2} - \phi_o)\sin(\phi_o) \right)}, \quad (5.8)$$

where ϕ_o is now in radians.

Using Eqs. 5.5- 5.8 it is possible to solve for the longitudinal separatrix, which separates stable deceleration from unstable motion inside the decelerator. These separatrices are shown (thick black lines) along with the results of Monte Carlo simulations of a QGD in the left column of Fig. 5.15 for successive phase angles. The longitudinal phase space is shown with each dot representing the position of a stable molecule. The lack of structure inside these separatrices is evidence of the lack of coupling between the transverse and longitudinal modes. The right column, which shows simulated ToF curves, reveals a single stable peak arriving at later times as ϕ_o is increased. These simulations are for a single $|2, \pm 2, +\rangle$ state of OH and do not exhibit the large background contribution of the other states of OH present in experimental ToF data.

From the comparison of the simulations with the analytical results represented by the separatrices, we see that the simple theory of Eqs. 5.5- 5.8 is quite accurate in describing the longitudinal performance of the QGD. Thus, by numerically integrating the area inside these separatrices, we can predict the longitudinal performance of the QGD relative to the traditional decelerator. As seen in Fig. 5.16(a), the energy removed per stage of the QGD is smaller than that of a traditional decelerator for all $0° < \phi_o < 90°$ because the decelerator stage spacing (in this simulation) is twice that of a traditional decelerator. For this reason, given the same number of deceleration stages, QGD deceleration with the same ϕ_o as in a traditional decelerator leads to a faster beam. When comparing the longitudinal acceptance of the two types of decelerators it is important to take the
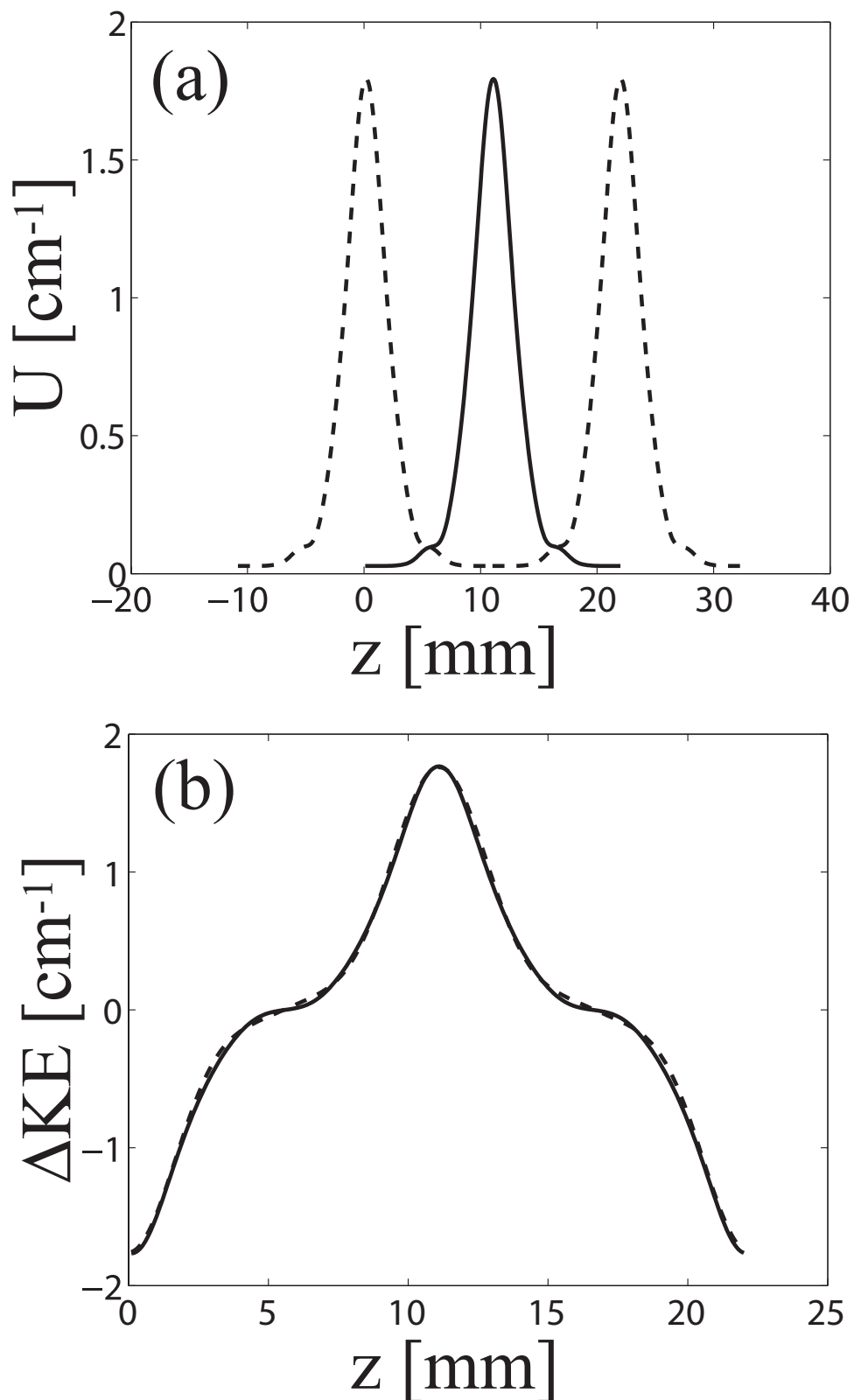
Figure 5.14: (a) The Stark shift of an OH molecule in the $|2, \pm 2, +\rangle$ state inside the QGD. The solid curve is the Stark shift due to the slowing electrodes, while the dashed curve is the Stark shift due to the electrodes that will be energized at the switching time. (b) The change in the molecule's kinetic energy as a function of position is shown (solid) as well as a fit of Eq. 5.4, including up to $n = 3$ (dashed). The solid curve is calculated from the subtraction of the two curves in panel (a).
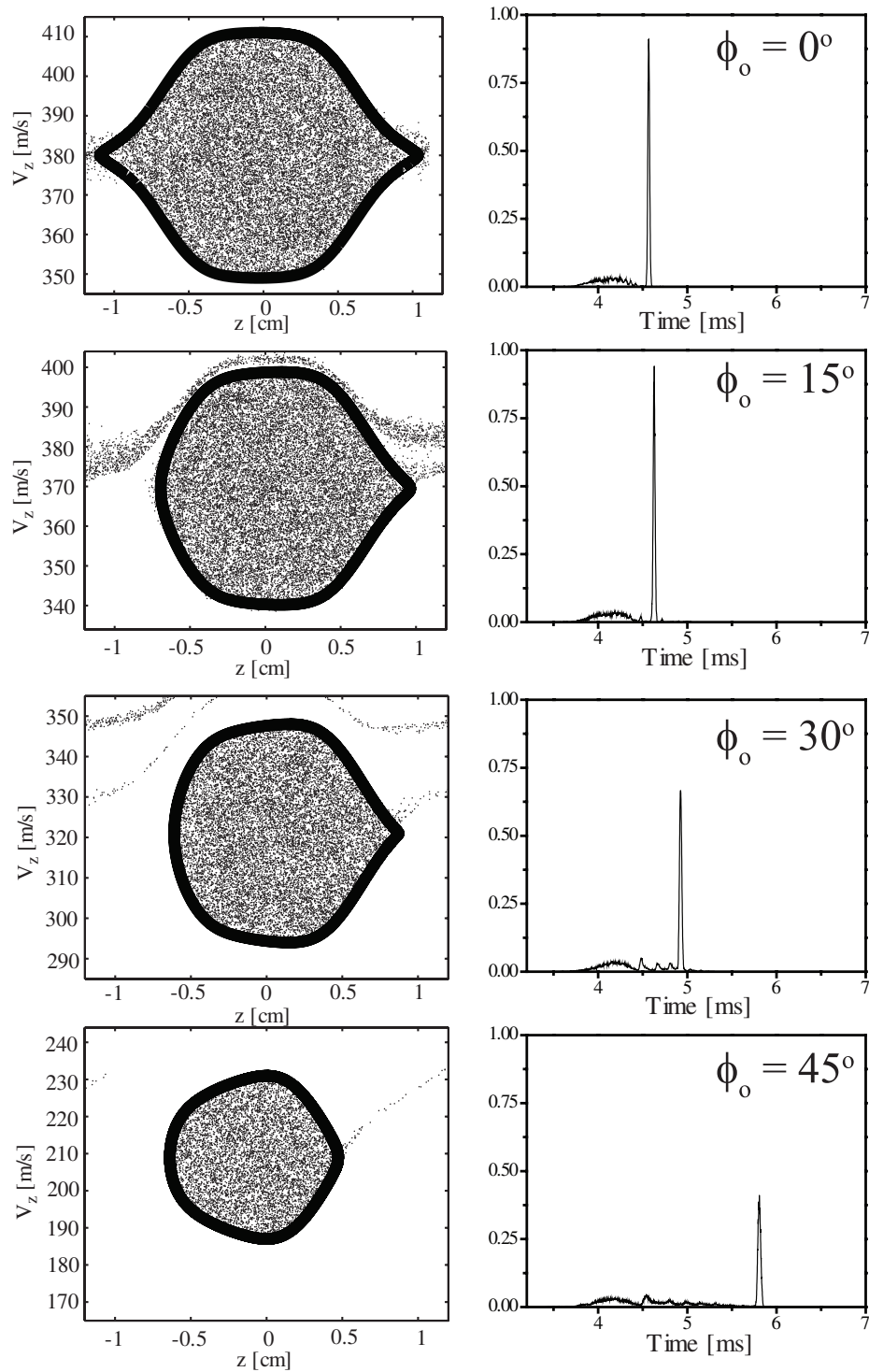
Figure 5.15: The left column is stable phase space of molecules decelerated inside the QGD. The solid line is the separatrix predicted by the theory, while the points represent positions of molecule in the 3D Monte Carlo simulations. The right column shows the ToF spectra of OH molecules in the $|2 \pm 2, +\rangle$ state at the exit of this decelerator which has 142 deceleration stages, along with 142 quadrupole stages.

limit of high phase angles where both values of ΔKE converge. Nonetheless, the longitudinal phase-space acceptance of the QGD shows some gain over that of traditional deceleration as shown in Fig. 5.16(b). This gain at a fixed energy loss per stage is primarily due to the increased physical size of the stable longitudinal phase space resulting from the larger deceleration stage spacing.

Since Fig. 5.16 compares only the total area inside the separatrix—and $S = 1$ deceleration does not completely fill this area due to the coupling effects—this gain is actually an underestimate of the QGD longitudinal performance. Furthermore, these graphs do not include transverse focusing effects, which can only be properly included through detailed simulation. The results of Monte Carlo simulations including these transverse effects are shown in Fig. 5.17. The number of decelerated molecules versus final speed is plotted for both the traditional decelerator operating at $S = 1$ and the QGD operating at two different quadrupole rod voltages, ± 1 kV and ± 3 kV. While the QGD initially delivers more molecules, once the molecules are decelerated below 100 m/s, the decelerated molecule number falls off abruptly. This behavior is expected since, for these simulations, the voltage on the quadrupole-guiding stages is held constant throughout the slowing sequence. As detailed in Eq. (3) of Ref. [112], the focal length of a transverse guiding element is directly proportional to the molecular kinetic energy. Therefore, as the mean speed of the packet is decreased, the molecules are overfocused and collide with the decelerator electrodes. This can be prevented by lowering the voltage on the quadrupole-guiding stages during the deceleration process. Figure 5.18 displays simulation results of deceleration with this dynamically scaled voltage compared to $S = 1$ slowing at $\phi_o = 30.43°$. For this simulation, the quadrupole voltages are scaled by $(v/v_{initial})^{0.875}$ after each deceleration stage, where v is the instantaneous packet velocity directly following each stage switch. The exponent of 0.875 is found empirically to produce the most gain at $v_{final} = 14$ m/s. For ease of simulation, the transverse forces are scaled by $(v/v_{initial})^{0.875}$ whenever the molecules are closer to a quadrupole-guiding stage than to a deceleration stage. While this may be a poor approximation at the lowest speeds, it will likely lead to an underestimate of the decelerated molecule number since the transverse guidance of the quadrupole-guiding stage extends beyond this regime. Even if it leads to an overestimate, proper control of the quadrupole
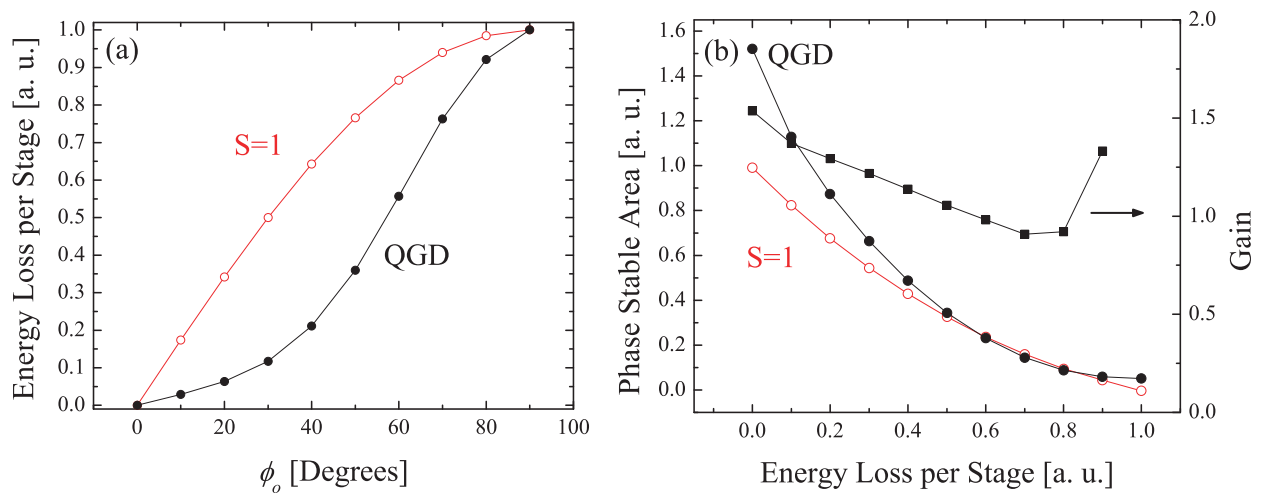
Figure 5.16: (a) The energy removed per stage as a function of phase angle for both traditional deceleration and deceleration with a QGD. Both curves are calculated for OH in the $|2, \pm2, +\rangle$ state and scaled down by 1.76 cm^{-1} at $\phi_o = 90°$. (b) The calculated longitudinal phase-stable area for deceleration versus energy loss per stage for traditional deceleration and deceleration with a QGD is plotted on the left axis. The gain of the QGD over traditional deceleration is plotted on the right axis. Note that for a given energy loss the gain in phase stable area due to the larger volume of the QGD is ≤ 1.5 for all $0° < \phi_o < 80°$.
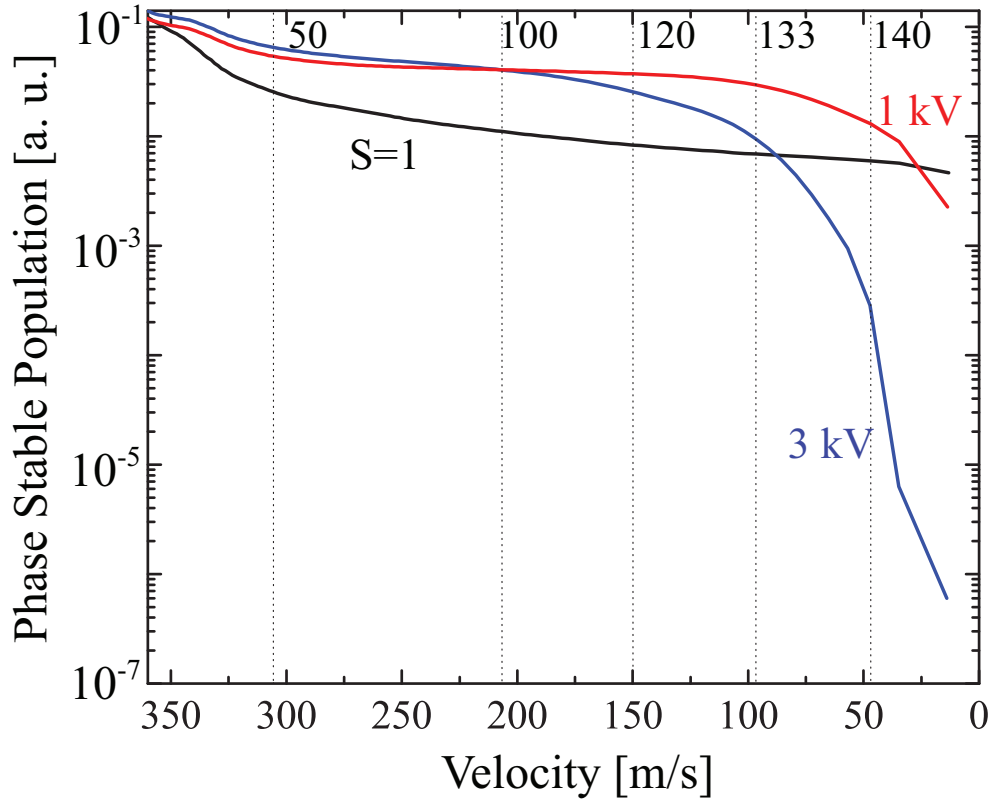
Figure 5.17: Simulations of the phase-stable molecule number as a function of stage number in the QGD and $S = 1$ decelerator. The voltage on the quadrupole stages of the QGD is held constant throughout the deceleration sequence. All simulation data is for $v_{final} = 14$ m/s. The traces shown are $S = 1$ deceleration at $\phi_o = 30.43°$, QGD operated with ± 1 kV on the quadrupoles, and QGD operated with ± 3 kV on the quadrupoles. Note the decrease in stable molecule number in the last several stages for the QGD results. This decrease is due to transverse overfocusing of the slow molecules through the final few quadrupole stages, and suggests that scaling of quadrupole voltage is necessary.

voltages may compensate any overfocusing introduced by the decelerating elements. As seen in Fig. 5.18, dynamically controlling the voltage of the quadrupole-guiding stages leads to a factor of 5 increase in decelerated number for larger velocities (>80 m/s) and delivers about 40% more decelerated molecules than traditional $S = 1$ deceleration provides at the lowest final speeds (14 m/s). Because the voltages applied to the quadrupole-guiding stages are relatively low, dynamic control of them should be possible using an analog waveform generator and high-voltage amplifier. It should be noted that the optimal voltage scaling may vary among decelerators since the real focal length depends sensitively on the electrode construction, and at low speeds the transverse focusing of the decelerator electrodes becomes significant. This is, presumably, because the overfocusing of the decelerator electrodes can be compensated to a certain degree by injecting molecules which are already slightly overfocused. In other words, two focusing stages can overcome the overfocusing of a single stage. Thus, it may be possible to use adaptive algorithms to optimize the quadrupole voltage or change the design of the decelerating electrodes so that they provide less transverse focusing, and maximize the number of decelerated molecules beyond what is reported here [111].

One important advantage of the QGD over traditional decelerators is its inherent ability to support more deceleration stages. Because the molecules experience a tunable transverse focusing element after each deceleration stage, there is little loss in efficiency by extending the number of deceleration stages. In fact, as seen in Fig. 5.19, there is essentially no loss until the molecules are decelerated to the lowest speeds previously discussed. This low-velocity loss is due to the aforementioned transverse overfocusing and longitudinal reflection. The former loss mechanism may be overcome, while the latter presents a fundamental limit. Even with this loss, the QGD outperforms both $S = 3$ (Fig. 5.10) and $S = 3+$ (Fig. 5.12). Thus, the QGD is an ideal decelerator for more efficiently producing cold molecules and, perhaps more importantly, the ideal decelerator for slowing molecules with poor Stark shift to mass ratios, like H_2O and SO_2.

In summary, we identify two specific loss mechanisms—transverse over-focusing and longitudinal reflection—observed in the operation of Stark decelerators and perform initial experiments and detailed Monte Carlo simulations to address them. While the use of decelerator overtones yields im-
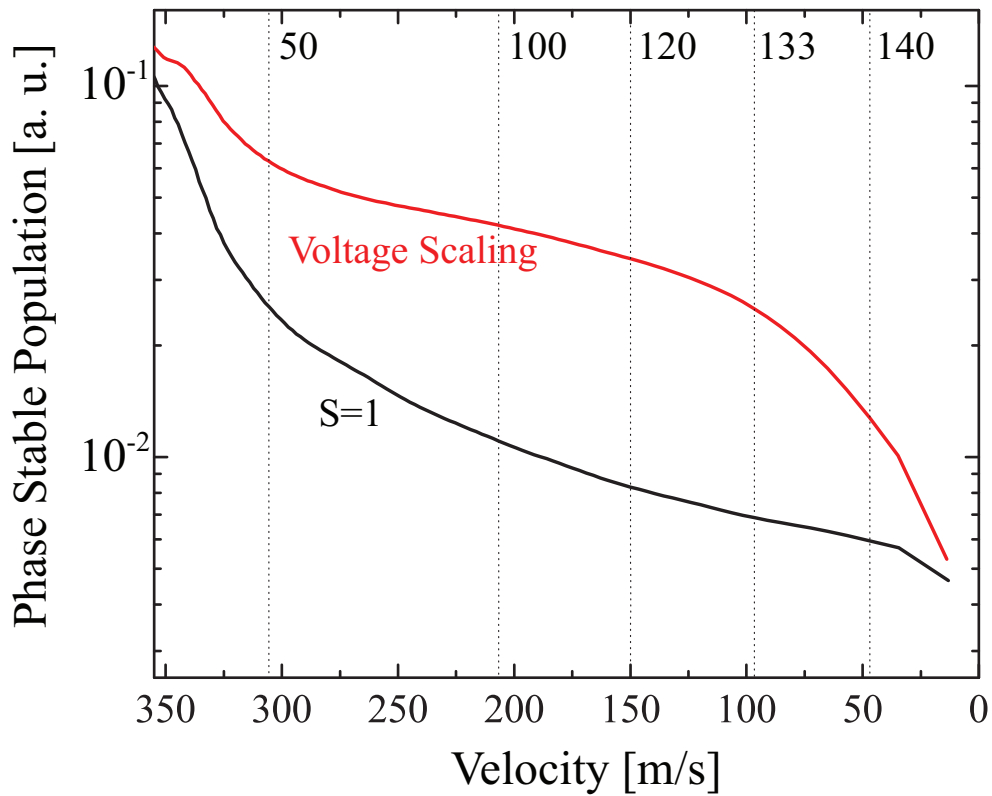
Figure 5.18: Monte Carlo simulation results for the decelerated molecule number using traditional $S = 1$ deceleration ($\phi_0 = 30.43°$) and deceleration using a QGD ($\phi_0 = 52.75°$) with a dynamic voltage scaling of $(v/v_{initial})^{0.875}$. For both curves, 142 stages of deceleration were used, and $v_{final} = 14$ m/s. The different phase angles chosen for the two decelerators are a result of their differing potential profiles for deceleration. The vertical dashed lines represent the deceleration stage at the given velocity. Note that when the quadrupole voltage within the QGD is scaled in this manner, we observe a 40% gain in molecule number at 14 m/s, and a factor of 5 gain over $S = 1$ at higher velocities.
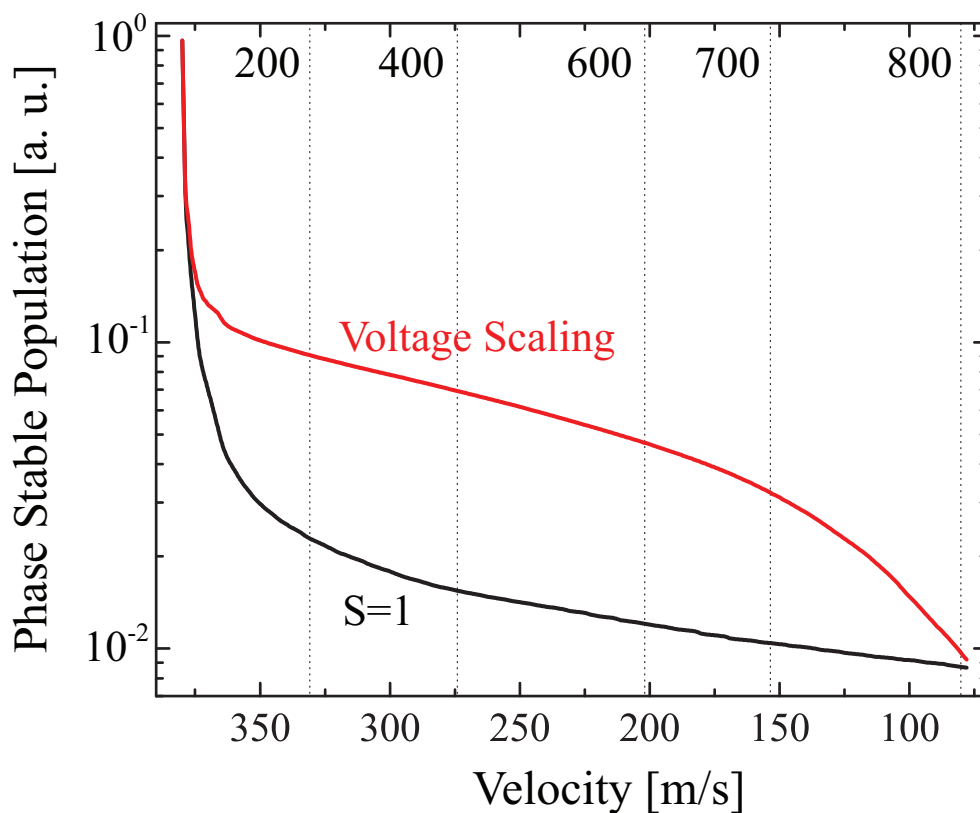
Figure 5.19: $S = 1$ simulation results for $v_{final} = 80$ m/s ($\phi_0 = 5.22°$) plotted along with simulation results using the voltage-scaled QGD to the same v_{final} ($\phi_0 = 23.5°$). The number labeling each vertical dashed line is the number of deceleration stages necessary to reach the given velocity. Note the large number of stages (803) used to reach 80 m/s, which suggests that a very long QGD may be employed for slowing molecules with a poor Stark shift to mass ratio.

provement over $S = 1$ deceleration at high to intermediate speeds ($v_{final} > 80$ m/s), the loss at very low velocities remains problematic. The QGD solves the problem of coupling between the transverse and longitudinal motions inside a Stark decelerator by introducing independent transverse focusing elements. By dynamically controlling the focal length (voltage) of these guiding elements, large improvements (factor of 5) in deceleration efficiency can be achieved for $v_{final} > 80$ m/s, which would prove useful for molecule collision studies [111]. Gains of 2 and 40% are also predicted for $v_{final} = 50$ m/s and 14 m/s, respectively. Electrostatic [103] and magneto-electrostatic [55] trapping experiments stand to benefit from such gain for $v_{final} \leq 50$ m/s. Furthermore, it appears that with dynamic control of the guiding stage focal length there should be no limit to the length of decelerator that can be built. This enables the deceleration of molecules with a poor Stark shift to mass ratio. However, we note that none of the techniques described in this chapter mitigate the longitudinal low-velocity loss due to reflection, which appears to be a fundamental component of Stark deceleration. Building upon the strong correlation between simulation and experimental results, we are confident that the simulations presented in this work provide a solid guideline for future implementations of Stark deceleration.

Chapter 6

Magnetic Trapping of OH

6.1   Magnetoelectrostatic Trapping

Neutral polar molecules are readily trapped in inhomogeneous electric fields [103, 113], how-
ever theory predicts that at high phase-space densities such traps will suffer from large inelastic
collision losses [114]. One possible solution is to trap strong-field seeking states via time-dependent
electric traps [115]. In contrast, we are interested in magnetically trapping these neutral polar
molecules so as to have the freedom to apply external electric fields to control collision dynamics
inside the trap. Highly vibrationally excited, triplet KRb molecules produced via photoassociation
have been magnetically trapped at a temperature of $\sim$300 μK and density of 10^4 cm^{-3} [116]. Buffer
gas cooling has been used to load a magnetic trap with ground-state CaH and NH molecules at
temperatures of hundreds of mK and densities of $\sim$$10^8$ cm^{-3} [117, 118]. In this section, we describe
our first realization of a magnetic trap for hydroxyl radical (OH) molecules. This work represents
the first observation of magnetically trapped OH and the lowest temperature (30 mK) yet achieved
for a magnetically-trapped polar molecule in its rovibronic ground state [64]. Moreover, we have
performed the first study of trap dynamics based on a single molecule possessing large magnetic and
electric dipole moments in B- and E-fields that are inhomogeneous and anisotropic. Interesting po-
lar molecule dynamics have been predicted at large field strengths [119]. Accurate correspondence
between experimental data and simulations is achieved only by accounting for the molecular state
mixing induced by the crossed fields. Large magnetic (B) fields may serve to suppress inelastic col-
lision losses [120] while at the same time sympathetic cooling of molecules via co-trapped ultracold

Figure 6.1: (a) Illustration of the magneto-electrostatic trap (MET) assembly. The terminus of the Stark decelerator (yellow, gray electrodes), shown to the left, couples state-selected cold OH molecules into the magnetic quadrupole (blue). The double-electrode structures within the electric quadrupole (red) allow for application of uniform electric fields within the magnetic trap. The ring (green) supports a 1 inch lens for collection of laser-induced fluorescence. (b) Plots of the magnetic field distributions within the MET for both stopping and trapping of decelerated OH molecules.

atoms may become feasible [121, 122]. In addition, the magnetic quadrupole trap described here permits the application of arbitrary external electric (E) fields to a large class of polar molecules—a necessary first step towards our recent achievement of observing cold dipolar collisions between OH and ND_3 [18].

To produce an OH sample suitable for magnetic trapping, we begin with a cold beam of ground state ($^2\Pi_{3/2}$) OH produced via a pulsed electric discharge through 2% H_2O vapor [62] seeded in 1.5 bar of Kr. A piezoelectric transducer valve [68] operating at 10 Hz provides a supersonic expansion of the OH/Kr mixture through a 1 mm nozzle. This results in a 490 m/s molecular packet with a 15% longitudinal ($\hat{z}$) velocity spread. The transverse ($\hat{\rho}$) velocity spread of the beam is limited to 2% by the 3 mm diameter molecular skimmer. Compared with a Xe expansion, the higher-velocity Kr expansion leads to less transverse beam loss within the current decelerator design. Thus, despite the fact that the Kr beam requires a higher phase angle for deceleration (smaller decelerator acceptance) it results in more decelerated molecules as described in Chapter 5. After passing through the skimmer, the OH packet is spatially matched to the decelerator entrance via an electrostatic hexapole. We utilize the 142 stages of our Stark decelerator to slow a 130 mK packet (in the co-moving frame) of OH to 20 m/s at a phase angle $\phi_0 = 47.45°$ for coupling into the magneto-electrostatic trap (MET). Decelerated OH packets are detected via laser-induced fluorescence (LIF) upon entering the MET, whose center lies 2.7 cm from the final pair of decelerator rods. The 282 nm pulsed LIF beam is oriented along the mutual longitudinal axis ($\hat{z}$) of the decelerator and MET, and the resulting 313 nm fluorescence is collected in a solid angle of 0.016 sr.

6.1.1 Design and Operation of the Magnetic Quadrupole Trap

The MET is illustrated in Fig. 6.1a, and consists of two copper coils operated in an anti-Helmholtz (field-opposing) configuration surrounded by an electric quadrupole. The center-to-center magnetic coil spacing is 1.5 cm, providing a field gradient of 6700 G/cm by passing 1500 A through the 4 turns of each water-cooled copper coil. To calculate the magnetic fields within the

coils for both stopping and trapping of OH, we use the closed-form expression for the magnetic field due to a current loop of radius A:

$$B_\rho = \frac{\mu_0 I}{2\pi} \frac{z}{\alpha^2 \beta \rho} \left[(A^2 + \rho^2 + z^2)E(k^2) - \alpha^2 K(k^2) \right] \tag{6.1}$$

$$B_z = \frac{\mu_0 I}{2\pi} \frac{1}{\alpha^2 \beta} \left[(A^2 - \rho^2 - z^2)E(k^2) + \alpha^2 K(k^2) \right] \tag{6.2}$$

where we define

$$\alpha^2 = (A - \rho)^2 + z^2 \tag{6.3}$$

$$\beta^2 = (A + \rho)^2 + z^2 \tag{6.4}$$

$$k^2 = 1 - \frac{\alpha^2}{\beta^2} \tag{6.5}$$

and the functions K and E are the complete elliptic integrals of the first and second kind, respectively. This functional form for B makes numerical evaluation rather straightforward in an environment like MATLAB and is an exact expression. Placing four coils each at $z = \pm 7.5$ mm with opposing currents of 1500 A, we produce the magnetic quadrupole fields $(B_\rho(z = 0), B_z(\rho = 0))$ of Fig. 6.1b (shown in black). The red curves of Fig. 6.1b are the same components of B but with only the back coil at a current of 2000 A. This configuration is used to initially stop the 20 m/s OH packet entering from the Stark decelerator. Given that OH has a magnetic dipole of $1.2\mu_B$, the longitudinal trap depth is ~ 400 mK. As is always the case with magnetic quadrupoles, the radial trap depth is one half of this value.

The electrodes surrounding the coils allow the application of an E-field to the trapped sample. The double- and single-rod electrodes that comprise the electric quadrupole allow the application of two distinct field configurations. A uniform bias electric field is created by grounding the single-rods while oppositely charging the opposing double-rods to ± 3 kV. Alternatively, we generate a quadrupole E-field by charging neighboring rods with opposite polarities of ± 9 kV. Shielding by the MET coils reduces the interior E-field by a factor of ~ 5. Figure 6.3 depicts the quadrupole electric field superimposed on the magnetic quadrupole field. Hydroxyl has both an appreciable magnetic and electric dipole, and we can easily alter the geometry of the trapping potential by

applying electric fields of variable magnitude and direction to the magnetically trapped sample.

To trap the incoming OH packet, the coil closer to the decelerator (front coil) is grounded while the coil further from the decelerator (back coil) operates at 2000 A for the duration of the 3.7 ms deceleration sequence. The effective magnetic dipole of OH in its $J = m_J = \frac{3}{2}$ state is 1.2 $\mu_B \simeq 0.81$ K/T, where μ_B is the Bohr magneton, allowing the back coil to stop molecules with velocity ≤ 22 m/s. The front coil is turned on after the 20 m/s molecules are stopped by the back coil, which occurs 2.65 ms after exiting the final deceleration stage. The trap switching is synchronous to the 20 m/s molecules since OH possessing larger longitudinal velocities escape the quadrupole field. For technical reasons, the two magnet coils are connected in series, causing the current in both coils to decrease from 2000 A to 1500 A over ∼800 μs once the front coil is switched into the circuit. To switch between stopping and trapping field configurations, we use two banks of twelve parallel MOSFETs each rated for 250 A (3000 A capacity per bank). The MOSFET banks are mounted on separate water-cooled base plates, and they are all synchronously controlled by the driver circuit depicted in Fig. 6.2.

6.1.2   Trap Dynamics in Combined Electric and Magnetic Fields

The OH ground state is best described by Hund's case (a), in which the spin ($|\Sigma| = \frac{1}{2}$) and orbital ($|\Lambda| = 1$) angular momenta are strongly coupled to the molecular axis, yielding the total angular momentum projection $|\Omega| = \frac{3}{2}$. The $|\Omega| = \frac{1}{2}$ state lies 126 cm^{-1} above this ground state. The nuclear spin of the hydrogen atom ($I = \frac{1}{2}$) leads to a hyperfine splitting of the ground state into $F = 2, 1$ components. In the presence of large external fields (E>1.7 kV/cm or B>100 G), the electron angular momentum and nuclear spin decouple [24], and one considers the total angular momentum $\mathbf{J}$, which includes nuclear and electronic orbital angular momentum as well as electron spin. The projections m_J of $\mathbf{J}$ are defined along the axis of the applied field. The ground state is further split into two opposite-parity states (f/e) by the coupling of electronic orbital angular momentum to nuclear rotation. This small Λ-doublet splitting of 1.69 GHz, along with the 1.67 Debye electric dipole, is responsible for the rather large Stark shift experienced
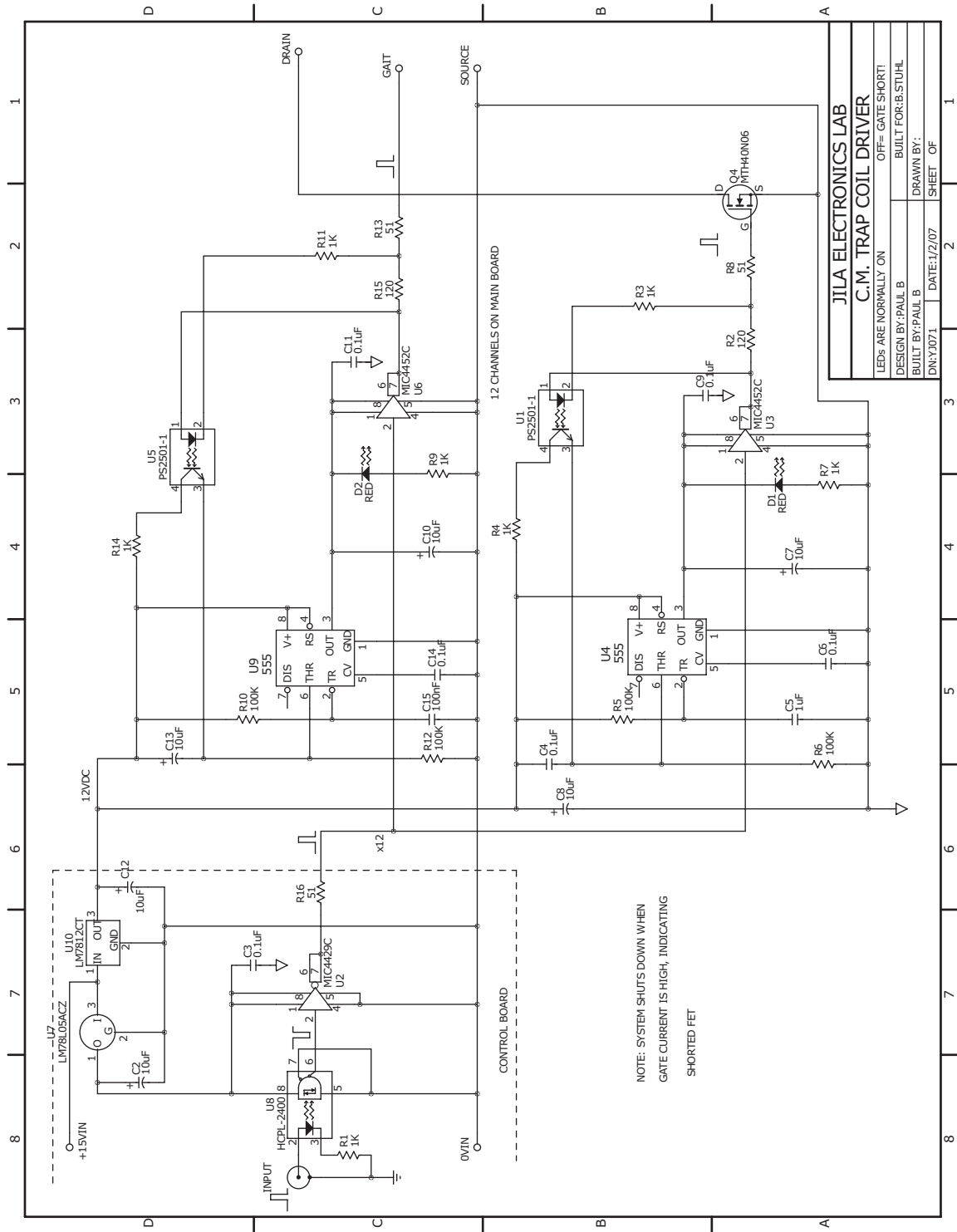
Figure 6.2: Schematic of the high-current switching circuit used to load Stark decelerated OH into the MET. The actual switching electronics consisted of 24 of these driver circuits operating 24 individual MOSFETs. Twelve MOSFETs in parallel carried the 2000 A current during the loading step while the other 12 where switched into the circuit to carry the 1500 A trapping current.

by OH molecules [21]. Fig. 6.3a and b show the Zeeman and Stark effects of the OH ground-state respectively. External electric fields can thus dramatically alter the potential confining the magnetically trapped molecules. Fig. 6.3c-e illustrate the field geometries within the MET. In the plane perpendicular to $\hat{z}$, Fig. 6.3c shows the radial B-field characteristic of a magnetic quadrupole, while Fig. 6.3d depicts the electric quadrupole field introduced by the electrode geometry. Fig. 6.3e illustrates both B (blue) and E (red) fields along $\hat{z}$.

The top potential surface of Fig. 6.3f represents the energy shift of the decelerated $|J = \frac{3}{2}, m_J = \frac{3}{2}\rangle$ state (E-fields couple e and f, therefore they are no longer good quantum numbers) within the combined quadrupole E- and B-fields present in the MET. The transverse profiles of the four deepest adiabatic potentials are depicted at the longitudinal trap center, where $\overrightarrow{B} \cdot \hat{z} = 0$. The remaining four surfaces (not shown) are simply inverted relative to those displayed, and are therefore anti-trapping. The three-dimensional MET potentials are calculated by diagonalizing an effective Hamiltonian that includes both Stark and Zeeman terms. Coupling between the ground $|J = \frac{3}{2}, \Omega = \frac{3}{2}\rangle$, and excited $|\frac{5}{2}, \frac{3}{2}\rangle$, $|\frac{1}{2}, \frac{1}{2}\rangle$, $|\frac{3}{2}, \frac{1}{2}\rangle$ states is included, for a total of 64 hyperfine components. The $|J = \frac{3}{2}, \Omega = \frac{3}{2}\rangle$, $|\frac{3}{2}, \frac{1}{2}\rangle$ coupling is the most critical, increasing the trap depth of the top surface of Fig. 6.3f by 11%. Addition of the remaining states modifies the potential by <0.1%. The square shape of the top surface is a result of the varying angle between E and B in the MET. The potentials from each field directly sum where the fields are collinear, but the trap shallows from this maximum value as the angle between E and B increases.

The Stark decelerator slows only those OH molecules in the electrically weak-field seeking (EWFS) component of the ground state, $i.e.$, the upper Λ-doublet. Of these EWFS molecules, only those with components $J = \frac{3}{2}$, $m_J = \pm\frac{3}{2}$ are synchronously slowed to 20 m/s. Because the positive m_J state is magnetically weak-field seeking (MWFS), only 50% of the decelerated molecular packet is trappable by the MET. The molecules experience a >100 G magnetic field at the last deceleration stage emanating from the back coil, which preserves the quantization of the decelerated state.

Figure 6.8 displays typical time-of-flight data resulting from the trapping sequence along with results from Monte Carlo simulation of the trap dynamics. The large initial peak is the decelerated
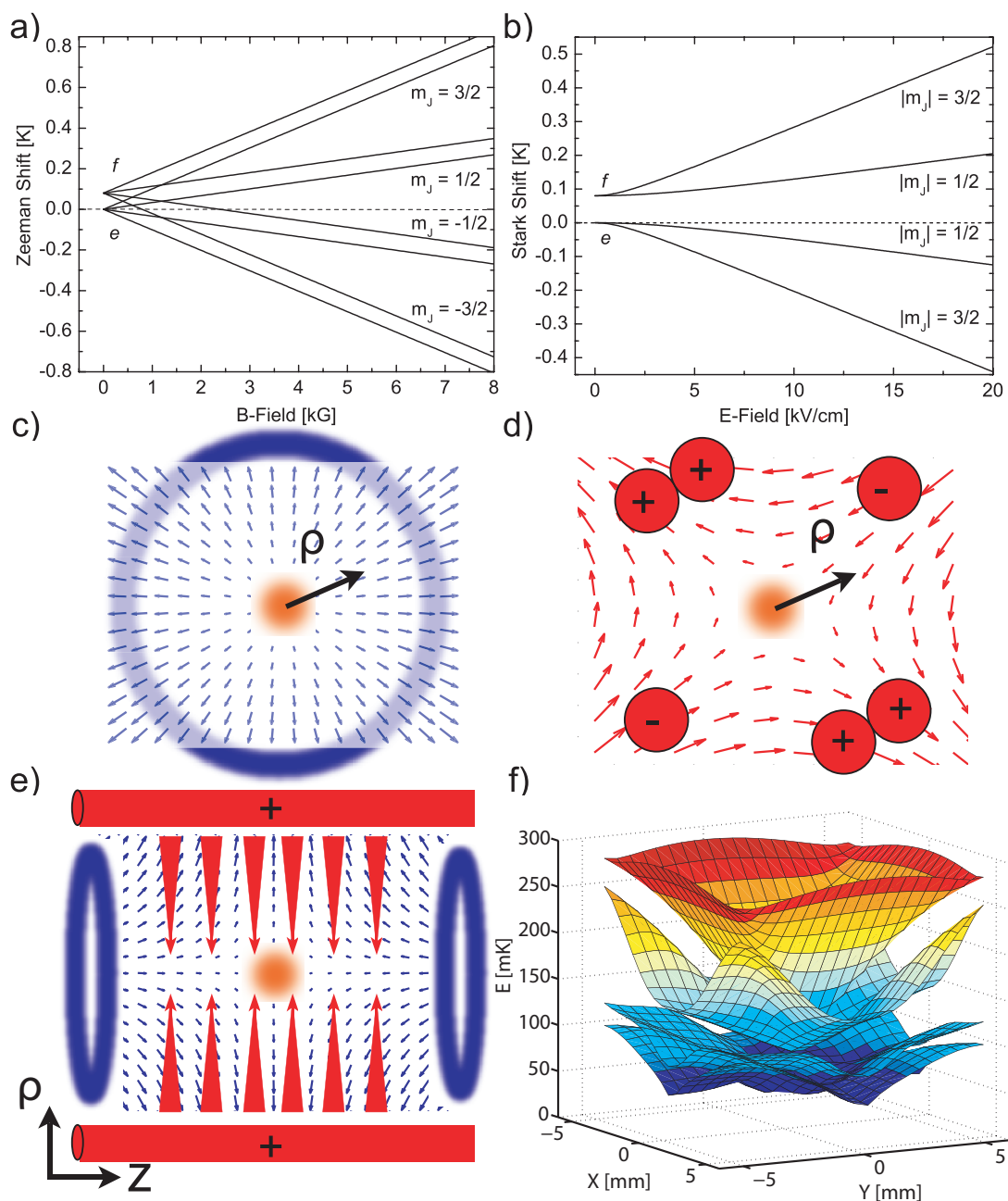
Figure 6.3: (a) Zeeman and (b) Stark effects of the ground state structure of OH. (c) Magnetic and (d) electric quadruple fields viewed from $\hat{z}$. (e) Side view of the MET configuration with quadrupole E and B fields. (f) Adiabatic potential surfaces for various components of OH ground state at the longitudinal MET center. The top surface depicts the decelerated/trapped $|J = \frac{3}{2}, m_J = \frac{3}{2}\rangle$ state.

a)

b)
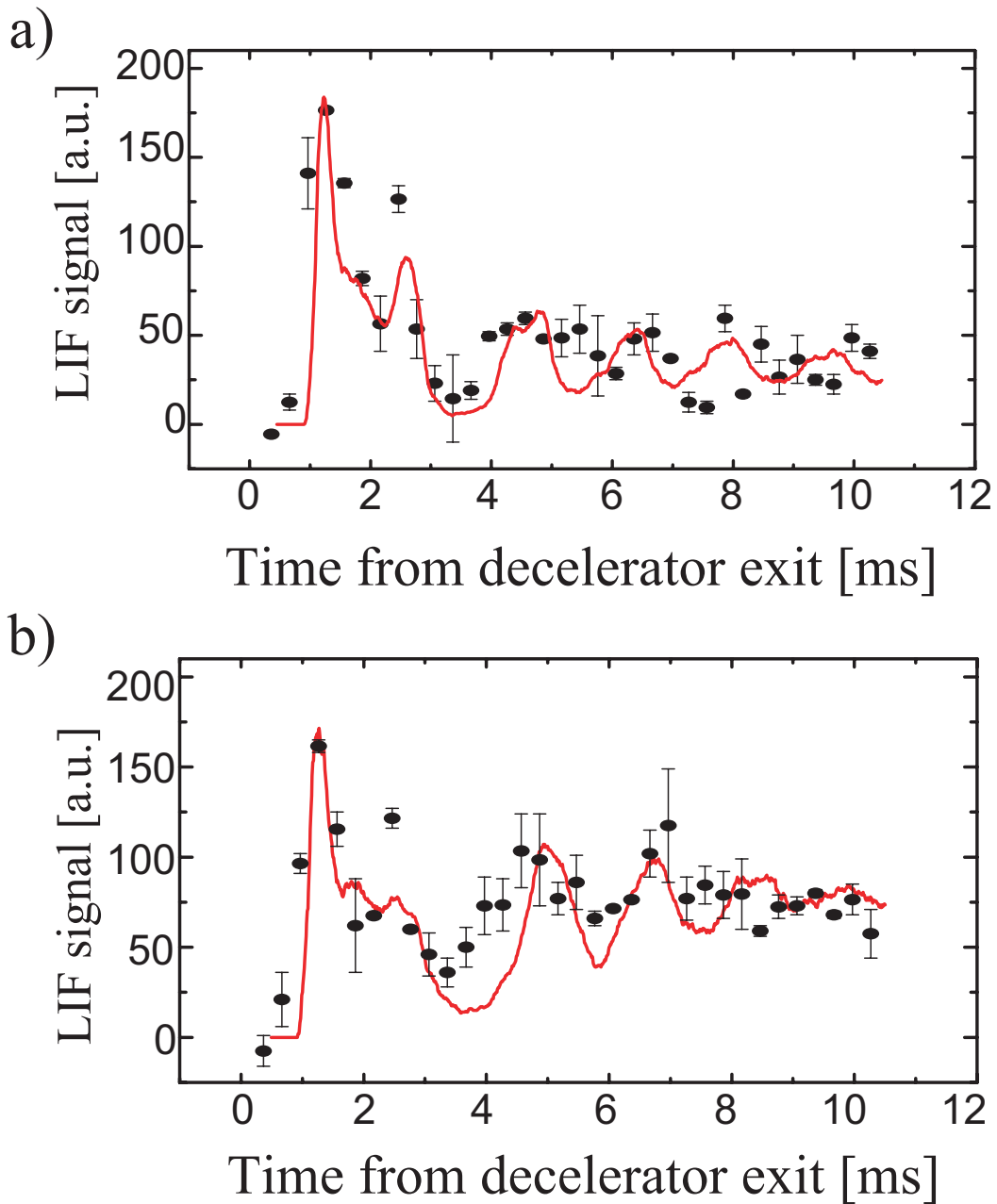
Figure 6.4: Time-of-flight data (points) and Monte Carlo simulation results (solid red line) for two different electric field configurations. The magnetic field switches from the stopping configuration to quadrupole trapping at $t = 2.65$ ms. (a) Magnetic trap only. (b) Stopping and trapping in the presence of combined electric and magnetic quadrupole fields. Note the larger steady-state trap population when the electric quadrupole is applied.

OH packet traversing the detection region at the center of the trap. All subsequent peaks are the result of oscillation in the $\hat{\rho}$ dimension, with a frequency of $\sim$650 Hz. Fluorescence is gathered in $\hat{\rho}$, and oscillations in $\hat{z}$ are not detectable since our detection region spans the entire visible trap length. The magnetic quadrupole trap is unable to confine all the molecules stopped by the back coil alone due to the 25% current drop, as is clear from the difference in signal height at $\sim$6 ms versus the steady-state level at, e.g., 14 ms. Note the larger steady-state population of Fig. 6.8(b) from the addition of a confining transverse electric quadrupole. Also visible is the shorter coherence time compared to Fig. 6.8(a), which results from trap distortion visible in Fig. 6.3f. An estimate of the density of trapped OH, as measured by LIF, gives $\sim 3 \times 10^3$ cm^{-3}. By comparison, the density of a packet "bunched" at a phase angle of $\phi_0 = 0°$ is 10^7 cm^{-3}, while the 20 m/s packet is 10^4 cm^{-3}. Monte Carlo analysis of the velocity distribution of the trapped OH yields temperatures of $\sim$30 mK. With our improved knowledge of the trap dynamics due to accurate Monte Carlo simulations, we expect to be able to trap 2-3 times more OH through modification of deceleration phase angle and trap switching times for optimal coupling of the slowed beam into the MET.

Higher decelerator phase angles should, in principle, produce a slower OH packet. However, below 20 m/s the OH population drops sharply and no further deceleration is observed. We attribute this effect to a reduction in the effective aperture seen by slow molecules as they traverse the final deceleration stage. The OH closest to the final decelerator rods see a larger longitudinal potential than those on-axis, and at sufficient phase angles, are stopped or reflected and hence cannot be observed in the MET region. Numerical models elucidate this effect, which may be mitigated by new decelerator designs [55].

The 10 Hz repetition rate of the Stark decelerator currently limits our trap interrogation time to 100 ms. Maintaining continuous currents of 1500 A presents technical challenges due to heating in both the switching transistors and cabling. To mitigate this, we operate the switching MOSFETs on a water-cooled copper plate and also run chilled water through the MET coils. Water-cooled cables are also necessary for such high-power operation. Not surprisingly, the largest ohmic heating in the system occurs at copper interfaces. Figure 6.5 shows electric field-free OH
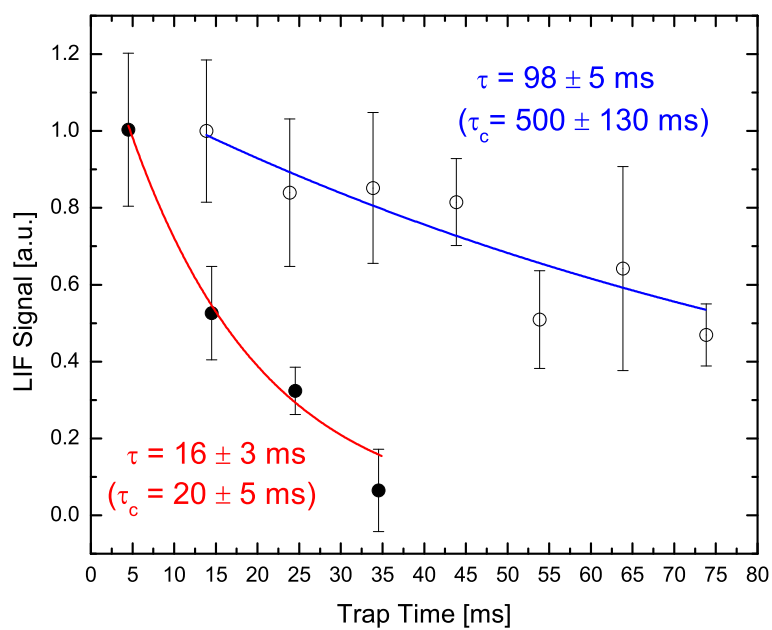
Figure 6.5: Measured (τ) and de-convolved collisional (τ_c) lifetimes of magnetically trapped OH at a background pressure of 1×10^{-6} Torr ($\bullet$, red line) and 4×10^{-8} Torr ($\circ$, blue line).

trap lifetimes measured in two different background pressure regimes: 1×10^{-6} and 4×10^{-8} Torr, both dominated by N_2 at 295 K. Non-ideal power supply control causes the trap current to decrease from 1500 A to 1160 A at a rate of 2000 A/s. This lowers the trap depth, resulting in a loss of $12 \pm 2 \text{ s}^{-1}$. After accounting for this loss mechanism, we find background collision-limited lifetimes of 20 ± 5 ms and 500 ± 130 ms for the two pressure regimes, respectively. These lifetimes allow an estimate of the OH-N_2 cross section of 500 ± 100 Å^2.

We have therefore magnetically confined ground state hydroxyl radicals in a MET that allows for the application of a variable E-field to the trapped polar molecules. Diagonalization of an effective Hamiltonian modelling the energy shift of OH in crossed E- and B-fields was necessary for accurate Monte Carlo simulation of the trap dynamics. Future experiments could quantify temperature dependent non-adiabatic transition rates between the different surfaces depicted in Fig. 6.3f akin to Majorana transitions observed in atomic magnetic quadrupole traps [56]. Furthermore, higher densities within the MET will facilitate the study of cold OH-OH collisions in variable electric fields. As rather modest electric fields are expected to modify collision cross sections between polar molecules by as much as 10^3 [114], crossed-beam experiments exploiting the MET described here will benefit from both low center-of-mass collision energies and tunable E-fields in the interaction region.

6.2 Permanent Magnet Trap

The MET described in the previous section is insufficient for molecular collision experiments due to its low density of trapped OH molecules ($\sim 10^3$ cm^{-3}) and the technical difficulties associated with operating a 2000 A switching system. Magnetic traps are still attractive for dipolar collision experiments since the external electric field may be varied, but it turns out that trapping with permanent magnets represents a much better route to confining a Stark decelerated OH beam. Given the large magnetic fields produced by rare-earth magnets of ~ 1 T, permanent magnets are a natural choice to replace the bulky water-cooled coils and switching circuitry of electromagnets. The difficulty with permanent magnets is precisely the inability to turn them off – specifically

when it comes to loading a slow packet of molecules. Nevertheless, we solve this problem by using the magnets themselves as "stopping" electrodes by charging them to ± 12 kV. This allows us to almost double the incoming OH velocity from the previous trap and stop molecules from a velocity of 36 m/s. Furthermore, the reduced size of the magnets allows us to match the volume of the trap exactly to the volume of the stopped packet, thereby minimizing any density reduction due to spatial mismatch.

A pulsed supersonic beam of OH radicals is produced as described in the previous section by striking an electric discharge through a mixture of 27 mbar H_2O and 1.5 bar Kr. The resulting OH beam consists of rotationally cold, $^2\Pi_{3/2}$ molecules whose center longitudinal velocity is 490 m/s. The packet passes through a 3 mm diameter skimmer and is then coupled via an electrostatic hexapole into the 142-stage Stark decelerator. The Stark decelerator slows weak-field seeking OH molecules residing in the $|J = 3/2, m_J = \pm 3/2, f\rangle$ state, where J represents total angular momentum and m_J is the projection of J along the electric (E) field axis. One difference from our MET loading procedure is that the Stark decelerator is now operated at a phase angle ϕ_0 of $50.352°$ in order to slow a 120 mK portion of the OH packet to 36 m/s. When slowing to velocities below 50 m/s, we observe maximum decelerator efficiency for $45° \leq \phi_0 \leq 55°$. Operation at these intermediate phase angles increases transverse packet confinement and reduces the coupling between transverse and longitudinal motion [99, 105].

We stop and confine the decelerated 36 m/s OH packet within a permanent magnetic trap whose center lies 1 cm from the final decelerator rod pair. This trap, depicted in Fig. 6.6a, represents a marked improvement over our previous MET in both design simplicity and ultimate trapping efficiency [64]. The magnetic trap is constructed by mounting two Ni-coated NdFeB permanent ring magnets in a field-opposing orientation such that a magnetic quadrupole field is produced between them as shown in Fig. 6.6b. The N42SH rating of these magnets ensures an operating temperature of up to $150°C$ and a residual magnetization of 1.24 T. However, we do measure reduced magnetization ($\sim 20\%$) when baking above $100°$. The inner and outer radii of the magnets measure 2 mm and 6 mm, respectively, while their thickness is 4 mm. The center-to-center magnet
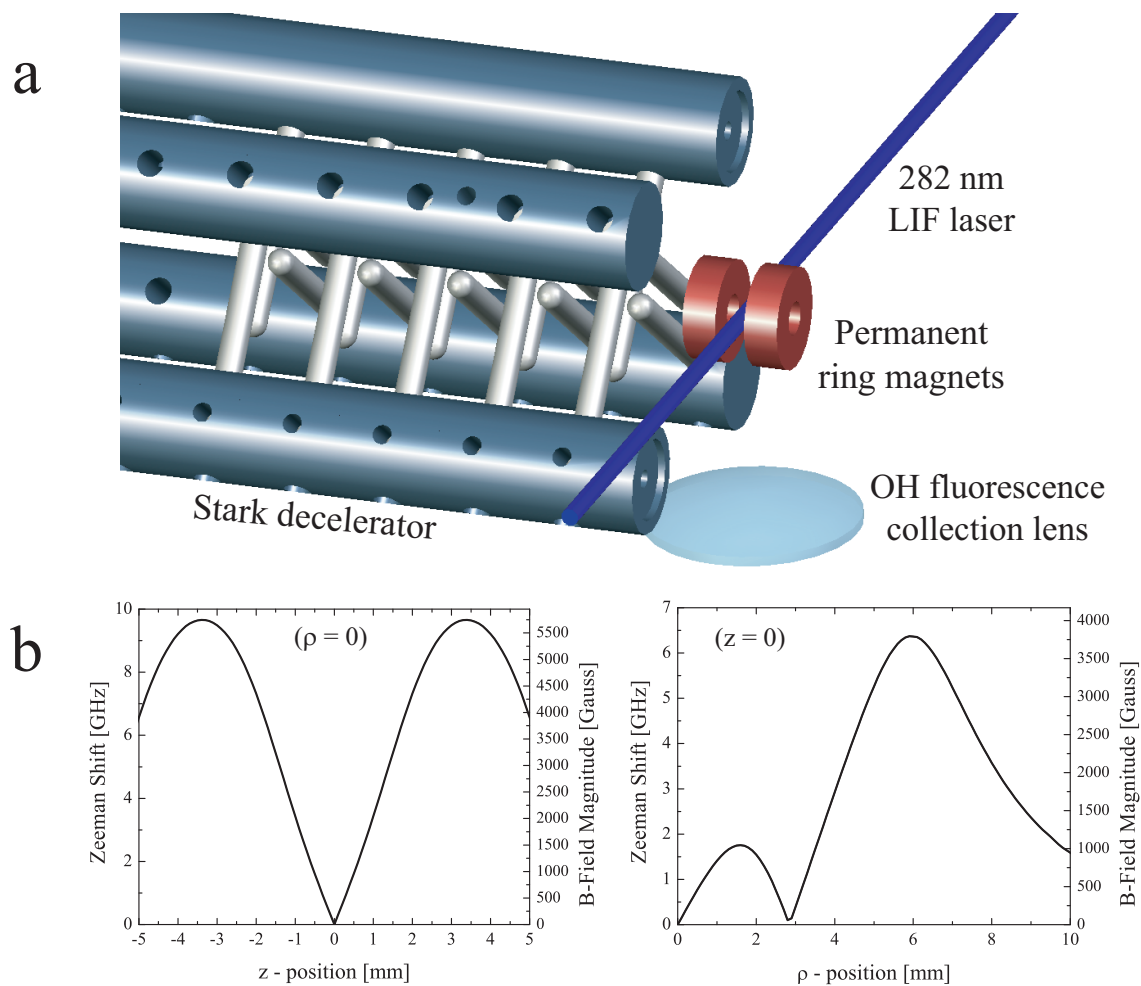
Figure 6.6: (a) Illustration of the permanent magnet trap and Stark decelerator. (b) Results of finite-element calculations of the magnetic field distribution within the permanent magnet trap. The small "lobe" observed in the ρ-dimension appears at the 2 mm inner radius of the magnet ring.

spacing of 7 mm in this magnetic trap yields a longitudinal magnetic (B) field gradient of 2 T/cm. This longitudinal separation matches the extent of the molecular packet entering the trap region from the Stark decelerator and therefore maximizes the trap density.

6.2.1 Loading the Permanent Magnet Trap

Figure 6.7 illustrates the trap loading sequence used with the magnetic trap of Fig. 6.6a. In Fig. 6.7a, the Ni coatings of the ring magnets are charged to ± 12 kV precisely 1 μs after the final deceleration stage is grounded. At this point, the magnets become high-voltage electrodes and serve as a final Stark-slowing stage for the 36 m/s molecules. In addition to the large stopping potential between the magnets, there exists a smaller potential between the final decelerator rod pair and the first trap magnet. This barrier reflects the small number of molecules with longitudinal velocity less than 25 m/s. However, the barrier's transverse E-field gradient serves to confine the slow molecules as they enter the trap region. The OH packet is brought to rest directly between the magnets in 400 μs, at which point the high voltage is switched off. Those hydroxyl radicals occupying the weak-magnetic-field-seeking $|3/2, 3/2, f\rangle$ state (50% of the stopped molecules) are then confined within a magnetic quadrupole trap measuring $k_B \times 480$ mK deep in the longitudinal dimension, where k_B is Boltzmann's constant. The trap potential is shown in Fig. 6.7b. We note that a permanent magnet was used to reflect a molecular beam [123], but here we present the first realization of a permanent magnetic trap for neutral molecules.

Typical time-of-flight data and corresponding three-dimensional Monte Carlo simulation results are displayed in Fig. 6.8a. Decelerated and trapped molecules are detected via laser-induced fluorescence (LIF). Lenses mounted in-vacuum allow for a fluorescence collection solid angle of ~ 0.1 sr. In Fig. 6.8(a), the large peak at 400 μs is the stopped OH packet imaged at trap center. Transverse oscillation of the trapped packet is observed in both data and simulation over 2 ms. The number and density of trapped OH are measured to be $>10^3$ and $\sim 10^6$ cm^{-3}, respectively. A temperature of 70 mK is estimated from Monte Carlo simulation, also consistent with the molecular packet delivered by the Stark decelerator. Due to the large quadrupole B-field present in the
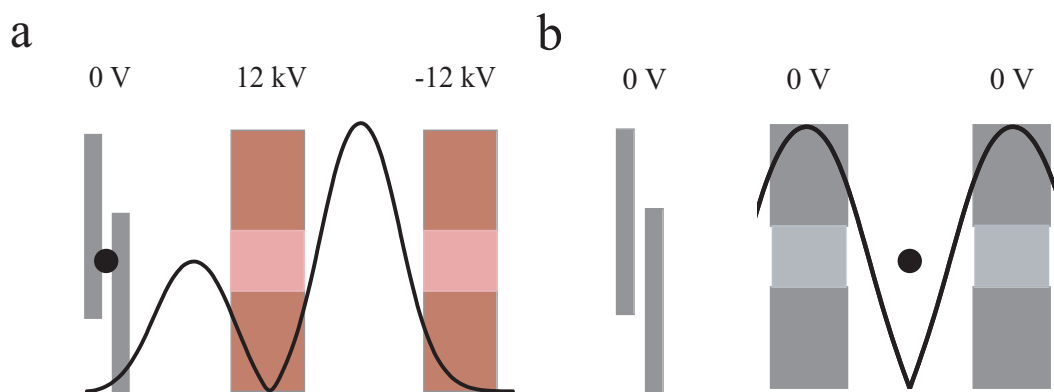
Figure 6.7: Illustration of the trap loading sequence. (a) High voltage is applied to the surfaces of the two permanent ring magnets 1 μs after the final deceleration stage (shown at left) is grounded. The OH packet is stopped directly between the two magnets by the electric field gradient in 400 μs. The stopping potential due to the applied electric field is depicted. (b) The magnet surfaces are grounded, leaving the packet trapped within the displayed permanent magnetic quadrupole potential.
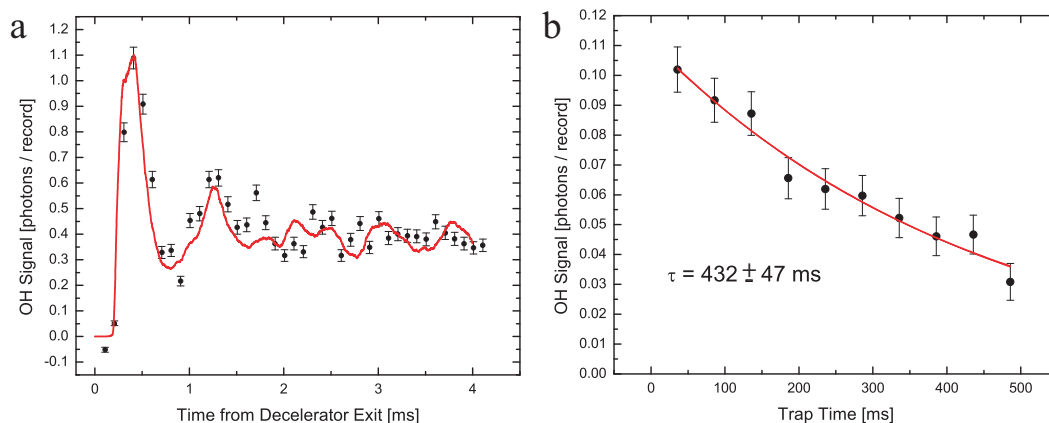
Figure 6.8: (a) Time-of-flight data (circles with error bars) and three-dimensional Monte Carlo simulations (solid line) corresponding to OH trap loading. Stopping E-fields are switched off at 400 μs, which leaves 50% of the stopped OH molecules trapped in the permanent magnetic quadrupole. (b) Measurement of the lifetime of OH trapped within the magnetic trap at a background pressure of 7.5×10^{-9} Torr. A single-exponential fit (solid line) of the data yields 432 ± 47 ms.

trap, only a fraction of the OH sample is detected as the longitudinal 5 GHz Zeeman shift near each magnet is larger than our LIF laser linewidth. This effect is included in the trap density estimates. Figure 6.8b displays the observed trap lifetime of 432 ± 47 ms, limited by collisions with background gas. The trap chamber pressure of 7.5×10^{-9} Torr consists of equal parts H_2O and Kr. Having improved on our original MET trap densities by three orders of magnitude, we can now use this trap for low-temperature [40] and cold [18] collision studies between external atomic and molecular beams. Also, we note that this trapping technique was recently adopted for dissipative multiple-loading of Stark decelerated NH [124, 125].

6.2.2   Current Conditioning of Magnetic Electrodes

As with the Stark decelerator electrodes, we must prepare the permanent ring magnets for pulsed application of large electric fields by current conditioning. We find that no additional material coatings beyond the outer Ni layer are necessary or desirable. In fact, even electro-polishing the magnets results in larger discharge currents than are obtained by simply picking the smoothest samples from a large batch. Here, the most likely culprit is unintended surface scratches throughout the electro-polishing process and subsequent cleaning. We have attempted coating the magnets with additional layers of Cu with the hope of obtaining a smoother surface, but it is likely that the lower work function of Cu led to enhanced discharging. The conditioning process consists of slowly raising the voltage on the magnets to ± 15 kV while monitoring the current draw through 100 MΩ limiting resistors. After this initial current conditioning, we remove the limiting resistors and slowing raise the voltage while switching the magnets with a ~ 500 μs pulse. We find that if the magnets are left for days without being switched, they must be reconditioned for reliable operation[*] . Therefore, we often reduce the magnet voltages to $\sim \pm 9$ kV for switching overnight.

---

[*] This is likely due to a long-term accumulation of paramagnetic contaminants onto the magnet surfaces from the vacuum chamber. Pulsing high voltage over time may serve to keep the surfaces clean through micro-discharge events.

Chapter 7

Collision Studies with Trapped OH Molecules

Research in the field of cold polar molecules is progressing rapidly. Magneto-association work utilizing laser-cooled alkali atoms has yielded $\sim$100 nK samples of KRb molecules in their vibrational ground state [79]. A number of other groups have produced vibrationally- or electronically-excited molecules via Feschbach and photoassociation techniques [95]. These systems are promising for the development of polar-molecule quantum computers [126] and for investigation of the anisotropic dipole-dipole interaction at ultracold temperatures [39, 127, 128]. In addition, cryogenic buffer gas cooling methods relying on thermalization of polar molecules with cold He have allowed for magnetic trapping of NH [118] and CaH [117] at temperatures of $\sim$ 1 K. Stark deceleration of supersonic molecular beams readily produces state-selected, $\sim$ 100 mK samples at densities of 10^6–10^8 cm^{-3}. As this technique allows complete control over a beam's center-of-mass velocity, Stark decelerated molecules have been used in crossed-beam collisions with atomic species [111] and precision spectroscopy experiments [129, 21, 24]. Spontaneous decay of long-lived vibrational excited states has also been directly observed in trapped OH [31] and NH [130] molecules. In this chapter, we describe our recent work extending experiments with trapped, cold molecules to include molecule-molecule collisions with magnetically-confined OH. As will be discussed, collisions between external beams and trapped molecules display unique dynamics that complement free-space inelastic collision experiments. Such beam-trap collisions display sensitivity to integral elastic, integral inelastic, and even differential elastic cross sections.

7.1   He-OH, D$_2$-OH Collisions

7.1.1   Motivation

Collisions between hydrogen (H, H$_2$) and larger polar molecules (OH, H$_2$O, CO, H$_2$CO, SiO) are of astrophysical interest due to their possible role as pumps for interstellar masers [131]. In particular, specific emission lines of interstellar OH (1720 MHz) and H$_2$CO (4.8 GHz) masers have been attributed to collision-induced inversion by H$_2$ [132, 133]. In the following discussion, we present collision cross sections for D$_2$–OH and He–OH collisions within a permanent magnet trap confining Stark-decelerated OH molecules. By directly comparing D$_2$–OH cross sections with those of the more theoretically tractable He–OH, we will aid molecular collision theory at energy scales below 100 cm^{-1}.

7.1.2   Experiment

The open structure of our permanent magnet trap allows for low center-of-mass energy (E$_{cm}$) collision studies between the trapped OH and external molecular or atomic beams. As large electric fields are used only for initial trap loading, there is no risk of voltage breakdown when pulsing such beams through the trap. Furthermore, though all He–OH and D$_2$–OH collisions reported herein were observed with the magnets grounded, a relatively small polarizing electric (E) field (few kV/cm) can be applied to the magnets after trap loading without loss of confined molecules— thereby enabling our more recent investigation of dipolar collisions between OH and ND$_3$ [18].

Operation of our Stark decelerator and permanent magnet trap are described in Chapters 5 and 6, respectively. For this external beam collision experiment, we decelerate and magnetically trap a 70 mK portion of an OH supersonic beam initially seeded in a Kr carrier gas. After baking the trap chamber to remove H$_2$O vapor, the OH trap lifetime of $\sim$ 500 ms is limited primarily by residual Kr gas from the supersonic expansion. However, when running the external He or D$_2$ beam, this lifetime drops by an order of magnitude due to the low pumping speed of the turbomolecular pump with regard to light species.
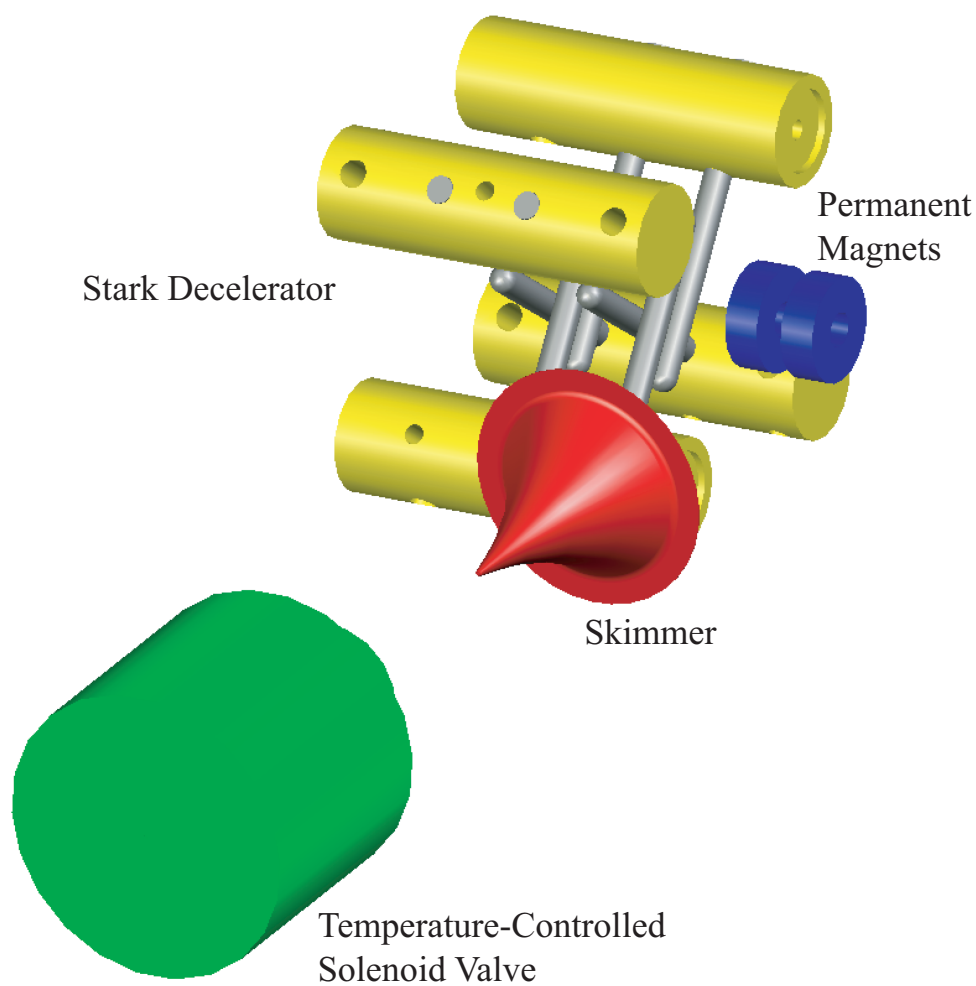
Figure 7.1: Illustration of the low-temperature He–OH, D_2–OH collision apparatus consisting of a Stark decelerator and permanent magnetic trap for OH (background) as well as a temperature-controlled pulsed solenoid valve and skimmer assembly for He and D_2 beams (foreground). Collisions between the external He or D_2 beams and trapped OH result in measurable OH trap loss.

To study collisions between trapped OH and He/D_2 beams, we place a pulsed solenoid valve (General Valve Series 99) and 1 mm diameter skimmer assembly, as shown in Fig. 7.1, such that the skimmed atomic or molecular beam passes directly between the trap magnets. The solenoid valve rests in a bath of liquid nitrogen while its 1 mm output nozzle is heated via 25 turns of manganin wire to allow for tuning of the beam velocity. The measured velocities of the He and D_2 beams as a function of output nozzle temperature are displayed in Fig. 7.2a. The velocities are determined using a combination of a miniature microphone-based pressure sensor and fast ionization gauge (FIG) placed 13 cm apart in the trap chamber. As expected, we observe that the beam velocities scale as the square-root of the nozzle temperature. This is verified by fitting the velocity distributions of Fig. 7.2a. The E_{cm} of the He–OH and D_2–OH systems can therefore be tuned to minima of $\sim$60 cm^{-1} and $\sim$145 cm^{-1}, respectively. The relatively low velocity of the He beam is most likely a result of the low stagnation pressure used (2.0 bar) along with the extended exit orifice of > 1 cm that could lead to a more isothermal as opposed to isentropic beam expansion. Our observation of enhanced He beam velocities at higher stagnation pressures supports this assertion. The stagnation pressure for the D_2 beam is 2.7 bar. To calibrate the relative densities of the colliding beams, we again use the FIG and obtain the temperature-dependent density curves of Fig. 7.2b. The uncertainty in the inter-species calibration of the ionization gauge is $\sim$10%. The measured 8% velocity spread of the supersonic He beam gives a collision energy resolution of 9 cm^{-1} at the lowest nozzle temperature.

Figure 7.3a displays the time dependence of OH trap loss as a supersonic beam of He traverses the magnetic trap. Trap density drops sharply over the first $\sim$1 ms after the solenoid valve is fired, then remains constant over the time scale shown. Although the partial pressure of the scattering gas in the trap chamber rises as the supersonic beam scatters from the chamber walls, we measure an OH trap lifetime of $>$50 ms following the initial collision. Such vastly different time scales allow us to differentiate between trap loss due to the supersonic beam and that resulting from background gas collisions. Trap loss at a given nozzle temperature is measured by repeatedly comparing OH population 1 ms *before* and 2 ms *after* the solenoid valve is triggered. The total cross sections
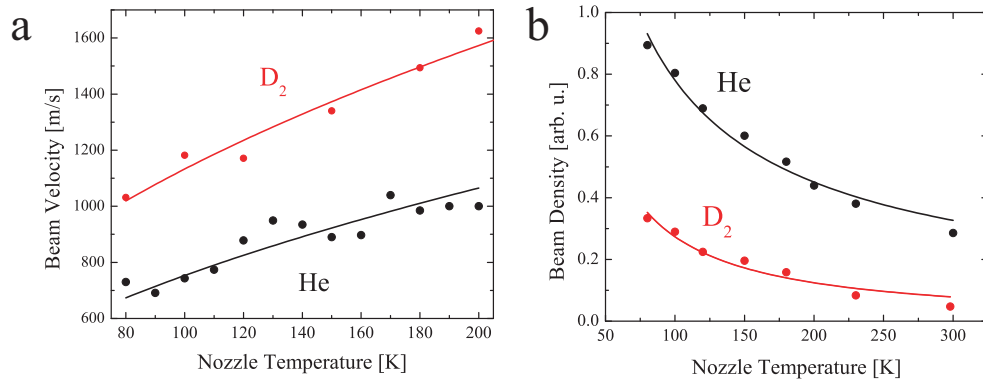
Figure 7.2: (a) Measurement of He and D_2 beam velocities as a function of valve nozzle temperature. The beam speeds were measured with a miniature microphone and fast ionization gauge placed 13 cm apart within the magnetic trap chamber. The solid lines are fits to the data indicating that, as expected, the measured beam velocity is proportional to the square root of nozzle temperature. (b) Calibration of He and D_2 beam density as a function of valve nozzle temperature. The relative density between He and D_2 is obtained by taking into account the different sensitivity of the fast ionization gauge to these two species.

of Fig. 7.3b are determined from the trap loss data by normalization to the corresponding beam flux of Fig. 7.2b measured with the fast ionization gauge at a given nozzle temperature. We also find that the trap loss scales linearly with the beam flux, confirming that we are operating in the single-collision regime.

An important advantage inherent to using trapped molecules as the scattering target is the ability to directly measure the absolute collision cross section. To do this, we use a leak valve to fill the trap chamber with a known pressure of He gas, then directly measure the OH trap lifetime at that pressure. The temperature of the chamber walls is 298 K, placing the E_{cm} of the thermal He–OH collisions at $\sim$250 cm^{-1}. The data point for He–OH collisions at 230 cm^{-1} from Fig. 7.3b is then scaled to this absolute cross section measuring 127 ± 18 Å^2.

For OH molecules in their ground electronic and vibrational state, the energy splitting of the two lowest lying rotational levels, $J = 3/2$ and $J = 5/2$, is 84 cm^{-1}. In a crossed-beam experiment, an abrupt decrease in the Xe–OH inelastic cross section was observed as E_{cm} was tuned below this value [111]. The He data of Fig. 7.3b possesses this feature. Because the magnetic trapping potential is sensitive to the internal state of the OH molecule, we cannot differentiate between trap

loss due to elastic or inelastic collisions. Nevertheless, such a sudden decrease of the total cross section below 84 cm^{-1} is indicative of threshold behavior. The collision cross section of D$_2$–OH is larger than that of He–OH. This is understandable since the D$_2$ beam is an ortho/para mixture and contains a large fraction of frozen-in $J = 1$ population. The ratio of the two cross sections at 230 cm^{-1} is consistent with previous H$_2$–OH and He–OH pressure-broadening measurements made at a temperature of 298 K [134]. The enhanced collision cross sections for D$_2$–OH result from the quadrupole moment of the D$_2$ $J = 1$ state that can interact strongly at long range with the OH dipole. Yet another striking feature of the collision data is the pronounced peak in the D$_2$–OH cross section for E$_{cm} \sim 305$ cm^{-1}. Although more theoretical consideration is warranted, the 300 cm^{-1} $J = 3 \leftarrow J = 1$ transition of the $^1\Sigma_g^+$ D$_2$ molecule may be contributing to the inelastic cross section at this energy. Another possible explanation is collision-induced decay of $J = 2$ molecules present in an imperfect D$_2$ supersonic expansion.

To summarize, we demonstrate a new permanent magnetic trap design that confines a dense sample of cold OH molecules as a cold collision target. Collision experiments consisting of velocity-tunable supersonic beams of He and D$_2$ intersecting the magnetically-trapped cold OH molecules yield absolute collision cross sections over an energy range of 60 cm^{-1} to 230 cm^{-1} and 145 cm^{-1} to 510 cm^{-1}, respectively. Threshold behavior is observed in He–OH collisions, and an enhancement of inelastic cross sections is seen in the D$_2$–OH system near 305 cm^{-1}. Having demonstrated the usefulness of this permanent magnetic trap for collision studies, future goals include using colder continuous beams of polar molecules as the colliding partner for OH. With the ability to apply a sufficiently strong polarizing field within the magnetic trap [135], we aim to reach sufficiently low E$_{cm}$ to observe dipole-dipole interactions.

7.1.3 Recent Developments

Kirste and co-workers have recently reported relative state-to-state inelastic cross sections between Stark decelerated OH and supersonic beams of He and D$_2$ [136]. With respect to D$_2$–OH collisions, they do not observe enhancement of the OH state-to-state inelastic cross section near
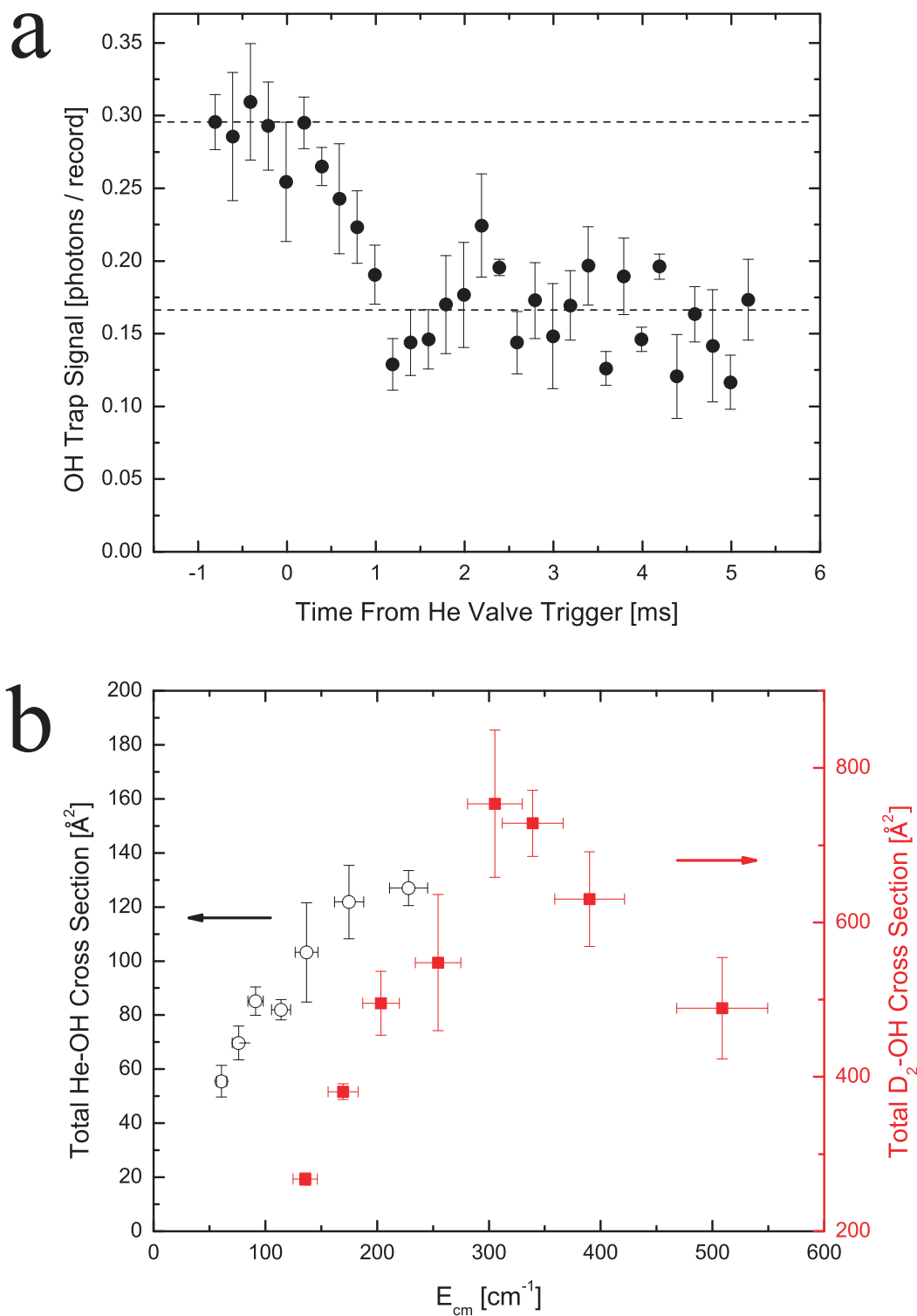
Figure 7.3: (a) Time dependence of OH trap loss due to collisions with a supersonic He beam. Trap density drops sharply over 1 ms upon He beam collisions, then remains constant over the time scale shown. The valve is triggered 20 ms after the magnetic trap is loaded. (b) Total collision cross sections for He–OH (open circles) and D_2–OH (squares) as a function of E_{cm}. The decrease in the He–OH cross section at low energy is attributed to reduced inelastic loss as E_{cm} drops below the 84 cm^{-1} splitting between the $J = 3/2$ and $J = 5/2$ states of the OH molecule.

the collision energy of 305 cm^{-1}. The primary difference between our experiment and that of Kirste et al is that our collision experiment involves trapped OH molecules, while their collisions take place in free space. In this way, we are sensitive to elastic as well as inelastic loss from the trap, while the results of Ref. [136] are not sensitive to elastic collisions at all. One possible explanation for both experimental results is that the inelastic collision near 300 cm^{-1} preferentially excites the D$_2$ molecule along the $J = 3 \leftarrow J = 1$ rotational transition, leaving the OH state unchanged. Such a collision will certainly cause OH trap loss in our system due to momentum exchange from the D$_2$ molecule. Since no rigorous quantum scattering calculations for D$_2$–OH have been performed to date, we cannot make concrete predictions as to the relative propensities for rotational transitions. However, future experiments sensitive to the internal state of the colliding D$_2$ molecule will invariably answer these intriguing questions.

7.2 Cold Dipolar Collisions between OH and ND$_3$

7.2.1 Motivation

For half a century, scattering of crossed atomic or molecular beams under single-collision conditions has remained the primary technique for investigation of inelastic and reactive dynamics at collision energies above $\sim$1 kcal/mol ($\sim$500 K) [137]. Experiments using electric field-aligned neutral polar molecules can probe the steric asymmetry of atom-molecule [138, 139, 140] and bi-molecular [141, 142] potential energy surfaces (PESs), but their large center-of-mass collision energies have precluded the observation of electric field modification of these potentials. However, in the cold collision regime where only tens of scattering partial waves contribute, one can move beyond molecular orientation and directly modify intermolecular dynamics via the long-range dipole interaction. The relatively low number densities (10^6-10^8 cm^{-3}) of cold molecule production techniques have thus far limited gas-phase collision experiments between state-selected distinct polar species to >300 K. We combine for the first time the methods of Stark deceleration, magnetic trapping, and buffer gas cooling to enhance molecular interaction time by $\sim$10^5 and overcome this
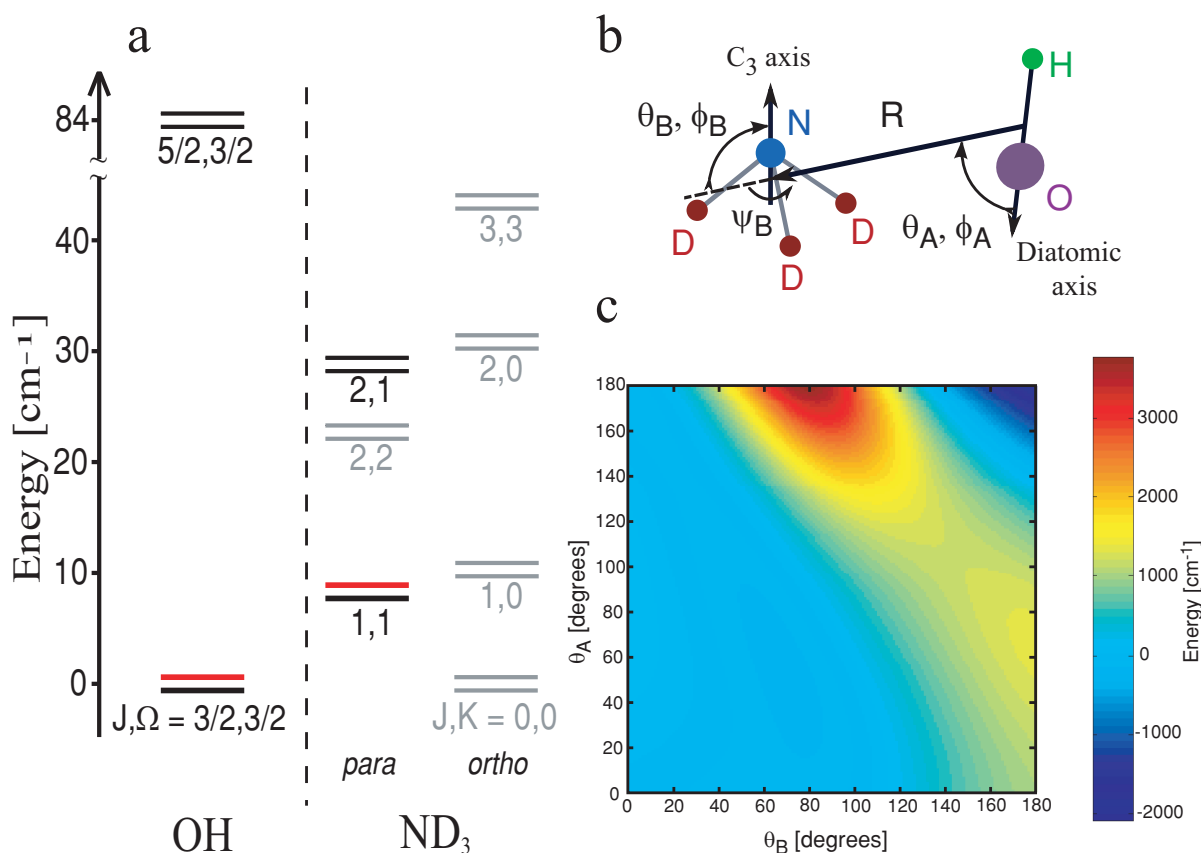
Figure 7.4: (a) Rotational structure of OH and ND_3 molecules. The parity-doublet splitting of each rotational level has been expanded for clarity, while the black and red parity levels are the ones included in the OH-ND_3 scattering calculation. The upper, red, parity states are those selected by the experimental apparatus for the cold collisions described herein. The Stark and Zeeman shifts of ground state OH and ND_3 are presented in Chapter 2. (b) Illustration of the Jacobi coordinates used for OH-ND_3 collision calculations. We define R as the distance between the molecular centers of mass while the Euler angles (θ_A, ϕ_A) and (θ_B, ϕ_B) give the orientation of the OH and ND_3 axes, respectively, in the body-fixed frame relative to R. The coordinate ψ_B specifies the orientation of the ND_3 monomer within the OH-ND_3 complex. The geometry $\phi_A = \phi_B = \theta_A = \theta_B = 0$ corresponds to the OH axis lying in the σ_v symmetry plane of ND_3 with the O atom facing the plane of D atoms. (c) Contour plot of the lowest adiabatic potential energy surface for the A'' state of the OH-ND_3 collision complex at $R = 3.1$ Å and $\phi_A = \phi_B = 0$ as a function of θ_A and θ_B. The color legend is scaled in units of cm^{-1}.

density limitation. Here we present the first observation of cold (5 K) heteromolecular dipolar collisions and describe the first theoretical study of scattering in the many partial-wave regime with chemically-relevant OH and ND_3 molecules.

The last decade has seen tremendous progress in the production of cold and ultracold polar molecules [12]. Application of these production techniques to the study of novel atom-molecule and molecule-molecule scattering has led gas-phase collision physics to new low temperature regimes. Specifically, crossed beam experiments using rare gas atoms and Stark decelerated OH ($^2\Pi$) molecules have allowed for the study of inelastic scattering at translational energies comparable to that of OH rotation ($\sim$100 K) [111, 143, 136]. By measuring collisional loss of a magnetically trapped OH target with incident beams of He or D_2, we have determined total trap loss cross sections at similar energies [40, 144]. Buffer gas cooling has been employed in the study of elastic and inelastic collisions of He-NH ($^3\Sigma$) [73, 72] and He-TiO [145]. Cold reactive collisions have been observed using a velocity-filtered room-temperature beam of CH_3F colliding with trapped Ca^+ atomic ions [146]. In the ultracold regime [79], bimolecular chemical reactions between ground-state KRb molecules at temperatures of a few hundred nanoKelvin have been directly controlled via external electric fields [39, 17], opening the door for experimental probes of quantum many-body effects in a dipolar molecular gas [16].

To observe dipolar collisions between state-selected OH and ND_3, we constructed a novel cold collision apparatus combining Stark decelerated and magnetically trapped OH with a continuous buffer gas cooled beam of ND_3, allowing interaction times of $\sim$1 s. In contrast to traditional scattering experiments, our measurement is sensitive to both inelastic and *elastic* collisions. Furthermore, fewer than 100 partial waves contribute to the 5 K collision — placing the OH-ND_3 interaction in an intermediate regime between gas-kinetic and quantum scattering. Theoretical OH-ND_3 cross sections computed from *ab initio* potentials are in good agreement with the measured zero-field trap loss cross section. Given the generality of buffer gas cooling and electro/magnetostatic velocity filtering, our apparatus allows for a large class of electric field dependent cold molecular collision studies.
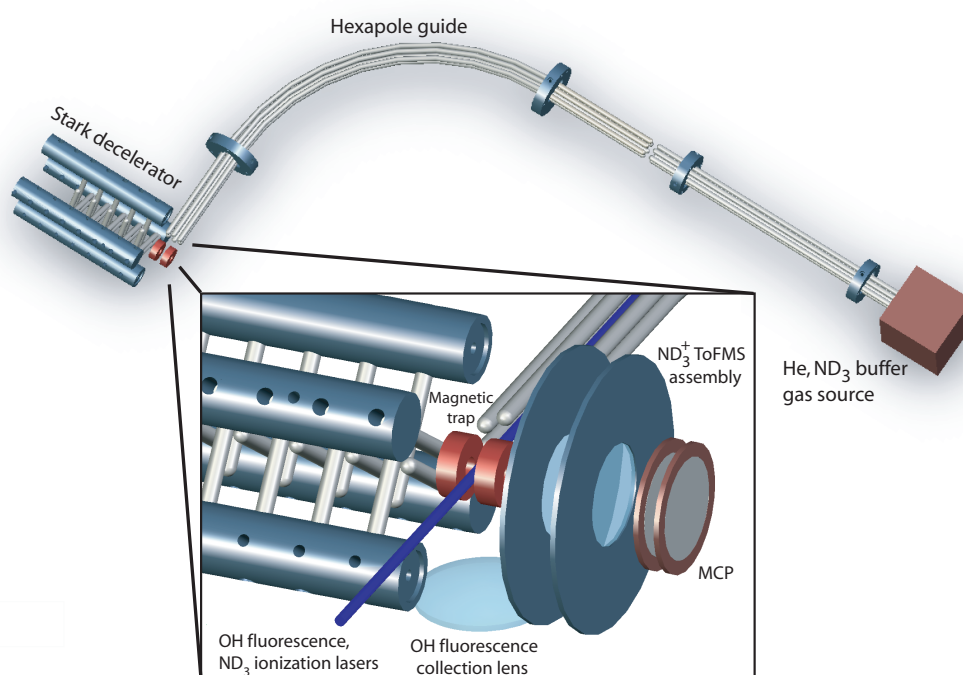
Figure 7.5: Illustration of the combined Stark decelerator, magnetic trap, and buffer gas beam assembly. The curved hexapole filters cold ND_3 from the He buffer gas and guides the continuous beam to the OH magnetic trap. (Inset) Closeup of the trap assembly showing the dual-species detection components. We detect OH and ND_3 in the collision region using laser-induced fluorescence (LIF) and resonance-enhanced multiphoton ionization (REMPI), respectively. Hydroxyl fluorescence at 313 nm is collected using a lens mounted 2.5 cm below the magnetic trap center. Ionized ND_3^+ molecules are accelerated to a microchannel plate (MCP) detector by placing 950 V on the front magnet, 0 V on the back magnet, and -1100 V on the acceleration plates that make up a time-of-flight mass spectrometer (ToFMS).

Two readily coolable species, hydroxyl and ammonia, are ubiquitous in atmospheric and astrophysical spectroscopy. Large interstellar clouds of OH and NH_3 (some co-located) have been detected in both absorption and maser emission along microwave parity-doublets [147]. In the troposphere, hydroxyl-ammonia reactions are the dominant mechanism for removal of NH_3 [148]. We choose to investigate electric field-dependent cold OH-ND_3 collisions due to the large static polarizability of both species and the near-degeneracy of the energy splittings of the OH Λ-doublet (0.056 cm^{-1}) and ND_3 inversion-doublet (0.053 cm^{-1}). The former allows for field orientation and precise control over the internal and external degrees of freedom of both molecules, while the latter has been shown to cause large enhancements in inelastic rates at room temperature [149]. Experimentally-relevant rotational and parity-doublet states of OH and ND_3 are illustrated in Fig. 7.4a.

7.2.2   Cold OH-ND_3 Collision Apparatus

The experimental setup consists of two distinct cold molecule apparatus as shown in Fig. 7.5: a Stark decelerator/magnetic trap assembly [64, 40] and a buffer-gas cooled continuous molecular beam source. A supersonic beam of OH molecules seeded in Kr is decelerated and trapped at a temperature of 70 mK and density of $\sim 10^6$ cm^{-3} as described in Ref. [40]. Only those OH molecules residing in the $^2\Pi_{3/2}$ $|F, M_F, p\rangle = |2, +2, f\rangle$ ground state are phase-stably Stark decelerated and magnetically trapped. Here F, M_F, and p denote the hyperfine quantum number, its projection on the external electric field axis, and the parity of the state, respectively. To detect trapped OH, the molecules are excited at the 282 nm $A^2\Sigma^+(v=1) \leftarrow X^2\Pi_{3/2}(v=0)$ transition. Fluorescence from the 313 nm $A^2\Sigma^+(v=1) \rightarrow X^2\Pi_{3/2}(v=1)$ decay is collected by a lens mounted to the magnetic trap assembly.

We employ buffer gas cooling and Stark velocity filtering to generate a continuous effusive beam of cold ND_3 molecules at a density of 10^8 cm^{-3} and mean velocity of 100 m/s. Our measured beam flux of 10^{11} s^{-1} is comparable to that of previous experiments [150, 83]. Cold ND_3 is generated in a copper cell filled with He buffer gas at 4.5 K. A 6 mm-diameter aperture is cut into the front
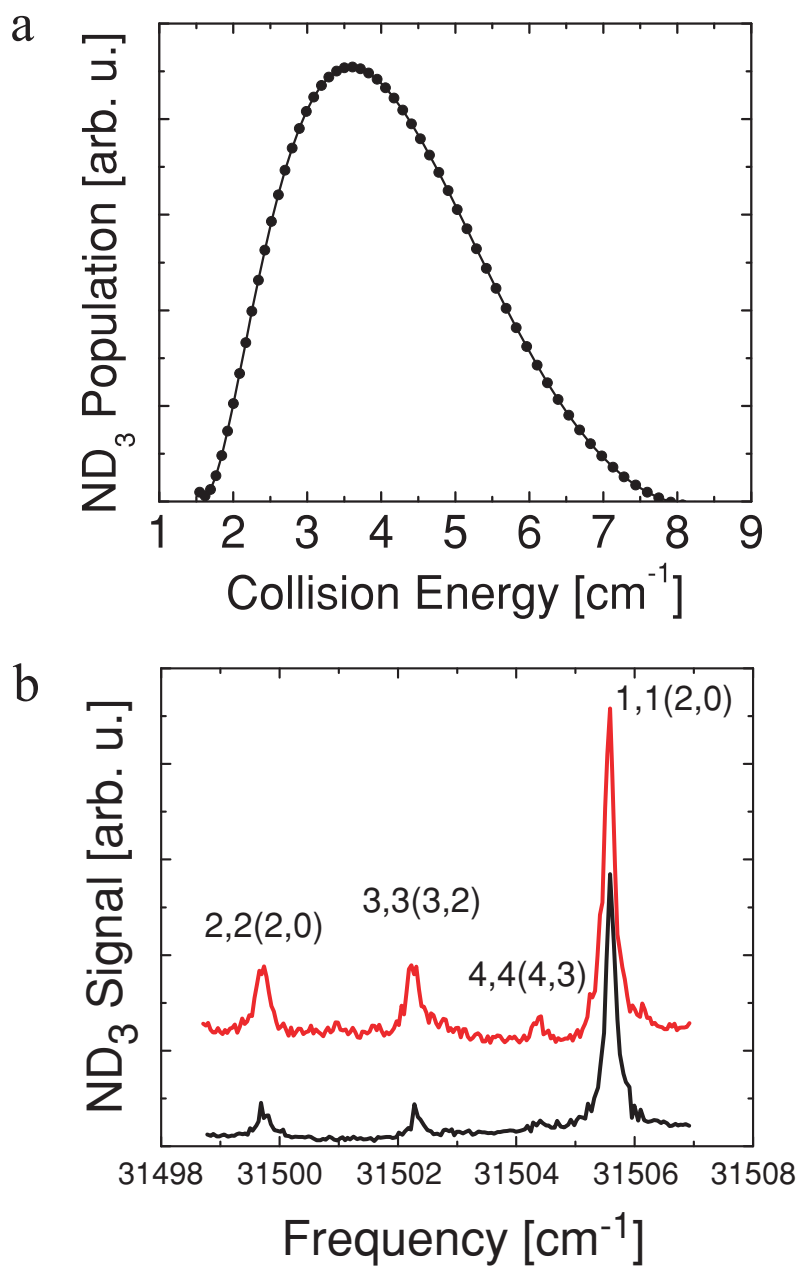
Figure 7.6: (a) Translational energy spectrum of the guided continuous ND_3 beam as measured by 2+1 REMPI in the collision region. (b) Rotationally-resolved REMPI spectrum of guided ND_3 molecules showing different J, K states. The upper red curve (offset for clarity) was taken at buffer gas flows of 2.0 and 2.5 sccm of He and ND_3, respectively. The lower black curve displays the smaller rotational temperature observed at 3.5 and 1.0 sccm. Intermediate rotational levels in the excited $\tilde{B}(v_2 = 5)$ electronic state are labeled in parentheses for each transition.

of the cell directly opposite the ND_3 inlet to allow the cold He/ND_3 mixture to escape. An electrostatic hexapole consisting of six 3 mm-diameter steel rods and possessing an inner diameter of 6 mm is mounted 2 mm from the cell aperture. This straight hexapole guide is 20 cm long and mounts to a 3 mm-thick gate valve which isolates the OH trap vacuum from the cryogenic vacuum. A curved hexapole is mounted just beyond the gate valve and follows a $90°$ bend at a radius of 13.5 cm. The hexapole guide terminates 1 cm from the permanent magnetic trap center. The curved hexapole filters cold ND_3 from the He buffer gas and sets an upper bound on the accepted forward velocity for weak-field seeking states ($\sim$150 m/s at ±5 kV for $|J, K\rangle = |1, 1\rangle$). The quantum numbers J and K denote the total molecular angular momentum and its projection on the ND_3 symmetry axis, respectively. Figure 7.6a displays the measured energy distribution of guided $|1, 1\rangle$ ND_3 molecules in the OH-ND_3 center-of-mass frame. To quantify the continuous beam velocity, the hexapole is switched so that guided ND_3 flux can be measured over different guiding durations. After including the guide path length, we differentiate a fit of the resulting curve to obtain the ND3 velocity distribution of Fig. 7.6a. Guided ND_3 is detected in the collision region using 2+1 resonance-enhanced multiphoton ionization (REMPI) [50] and subsequent ion detection. To accomplish this, ND_3 in the $|1, 1\rangle$ state is resonantly ionized between the trap magnets using a focused 317.4 nm, 10 ns laser pulse. To accelerate ions to a microchannel plate (MCP) detector (see Fig. 7.5), the trap magnets are charged to a potential difference of 950 V. After extraction from the trap, ions enter a 2 cm long field-free region and are subsequently detected by the MCP.

Our dual-detection scheme permits characterization of the state purity of both OH and ND_3. Due to the state selectivity of Stark deceleration and magnetic trapping, perfect OH rotational, Λ-doublet, and hyperfine state purity is achieved. Vibrationally excited ($v = 1$) OH are phase stably decelerated with $v = 0$ molecules, but <5% of OH are initially produced in the $v = 1$ state [75]. We also characterize the ND_3 rotational distribution within the collision region. The rotational structure of ND_3 is shown in Fig. 7.4a while Fig. 7.6b displays the measured rotational spectra of guided ND_3 molecules for two different buffer gas flows – 2.0 sccm He and 2.5 sccm ND_3 (upper curve) and 3.5 sccm He and 1.0 sccm ND_3 (lower curve). A standard cubic centimeter per

minute (sccm) is equivalent to 4.4×10^{17} s^{-1}. As the ratio of He to ND$_3$ flow is increased, the two-state ($|1,1\rangle$, $|2,2\rangle$) rotational temperature drops from 6.3 K to 5.4 K. With the larger He:ND$_3$ flow ratio, the relative guided populations of anti-symmetric (weak-field seeking) $|1,1\rangle$, $|2,2\rangle$, $|3,3\rangle$, and $|4,4\rangle$ states are 87%, 9%, 4%, and <1%, respectively. This ground state fraction is similar to that measured by depletion spectroscopy of a buffer gas cooled H$_2$CO beam [150]. States with $K = 0$ do not exhibit a first-order Stark shift and are not guided. Also, at this flow and guide voltage (± 5 kV), no population is observed in those states where $J \neq K$. Our choice of 3.5/1.0 sccm for the collision experiment is a compromise between maximizing $|1,1\rangle$ flux while minimizing rotational temperature.

To quantify total trap loss cross sections between OH and ND$_3$, it is necessary to measure both collision-induced OH trap loss and absolute colliding ND$_3$ density. Loss of trapped OH is measured as shown in Fig. 7.7a over a period of 160 ms. First, the background-gas limited trap decay rate (γ_{off}) is measured with the ND$_3$ flow off. This decay rate is determined by a single-exponential fit to the data. The value of γ_{off} is set by the presence of residual Kr in the trap chamber and is typically 2-3 s^{-1} at a pulsed-valve repetition rate of 5 Hz. The cold ND$_3$ beam is then turned on and the loss rate due to background gas plus cold ND$_3$ (γ_{on}) is measured. The collision-induced loss rate (γ_{coll}) is the difference of the two rates. This differential measurement makes γ_{coll} insensitive to day-to-day variations in background pressure, and yields a single-measurement fractional error of $\sim$30-40% in the available runtime of 1 hr. To investigate the effect of an external electric field on the cross section, we apply two distinct electric field configurations to the colliding molecules. We define the polarizing electric field for a given molecule as $E_{\text{pol}} = \Delta/2\mu$ where μ is the molecular permanent dipole moment and Δ is the parity-doublet splitting (E_{pol}=1.7 kV/cm for OH and 2.0 kV/cm for ND$_3$). For both field distributions, $E > 2$ kV/cm throughout the collision region, polarizing both colliding species. One E-field distribution is produced by charging the trap magnets themselves and lowers the OH radial trap depth by $\sim$20% due to the relative orientations of E- and B-fields within the collision region. The alternate field distribution is created by charging a stainless steel cup placed between the rear trap magnet and time-of-flight mass spectrometer. The resulting distinct
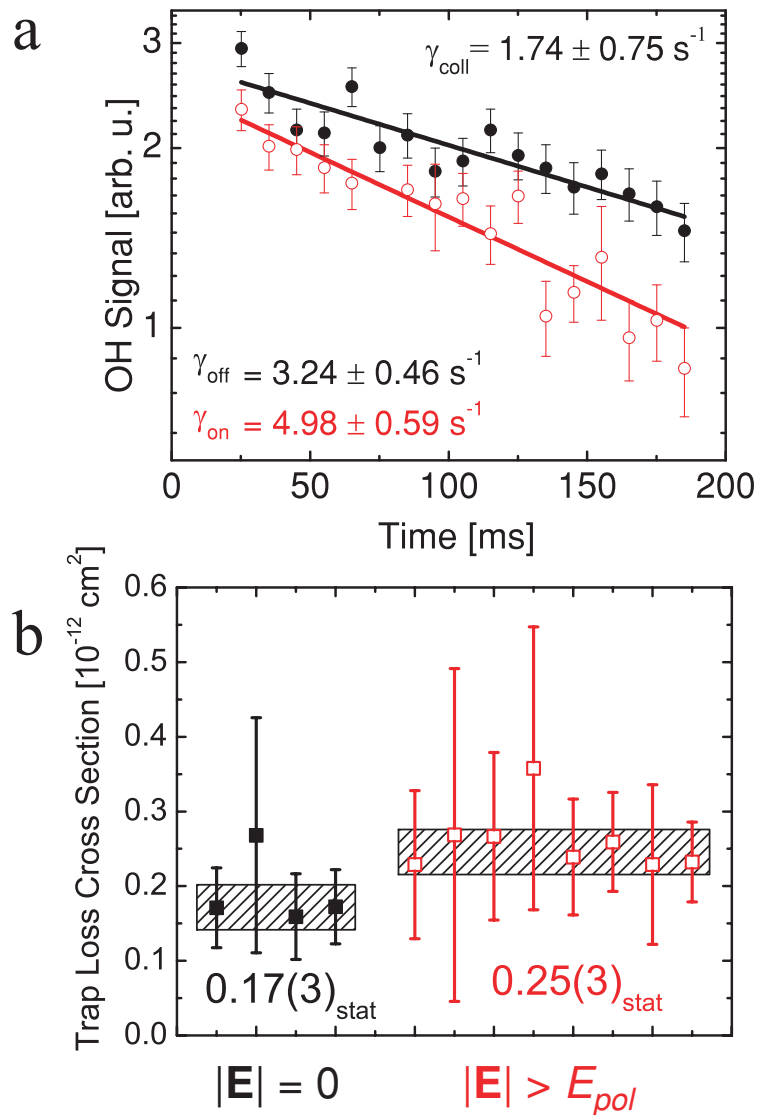
Figure 7.7: (a) Semi-logarithmic plot of OH trap decay rates with (○) and without (●) the colliding ND$_3$ beam. The decay rate due solely to cold OH-ND$_3$ collisions is $\gamma_{coll} = \gamma_{on} - \gamma_{off}$. (b) Plot of all experimental runs measuring total cross sections with (□) and without (■) a polarizing electric field. Average cross sections are determined from the weighted mean of all points and errors for the given E-field condition. The cross-hatched regions represent one statistical standard error. Individual error bars for each experimental run are obtained by propagating the standard deviation from exponential fits of γ_{on} and γ_{off} to γ_{coll}.

distribution between the grounded magnets increases the radial trap depth by ~40%. Polarization of OH and ND_3 under both field configurations is experimentally verified in the collision region through spectroscopic measurement of the population of cold ND_3 molecules in the strong-field seeking (unguided) $|1,1\rangle$ state. This population is measured as a direct result of inversion-state mixing under the polarizing electric fields and is not detected in the absence of either electric field configuration. We observe no difference in collisional loss between these two configurations, and thus the changes in trap loss arise directly from the enhanced dipolar interactions between OH-ND_3 under the applied E-field.

To determine the value of the loss cross section, $\sigma_{\mathrm{exp}}^{\mathrm{loss}}$, we use REMPI to calibrate the absolute density of the continuous ND_3 beam within the collision region for each measurement of γ_{coll}. Conversion of MCP output current to absolute molecule density is notoriously difficult due to unknown ionization volume/efficiency and uncertain MCP gain. To sidestep these issues, a leak valve and calibrated quadrupole mass spectrometer are used to admit a known pressure of 295 K ND_3 gas into the trap chamber. The measured ND_3 pressure is then scaled down by the Boltzmann fraction of molecules in the $|1,1\rangle$ anti-symmetric state at thermal equilibrium (4.7×10^{-3}), and an absolute ND_3 density is assigned to the observed MCP output current. Provided the cold beam is much larger than the ionization volume (true in our system), this calibration procedure is insensitive to the above problems. We also correct for overlap of REMPI transitions in the 295 K ND_3 spectrum as described in Chapter 4. The relatively small rotational energy splittings of ND_3 displayed in Fig. 7.4a lead to a congested spectrum at room temperature. Failure to account for overlap of transitions through the intermediate $\tilde{B}(v_2 = 5)$ state would lead to an underestimate of the cold beam density and concomitant overestimate of cross sections. Finally, a total trap loss cross section is determined for each experimental run as $\sigma_{\mathrm{exp}}^{\mathrm{loss}} = \gamma_{\mathrm{coll}}(n_0 v_{\mathrm{rel}})^{-1}$, where n_0 is the measured density of ND_3 and v_{rel} is the mean relative molecule velocity.

7.2.3   OH-ND$_3$ Collision Theory

A complete theoretical description of the OH-ND$_3$ collision at 5 K is complicated by the $^2\Pi$ symmetry of ground-state hydroxyl. Interactions including Π molecules are characterized by multiple electronic potentials, avoided crossings, and conical intersections. As such, scattering calculations based on *ab initio* potential energy surfaces have thus far been limited to Σ molecules [151, 152] or collisions between Π molecules and rare gas atoms or closed-shell diatomics with simple rotational structure [153, 154]. A full description of the theory results summarized here will be published elsewhere [155].

To describe the OH-ND$_3$ collision complex, we calculate the two lowest adiabatic PESs of A' and A'' symmetries using a spin-Restricted Coupled Cluster method with Single, Double, and non-iterative Triple excitations (RCCSD(T)) as implemented in MOLPRO [156]. An augmented correlation-consistent triple zeta basis (aug-cc-pVTZ) is used for both N and O atoms [157]. As illustrated in Fig. 7.4b, we define R as the distance between the molecular centers of mass while the Euler angles (θ_A, ϕ_A) and (θ_B, ϕ_B) give the orientation of the OH and ND$_3$ axes, respectively, in the body-fixed frame relative to R. A third angle, ψ_B, gives the orientation of the ND$_3$ monomer about its C_3 symmetry axis. Figure 7.4c shows the lowest adiabatic PES of A'' symmetry as a function of the orientation angles θ_A and θ_B for $R = 3.1$ Å and $\phi = 0$. Following the diagonal line defined by $\theta_A = \theta_B$, a barrier of ~ 1000 cm^{-1} is observed between head-to-tail ND$_3 \cdots$OH and D$_3$N$\cdots$HO configurations, demonstrating the large anisotropy of the OH-ND$_3$ interaction.

To elucidate the dynamics of cold OH-ND$_3$ collisions, we developed and implemented a rigorous quantum scattering approach based on the close-coupling (CC) expansion of the wave function of the collision complex using the total angular momentum representation in the body-fixed coordinate frame. The matrix elements of the Hamiltonian are evaluated analytically by expanding the angular dependence of the *ab initio* PES in spherical harmonics and retaining only the lowest-order terms, including the isotropic term $V_{000}(R)$ and the dipolar term $V_{112}(R)$. The model PES produced in this way correctly reproduces both the isotropic and long-range anisotropic parts of the

OH-ND$_3$ interaction, which are of crucial importance for cold collisions. Test calculations show that short-range anisotropic terms $V_{110}(R)$ and $V_{101}(R)$ have a minor influence on collision dynamics above 1 K.

The CC equations are solved numerically to produce converged S-matrix elements and scattering cross sections for collision energies between 0.5 and 8 cm^{-1}, which are convoluted with the beam distribution function shown in Fig. 7.6a to enable direct comparison with experimental data. The cross sections for trap loss are evaluated by integrating the differential cross section (DCS) over a restricted angular range $[\theta_{\min}, \pi]$. The cutoff angle $\theta_{\min}$ serves to subtract contributions from forward-scattered elastic collision products that do not have enough kinetic energy to leave the trap.

7.2.4   Experiment/Theory Results

The measured total trap loss cross sections are displayed in Fig. 7.7b. Each point represents a distinct cross section measurement and the average results for zero and non-zero electric field are determined as the weighted mean of each data set. The cross-hatched areas illustrate one statistical standard error centered at the weighted mean of each set. In addition to the statistical error, we estimate that the ND$_3$ leak pressure calibration, 295 K REMPI line-overlap correction, and our use of v$_{\text{rel}}$ = 100 m/s in obtaining $\sigma_{\exp}^{\text{loss}}$ add a common 50% systematic uncertainty to both absolute measurements. We attribute the largest contribution to systematic error to the line-overlap correction factor described in Chapter 4.

Figure 7.8a shows the calculated cross sections for elastic scattering and inelastic relaxation in OH-ND$_3$ collisions as functions of collision energy ($\mathcal{E}_C$). The cross sections are extremely large, exceeding typical gas-kinetic values by orders of magnitude. This dramatic enhancement is a direct manifestation of the dipolar interaction, which induces direct couplings between the opposite parity levels. Because of the long-range couplings, both elastic and inelastic cross sections are dominated by collisions occurring at large impact parameters. A partial-wave analysis of the cross sections at $\mathcal{E}_C = 5$ K reveals contributions from as many as 90 partial waves, and the dependences $\sigma_{\text{el}}(J_{tot})$ and
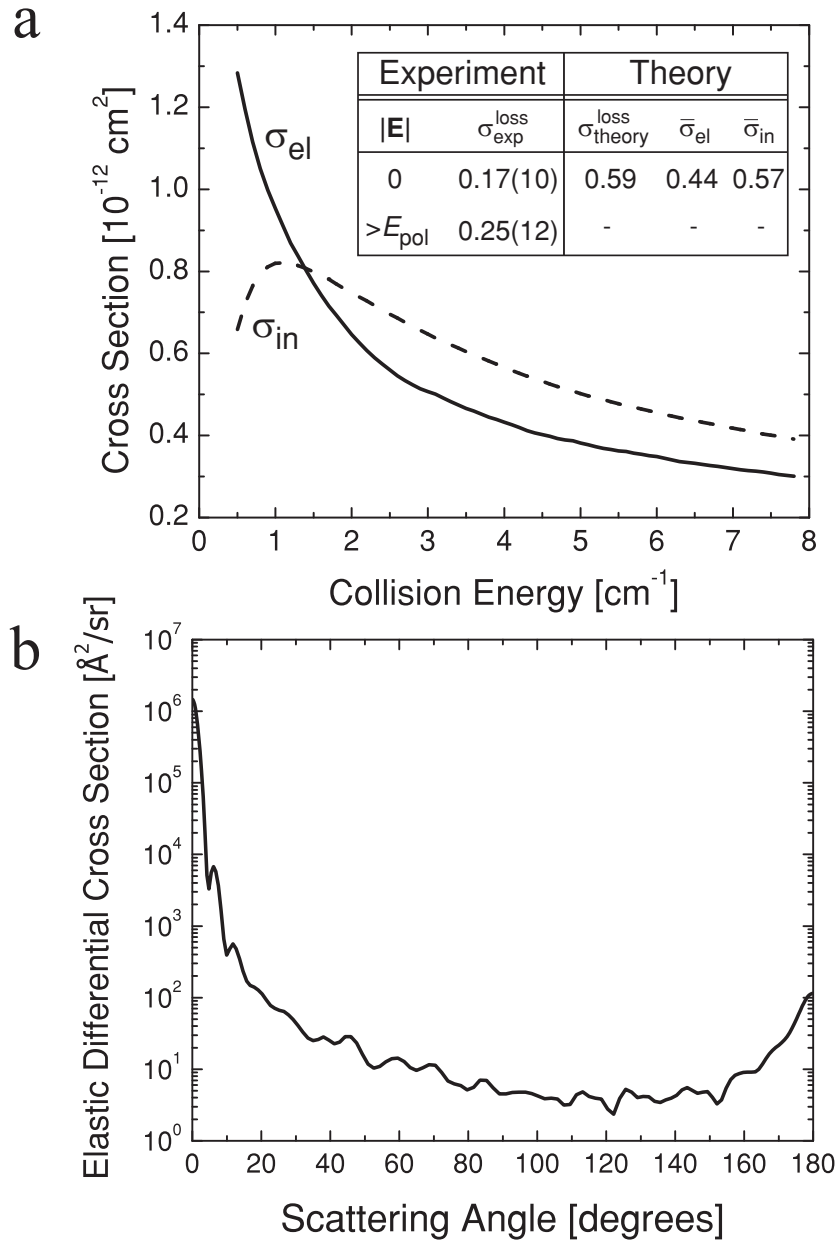
Figure 7.8: (a) Plot of theoretical OH-ND$_3$ elastic (σ_{el}) and inelastic (σ_{in}) cross sections over the experimental collision energy range. (Inset) Theoretical and experimental trap loss cross sections, with numbers in parentheses representing combined statistical and systematic errors. Experimental loss cross sections σ_{exp}^{loss} are shown for both unpolarized and polarized colliding molecules. The σ_{theory}^{loss} value includes the effect of reduced elastic loss from glancing collisions due to trap confinement. All cross sections are given in units of 10^{-12} cm^2. The quantities $\bar{\sigma}_{el}$ and $\bar{\sigma}_{in}$ are the theoretical elastic and inelastic cross sections, respectively, in the absence of trapping potentials and averaged over the experimental collision energy distribution of Fig. 7.6a. (b) Semi-logarithmic plot of the theoretical differential cross section for 5 K elastic OH-ND$_3$ collisions in units of Å^2/sr. This result is used to calculate σ_{theory}^{loss} from the free-space elastic and inelastic cross sections of panel (a). The forward-peaked nature of the elastic collision leads to a factor of 25 suppression of OH elastic loss at our finite radial magnetic trap depth of 240 mK.

$\sigma_{\mathrm{in}}(J_{tot})$ peak at $J_{tot} = 30.5$ and $J_{tot} = 50.5$, respectively, where J_{tot} is the total angular momentum of the collision complex. At $\mathcal{E}_C > 1$ K, the cross sections decrease monotonically with increasing $\mathcal{E}_C$, following the dependence $\sigma(\mathcal{E}_C) \propto \mathcal{E}_C^{-2/3}$. This result can be obtained analytically using the Langevin capture model [158] for a purely dipolar potential, demonstrating that the variation of the cross sections with collision energy is determined by the dipolar interaction.

A more detailed theoretical analysis in the absence of external fields shows that the inelastic cross section associated with both OH and ND_3 changing their parity-doublet state is 0.34×10^{-12} cm^2, more than 6 times larger than that for only one partner changing state. This propensity rule follows from the symmetry properties of the matrix elements of the dipolar interaction in the scattering basis. The inset table of Fig. 7.8a compares the measured and theoretical trap loss cross sections. The $\sigma_{\mathrm{theory}}^{\mathrm{loss}}$ number is calculated using the OH-ND_3 elastic differential cross section (DCS) of Fig. 7.8b and includes the recently-elucidated effect of trap confinement on measured collisional loss at low momentum transfer [40, 159, 144]. Since glancing elastic collisions can leave scattered OH trapped, the measured $\sigma_{\mathrm{exp}}^{\mathrm{loss}}$ must be compared with $\sigma_{\mathrm{theory}}^{\mathrm{loss}} = \bar{\sigma}_{\mathrm{el}}' + \bar{\sigma}_{\mathrm{in}}$, where $\bar{\sigma}_{\mathrm{in}}$ is the velocity-averaged inelastic cross section and $\bar{\sigma}_{\mathrm{el}}'$ is the velocity-averaged elastic loss cross section that includes the trap loss suppression effect ($\bar{\sigma}_{\mathrm{el}}'/\bar{\sigma}_{\mathrm{el}} = 0.04$). The forward-peaked structure of the OH-ND_3 DCS is responsible for this large reduction in elastic loss. Our measurement validates the large theoretical prediction of $\bar{\sigma}_{\mathrm{el}} + \bar{\sigma}_{\mathrm{in}} = 1.0 \times 10^{-12}$ cm^2 attributed to the OH-ND_3 dipolar interaction.

We observe enhancement of $\sigma_{\mathrm{exp}}^{\mathrm{loss}}$ by a factor of 1.4(3) when both molecules are polarized by an external E-field. This signals an increase of the total cross section ($\bar{\sigma}_{\mathrm{el}} + \bar{\sigma}_{\mathrm{in}}$) since experimentally we observe no dependence of loss on trap depth. More work is required to compute a field-dependent $\sigma_{\mathrm{theory}}^{\mathrm{loss}}$ from the *ab initio* PESs. However, we can estimate field-dependent elastic cross sections using the semiclassical Eikonal approximation as described in Section 7.3. The result of this calculation combined with the above values of $\bar{\sigma}_{\mathrm{in}}$ and $\bar{\sigma}_{\mathrm{el}}'/\bar{\sigma}_{\mathrm{el}}$ predicts a factor of 1.2 enhancement of the measured loss cross section when both molecules are polarized. This suggests that the elastic cross section plays a dominant role in the measured increase in trap loss.

7.3   Semiclassical Estimate of Elastic Cross Sections

7.3.1   Eikonal Approximation

When treating scattering problems in the limit where the collision energy is larger than the scattering potential, the semiclassical Eikonal approximation is valid [160]. This treatment assumes that the center-of-mass follows a straight-line path over the interaction length of the scattering potential, $V(R)$, where R is the distance between colliding partners. Within this framework, we may write the scattering amplitude $f(\theta)$ for scattering angle θ as

$$f(\theta) = -ik \int_0^\infty dbb J_0(kb\theta) \left[e^{2i\Delta(b)} - 1 \right] \tag{7.1}$$

where b is the impact parameter, k is the collision wavevector, and the phase term $\Delta(b)$ is defined as

$$\Delta(b) \equiv -\frac{M}{2k\hbar^2} \int_{-\infty}^{+\infty} V(\sqrt{b^2 + z^2})dz. \tag{7.2}$$

In the above definition, $M = M_1 M_2/(M_1 + M_2)$ is the reduced mass of the scattering partners with masses M_1, M_2. Knowledge of the scattering amplitude allows computation of the differential $(d\sigma/d\Omega)$ and integral (σ) elastic cross sections:

$$\frac{d\sigma}{d\Omega} = |f(\theta)|^2 \tag{7.3}$$

$$\sigma = \int \frac{d\sigma}{d\Omega} d\Omega = 2\pi \int_{\theta_{min}}^{\pi} \frac{d\sigma}{d\Omega} \sin\theta d\theta. \tag{7.4}$$

Note that we have included the term θ_{min} in the integration limits of Eq. 7.4. For collisions in free space where detection is sensitive to scattering over all θ, the minimum scattering angle is zero. However, if the detection of scattering products has a limited angular resolution or one is sensitive to collisional trap loss due to some minimum amount of momentum transfer [159, 144], then $0 < \theta_{min} < \pi$. For our collisional trap loss meaurements, we can precisely define the minimum scattering angle as [159]

$$\theta_{min} = \arccos\left(1 - \frac{M_T U_T}{M^2 \mathrm{v}^2} \right) \tag{7.5}$$

where M_T is the mass of the trapped species, U_T is the trap depth, and v is the relative velocity of the scatterers. Specializing to the parameters of our OH-ND$_3$ collision experiment, we obtain $\theta_{min} = 13°$.

7.3.2   Model OH-ND$_3$ Scattering Potentials

The intermolecular potential of the OH-ND$_3$ complex is rather anisotropic as evidenced by Fig. 7.4. However, to estimate the semiclassical scattering cross section for unpolarized molecules, it is useful to ascribe an isotropic and attractive Van der Waals potential of the form

$$V(R) = -\frac{C_6}{R^6} \tag{7.6}$$

where the magnitude of the C_6 coefficient can be estimated from the dynamic polarizability according to [161]

$$C_6 = \frac{3}{\pi} \int_0^\infty \alpha_{OH}(i\omega)\alpha_{ND3}(i\omega)d\omega. \tag{7.7}$$

The individual polarizabilities $\alpha(i\omega)$ can be computed from the energy level structure (E_j) and transition dipole moments of the given atom or molecule as

$$\alpha(i\omega) = \frac{2}{3}\sum_j \frac{(E_k - E_j)|\langle j|\mu|k\rangle|^2}{(E_k - E_j)^2 + \omega^2}. \tag{7.8}$$

Performing the sum over rotational and electronic states of OH and ND$_3$, we find that the dominant contribution to the C_6 coefficient originates from their near-degenerate parity-doublet splittings. Working in atomic units, we obtain $C_6 = 21,380$ a.u. with only a 0.01% contribution from states other than the ground Λ and inversion doublets.

When an external electric field is applied within the collision region to polarize both OH and ND$_3$, we assume the interaction potential takes an anisotropic dipolar form given by [4]

$$V(R) = \langle\mu_{OH}\rangle\langle\mu_{ND3}\rangle\frac{[1 - 3\cos^2\Theta]}{R^3} \tag{7.9}$$

where Θ is the angle between the molecules' symmetry axes and $\langle\mu_{OH}\rangle = 1.0$ D, $\langle\mu_{ND3}\rangle = 0.77$ D are the expectation values of the OH and ND$_3$ permanent electric dipoles, respectively.

7.3.3   Elastic Cross Section Estimates

The quickest way to obtain elastic collision cross sections for $\theta_{min} = 0$ is to apply the optical theorem to the scattering cross section $f(\theta)$. This gives the rather simple result [160]

$$\sigma = \frac{4\pi}{k}\mathrm{Im}f(\theta = 0) = 4\pi \int_0^\infty dbb[1 - \cos 2\Delta(b)]. \tag{7.10}$$

Inserting the Van der Waals potential yields the cross section (in atomic units)

$$\sigma_{C6} = 4\pi \left(\frac{3\pi MC_6}{8k}\right)^{\frac{2}{5}} \times \int_0^\infty dxx[1 - \cos\frac{1}{x^5}] \tag{7.11}$$

$$\simeq 4\pi \left(\frac{3\pi C_6}{8\mathrm{v}}\right)^{\frac{2}{5}} (0.602). \tag{7.12}$$

Bohn and co-workers use the Eikonal approximation with the dipolar potential of Eq. 7.9 to arrive at the following compact form for the dipolar elastic cross section [4]:

$$\sigma_{dip} = \frac{8\pi}{3}\frac{\langle\mu_{OH}\rangle\langle\mu_{ND3}\rangle}{\mathrm{v}}. \tag{7.13}$$

The relative velocity dependence of both the C_6 and dipolar cross sections are shown in Fig. 7.9. At the relative velocity of 100 m/s, the elastic cross section enhancement due to the dipolar interaction is ~ 6.

Integrating the unpolarized cross section over the experimental collision energy range of Fig. 7.6a, we obtain $\bar{\sigma}_{\mathrm{Eik}} = 0.50 \times 10^{-12}$ cm^2. The velocity-averaged dipolar cross section is $\bar{\sigma}_{\mathrm{Eik}}^{\mathrm{dip}} = 3.0 \times 10^{-12}$ cm^2. Including the values of $\bar{\sigma}_{\mathrm{in}} = 0.57 \times 10^{-12}$ cm^2 and $(\bar{\sigma}_{\mathrm{el}}'/\bar{\sigma}_{\mathrm{el}}) = 0.04$ obtained from the *ab initio* PESs, semiclassical theory predicts a factor of 1.2 enhancement in the measured loss cross section when both species are polarized — in agreement with the measured value of 1.4(3). It is possible that $\bar{\sigma}_{\mathrm{in}}$ will not change in the presence of the external E-field since the dipole potential contributes weakly at short-range.
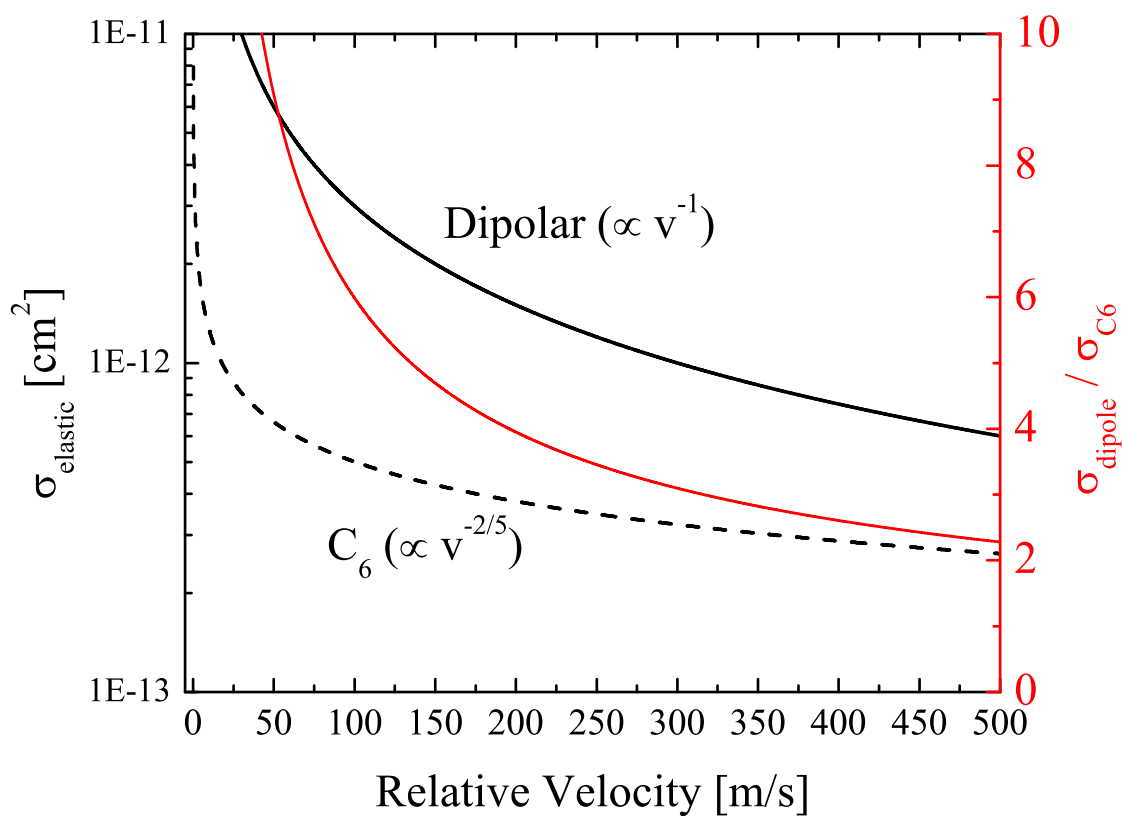
Figure 7.9: Plot of the Eikonal estimates for the elastic collision cross section between OH and ND$_3$ molecules. At the experimental relative velocity of 100 m/s, the electric field is expected to increase the elastic cross section by a factor of ~ 6.

7.4 Future Directions

7.4.1 Quantifying State-to-State Inelastic Cross Sections

The collision measurement described in Section 7.2 is a first step towards full experimental characterization of the OH-ND$_3$ elastic and inelastic cross sections within a variable electric field. We are most sensitive to the integrated total OH trap loss due to collisions with the external ND$_3$ beam. However, it may also be possible to directly detect product states from the inelastic collisions. It will be difficult to measure the inelastic collision products of ND$_3$ since they will not be trapped and, hence, will not accumulate over the > 100 ms measurement duration. Without the ability to accumulate these scattered molecules, this state-to-state measurement will be effectively identical to a traditional crossed-beam scattering experiment. In this case, we may estimate the number of detected ions from the collision products, $N_\downarrow$, residing in the lower-inversion state for a single laser shot as

$$N_\downarrow = n_T n_B \sigma_{\gamma \to \gamma'} V_{det} \mathrm{v}_{rel} \tau_{dwell} D_{eff} S_\downarrow \qquad (7.14)$$

where V_{det} is the laser detection volume, D_{eff} is the combined ionization/detection efficiency, $S_\downarrow$ is the transition strength of the relevant REMPI line, $\sigma_{\gamma \to \gamma'}$ is the inelastic state-to-state cross section, τ_{dwell} is the dwell time of the scattered ND$_3$ molecule within the detection volume, and n_T (n_B) is the target (beam) molecular number density. Comparing with the measured signal from the guided upper-inversion state, $N_\uparrow = n_B D_{eff} V_{det} S_\uparrow$, we have

$$N_\downarrow / N_\uparrow = n_T \mathrm{v}_{rel} \sigma_{\gamma \to \gamma'} \tau_{dwell} \frac{S_\downarrow}{S_\uparrow}. \qquad (7.15)$$

Inserting realistic parameters into Eq. 7.15, we expect $N_\downarrow / N_\uparrow \sim 10^{-8}$ for a state-to-state cross section of $\sim 10^{-13}$ cm^2. This would constitute a rather heroic measurement at our current OH and ND$_3$ densities.

One possible alternative to an impulsive measurement of ND$_3$ products is to look for accumulated inelastic products of OH. Certain angular momentum projections within the lower Λ-doublet of OH (e.g. $|J, \Omega, M_J, p\rangle = |3/2, 3/2, +3/2, e\rangle$) will remain within the magnetic trap if not given

sufficient kinetic energy to overcome the confining potential. Because of the symmetry of the excited $^2\Sigma^+$ state of OH used for LIF detection, these lower-Λ-doublet molecules are registered as loss when detecting along the Q-branch transitions. Nevertheless, fluorescence detection along the P_1 branch will permit direct measurement of these accumulated products. An experiment of this kind would be the first state-to-state inelastic scattering measurement using accumulated, trapped cold molecules.

7.4.2 Orientation-Dependent OH-ND$_3$ Collisions

As described in Section 7.2.4, zero-field *ab initio* theory predicts a strong propensity for both OH and ND$_3$ to flip their parity-doublet state in an inelastic collision. A state-to-state detection experiment like the one described in the previous section would help quantify this inelastic cross section. However, one can also envision changing the parity of the trapped OH sample ($f \rightarrow e$) before colliding with the guided ND$_3$ molecules. This would change the energetics and overall symmetry of the collision complex. In addition, under an applied electric field the OH and ND$_3$ dipoles would be anti-aligned with respect to the local electric field vector. To the degree that we are sensitive to collisions at different relative OH-ND$_3$ angles, this may yield different dipolar collision behavior from what is observed under the current conditions [18].

To accomplish the parity-state transfer of trapped OH molecules ($|3/2, 3/2, +3/2, f\rangle \rightarrow |3/2, 3/2, +3/2, e\rangle$), we will implement adiabatic rapid passage (ARP) using microwave fields coupled directly to the trap magnets. The ARP technique of sweeping the microwave frequency across the $e \rightarrow f$ transition will allow $> 90\%$ transfer efficiency of the trapped molecules despite the different Zeeman shifts at different positions within the permanent magnet trap [162]. Having previously performed direct microwave spectroscopy to determine the differential Landé g-factor of the OH Λ-doublet transition ($\Delta g = 1.265(7) \times 10^{-3}$) [24], we must sweep the microwave frequency $\sim \pm 20$ MHz relative to the Zeeman-shifted transition center frequency to achieve efficient population transfer* . Production of these trapped $|3/2, 3/2, +3/2, e\rangle$ molecules will also permit study of

---

* The Monte Carlo simulations for the in-trap OH microwave transfer were performed by Mark Yeo.

non-adiabatic transitions in combined electric and magnetic fields as described in Chapter 2.

Bibliography

[1] J. A. Coxon. Can. J. Phys., 58:933, 1980.

[2] NIST Chemistry WebBook http://webbook.nist.gov/chemistry.

[3] R. A. Smith, T. Ditmire, and J. W. G. Tisch. Rev. Sci. Instrum., 69:3798–3804, 1998.

[4] J. L. Bohn, M. Cavagnero, and C. Ticknor. New J. Phys., 11:055039, 2009.

[5] E. R. Hudson et al. Eur. Phys. J. D, 31:351, 2004.

[6] M. H. Anderson, J. R. Enshner, M. R. Matthews, C. E. Wieman, and E. A. Cornell. Science, 269:198–201, 1995.

[7] M. R. Andrews, M.-O. Mewes, N. J. van Druten, D. S. Durfee, and W. Ketterle. Science, 273:84–87, 1996.

[8] B. DeMarco and D. S. Jin. Science, 285:1703–1706, 1999.

[9] M. Greiner, O. Mandel, T. Esslinger, T. W. Hansch, and I. Bloch. Nature, 415:39–44, 2002.

[10] S. A. Diddams, J. C. Bergquist, S. R. Jefferts, and C. W. Oates. Science, 306:1318–1324, 2004.

[11] S. Inouye et al. Nature, 392:151–154, 1998.

[12] L. D. Carr, D. Demille, R. V. Krems, and J. Ye. New J. Phys., 11:055049, 2009.

[13] T. Lahaye, C. Menotti, L. Santos, M. Lewenstein, and T. Pfau. Rep. Prog. Phys., 72:126401, 2009.

[14] D. Demille. Phys. Rev. Lett., 88:067901, 2002.

[15] A. Andre et al. Nature Phys., 2:636–642, 2006.

[16] A. Micheli et al. Nature Phys., 2:341, 2006.

[17] K. K. Ni et al. Nature, 464:1324–1328, 2010.

[18] B. C. Sawyer et al. Nature Phys., 2010. in press.

[19] H.L. Bethlem, G. Berden, and G. Meijer. Phys. Rev. Lett., 83:1558, 1999.

[20] J. D. Weinstein et al. J. Chem. Phys., 109:2656–2661, 1998.

[21] E. R. Hudson, H. J. Lewandowski, B. C. Sawyer, and J. Ye. Phys. Rev. Lett., 96:143004, 2006.

[22] J. Darling. Phys. Rev. Lett., 91:011301, 2003.

[23] E. R. Hudson. Experiments on Cold Molecules Produced via Stark Deceleration. PhD thesis, University of Colorado, Boulder, Colorado, 2006.

[24] B. L. Lev, E. R. Meyer, E. R. Hudson, B. C. Sawyer, J. L. Bohn, and J. Ye. Phys. Rev. A, 74:061402(R), 2006.

[25] N. Kanekar, J. N. Chengalur, and T. Ghosh. ApJ, 716:L23, 2010.

[26] J. K. Webb, J. A. King, M. T. Murphy, V. V. Flambaum, R. F. Carswell, and M. B. Bainbridge, 2010. arXiv:1008.3907v1.

[27] M. G. Kozlov and L. N. Labzowsky. J. Phys. B: At. Mol. Opt. Phys., 28:1933–1961, 1995.

[28] D. Kawall, F. Bay, S. Bickman, Y. Jiang, and D. Demille. Phys. Rev. Lett., 92:133007, 2004.

[29] A. Vutha et al. J. Phys. B: At. Mol. Opt. Phys., 43:074007, 2010.

[30] M.R. Tarbutt, H.L. Bethlem, J.J. Hudson, V.L. Ryabov, V.A. Ryzhov, B.E. Sauer, G. Meijer, and E.A. Hinds. Phys. Rev. Lett., 92:173002, 2004.

[31] S. Y. T. van de Meerakker et al. Phys. Rev. Lett., 95:013003, 2005.

[32] J. J. Gilijamse et al. J. Chem. Phys., 127:221102, 2007.

[33] W. C. Campbell, G. C. Groenenboom, H.-I. Lu, E. Tsikata, and J. M. Doyle. Phys. Rev. Lett., 100:083003, 2008.

[34] B. K. Stuhl, B. C. Sawyer, D. Wang, and J. Ye. Phys. Rev. Lett., 101:243002, 208.

[35] M. Kozlov and D. Demille. Phys. Rev. Lett., 89:133001, 2002.

[36] M. R. Tarbutt, J. J. Hudson, B. E. Sauer, and E. A. Hinds. Faraday Discussions, 142:37, 2009.

[37] A. E. Leanhardt et al. arXiv:1008.2997v1.

[38] D. Demille, S. Sainis, J. Sage, T. Bergeman, S. Kotochigova, and E. Tiesinga. Phys. Rev. Lett., 100:043202, 2008.

[39] S. Ospelkaus et al. Science, 327:853–857, 2010.

[40] B. C. Sawyer, B. K. Stuhl, D. Wang, M. Yeo, and J. Ye. Phys. Rev. Lett., 101:203203, 2008.

[41] J. Brown and A. Carrington. Rotational Spectroscopy of Diatomic Molecules. Cambridge University Press, 2003.

[42] T. D. Varberg and K. M. Evenson. J. Mol. Spectrosc., 157:55, 1993.

[43] G. Herzberg. <u>Molecular Spectra and Molecular Structure</u>, volume 1. Krieger Publishing Company, 1966.

[44] C.H. Townes and A.L. Schawlow. <u>Microwave Spectroscopy</u>. Dover, New York, 1975.

[45] A. J. Grimley and B. D. Kay. <u>Chem. Phys. Lett.</u>, 98:359, 1983.

[46] M. N. R. Ashfold, R. N. Dixon, R. J. Strickland, and C. M. Western. <u>Chem. Phys. Lett.</u>, 138:201, 1987.

[47] G. C. Nieman and S. D. Colson. <u>J. Chem. Phys.</u>, 71:571, 1979.

[48] C. McRaven, J. Alnis, B. Furneaux, and N. Schafer-Ray. <u>J. Phys. Chem. A</u>, 107:7138, 2003.

[49] E. de Beer, M. P. Koopmans, c. A. de Lange, Y. Wang, and W. A. Chupka. <u>J. Chem. Phys.</u>, 94:7634, 1991.

[50] J. Bentley, B. J. Cotterell, A. Langham, and R. J. Stickland. <u>Chem. Phys. Lett.</u>, 332:85, 2000.

[51] G. Herzberg. <u>Molecular Spectra and Molecular Structure</u>, volume 3. D. Van Nostrand Company, Inc, 1950.

[52] R. N. Dixon, J. M. Bayley, and M. N. R. Ashfold. <u>Chem. Phys.</u>, 84:21, 1984.

[53] C. Ticknor and J. L. Bohn. <u>Phys. Rev. A</u>, 71:022709, 2005.

[54] M. N. R. Ashfold, R. N. Dixon, N. Little, R. J. Stickland, and C. M. Western. <u>J. Chem. Phys.</u>, 89:1754, 1988.

[55] B. C. Sawyer, B. L. Lev, E. R. Hudson, B. K. Stuhl, M. Lara, J. L. Bohn, and J. Ye. <u>Phys. Rev. Lett.</u>, 98:253002, 2007.

[56] M. Lara, B. L. Lev, and J. L. Bohn. <u>Phys. Rev. A</u>, 78:033433, 2008.

[57] J. R. Rubbmark, M. M. Kash, M. G. Littman, and D. Kleppner. <u>Phys. Rev. A</u>, 23:3107, 1981.

[58] G. Scoles, editor. <u>Atomic and Molecular Beam Methods</u>, volume 1. Oxford University Press, New York, 1988.

[59] G. Brusdeylins and H. D. Meyer. In R. Campargue, editor, <u>Rarefied gas dynamics, Proceedings of the 11th International Symposium</u>, volume 2, page 919, Commissiarat a l'Energie Atomique, Paris, France, 1979.

[60] B. D. Kay and A. J. Grimley. <u>Chem. Phys. Lett.</u>, 127:303–308, 1986.

[61] W. Christen, K. Rademann, and U. Even. <u>J. Chem. Phys.</u>, 125:174307, 2006.

[62] H. J. Lewandowski, E. R. Hudson, J.R. Bochinksi, and J. Ye. <u>Chem. Phys. Lett.</u>, 395:53, 2004.

[63] E. R. Hudson et al. <u>Phys. Rev. A</u>, 76:063404, 2006.

[64] B. C. Sawyer et al. Phys. Rev. Lett., 98:253002, 2007.

[65] O. F. Hagena. Rev. Sci. Inst., 62:2038, 1991.

[66] L. Li and D. M. Lubman. Rev. Sci. Instrum., 60:499, 1989.

[67] S. Y. T. van de Meerakker, Private Communication.

[68] D. Proch and T. Trickl. Rev. Sci. Instrum., 60:713, 1989.

[69] M. Hillenkamp, S. Keinan, and U. Even. J. Chem. Phys., 118:8699–8705, 2003.

[70] G.-H. Leu, C.-W. Hwang, and I-C. Chen. Chem. Phys. Lett., 257:481–486, 1996.

[71] K.-H. Gericke, S. Klee, F. J. Comes, and R. N. Dixon. J. Chem. Phys., 85:4463–4479, 1986.

[72] W. C. Campbell et al. Phys. Rev. Lett., 102:013003, 2009.

[73] W. C. Campbell, E. Tsikata, H.-I. Lu, L. D. van Buuren, and J. M. Doyle. Phys. Rev. Lett., 98:213001, 2007.

[74] M. T. Hummon et al. 2010. arXiv:1009.2513v1.

[75] J.R. Bochinksi, E. R. Hudson, H. J. Lewandowski, and J. Ye. Phys. Rev. A, 70:043410, 2004.

[76] S. D. Hogan, A. W. Wiederkehr, H. Schmutz, and F. Merkt. Phys. Rev. Lett., 101:143001, 2008.

[77] E. Narevicius et al. Phys. Rev. Lett., 100:093003, 2008.

[78] J. Sage, S. Sainis, T. Bergeman, and D. Demille. Phys. Rev. Lett., 94:203001, 2005.

[79] K.-K. Ni et al. Science, 322:231–235, 2008.

[80] F. Pobell. Matter and Methods at Low Temperatures. Springer-Verlag, 2 edition, 1996.

[81] J. W. Ekin. Experimental Techniques for Low-Temperature Measurements: Cryostat Design, Material Properties, and Superconductor Critical-Current Testing. Oxford University Press, 2006.

[82] D. Patterson. private communication.

[83] D. Patterson, J. Rasmussen, and J. M. Doyle. New J. Phys., 11:055018, 2009.

[84] D. Demille. AFOSR Ultracold Molecules MURI Review.

[85] C. Sommer et al. Faraday Discuss., 142:203–220, 2009.

[86] D. Patterson and J. M. Doyle. J. Chem. Phys., 126:154307, 2007.

[87] L. D. van Buuren et al. Phys. Rev. Lett., 102:033001, 2009.

[88] C. Sommer et al. Phys. Rev. A, 82:013410, 2010.

[89] W. C. Wiley and I. H. McLaren. Rev. Sci. Instrum., 26:1150–1157, 1955.

[90] L. Fusina and G. Di Lonardo. J. Mol. Spectrosc., 112:211–221, 1985.

[91] A. V. Avdeenkov and J. L. Bohn. Phys. Rev. A, 66:052718, 2002.

[92] Eric R. Hudson et al. Phys. Rev. A, 73:063404, 2006.

[93] D. DeMille. Phys. Rev. Lett., 88:067901, 2002.

[94] J. D. Weinstein, R. deCarvalho, T. Guillet, B. Friedrich, and J. M. Doyle. Nature, 395:148, 1998.

[95] Kevin M. Jones et al. Rev. Mod. Phys., 78:483, 2006.

[96] A. J. Kerman, J. M. Sage, S. Sainis, T. Bergeman, and D. Demille.

[97] H. L. Bethlem, G. Berden, and G. Meijer. Phys. Rev. Lett., 83:1558, 1999.

[98] H. L. Bethlem et al. Phys. Rev. A, 65:053416, 2002.

[99] S. Y. T. van de Meerakker, I. Labazan, S. Hoekstra, J. Kupper, and G. Meijer. J. Phys. B, 39:S1077–S1084, 2006.

[100] S. K. Tokunaga, J. M. Dyne, E. A. Hinds, and M. R. Tarbutt. New J. Phys., 11:055038, 2009.

[101] O. Bucicov, M. Nowak, S. Jung, G. Meijer, E. Tiemann, and C. Lisdat. Eur. Phys. J. D, 46:463–469, 2008.

[102] R. Latham. High Voltage Vacuum Insulation. Academic Press, London, 1995.

[103] S. Y. T. van de Meerakker et al. Phys. Rev. Lett., 94:023004, 2005.

[104] H. L. Bethlem, G. Berden, A. J. A. van Roij, F. M. H. Crompvoets, and G. Meijer. Phys. Rev. Lett., 84:5744–5747, 2000.

[105] B. C. Sawyer, B. K. Stuhl, B. L. Lev, J. Ye, and E. R. Hudson. Eur. Phys. J. D, 48:197–209, 2008.

[106] F. M. H. Crompvoets, H. L. Bethlem, J. Kupper, A.J.A. van Roij, and G. Meijer. Phys. Rev. A, 69:063406, 2004.

[107] H. Wiedemann. Particle Accelerator Physics I: Basic Principles and Linear Beam Dynamics. Berlin, 2nd edition, 2004.

[108] Sebastiaan Y. T. van de Meerakker, Nicolas Vanhaecke, Hendrick L. Bethlem, and Gerard Meijer. Phys. Rev. A, 71:053409, 2005.

[109] T. Suzuki. Particle Accelerators, 18:115, 1985.

[110] Sebastiaan Y. T. van de Meerakker, Nicolas Vanhaecke, Hendrick L. Bethlem, and Gerard Meijer. Phys. Rev. A, 73:023401, 2006.

[111] J. J. Gilijamse et al. Science, 313:1617–1620, 2006.

[112] J. R. Bochinski et al. Phys. Rev. A, 70:043410, 2004.

[113] T. Rieger et al. Phys. Rev. Lett., 95:173002, 2005.

[114] A.V. Avdeenkov and J.L. Bohn. Phys. Rev. A, 66:052718, 2002.

[115] J. van Veldhoven H. L. Bethlem and G. Meijer. Phys. Rev. Lett., 94:083001, 2005.

[116] D. Wang et al. Phys. Rev. Lett., 93:243005, 2004.

[117] J.D. Weinstein et al. Nature, 395:148, 1998.

[118] W. C. Campbell et al. Phys. Rev. Lett., 98:213001, 2007.

[119] T. V. Tscherbul and R. Krems. Phys. Rev. Lett., 97:083201, 2006.

[120] C. Ticknor and J. L. Bohn. Phys. Rev. A, 71:022709, 2005.

[121] M. Lara et al. Phys. Rev. A, 75:012704, 2007.

[122] P. Soldan and J. M. Hutson. Phys. Rev. Lett., 92:163202, 2004.

[123] M. Metsala, J. J. Gilijamse, S. Hoekstra, S. Y. T. van de Meerakker, and G. Meijer. New J. Phys., 10:053018, 2008.

[124] S. Y. T. van de Meerakker et al. Phys. Rev. A, 64:041401, 2001.

[125] S. Hoekstra. private communication.

[126] D. Demille. Phys. Rev. Lett., 88:067901, 2002.

[127] A. V. Avdeenkov, D. C. E. Bortolotti, and J. L. Bohn. Phys. Rev. A, 69:012710, 2004.

[128] A. Micheli et al. Nature Physics, 2:341, 2006.

[129] J. J. Hudson et al. Phys. Rev. Lett., 89:023003, 2002.

[130] W. C. Campbell et al. Phys. Rev. Lett., 100:083003, 2008.

[131] M. Elitzur. Rev. Mod. Phys., 54:1225, 1982.

[132] J. Guibert et al. Astron. Astrophys., 62:305, 1978.

[133] I. M. Hoffman et al. Astrophys. J., 598:1061, 2003.

[134] K. Park et al. J. Quant. Spectrosc. Radiat. Transfer, 55:285, 1995.

[135] R. V. Krems. Phys. Rev. Lett., 96:123202, 2006.

[136] M. Kirste et al. Phys. Rev. A, 82:042717, 2010.

[137] G. Scoles et al., editors. Atomic and Molecular Beam Methods. Oxford Univ. Pr., Cary, NC, USA, 1988.

[138] M. C. van Beek et al. Phys. Rev. Lett., 86:4001, 2001.

[139] M. H. Alexander et al. Investigation of steric effects in inelastic collisions of no with ar. J. Chem. Phys., 112:8017, 2000.

[140] M. J. L. de Lange et al. J. Chem. Phys., 121:11691, 2004.

[141] R. Cireasa et al. J. Chem. Phys., 123:64310, 2007.

[142] C. A. Taatjes et al. J. Phys. Chem. A, 111:7631, 2007.

[143] L. Scharfenberg et al. Phys. Chem. Chem. Phys., 12:10660–10670, 2010.

[144] T. V. Tscherbul, Z. Pavlovic, H. R. Sadeghpour, R. Côté, and A. Dalgarno. Phys. Rev. A, 82:022704, 2010.

[145] M.-J. Lu and J. D. Weinstein. New J. Phys., 11:055015, 2009.

[146] S. Willitsch, M. T. Bell, A. D. Gingell, S. R. Procter, and T. P. Softley. Phys. Rev. Lett., 100:043203, 2008.

[147] K. R. Lang and R. F. Wilson. Astrophys. J., 238:867, 1980.

[148] J. C. McConnell. J. Geophys. Res., 78:7812, 1973.

[149] T. Ridley et al. J. Chem. Phys., 131:234302, 2009.

[150] L. D. van Buuren et al. Phys. Rev. Lett., 102:033001, 2009.

[151] H. Cybulski et al. J. Chem. Phys., 122:094307, 2005.

[152] J. Perez-Rios et al. J. Phys. Chem. A, 113:14952–14960, 2009.

[153] T. V. Tscherbul, Y. V. Suleimanov, V. Aquilanti, and R. V. Krems. New J. Phys., 11:055021, 2009.

[154] A. R. Offer, M. C. van Hemert, and E. F. van Dishoeck. J. Chem. Phys., 100:362–378, 1994.

[155] T. V. Tscherbul et al. in preparation.

[156] H. J. Werner et al. Molpro, version 2008.1, a package of *ab initio* programs. see http://www.molpro.net.

[157] T. H. Dunning, Jr. J. Chem. Phys., 90:1007, 1989.

[158] M. T. Bell and T. P. Softley. Mol. Phys., 107:99–132, 2009.

[159] D. E. Fagnan et al. Phys. Rev. A, 80:022712, 2009.

[160] J.J. Sakurai. Modern Quantum Mechanics. Addison-Wesley, Reading, Massachussets.

[161] A. Derevianko, J. F. Babb, and A. Dalgarno. Phys. Rev. A, 63:052704, 2001.

[162] H. J. Metcalf and P. van der Straten. Laser Cooling and Trapping. Springer Publishing Co., New York, NY, 1999.

Appendix A

List of 2_0^5 ND$_3$ REMPI Transitions

For reference, a list of 2_0^5 REMPI transition frequencies and relative line strengths for ND$_3$ molecules is provided in the table below. The line strengths include only the angular momenta of the upper and lower states and do not account for nuclear or J degeneracy factors which ultimately must be included to simulate a thermal spectrum. To facilitate direct comparison with experimental spectra, the transition frequencies are given as single-photon energies in units of cm^{-1}. Only the ground state ($\tilde{X}^1 A'_1$ ($v_2 = 0$)) angular momentum quantum numbers J'' and K'' are given since K' levels in the intermediate $\tilde{B}^1 E''$ ($v_2 = 5$) state are mixed due to l-type doubling. Calculation of these transition frequencies and line strengths for ND$_3$ is detailed in Chapter 2.

J''	K''	Transition Frequency [cm^{-1}]	Strength	State Energy [cm^{-1}]
1	1	31496.612	0.9	8.3202
1	1	31505.576	1.4405	8.3202
1	1	31497.52	1.0595	8.3202
1	1	31519.023	0.48607	8.3202
1	1	31510.944	2.1139	8.3202
1	0	31492.55	1.8	10.3373
1	0	31501.194	1	10.3373
1	0	31515.341	3.2	10.3373
2	2	31490.7	1	22.8376

2	2	31499.662	2.1429	22.8376
2	2	31513.1	1.4263	22.8376
2	2	31497.003	2.5737	22.8376
2	2	31531.006	0.28639	22.8376
2	2	31514.911	2.5707	22.8376
2	1	31481.848	1	28.8846
2	1	31486.33	0.5	28.8846
2	1	31495.294	0.40045	28.8846
2	1	31487.238	2.0996	28.8846
2	1	31508.741	1.9942	28.8846
2	1	31500.661	0.0058184	28.8846
2	1	31526.671	0.82356	28.8846
2	1	31518.517	3.1764	28.8846
2	0	31482.11	3	30.9003
2	0	31491.39	0.71429	30.9003
2	0	31504.106	2	30.9003
2	0	31523.265	4.2857	30.9003
3	3	31488.838	2.5	43.6108
3	3	31502.281	2.9167	43.6108
3	3	31520.19	1.2679	43.6108
3	3	31496.06	4.2821	43.6108
3	3	31542.555	0.18097	43.6108
3	3	31518.455	2.8524	43.6108
3	2	31475.279	2	53.6787
3	2	31497.679	1.8368	53.6787
3	2	31481.583	2.8299	53.6787
3	2	31515.586	2.3742	53.6787

3	2	31499.49	0.42579	53.6787
3	2	31537.952	0.59133	53.6787
3	2	31521.823	3.942	53.6787
3	1	31470.912	1.6	59.7196
3	1	31479.877	1.0595	59.7196
3	1	31471.82	1.4405	59.7196
3	1	31493.324	0.30658	59.7196
3	1	31485.244	1.6768	59.7196
3	1	31511.253	2.6268	59.7196
3	1	31503.099	0.12324	59.7196
3	1	31533.665	1.0336	59.7196
3	1	31525.35	4.133	59.7196
3	0	31466.852	1.2	61.7332
3	0	31475.496	4	61.7332
3	0	31489.643	0.46667	61.7332
3	0	31506.26	3	61.7332
3	0	31530.571	5.3333	61.7332
4	4	31486.542	4.2	70.6487
4	4	31504.468	3.4364	70.6487
4	4	31526.851	1.1124	70.6487
4	4	31494.687	6.0876	70.6487
4	4	31553.673	0.12195	70.6487
4	4	31521.578	3.0417	70.6487
4	3	31468.281	2.5	84.7242
4	3	31481.724	0.35	84.7242
4	3	31499.634	3.1814	84.7242
4	3	31475.503	3.3231	84.7242

4	3	31521.998	2.3798	84.7242
4	3	31497.898	1.3202	84.7242
4	3	31548.802	0.42031	84.7242
4	3	31524.704	4.5251	84.7242
4	2	31463.692	2.8571	94.7783
4	2	31477.129	0.27261	94.7783
4	2	31461.033	1.3274	94.7783
4	2	31495.036	1.5862	94.7783
4	2	31478.941	2.9021	94.7783
4	2	31517.402	3.1869	94.7783
4	2	31501.273	0.013098	94.7783
4	2	31544.218	0.85275	94.7783
4	2	31527.996	5.0018	94.7783
4	1	31459.331	2.0996	100.8108
4	1	31451.274	0.40045	100.8108
4	1	31472.778	1.7093	100.8108
4	1	31464.698	2.2407	100.8108
4	1	31490.708	0.2783	100.8108
4	1	31482.554	1.3172	100.8108
4	1	31513.119	3.3564	100.8108
4	1	31504.805	0.34365	100.8108
4	1	31540.01	1.1235	100.8108
4	1	31531.409	5.131	100.8108
4	0	31455.429	2.2857	102.8217
4	0	31468.146	5	102.8217
4	0	31487.304	0.35065	102.8217
4	0	31507.643	4	102.8217

4	0	31537.244	6.3636	102.8217
5	5	31483.808	6	103.964
5	5	31506.224	3.8077	103.964
5	5	31533.083	0.98001	103.964
5	5	31492.883	7.9486	103.964
5	5	31564.364	0.086284	103.964
5	5	31524.28	3.1775	103.964
5	4	31460.852	2.8	122.0295
5	4	31478.778	1.2	122.0295
5	4	31501.161	4.2777	122.0295
5	4	31468.997	3.6761	122.0295
5	4	31527.982	2.2625	122.0295
5	4	31495.887	2.5089	122.0295
5	4	31559.223	0.30645	122.0295
5	4	31527.172	4.9683	122.0295
5	3	31456.046	3.7333	136.0808
5	3	31473.955	0.00036435	136.0808
5	3	31449.825	1.1996	136.0808
5	3	31496.32	3.0564	136.0808
5	3	31472.22	3.9103	136.0808
5	3	31523.124	3.3543	136.0808
5	3	31499.026	0.31709	136.0808
5	3	31554.351	0.65768	136.0808
5	3	31530.206	5.7709	136.0808
6	6	31480.631	7.8571	143.5732
6	6	31507.545	4.0857	143.5732
6	6	31538.887	0.87012	143.5732

6	6	31490.643	9.8442	143.5732
6	6	31574.632	0.063348	143.5732
6	6	31526.56	3.2795	143.5732
5	2	31451.46	3.4643	146.1176
5	2	31435.363	0.26908	146.1176
5	2	31469.366	0.80643	146.1176
5	2	31453.271	2.3936	146.1176
5	2	31491.733	1.4247	146.1176
5	2	31475.603	2.5804	146.1176
5	2	31518.548	3.9762	146.1176
5	2	31502.326	0.052408	146.1176
5	2	31549.798	1.0482	146.1176
5	2	31533.398	5.9847	146.1176
5	1	31447.114	2.5039	152.1398
5	1	31439.034	0.96276	152.1398
5	1	31465.043	2.478	152.1398
5	1	31456.889	2.722	152.1398
5	1	31487.455	0.27463	152.1398
5	1	31479.14	1.051	152.1398
5	1	31514.345	4.1903	152.1398
5	1	31505.745	0.50965	152.1398
5	1	31545.706	1.1101	152.1398
5	1	31536.655	6.1976	152.1398
5	0	31443.436	3.3333	154.1472
5	0	31460.053	6	154.1472
5	0	31484.364	0.28205	154.1472
5	0	31508.244	5	154.1472

5	0	31543.265	7.3846	154.1472
6	5	31452.987	3	165.6068
6	5	31475.403	2.3571	165.6068
6	5	31502.262	5.1594	165.6068
6	5	31462.061	3.9406	165.6068
6	5	31533.543	2.1103	165.6068
6	5	31493.459	3.8897	165.6068
6	5	31569.22	0.22937	165.6068
6	5	31529.23	5.3135	165.6068
6	4	31447.975	4.3636	183.6349
6	4	31470.358	0.19864	183.6349
6	4	31438.194	1.0871	183.6349
6	4	31497.18	4.4269	183.6349
6	4	31465.084	4.7238	183.6349
6	4	31528.42	3.3298	183.6349
6	4	31496.369	0.95594	183.6349
6	4	31564.057	0.50759	183.6349
6	4	31532.008	6.4067	183.6349
7	7	31477.004	9.75	189.4968
7	7	31508.427	4.3015	189.4968
7	7	31544.262	0.7788	189.4968
7	7	31487.961	11.7629	189.4968
7	7	31584.477	0.047859	189.4968
7	7	31528.415	3.359	189.4968
6	3	31443.167	4.5503	197.6572
6	3	31419.036	0.19515	197.6572
6	3	31465.531	0.21815	197.6572

6	3	31441.431	2.3676	197.6572
6	3	31492.336	2.8879	197.6572
6	3	31468.238	3.781	197.6572
6	3	31523.562	4.26	197.6572
6	3	31499.418	0.025678	197.6572
6	3	31559.19	0.86313	197.6572
6	3	31534.93	6.8512	197.6572
6	2	31438.588	3.9467	207.6734
6	2	31422.493	0.70781	207.6734
6	2	31460.955	1.4693	207.6734
6	2	31444.825	3.1878	207.6734
6	2	31487.77	1.3239	207.6734
6	2	31471.548	2.2216	207.6734
6	2	31519.02	4.7903	207.6734
6	2	31502.621	0.20967	207.6734
6	2	31554.688	1.1699	207.6734
6	2	31537.996	6.9729	207.6734
6	1	31434.272	2.7933	213.6831
6	1	31426.118	1.6612	213.6831
6	1	31456.683	3.3866	213.6831
6	1	31448.369	2.9706	213.6831
6	1	31483.573	0.2825	213.6831
6	1	31474.973	0.84867	213.6831
6	1	31514.934	5.1221	213.6831
6	1	31505.884	0.59219	213.6831
6	1	31550.75	1.0216	213.6831
6	1	31541.053	7.3213	213.6831

7	6	31444.682	3.1429	215.4719
7	6	31471.596	3.7143	215.4719
7	6	31502.938	5.875	215.4719
7	6	31454.693	4.146	215.4719
7	6	31538.683	1.9552	215.4719
7	6	31490.611	5.402	215.4719
7	6	31578.799	0.17562	215.4719
7	6	31530.881	5.5891	215.4719
6	0	31430.872	4.3636	215.6864
6	0	31451.211	7	215.6864
6	0	31480.811	0.23636	215.6864
6	0	31508.046	6	215.6864
6	0	31548.613	8.4	215.6864
7	5	31439.48	4.8352	237.4521
7	5	31466.339	0.75781	237.4521
7	5	31426.139	0.99219	237.4521
7	5	31497.62	5.6357	237.4521
7	5	31457.536	5.3852	237.4521
7	5	31533.297	3.217	237.4521
7	5	31493.308	1.8485	237.4521
7	5	31573.342	0.39627	237.4521
7	5	31533.41	6.9322	237.4521
8	8	31472.918	11.6667	241.7592
8	8	31508.865	4.4737	241.7592
8	8	31549.204	0.70227	241.7592
8	8	31484.83	13.6977	241.7592
8	8	31593.899	0.036986	241.7592

8	8	31529.84	3.4227	241.7592
7	4	31434.457	5.4112	255.4368
7	4	31402.293	0.14921	255.4368
7	4	31461.279	0.0023134	255.4368
7	4	31429.183	2.2834	255.4368
7	4	31492.519	4.3728	255.4368
7	4	31460.468	4.8483	255.4368
7	4	31528.156	4.3284	255.4368
7	4	31496.107	0.29062	255.4368
7	4	31568.161	0.69688	255.4368
7	4	31536.053	7.6168	255.4368
7	3	31429.647	5.1647	269.4255
7	3	31405.547	0.54958	269.4255
7	3	31456.452	0.6928	269.4255
7	3	31432.353	3.3429	269.4255
7	3	31487.678	2.7431	269.4255
7	3	31463.534	3.4492	269.4255
7	3	31523.306	5.1444	269.4255
7	3	31499.046	0.016275	269.4255
7	3	31563.31	1.0213	269.4255
7	3	31538.841	7.8757	269.4255
8	7	31435.93	3.25	271.6448
8	7	31467.353	5.2083	271.6448
8	7	31503.188	6.4641	271.6448
8	7	31446.887	4.31	271.6448
8	7	31543.403	1.8086	271.6448
8	7	31487.341	7.0081	271.6448

8	7	31587.963	0.13703	271.6448
8	7	31532.124	5.8138	271.6448
7	2	31425.083	4.3277	279.4177
7	2	31408.953	1.2767	279.4177
7	2	31451.898	2.2404	279.4177
7	2	31435.676	3.7596	279.4177
7	2	31483.148	1.2626	279.4177
7	2	31466.748	1.8935	279.4177
7	2	31518.816	5.6524	279.4177
7	2	31502.124	0.37139	279.4177
7	2	31558.879	1.2189	279.4177
7	2	31541.751	7.9968	279.4177
7	1	31420.818	2.9488	285.4131
7	1	31412.504	2.5017	285.4131
7	1	31447.708	4.4402	285.4131
7	1	31439.108	3.0241	285.4131
7	1	31479.069	0.29515	285.4131
7	1	31470.019	0.69022	285.4131
7	1	31514.885	6.1319	285.4131
7	1	31505.188	0.6002	285.4131
7	1	31555.129	0.89057	285.4131
7	1	31544.569	8.4771	285.4131
7	0	31417.732	5.3846	287.4116
7	0	31441.612	8	287.4116
7	0	31476.632	0.20362	287.4116
7	0	31507.03	7	287.4116
7	0	31553.267	9.4118	287.4116

8	6	31430.558	5.2	297.5479
8	6	31461.9	1.5873	297.5479
8	6	31413.655	0.91265	297.5479
8	6	31497.644	6.6854	297.5479
8	6	31449.573	5.9304	297.5479
8	6	31537.761	3.0667	297.5479
8	6	31489.843	2.9333	297.5479
8	6	31582.215	0.31337	297.5479
8	6	31534.417	7.3708	297.5479
9	9	31468.364	13.6	300.3891
9	9	31508.851	4.6143	300.3891
9	9	31553.708	0.63749	300.3891
9	9	31481.241	15.6443	300.3891
9	9	31602.896	0.029109	300.3891
9	9	31530.829	3.4748	300.3891
8	5	31425.332	6.1028	319.4676
8	5	31385.131	0.11864	319.4676
8	5	31456.612	0.12163	319.4676
8	5	31416.528	2.1819	319.4676
8	5	31492.29	5.7704	319.4676
8	5	31452.3	5.7792	319.4676
8	5	31532.335	4.2747	319.4676
8	5	31492.402	0.80859	319.4676
8	5	31576.715	0.56267	319.4676
8	5	31536.784	8.2794	319.4676
9	8	31426.723	3.3333	334.1494
9	8	31462.67	6.8	334.1494

9	8	31503.009	6.9561	334.1494
9	8	31438.635	4.4439	334.1494
9	8	31547.704	1.6742	334.1494
9	8	31483.645	8.6834	334.1494
9	8	31596.715	0.10863	334.1494
9	8	31532.958	6.0005	334.1494
8	4	31420.296	6.1863	337.403
8	4	31388.2	0.44223	337.403
8	4	31451.536	0.20525	337.403
8	4	31419.485	3.3662	337.403
8	4	31487.173	4.2667	337.403
8	4	31455.124	4.6211	337.403
8	4	31527.177	5.2884	337.403
8	4	31495.07	0.044956	337.403
8	4	31571.52	0.85714	337.403
8	4	31539.273	8.7218	337.403
8	3	31415.488	5.6447	351.3534
8	3	31391.39	1.0339	351.3534
8	3	31446.714	1.3262	351.3534
8	3	31422.57	4.1202	351.3534
8	3	31482.342	2.6317	351.3534
8	3	31458.082	3.0722	351.3534
8	3	31522.346	6.0375	351.3534
8	3	31497.877	0.11254	351.3534
8	3	31566.697	1.1255	351.3534
8	3	31541.901	8.8955	351.3534
8	2	31410.948	4.6067	361.3184

8	2	31394.726	1.9647	361.3184
8	2	31442.198	3.1207	361.3184
8	2	31425.798	4.1412	361.3184
8	2	31477.865	1.2269	361.3184
8	2	31461.173	1.6065	361.3184
8	2	31517.929	6.5715	361.3184
8	2	31500.8	0.49519	361.3184
8	2	31562.36	1.2033	361.3184
8	2	31544.624	9.0634	361.3184
9	7	31421.205	5.4902	363.9417
9	7	31457.039	2.6211	363.9417
9	7	31400.738	0.8456	363.9417
9	7	31497.254	7.5952	363.9417
9	7	31441.193	6.386	363.9417
9	7	31541.815	2.9038	363.9417
9	7	31485.976	4.1659	363.9417
9	7	31590.682	0.25082	363.9417
9	7	31535.034	7.7414	363.9417
10	10	31463.33	15.5455	365.4195
10	10	31508.376	4.7312	365.4195
10	10	31557.769	0.58208	365.4195
10	10	31477.182	17.5997	365.4195
10	10	31611.464	0.023255	365.4195
10	10	31531.374	3.5182	365.4195
8	1	31406.766	2.9634	367.2975
8	1	31398.166	3.4866	367.2975
8	1	31438.127	5.6235	367.2975

8	1	31429.076	2.9181	367.2975
8	1	31473.943	0.30811	367.2975
8	1	31464.246	0.56426	367.2975
8	1	31514.187	7.1933	367.2975
8	1	31503.626	0.55668	367.2975
8	1	31558.824	0.7459	367.2975
8	1	31547.172	9.6401	367.2975
8	0	31404.009	6.4	369.2906
8	0	31431.244	9	369.2906
8	0	31471.811	0.17895	369.2906
8	0	31505.177	8	369.2906
8	0	31557.201	10.4211	369.2906
9	6	31415.792	6.6675	389.7644
9	6	31367.547	0.097201	389.7644
9	6	31451.536	0.52094	389.7644
9	6	31403.465	2.0791	389.7644
9	6	31491.652	7.047	389.7644
9	6	31443.735	6.5883	389.7644
9	6	31536.107	4.1547	389.7644
9	6	31488.309	1.5362	389.7644
9	6	31584.862	0.45674	389.7644
9	6	31537.133	8.8524	389.7644
10	9	31417.051	3.4	403.0141
10	9	31457.538	8.4636	403.0141
10	9	31502.396	7.3722	403.0141
10	9	31429.928	4.5554	403.0141
10	9	31551.583	1.5525	403.0141

10	9	31479.517	10.4111	403.0141
10	9	31605.057	0.087252	403.0141
10	9	31533.379	6.1578	403.0141
9	5	31410.538	7.0461	411.6164
9	5	31370.454	0.3657	411.6164
9	5	31446.215	0.0071994	411.6164
9	5	31406.225	3.3261	411.6164
9	5	31486.26	5.7691	411.6164
9	5	31446.327	5.7001	411.6164
9	5	31530.641	5.2938	411.6164
9	5	31490.71	0.29707	411.6164
9	5	31579.32	0.71208	411.6164
9	5	31539.317	9.4827	411.6164
9	4	31405.49	6.7857	429.4967
9	4	31373.438	0.86131	429.4967
9	4	31441.126	0.64629	429.4967
9	4	31409.077	4.287	429.4967
9	4	31481.131	4.159	429.4967
9	4	31449.023	4.2606	429.4967
9	4	31525.473	6.2351	429.4967
9	4	31493.226	0.0012281	429.4967
9	4	31574.12	0.97857	429.4967
9	4	31541.627	9.7851	429.4967
10	8	31411.416	5.7263	436.6569
10	8	31451.755	3.8114	436.6569
10	8	31387.381	0.78859	436.6569
10	8	31496.45	8.3865	436.6569

190

10	8	31432.392	6.7718	436.6569
10	8	31545.462	2.7407	436.6569
10	8	31481.704	5.5139	436.6569
10	8	31598.747	0.20291	436.6569
10	8	31535.261	8.058	436.6569
11	11	31457.802	17.5	436.8882
11	11	31507.43	4.83	436.8882
11	11	31561.378	0.53423	436.8882
11	11	31472.643	19.5619	436.8882
11	11	31619.598	0.01881	436.8882
11	11	31531.465	3.555	436.8882
9	3	31400.689	6.013	443.4044
9	3	31376.545	1.634	443.4044
9	3	31436.316	2.0846	443.4044
9	3	31412.057	4.7154	443.4044
9	3	31476.32	2.5501	443.4044
9	3	31451.852	2.7029	443.4044
9	3	31520.672	6.957	443.4044
9	3	31495.876	0.23391	443.4044
9	3	31569.339	1.1749	443.4044
9	3	31544.07	9.9342	443.4044
9	2	31396.188	4.7781	453.339
9	2	31379.788	2.7709	453.339
9	2	31431.855	4.1125	453.339
9	2	31415.163	4.3541	453.339
9	2	31471.918	1.2069	453.339
9	2	31454.79	1.3584	453.339

9	2	31516.35	7.5469	453.339
9	2	31498.613	0.56829	453.339
9	2	31565.116	1.1364	453.339
9	2	31546.575	10.1675	453.339
9	1	31392.126	2.8491	459.2999
9	1	31383.075	4.6019	459.2999
9	1	31427.942	6.9022	459.2999
9	1	31418.245	2.6978	459.2999
9	1	31468.186	0.31847	459.2999
9	1	31457.625	0.46388	459.2999
9	1	31512.823	8.2807	459.2999
9	1	31501.171	0.48598	459.2999
9	1	31561.807	0.60727	459.2999
9	1	31548.835	10.7927	459.2999
9	0	31389.695	7.4118	461.2869
9	0	31420.093	10	461.2869
9	0	31466.33	0.15966	461.2869
9	0	31502.464	9	461.2869
9	0	31560.388	11.4286	461.2869
10	7	31405.837	7.136	466.3462
10	7	31349.536	0.081548	466.3462
10	7	31446.052	1.1493	466.3462
10	7	31389.991	1.981	466.3462
10	7	31490.612	8.1991	466.3462
10	7	31434.773	7.2934	466.3462
10	7	31539.479	4.0005	466.3462
10	7	31483.831	2.4359	466.3462

10	7	31592.611	0.37323	466.3462
10	7	31537.107	9.3501	466.3462
11	10	31406.904	3.4545	478.2712
11	10	31451.95	10.1818	478.2712
11	10	31501.343	7.7285	478.2712
11	10	31420.757	4.6497	478.2712
11	10	31555.038	1.4429	478.2712
11	10	31474.948	12.1795	478.2712
11	10	31612.987	0.070864	478.2712
11	10	31533.382	6.2922	478.2712
10	6	31400.378	7.7751	492.0803
10	6	31352.307	0.30908	492.0803
10	6	31440.495	0.071861	492.0803
10	6	31392.577	3.2554	492.0803
10	6	31484.949	7.1951	492.0803
10	6	31437.151	6.6788	492.0803
10	6	31533.704	5.2131	492.0803
10	6	31485.975	0.75055	492.0803
10	6	31586.719	0.59089	492.0803
10	6	31538.99	10.1601	492.0803
10	5	31395.095	7.776	513.8577
10	5	31355.105	0.73273	513.8577
10	5	31435.14	0.21284	513.8577
10	5	31395.207	4.3478	513.8577
10	5	31479.52	5.7177	513.8577
10	5	31439.589	5.4026	513.8577
10	5	31528.2	6.2911	513.8577

10	5	31488.196	0.072516	513.8577
10	5	31581.139	0.83386	513.8577
10	5	31540.968	10.6128	513.8577
12	12	31451.766	19.4615	514.8376
12	12	31505.999	4.9145	514.8376
12	12	31564.526	0.49256	514.8376
12	12	31467.607	21.5294	514.8376
12	12	31627.291	0.015373	514.8376
12	12	31531.089	3.5866	514.8376
11	9	31401.185	5.9221	515.7213
11	9	31446.042	5.124	515.7213
11	9	31373.574	0.73966	515.7213
11	9	31495.229	9.0784	515.7213
11	9	31423.163	7.1023	515.7213
11	9	31548.703	2.5833	515.7213
11	9	31477.025	6.9534	515.7213
11	9	31606.415	0.16569	515.7213
11	9	31535.098	8.3312	515.7213
10	4	31390.036	7.251	531.6772
10	4	31357.987	1.3946	531.6772
10	4	31430.04	1.2554	531.6772
10	4	31397.933	5.0416	531.6772
10	4	31474.383	4.0659	531.6772
10	4	31442.135	3.8579	531.6772
10	4	31523.029	7.1874	531.6772
10	4	31490.537	0.049002	531.6772
10	4	31575.94	1.0567	531.6772

10	4	31543.075	10.8405	531.6772
10	3	31385.25	6.2761	545.5378
10	3	31360.99	2.3449	545.5378
10	3	31425.253	2.9561	545.5378
10	3	31400.785	5.1439	545.5378
10	3	31469.605	2.4915	545.5378
10	3	31444.809	2.359	545.5378
10	3	31518.272	7.9123	545.5378
10	3	31493.004	0.3422	545.5378
10	3	31571.216	1.1736	545.5378
10	3	31545.306	11.0003	545.5378
11	8	31395.465	7.5303	549.2359
11	8	31331.091	0.069737	549.2359
11	8	31440.16	1.9645	549.2359
11	8	31376.102	1.89	549.2359
11	8	31489.172	9.2346	549.2359
11	8	31425.415	7.9109	549.2359
11	8	31542.457	3.8308	549.2359
11	8	31478.971	3.4769	549.2359
11	8	31599.969	0.30701	549.2359
11	8	31536.71	9.7853	549.2359
10	2	31380.805	4.8383	555.4388
10	2	31364.113	3.6951	555.4388
10	2	31420.868	5.2134	555.4388
10	2	31403.74	4.4169	555.4388
10	2	31465.3	1.1954	555.4388
10	2	31447.563	1.1453	555.4388

10	2	31514.066	8.5711	555.4388
10	2	31495.525	0.5925	555.4388
10	2	31567.127	1.0343	555.4388
10	2	31547.566	11.2978	555.4388
12	11	31396.267	3.5	559.958
12	11	31445.895	11.9423	559.958
12	11	31499.843	8.0367	559.958
12	11	31411.108	4.7304	559.958
12	11	31558.063	1.3442	559.958
12	11	31469.93	13.98	559.958
12	11	31620.502	0.058094	559.958
12	11	31532.961	6.4083	559.958
10	1	31376.902	2.6362	561.3796
10	1	31367.205	5.8165	561.3796
10	1	31417.146	8.2325	561.3796
10	1	31406.585	2.4129	561.3796
10	1	31461.783	0.3248	561.3796
10	1	31450.131	0.38423	561.3796
10	1	31510.767	9.3748	561.3796
10	1	31497.795	0.40702	561.3796
10	1	31564.046	0.48499	561.3796
10	1	31549.53	11.9261	561.3796
10	0	31374.777	8.4211	563.3599
10	0	31408.143	11	563.3599
10	0	31460.167	0.14416	563.3599
10	0	31498.864	10	563.3599
10	0	31562.798	12.4348	563.3599

11	7	31389.819	8.399	578.8129
11	7	31333.757	0.2659	578.8129
11	7	31434.379	0.36558	578.8129
11	7	31378.54	3.1708	578.8129
11	7	31483.246	8.5234	578.8129
11	7	31427.598	7.5617	578.8129
11	7	31536.378	5.0804	578.8129
11	7	31480.873	1.3793	578.8129
11	7	31593.728	0.49134	578.8129
11	7	31538.302	10.7625	578.8129
13	13	31445.203	21.4286	599.3149
13	13	31504.069	4.9877	599.3149
13	13	31567.199	0.45598	599.3149
13	13	31462.059	23.5012	599.3149
13	13	31634.533	0.012674	599.3149
13	13	31530.234	3.6139	599.3149